THÈSE

en vue de l'obtention du grade de

Docteur d'Aix-Marseille Université

Spécialité : Mécanique et physique des fluides

Laboratoire IRPHÉ UMR7342

École Doctorale 353

Soutenance prévue le 4/06/2019
par **Jean-Baptiste Wacheul**

Étude de la fragmentation de métal liquide en chute libre dans un environnement visqueux : application à la formation des planètes

---

Sous la direction de Michaël Le Bars

Devant la commission d'examen formée de :

M.	Jacques Magnaudet	*IMFT*	Rapporteur
M.	Nicolas Coltice	*ENS Ulm*	Rapporteur
M.	Renaud Deguen	*LGLTPE*	Examinateur
Mme.	Laurence Bergougnoux	*IUSTI*	Examinateur
M.	Emmanuel Villermaux	*IRPHE*	Examinateur
M.	Henri Samuel	*IPGP*	Examinateur
M.	Michaël Le Bars	*IRPHE*	Directeur de thèse

Institut de Recherche sur les
Phénomène Hors Équilibre
49 rue Joliot-Curie
13384 Marseille CEDEX 13

École doctorale 353
5 rue Enrico Fermi
13453 Marseille CEDEX 13

Remerciements

Table des matières

Table des figures

Chapitre I

Introduction aux problèmes abordés

A La formation des planètes telluriques

1 Naissance du système solaire et accrétion des planètes

Il était une fois l'Univers. Notre modeste entendement peine à faire naître une image en réponse à une telle introduction mais c'est pourtant de notre Univers dont nous allons parler dans ce manuscrit. Dès à présent, il nous faut être clément avec notre entendement, sans quoi cette lecture commencerait par un vertige, en se limitant au fonctionnement actuel de notre Univers et non pas à son histoire toute entière. De même, nous faisons remarquer au lecteur que l'esprit le plus patient au monde ne pourrait pas contempler son imagination suffisamment longtemps pour recréer une image honnête de notre Univers, tant ses dimensions nous sont étrangères. Les plus chanceux d'entre nous peuvent se vanter d'avoir un jour observé une galaxie dans un télescope. Et pourtant il en existe des amas, formant une sorte de réseau, chacun séparé par des espaces plus grands encore. En toute modestie, nous allons donc nous contenter de fabriquer des planètes, des planètes particulières qui plus est, car il s'agit de la classe de planètes ressemblant à la notre, des planètes telluriques. Définir une planète tellurique constitue une anticipation à cette étape de notre exposé, car il nous faut dire quelques mots sur le contexte plus général de la formation de ces planètes. Il nous faut parler de la genèse des systèmes solaires. Permettons-nous tout de même un pas de fourmi dans cette anticipation en posant cette idée simple qui guidera la compréhension : ce sont les différents processus que subiront les constituants des planètes qui définiront une classe de planètes dite telluriques.

Précisons. Réduisons la physique de notre Univers à une physique Newtonienne ainsi qu'à un brin de physique nucléaire. Ou plutôt deux brins : la fusion nucléaire qui allumera notre étoile et la désintégration radioactive, qui entrainera la transformation d'éléments chimiques en d'autres, enregistrant dans les matériaux la trace d'évènements passés. Donnons-nous une composition moyenne de l'Univers visible (la matière noire elle aussi échappera à un traitement sérieux dans ce modeste exposé). L'hydrogène en composera la majorité mais ce sont les très rares éléments formés par l'explosion d'étoiles mortes il y a bien longtemps qui occuperont la majorité de nos considérations. De manière générale, les bilans chimiques se feront sur les éléments de numéro atomique inférieur à celui du fer, fer inclus. Les autres éléments, très minoritaires, n'en sont pas moins importants car ils prennent le statut de traceurs dans les processus que subit la matière pendant la formation

des planètes. Donnons-nous un état de la matière : celle-ci est à l'époque sous forme de gaz.

Cette image simple nous la prendrons comme point de départ. Un système solaire commence donc par être un nuage de gaz moléculaire. Ce gaz est confiné seulement par sa propre gravité, de sorte que sa pression est infime. Néanmoins, il se refroidit sur les bords par radiation, et en parallèle se contracte, sa densité augmente. D'autre part, ce nuage tourne sur lui même, mais cette rotation n'est pas uniforme. L'équilibre des forces d'un point de vue local est donc entre la pression, la gravité, et la force centrifuge ce qui tend à former un disque plus dense vers le plan équatorial et plus dense à mesure que l'on s'aventure vers le centre. Cet équilibre de forces associé à ces variations de densité est sujet à des instabilités (**?**, **?**) qui tendent à dissiper l'énergie cinétique. A l'échelle globale de ce disque proto-planétaire, cette dissipation se traduit elle aussi par une contraction.

La pression augmente donc dans le disque proto-planétaire jusqu'à allumer des réactions nucléaires en son centre. Ici, un équilibre est rapidement atteint entre la gravité et le gain de pression dû à la chaleur de la fusion nucléaire. C'est ce gigantesque réacteur central qui deviendra notre étoile. La pression, ainsi que des anomalies locales de température permettent aussi aux éléments dits réfractaires (favorables à la condensation solide) de former la phase solide la plus vieille que l'on ait pu découvrir dans le système solaire. Ces cristaux sont réunis en des inclusions riches en calcium et aluminium (CAI) dans les météorites considérées comme des systèmes fermés à partir de leur dernière solidification. En 2002, Amelin et collègues (**?**) ont mesuré la quantité d' ^{235}U , ^{238}U , ^{207}Pb et ^{206}Pb dans plusieurs échantillons météoriques. L' ^{235}U se décompose en ^{207}Pb et l' ^{238}U en ^{206}Pb mais en suivant des temps caractéristiques très différents, ce qui permit à Amelin et collègues (**?**) de déduire l'âge de la fermeture du système, c'est-à-dire de la formation des CAI. Celui-ci est d'environ 4570 Ma. Du fait de leur cristallisation précoce au sein de leur système solaire, ces CAI sont très importantes vis-à-vis de la datation du système solaire et leurs compositions en éléments réfractaires et en isotopes issus de désintégrations radioactives souvent prises pour référence. Les datations des objets du système solaire à partir des proportions des différents éléments impliqués dans les décompositions nucléaires sont donc généralement des datations relatives où la formation des CAI constitue l'origine du temps.

Après la cristallisation des premières phases solides, le disque proto-planétaire rentre dans l'étape de sa formation qui est à ce jour la moins bien connue : les poussières s'agrègent peu à peu pour former des objets de toutes tailles allant du centimètre au kilomètre. Les mécanismes pour réussir à former des objets cohérents sont limités par le fait que les deux interactions possibles, les forces de surface et la gravité, sont relativement faibles sur cette gamme de taille. S'il est possible que de la turbulence soit présente au sein du disque pour produire des anomalies de densité locales (**?**, **?**), les forces en question semblent incapables pour l'instant d'expliquer la stabilisation de telles masses. Malgré cela, les preuves de la formation précoce ($<$ 3Ma) d'objets de taille kilométrique au sein du système solaire que l'on retrouve maintenant dans la ceinture de Kuiper semblent confirmer ce scénario (**?**, **?**).

Parmi les différentes phases solides qui cristallisent dans le disque protoplanétaires, l'état d'oxydo-réduction des éléments dicte deux types de phases qui sont immiscibles même fondues : des cristaux ioniques et des métaux. Paradoxalement ces métaux et cristaux sont d'une certaine manière mélangés car lors de l'agrégation des poussières, aucun tri significatif n'est possible et la grande majorité des météorites retrouvées ont une texture où le métal et les cristaux ioniques se cotoient à l'échelle du millimètre. Le métal qui

est constitué principalement de fer et de nickel, est beaucoup plus dense que les cristaux ioniques (principalement des silicates et des oxydes). De ce fait, pour les objets les plus grands (*i.e.* qui ont la gravité la plus forte), cette différence de densité fait qu'être constitué d'un matériau homogène correspond à un maximum de potentiel gravitationnel. C'est pourquoi des objets comme la Terre sont différenciés : le métal a majoritairement migré au centre, constituant un noyau et les silicates sont restés dans les couches externes, formant le manteau. On sait d'ailleurs qu'un certain nombre de petits objets (appelé planétésimaux) se sont différenciés très rapidement (**?**, **?**, **?**, **?**, **?**) : cette différenciation ne peut se produire pour des objets avec une gravité si faible sans qu'une fusion quasi totale de l'objet n'ait lieu. La seule source d'énergie qui pourrait expliquer une fusion aussi rapide sur un corps aussi petit est la décomposition radioactive d' ^{26}Al, et comme celui-ci se décompose sur un temps caractéristique de l'ordre de 1 Ma, cela implique que l'agrégation n'a pu être moins rapide.

D'une manière générale, la différenciation des planétésimaux et protoplanètes est un évènement qui se passe contemporainement à l'agrégation d'objets de plus en plus grands. Le jeune système solaire va d'abord passer par une phase de croissance en cascades (**?**, **?**), où les interactions entre planétésimaux (d'une taille initiale de l'ordre de 10km) favorisent les collisions faisant croître les plus gros d'entre eux. D'après les simulations kepleriennes à N-corps, cette phase de croissance explosive voit l'apparition de proto-planètes (**?**, **?**) : des objets ayant la masse d'une fraction de celle de la Terre. Ces proto-planètes ont un taux de croissance plus important encore que les planétésimaux encore présents dans le système solaire. Leurs orbites ne sont pas stables et elles croissent donc en collectant la masse restante. En conséquence, les dernières collisions impliquent des proto-planètes avec des objets relativement grands allant des derniers planétésimaux restant à d'autres proto-planètes (figure **??**).

Si l'agrégation de la matière solide en des objets de plus en plus grands va nous intéresser particulièrement, l'histoire des éléments volatiles (par opposition aux éléments réfractaires) apporte d'autres domaines de complexités à l'étude des premiers âges du système solaire. En effet, les volatiles sont les éléments qui tendent à rester gazeux. De ce fait, ils subissent une migration à l'allumage du soleil et s'accumulent principalement au-delà d'une limite que l'on appelle la snow line. C'est principalement cette limite qui va définir les objets telluriques : ces derniers sont des corps qui se sont formés trop proches, ou qui n'ont pas gagné assez de masse avant l'apparition de cette snow line pour retenir la majorité des éléments volatiles de leur voisinage. L'objet tellurique le plus étudié est la Terre, pourtant même sur Terre les quantités de volatiles retenus posent questions. Pour n'en citer qu'une, l'hydrogène de nos océans par exemple. Deux raisons principales sont à pointer du doigt concernant ce problème : les volatiles restent très longtemps gazeux et tendent à être repoussés au-delà de la snow line, mais ils sont aussi solubles dans les phases condensées. Ces phases condensées peuvent dégazer durant l'accrétion des objets telluriques, mais le temps caractéristique est très dépendant du régime géodynamique dans lequel ces objets sont. Autrement dit, est-ce que ces objets sont rigides ou est-ce qu'ils sont partiellement fondus, rendant possibles des mouvements de convection capables de réduire drastiquement le temps caractéristique de dégazage. Dans le cas des dernières collisions entre proto-planètes, une vaporisation sous l'effet de l'onde de choc est même à envisager, auquel cas une quantité importante de volatiles pourrait être perdue (**?**). En outre, nous avons mentionné que l'état d'oxydo-réduction des éléments réfractaires conditionne leur

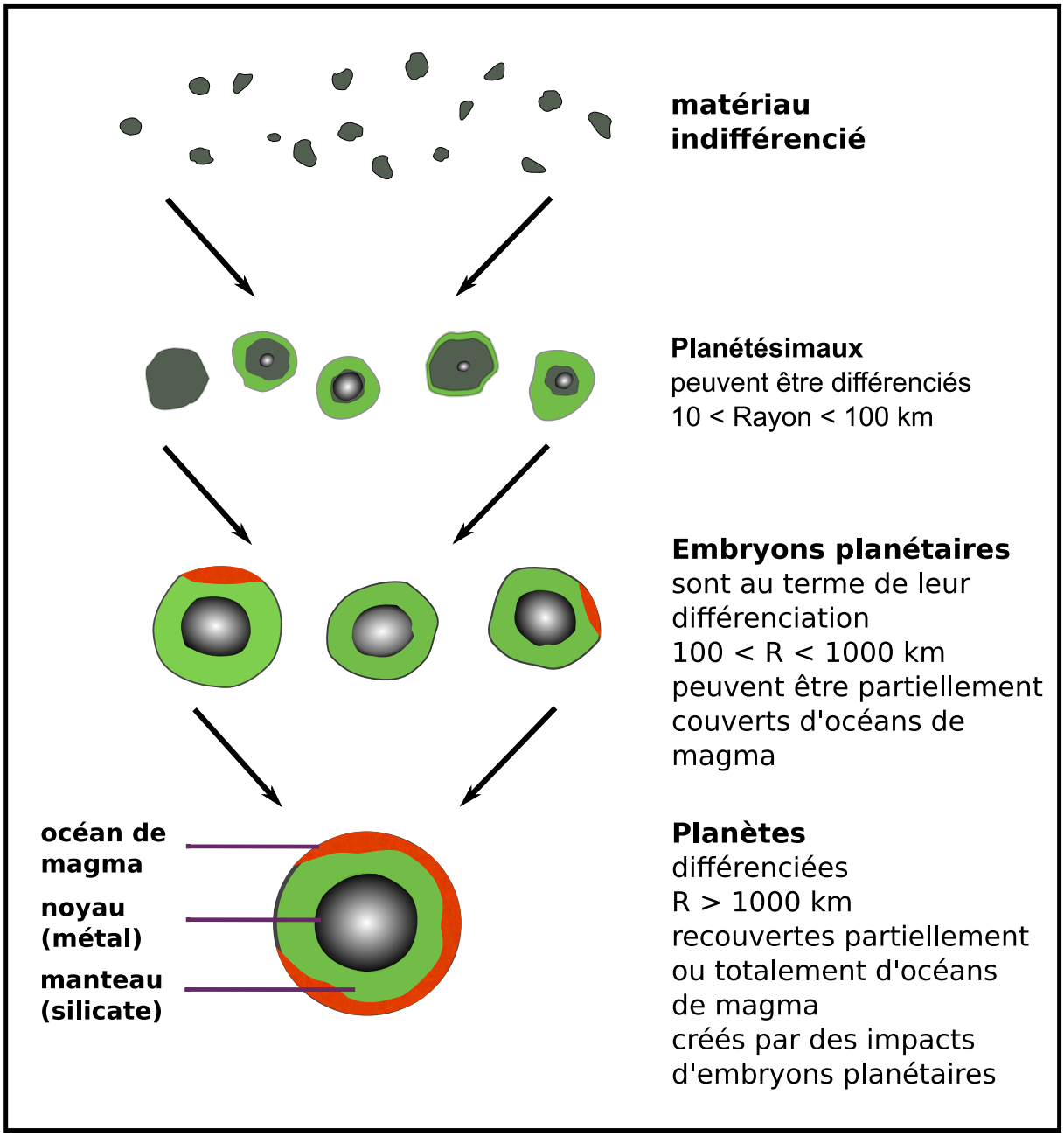

FIGURE I.1 – Schéma représentant les étapes de l'accrétion des matériaux primitifs du système solaire par collisions successives.

répartition entre le métal et les cristaux ioniques. En particulier, la quantité de soufre (?) ainsi que d'oxygène semble être des variables ajustables de la chimie des objets telluriques. Des objets dits réduits (avec une concentration en oxygène peu importante) voient plus d'éléments passer dans la phase métallique (en particulier Fe et Si) et peuvent ainsi présenter un noyau métallique plus gros en proportion que des corps plus oxydés.

2 Indétermination composition-processus

Nous avons accès à un échantillon d'objets qui sont présents depuis le début du système solaire (à commencer par la Terre, le Soleil, les météorites, les échantillons lunaires ...) mais la variété des processus qui ont transformé la composition locale et globale de ces objets rend la tâche comparable à dénouer le nœud gordien. La composition actuelle des objets en question n'est pas toujours connue (la totalité de la Terre ne peut pas être analysée), cette composition a évolué au cours du temps, et son état initial est mal contraint. L'art consiste donc à inverser la chronologie et l'intensité de ces processus grâce aux compositions locales et globales. Comme le montre le cas simple de CAI, cela nous est au moins partiellement accessible grâce à la définition de systèmes chimiques ainsi que l'usage de l'intégralité des relations de conservation que l'on peut dégager de la classification périodique des éléments.

Deux tendances majeures dans les propriétés des éléments chimiques vont induire du tri au cours de la formation des planètes. En premier, le caractère volatile mentionné précédemment tend à trier les éléments entre solides et gaz/liquides et, à cause d'un tri précoce entre ces phases dans le disque proto-planétaire, définit aussi la dichotomie planète gazeuse/planète tellurique. Il s'oppose au caractère réfractaire. En deuxième, le caractère lithophile des éléments, lié à l'état d'oxydation, est la propension à se concentrer dans les cristaux ioniques (des silicates en grande partie) plutôt que dans le métal (principalement du fer). Il s'oppose au caractère sidérophile. A ces deux polarités se superposent les isotopes de chacun de ces éléments, en particulier les isotopes radioactifs. Grâce aux différents temps de décroissance radioactifs, les données recueillies par les géochimistes permettent de sonder à la fois l'intensité et la chronologie des processus ayant été à l'oeuvre dans l'enfance du système solaire (cf. **??**).

Attardons nous sur un example qui nous est proche, tant et si bien qu'il est un enjeu de la présente étude. Le tungstène (W) est un élément à tendance sidérophile tandis que le hafnium (Hf) est un élément à tendance lithophile. Au moment de la formation du système solaire, le ^{182}Hf est présent en quantité significative mais en pleine décomposition radioactive en ^{182}W. La différence de partition entre Hf et W signifie que tout excès de ^{182}W dans la phase silicatée est du à un excès de ^{182}Hf au moment où le système "silicate" se retrouve incapable d'échanger des éléments avec le système "fer", au moment où il est isolé. Cet évènement est considéré comme le moment où le corps tellurique d'où vient l'échantillon considéré s'est différencié. Ainsi il est généralement admis que l'on peut déterminer la date de la formation du noyau terrestre, martien etc. en remontant à la quantité de ^{182} Hf au dernier contact entre le métal et les silicates (cf. fig. **??**).

Dater le moment où le métal et les silicates se sont complètement équilibrés est toutefois un réel défi (**?**, **?**, **?**). Si la formation du noyau est certainement un processus qui fait passer le métal et le silicate d'un complet équilibre chimique à une relative isolation chimique (car les distances de diffusion typiques passent de l'échelle du grain à plusieurs kilomètres), des collisions entre proto-planètes peuvent se produire et c'est alors l'occasion pour le métal et le silicate de se mélanger une dernière fois. Ce mélange est très probablement partiel. En addition de quoi le coefficient de partition du ^{182}W dépend de la pression, de la température et de la fugacité de l'oxygène dans lesquels vont se produire ce mélange partiel. C'est le problème sur lequel cette étude s'est concentrée : quelles sont les conditions déterminant la ré-équilibration partielle du fer et du silicate après un impact entre proto-planètes telluriques. Nous avons détaillé le cas de l'équilibrage du tungstène comme générant des indéterminations dans les interprétations actuelles des données géochimiques. De la même

TABLE 1. Main isotopic decay systems in use in studying the origin and early evolution of the terrestrial planets.

Parent	Daughter(s)	Half-Life (yr)	Status*	Principal Applications and Comments
Long-lived				
^{40}K (10.7%)	^{40}Ar	1.25×10^{9}	✓	Chronology, especially lunar bombardment
^{40}K (89.3%)	^{40}Ca	1.25×10^{9}	✓	Not used greatly
^{87}Rb	^{87}Sr	4.75×10^{10}	✓	Chronology, refractory/volatile fractionations
^{138}La (66.4%)	^{138}Ba	1.05×10^{11}	✓	Not used greatly
^{138}La (33.6%)	^{138}Ce	1.05×10^{11}	✓	Not used greatly
^{147}Sm	^{143}Nd	1.06×10^{11}	✓	Chronology and early silicate differentiation
^{176}Lu	^{176}Hf	3.57×10^{10}	✓	Chronology and early silicate differentiation
^{187}Re	^{187}Os	4.23×10^{10}	✓	Chronology of metals
^{190}Pt	^{186}Os	6.5×10^{11}	✓	Not used greatly
^{232}Th	^{208}Pb	1.40×10^{10}	✓	Time-averaged Th/U
^{235}U	^{207}Pb	7.04×10^{8}	✓	Chronology, refractory/volatile fractionations
^{238}U	^{206}Pb	4.47×10^{9}	✓	Chronology, refractory/volatile fractionations
Extinct				
^{7}Be	^{7}Li	1.459×10^{-1}	?	CAI formation
^{10}Be	^{10}B	1.5×10^{6}	✓	CAI formation
^{26}Al	^{26}Mg	7.3×10^{5}	✓	CAIs, chondrules, early silicate melting, heat
^{41}Ca	^{41}K	1.04×10^{5}	✓	CAI formation
^{53}Mn	^{53}Cr	3.7×10^{6}	✓	Early silicate melting and provenance
^{60}Fe	^{60}Ni	1.49×10^{6}	✓	Massive star signature, early metals, heat
^{92}Nb	^{92}Zr	3.6×10^{7}	✓	*p*-process signature, disk heterogeneity
^{93}Zr	^{93}Nb	1.53×10^{6}	?	Daughter is monoisotopic
^{97}Tc	^{97}Mo	2.6×10^{6}	?	*p*-process signature, disk heterogeneity
^{98}Tc	^{98}Mo	4.2×10^{6}	?	*s*-process signature, disk heterogeneity
^{99}Tc	^{99}Ru	2.13×10^{5}	?	*s*-process signature, disk heterogeneity
^{107}Pd	^{107}Ag	6.5×10^{6}	✓	Metal and refractory/volatile chronology
^{126}Sn	^{126}Te	2.35×10^{5}	?	*r*-process signature
^{129}I	^{129}Xe	1.57×10^{7}	✓	CAI, chondrule chronology, degassing
^{135}Cs	^{135}Ba	2.3×10^{6}	?	Refractory/volatile fractionations
^{146}Sm	^{142}Nd	1.03×10^{8}	✓	Early solar system, crustal evolution
^{182}Hf	^{182}W	8.9×10^{6}	✓	*r*-process, metal, accretion chronology
^{205}Pb	^{205}Tl	1.5×10^{7}	✓	*s*-process signature
^{244}Pu	^{136}Xe†	8×10^{7}	✓	CAI, chondrule chronology, degassing
^{247}Cm	^{235}U	1.6×10^{7}	?	Supernova *r*-process

*A check mark means that the nuclide's presence or former presence has been established. Nuclides with a question mark are still not convincingly demonstrated.
† Spontaneous fissionogenic product.

FIGURE I.2 – Tableau extrait de **?** présentant les paires d'éléments père/fis liés par la désintégration radioactive (un atome de "père" se désintègre spontanément en un atome de "fils") utilisés dans la datation des différents processus ayant été à l'œuvre lors de la formation du système solaire.

manière, des éléments chimiques majeurs font question comme le souffre, l'oxygène, le silicium etc. et peuvent avoir été échangés entre le métal et les silicates dans les mêmes circonstances. En addition, les études actuelles laissent à penser que le matériel accrété à la Terre contient une certaine tendance : la matière accrétée plus tardivement aurait été plus oxydée (**?**, **?** ,**?**, **?**, **?**). On remarquera alors un des chemins d'inversion de la composition : l'âge de différenciation est estimé grâce au chronomètre ^{182}Hf/ ^{182}W. Cette quantité dépend

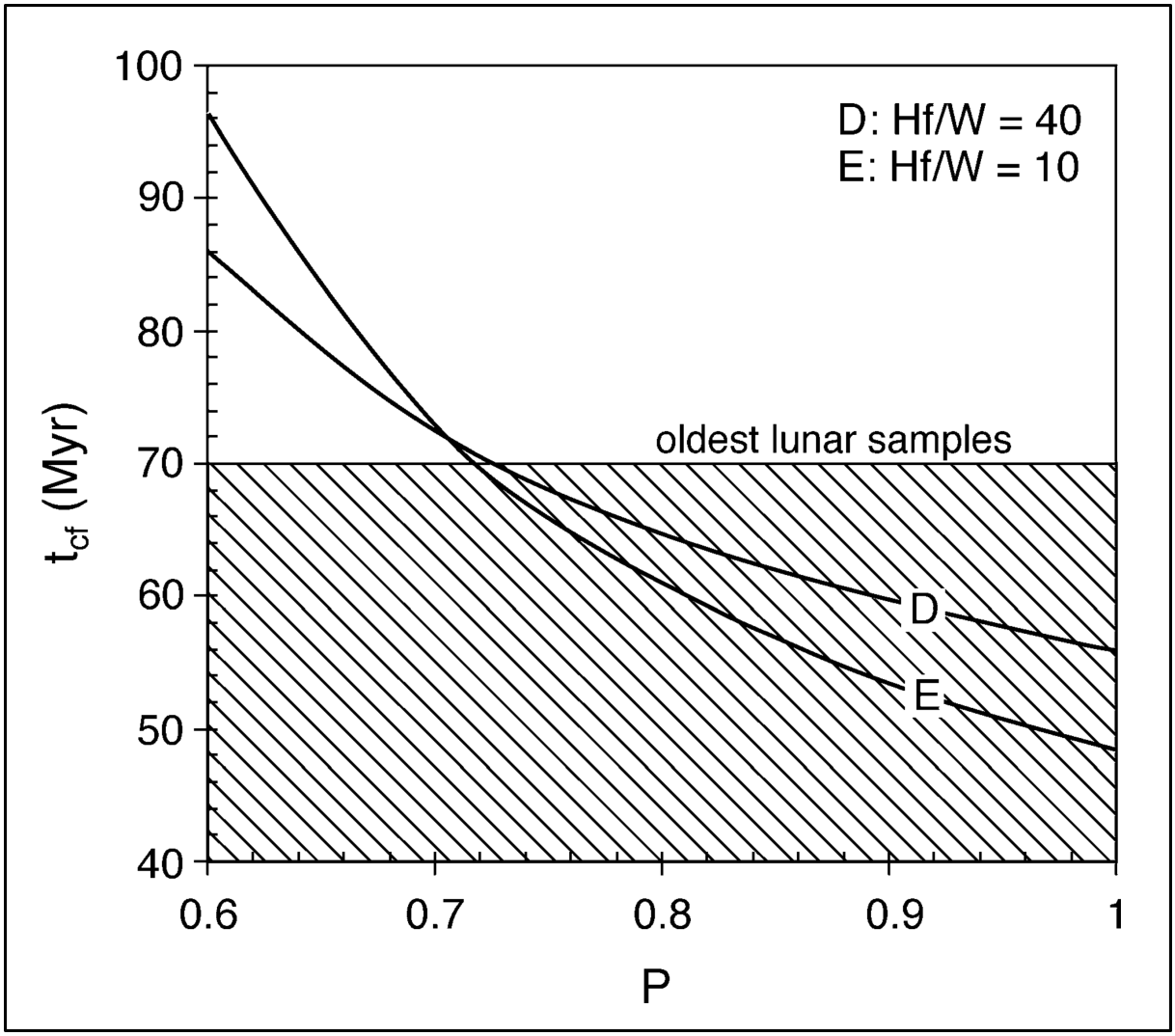

FIGURE I.3 – Graphique montrant l'âge calculé du noyau terrestre en fonction du degré d'équilibration P entre le matériau brut (métal et silicate) s'étant ajouté à la Terre après la formation du noyau (extrait de **?**). Les deux courbes sont réalisées à partir de deux valeurs différentes du rapport des quantités des éléments Hf et W dans la roche initiale. La ligne horizontale représente l'âge des roches lunaires, qui, d'après le scénario de la formation de la Lune via un impact géant, ne peut être plus ancien que la formation du noyau. Ce dernier aurait en effet de toute façon été formé à la suite d'un tel impact.

du brassage provoqué par l'impact, dont la magnitude est modulée par les coefficients de diffusion. Ces derniers sont influencés par la fugacité de l'oxygène, par la pression et par la température (**?**, **?**). Cette dernière peut évoluer au cours de l'accrétion des différents objets à la proto-Terre. A mesure que l'interprétation du chronomètre est corrigée de l'influence des impacts, on doit vérifier la compatibilité de la chronologie résultante avec l'arrivée de planétésimaux de la composition en question.

Parallèlement à la composition, l'impact entre proto-planètes est aussi capable de mélanger la température. Mais à cause des impacts eux-même et de la différence de répartition des radio-nucléides entre le métal et les silicates, les proto-planétes sont aussi

inhomogènes en température. L'état initial thermique du manteau (silicate) et du noyau (fer) est donc potentiellement fortement influencé par les impacts. Le champ magnétique terrestre étant généralement considéré comme une conséquence de la convection naturelle du noyau, on peut concevoir que les ramifications de ces collisions géantes s'étendent très au-delà de l'enfance de la Terre.

3 L'écoulement post-impact

Les impacts entre proto-planètes impliquent de grandes quantités d'énergie cinétique. Typiquement, ils se passent à des vitesses de l'ordre de la vitesse d'échappement des planètes. Prenons deux planètes ayant une masse d'un huitième de la masse de la Terre, soit $M = 7,5.10^{23} kg$. En première approximation, on prendra leur rayon égal à un demi rayon de la Terre, soit $R = 3,2.10^{6} m$. L'énergie cinétique par unité de masse e est donc :

$$e = \frac{G.M}{R} = 1,56.10^{7} J.kg^{-1} \tag{I.1}$$

La vitesse d'échappement v est donc donnée par :

$$v = \sqrt{2.e} = 7,9.10^{3} m.s^{-1} \tag{I.2}$$

avec G la constante de gravitation universelle. En considérant que la capacité thermique massique des silicates est de l'ordre d'environ 1000 $J.K^{-1}.kg^{-1}$, cette énergie cinétique par unité de masse, complètement convertie en énergie thermique, correspondrait à une élévation de température de l'ordre de $10^4 K$. Cette quantité d'énergie est donc suffisante pour produire une fusion de grande ampleur du manteau (**?** , **?**, **?**, **?**). Étant donnée la rapidité avec laquelle cette énergie est délivrée, il est généralement admis que les planètes telluriques voient leur manteau de silicate fondre en un océan de magma à la suite de ces impacts (**?**, **?**). De plus, si l'agrégation de ces proto-planètes est suffisamment rapide, elles peuvent contenir un résidu important de l'énergie apportée par la décomposition de l' ^{26}Al, qui peut dans certains cas être suffisant pour passer le solidus (**?**) et ainsi provoquer une fusion à grande échelle du manteau (fig. **??**). La Terre a donc connu très probablement une ou plusieurs phases d'océan de magma profond (**?**) alors que des impacteurs différenciés de plus en plus grands (en moyenne) viennent l'impacter. Il en résulte un écoulement diphasique à grande échelle (**?**) entre le magma et le fer liquide.

Bien que les simulations actuelles soient très limitées par les différentes échelles de physique à considérer, il semble que l'impact lui-même provoque un mélange limité du noyau de fer liquide, qui tend à se déformer en un pancake à la surface de l'océan de magma (**?**, **?**). Ce métal, bien que déjà partiellement mélangé, ne peut toutefois pas stagner à la surface après l'impact et va rapidement tomber au fond de l'océan de magma à cause de sa forte différence de densité avec celui-ci (la différence de densité $\Delta\rho$ est d'environ 4000 $kg.m^{-3}$ entre le fer liquide et le magma). Introduisons dès maintenant les paramètres dominants de cette dynamique. L'échelle typique de notre écoulement est voisine de celle du rayon de l'impacteur R et peut donc varier avec l'impacteur. Elle peut aller jusqu'à $R \sim 1000\ km$. D'après les simulations *ab initio* (**?**) et les expériences (**?**, **?**) la viscosité dynamique du magma peut varier de $10^{-3}\ Pa.s$ à $10^{2}\ Pa.s$. À ces échelles, la viscosité ne peut influer significativement la vitesse typique de l'écoulement. Cette hypothèse se vérifie en se donnant la loi d'échelle non visqueuse pour la vitesse de chute du métal, et

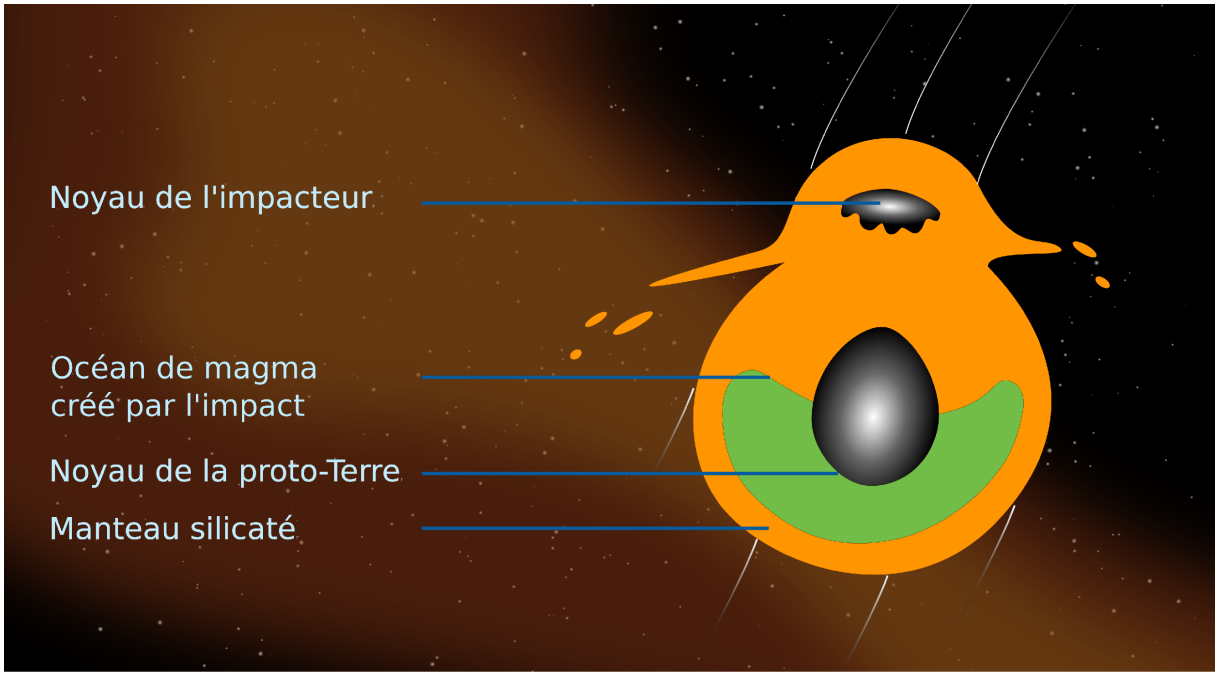

FIGURE I.4 – Schéma représentant une collision entre une proto-planète tellurique et un planétésimal après la différenciation du matériau brut des planètes en un noyau de métal liquide et un manteau de roches silicatées fondues.

en calculant le nombre de Reynolds de l'écoulement à partir de cette vitesse. Lorsque la viscosité n'importe pas, la vitesse terminale d'une masse de fer liquide de rayon R (plus tard appelé diapir) est atteinte après une phase d'accélération qui voit la flottabilité être compensée par la pression dynamique. Une fois intégré sur la surface exposée à l'écoulement cela donne :

$$Cd \cdot \frac{1}{2}\rho_a U^2 \cdot S \sim \Delta\rho g R^3 \qquad \text{avec} \qquad \Delta\rho = \rho_m - \rho_a \tag{I.3}$$

Cd est le coefficient de trainée, un nombre sans dimension dont l'ordre de grandeur est 1, ρ_m est la masse volumique du fer liquide (environ $7000 kg.m^{-3}$) et ρ_a celle les silicates fondus (environ $3000 kg.m^{-3}$) et S est l'aire de surface projetée du diapir dans le plan perpendiculaire à l'écoulement. En supposant que cette aire est environ égale à celle d'une sphère, on a

$$U \sim \left(\frac{\Delta\rho}{\rho_a}.g.R\right)^{\frac{1}{2}}. \tag{I.4}$$

où U est la vitesse de chute du fer liquide. Le nombre de Reynolds Re compare l'inertie de l'écoulement aux forces de viscosité. Il doit être très supérieur à 1 pour vérifier l'hypothèse non-visqueuse. On prend l'accélération de la gravité g égale à sa valeur actuelle de $9.81 m.s^{-2}$. L'ordre de grandeur de la vitesse non visqueuse (newtonienne) est de $10^3\ m.s^{-1}$. On peut donc calculer le nombre de Reynolds

$$Re = \frac{\rho_a.U.R}{\eta_a} \tag{I.5}$$

Que l'on prenne les vitesses d'impact ou la vitesse newtonienne de chute du diapir, on trouve $10^{10} \leq Re \leq 10^{15}$. L'autre nombre sans dimension dominant la dynamique globale est le nombre de Weber We, qui compare l'inertie et la tension de surface entre les deux fluides :

$$We = \frac{\rho_a.U^2.R}{\sigma} \tag{I.6}$$

où σ est la tension de surface entre les deux fluides ($\simeq 1 J.m^{-2}$ entre le fer et le magma). Pour les impacts géants, $We \sim 10^{16}$. Le nombre de Reynolds et le nombre de Weber étant tous les deux très supérieurs à 1, l'écoulement post-impact est reconnu dans la littérature comme étant un écoulement très turbulent et où la tension de surface ne peut s'opposer aux variations de pression dynamique dues aux mouvements de l'écoulement, *i.e.* il est sujet à une fragmentation rapide. En marchant dans les traces des auteurs qui ont estimé la taille limite d'une goutte stable en chute libre dans un océan de magma au moment de la différenciation du noyau (**?**, **?**, **?**), il a été communément supposé que le fer liquide se fragmenterait très rapidement en de petites gouttes de la taille capillaire (**?**, **?**, **?**). En effet l'échelle capillaire l_σ est l'échelle à laquelle la tension de surface compense la pression due à la différence de densité. Comme on a supposé que la pression dynamique équilibre la pression due à la différence de densité (vitesse terminale newtonienne), il en résulte que l'échelle à laquelle la tension de surface empêche la pression dynamique de fragmenter les gouttes est bien l'échelle capillaire :

$$l_\sigma \sim \sqrt{\frac{\sigma}{\Delta\rho.g}}. \tag{I.7}$$

Pour la Terre, cette échelle est de l'ordre de un centimètre. C'est pourquoi dans la littérature il est fréquent de supposer que l'équilibration se produit à l'échelle d'une goutte centimétrique chutant à sa vitesse terminale (**?**, **?**) ce qui, d'après les théories de transferts diffusifs et les simulations (**?** , **?** , **?**), correspond à une équilibration rapide : la longueur d'équilibration n'excède pas 100 m pour l'équilibration chimique et quelques mètres pour l'équilibration thermique. Néanmoins, il est peu probable que l'on puisse simplifier l'écoulement post-impact à ce point. Tout d'abord, il n'est pas certain qu'un diapir résultant d'un impact géant avec $R \sim 10^6$ m puisse se fragmenter avant d'atteindre le fond de l'océan de magma (**?**), en partie à cause de l'auto-gravité du noyau qui tend à ralentir son mélange, et en partie à cause du rapport d'aspect entre le rayon du diapir et la profondeur de l'océan de magma. Plus précisément, H. Samuel en 2012 (**?**) a montré à l'aide de simulations axisymétriques qu'une distance incompressible était à attendre afin que le processus de fragmentation puisse produire des gouttes de taille propre à une équilibration rapide, ce qui est confirmé par les connaissances sur la fragmentation des gouttes d'eau en chute libre dans l'air (**?**). Parallèlement, R. Deguen et ses collaborateurs en 2011 (**?**) ont souligné que l'écoulement qui suit immédiatement la fragmentation ne peut être considéré comme un ensemble de gouttes chutant indépendamment les unes des autres. En effet, si l'on en croit les estimations de dilution du fer liquide dans le magma due à l'impact seul (**?**, **?**), on peut s'attendre à un facteur de 10 à 100. La poussée d'Archimède totale du diapir est conservée car le "volume de fluide déplacé" est celui du fer, qui ne change pas. Autrement dit la flottabilité ne change pas mais la surface de cette masse de fluide dilué est multipliée au maximum par $100^{\frac{2}{3}}$, ce qui diminue la vitesse d'après

l'équation **??** d'un facteur $100^{\frac{1}{3}}$. Pour un diapir de 10 km de rayon, cette estimation conservative laisse la vitesse de l'ordre de 100 $m.s^{-1}$. Par ailleurs, en utilisant la même loi d'échelle pour les gouttes de taille l_σ, leur vitesse ne dépasse pas $1m.s^{-1}$. C'est pourquoi les gouttes de métal ne peuvent chuter individuellement mais commencent au contraire à chuter collectivement. Le nombre de Rouse $\mathcal{R}$ décrit cette transition entre mouvement collectif et chute des gouttes indépendamment les unes des autres. Il est défini comme le rapport de la vitesse de chute terminale des gouttes v_s et la vitesse typique de l'écoulement U :

$$\mathcal{R} = \frac{v_s}{U} \tag{I.8}$$

Comme le montre la figure **??** extraite de l'étude de R. Deguen de 2011 (**?**) qui montre plusieurs expériences de lâché de fluide chargé en particules ayant un nombre de Rouse autour de la transition, les particules sont prisonnières d'un écoulement à grande échelle tant que $\mathcal{R} << 1$. La différence de densité de la suspension est intialement d'une valeur à peu près constante entre les expériences.

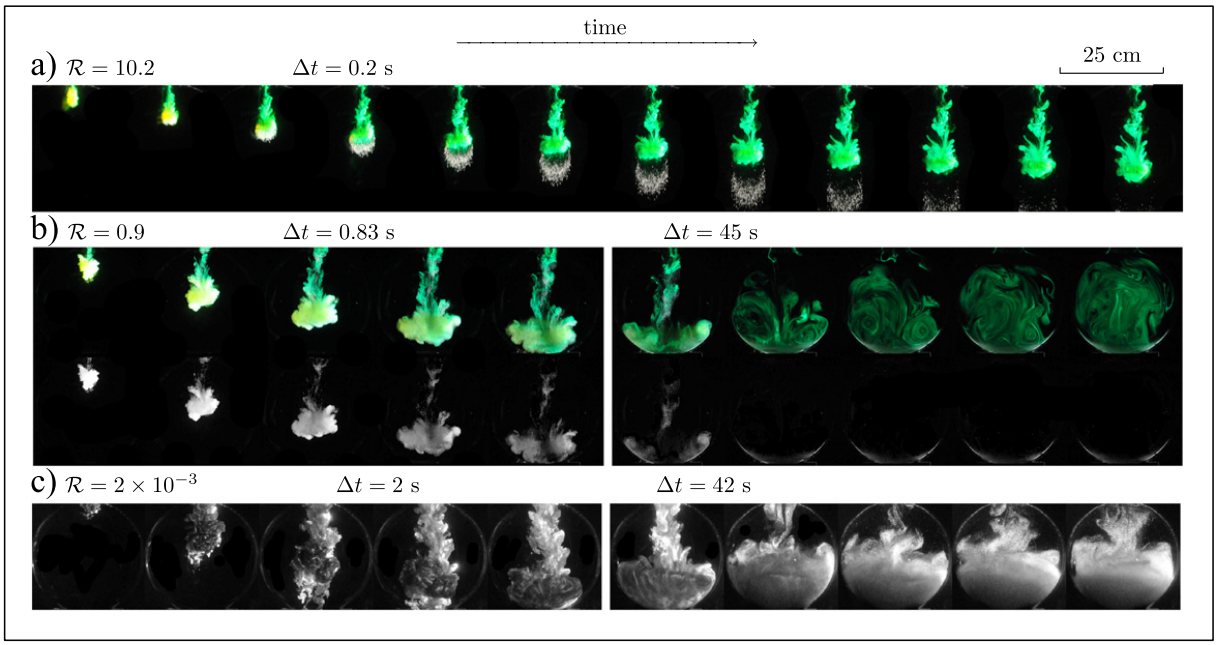

FIGURE I.5 – Série de photos extraite de **?** montrant le lâché d'une suspension de particules. Les images en noir et blanc montrent les particules et les images en couleur montrent par fluorescence d'un colorant le fluide ayant été relâché avec les particules. Trois expériences sont montrées avec des particules monodisperses dont le diamètre est croissant de bas en haut. La vitesse de sédimentation des particules relativement à la vitesse de chute globale $\mathcal{R}$ est donc croissante de bas en haut.

Pour décrire quantitativement ce moment collectif à l'échelle de l'océan de magma, on peut assimiler le mélange fer liquide et magma à un fluide miscible de densité supérieure au fluide environnant (on ignore les interfaces en jugeant que comme $We >> 1$, la tension de surface n'a pas d'effet significatif à grande échelle). Le lâché d'une masse finie et localisée de fluide dense dans un autre fluide en l'absence d'effets visqueux notables forme un écoulement bien connu de la littérature (**?**, **?**, **?**, **?**) appelé thermique turbulent. Ce

modèle peut aussi s'appliquer aux suspensions de particules (**?**, **?**) et de gouttes (**?**, **?**). Il prédit la dilution de la masse de fer liquide en fonction de la profondeur ce qui permet de quantifier précisément quelles quantités de chaleur ou d'éléments tels que le tungstène peuvent être échangées, ce qui permet d'apporter un argument physique aux proportions de manteau équilibré utilisées dans les modèles de construction de la Terre (**?**, **?**). De plus des expériences récentes suggèrent que ce modèle peut être appliqué avant même que le métal ne se fragmente (**?**, **?**), ce qui ouvre la voie à la quantification des échanges entre fer liquide et silicates avant la fragmentation (**?**). Nous détaillerons le modèle de thermique turbulent dans la partie 1.F.

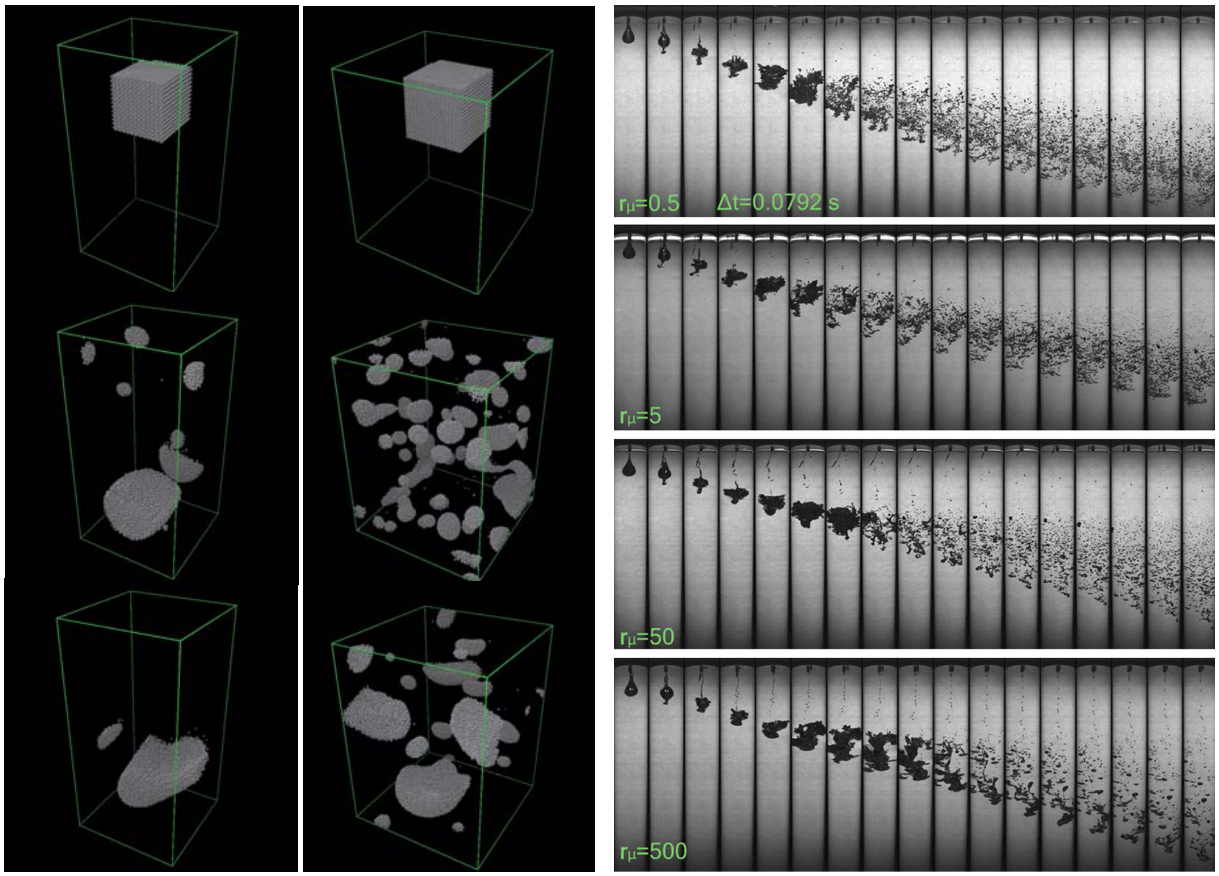

FIGURE I.6 – Panneau de gauche : graphes d'isocontours de densité d'une simulation 3D d'écoulement diphasique gravitaire avec $Re = 15$, $We = 4.5$, $R_\mu = 1$ et $\frac{rho_m}{\rho_a} = 2$ (extraite d' **?**). Panneau de droite : série de photos issues d'expériences de chute de gallium liquide dans un mélange d'eau et de glycérol. Le rayon initial du diapir de gallium est le même pour chaque expérience à environ $0.031m$ et la viscosité du fluide ambient est croissante de haut en bas. Ceci correspond à $We = 48$, $\frac{rho_m}{\rho_a} = 6$, et de bas en haut $Re = 30$ et $R_\mu = 500$, $Re = 300$ et $R_\mu = 50$, $Re = 2600$ et $R_\mu = 5$, $Re = 52000$ et $R_\mu = 0.5$.

Parallèlement, la supposition selon laquelle la taille finale de goutte correspondrait à une unique valeur n'a été testée que par un nombre très limité d'études. H. Ichikawa et collègues (**?**) ont reporté en 2010 des simulations en 3D (cf. fig. **??**, panneau de gauche) dans lesquelles une distribution de tailles de goutte apparaissait. Néanmoins, le domaine de simulation étant périodique dans la direction de chute, les gouttes ne pouvaient pas

présenter de mouvement collectif à cause de l'écoulement de retour. Puisque c'est ce mouvement à grande échelle qui injecte l'énergie qui cascade aux échelles où la tension superficielle forme les gouttes, il n'est pas certain que la physique de la fragmentation de l'écoulement post-impact soit proprement capturée. Dans une étude précédant ce travail de thèse (**?**), nous avons réalisé des expériences utilisant un système de fluides analogues nous permettant de faire varier le rapport de viscosité entre les 2 fluides de façon systématique (cf. fig. **??**, panneau de droite), un paramètre négligé des études sur le sujet de l'écoulement post-impact. Nous avons pu constater une stabilisation de gouttes de plus grande taille pour des rapports de viscosité plus hauts, mais ces résultats sont restés majoritairement qualitatifs en raison de la taille de l'expérience, qui gênait la visualisation et provoquait des effets de bords.

En conclusion, le présent manuscrit a pour but de faire le rapport de nouvelles expériences dédiées à faire progresser la quantification de la dilution du fer liquide au cours de sa chute dans l'océan de magma, ainsi que les échanges diffusifs pouvant avoir lieu entre les deux phases dans ce contexte.

B Paramètres adimensionnés de la chute libre d'une masse localisée de fluide immiscible

Afin d'étudier l'écoulement post-impact, on partira d'une situation simplifiée où une masse de liquide est lâchée de façon localisée (le diapir) et sans vitesse initiale sous la surface d'un autre fluide de densité inférieure avec lequel il est immiscible. Les deux fluides seront considérés Newtoniens. De façon générale, la dynamique de l'écoulement résultant est décrite complètement par un ensemble de 3 équations que sont les équations de Navier-Stokes dans le fluide ambiant et dans le fluide du diapir, et l'équation du saut de pression de Laplace. On suppose l'écoulement incompressible. En version adimensionnée par les propriétés du fluide ambiant, l'équation de Navier-Stokes dans le fluide du diapir fait apparaître :

$$\frac{d\tilde{\vec{u}}}{d\tilde{t}} + \left(\tilde{\vec{u}}.\nabla\right)\tilde{\vec{u}} = \frac{1}{\tilde{\rho}}.\left(-\nabla\tilde{p} + Cd.\vec{e_z} + \frac{1}{R_\mu}\cdot\frac{1}{Re}.\triangle\,\tilde{\vec{u}}\right) \tag{I.9}$$

Les variables et les opérateurs différentiels ont été adimensionnés par U la vitesse typique du diapir, R son rayon initial (il est supposé initialement sphérique), et la densité du fluide ambiant ρ_a. $\vec{e_z}$ est le vecteur unitaire de l'axe vertical, orienté vers le haut. On peut retrouver l'équation de Navier-Stokes pour le fluide ambiant en prenant respectivement 1, 1 et 0 comme valeurs pour le rapport de viscosité $R_\mu = \frac{\mu_a}{\mu_m}$, le rapport de densité $\tilde{\rho} = \frac{\rho_m}{\rho_a}$ et le coefficient de trainée. $\tilde{p}$ est la pression non-hydrostatique (dynamique), la partie hydrostatique étant contenue dans le terme de flottabilité qui adimensionnée donne Cd. En supposant que Re tend vers l'infini, on retrouve l'équilibre implicite entre la poussée d'Archimède et la pression dynamique lorsque la vitesse est de l'ordre de la vitesse terminale, avec un coefficient de trainé de l'ordre de 1 (equation **??**). Dans le fluide ambiant, le terme d'advection équilibre la pression dynamique ($(\tilde{u}.\nabla)\,\tilde{u} \simeq -\frac{1}{\tilde{\rho}}.\nabla\tilde{p}$). Á l'échelle du diapir, la pression dynamique équilibre la flottabilité ($\nabla\tilde{p} \simeq Cd$).

Le nombre de Mach Ma est le rapport de la vitesse des ondes de pressions sur la vitesse typique de l'écoulement. Il apparait dans la version compressible de l'équation

de Navier-Stokes. Pour des impacts géants ($R \gtrsim 1000\ km$), on a vu que la vitesse est de l'ordre de $10^4\ km.s^{-1}$, ce qui est aussi l'ordre de grandeur de la vitesse des ondes de pression. Les écoulements pour les impacts les plus grands sont donc marqués par des effets compressibles. Notre expérience se limitera à des régimes où les effets compressibles sont négligeables.

La dernière équation, le saut de pression de Laplace, s'applique à l'interface entre les deux fluides.

$$\Delta p_{inter} = \sigma\kappa \tag{I.10}$$

Δp_{inter} est la différence de pression à l'interface et κ est la courbure de l'interface. En suivant l'idée que l'équilibre pression dynamique et inertie de l'écoulement domine la dynamique, le rapport entre la pression dynamique et le saut de pression capillaire est donné par le nombre de Weber

$$\frac{\Delta p_{inter}}{\nabla p} \sim \frac{\sigma.\frac{1}{R}}{\rho_a.U^2} = We^{-1} \tag{I.11}$$

Pour les discussions qui vont suivre, les nombres sans dimension qui nous importeront pour la description seront donc :

$$Re = \frac{\rho_a.U.R}{\mu_a} \quad We = \frac{\rho_a.U^2.R}{\sigma} \quad R_\mu = \frac{\mu_a}{\mu_m}$$

$$Cd = \frac{8}{3}\frac{\Delta\rho.g.R}{\rho_a.U^2} \qquad \tilde{\rho} = \frac{\rho_m}{\rho_a}$$

Il est important de noter que pour des petites gouttes ou à l'occasion de considérations locales, l'équilibre entre l'inertie de l'écoulement et la flottabilité ne sera pas forcément respecté, on parlera alors aussi en terme de nombre de Bond, qui compare les forces de flottabilité avec la tension de surface :

$$Bo = \frac{\Delta\rho g R^2}{\sigma} \tag{I.12}$$

Quand l'équilibre entre l'inertie de l'écoulement et la flottabilité est vérifiée, on a donc l'égalité :

$$Bo = \frac{3}{8}Cd.We \tag{I.13}$$

qui rend redondant l'utilisation du nombre de Bond pour décrire les grandes échelles de l'écoulement. En dernier lieu, on pourra aussi parler en terme de nombre de Morton, à des fins de comparaison avec la littérature :

$$Mo = \frac{g.\mu_m^4.\Delta\rho}{\rho_m^2.\sigma^3} \tag{I.14}$$

Le nombre de Morton est très largement utilisé dans la littérature de façon adjointe au nombre de Bond afin d'étudier l'influence des propriétés physiques des différents fluides sur la dynamique à l'aide d'un nombre maximum de paramètres adimensionnés définis de façon *a priori*. Cependant, son interprétation physique apparaît moins directe, et nous nous contenterons de mentionner le nombre de Morton dans le seul but de comparer à des

études précédentes, et d'extrapoler leurs nombreux résultats à notre système de fluide en dépit d'un nombre de Morton différent.

C Vitesse de chute de gouttes

Les gouttes en chute libre, au sens large, c'est-à-dire une masse continue et localisée de fluide évoluant dans un fluide immiscible de densité différente, en étant soumis à sa poussée d'Archimède et sa trainée, sont ubiquistes. En particulier dans les applications industrielles où le passage d'un fluide dans un autre sous forme de gouttes permet d'extraire de façon sélective et contrôlée des composés chimiques, ou même d'en déposer. Une littérature considérable (**?**, **?**) existe donc sur les différents paramètres régissant le transfert de masse entre une goutte et le fluide stagnant dans lequel elle évolue, en particulier la vitesse de sédimentation. Il n'est pas ici question de ne serait-ce que toucher à une synthèse de cette littérature, puisque l'hypothèse de stabilité de la goutte et l'hypothèse de fluide stagnant ne seront jamais simultanément vérifiées dans notre problème. On se contentera donc de résumer les tendances globales qui dominent la chute libre des gouttes.

En persistant dans notre formalisme, on peut définir le coefficient de trainée de la même manière que précédemment, mais sa généralisation aux domaines où les forces de viscosités sont très supérieures à l'inertie de l'écoulement implique que la vitesse de chute va être déterminée par les forces de viscosité, donc que le coefficient de trainée va dépendre du nombre de Reynolds. De plus, comme les frottements visqueux sur la surface de la goutte vont entrainer un écoulement à l'intérieur de la goutte et ainsi répartir le travail résistant des forces visqueuses (**?**, **?**), la solution dépend de R_μ :

$$Cd(Re) = \frac{12}{Re}.\left(\frac{\frac{2}{3}+\frac{1}{R_\mu}}{1+\frac{1}{R_\mu}}\right). \tag{I.15}$$

A mesure que le nombre de Reynolds se rapproche de 1, l'inertie du fluide déplacé par la goutte commence à se surajouter sur la trainée visqueuse : une correction en Re permet de prédire la vitesse de sédimentation jusqu'à environ $Re \simeq 1$ (**?**)

$$Cd(Re) = \frac{12}{Re}.\left(\left(\frac{\frac{2}{3}+\frac{1}{R_\mu}}{1+\frac{1}{R_\mu}}\right)+\frac{3}{8}.Re.\left(\frac{\frac{2}{3}+\frac{1}{R_\mu}}{1+\frac{1}{R_\mu}}\right)^2\right). \tag{I.16}$$

Pour des rapports de viscosité non nuls, à mesure que le nombre de Reynolds augmente, la viscosité de l'intérieur commence à prendre une importance trop grande et l'écoulement se réorganise ; plus précisément il existe un nombre de Reynolds pour lequel une goutte même sphérique voit ses couches limites se décrocher. Une bulle de recirculation se forme à l'arrière de la goutte et définit un domaine, en dehors de la goutte, où les lignes de courant sont fermées. Ceci conduit à une augmentation des effets inertiels vis à vis des effets visqueux. La loi d'échelle du coefficient de trainée converge donc vers une valeur unique. Pour des bulles d'air, cette valeur a été calculée (**?**) dans la limite des nombres de Weber et Reynolds tendant vers l'infini, et des expériences (**?**) donnent une valeur proche pour les gouttes (R_μ non nul) :

$$Cd(Re) = \frac{8}{3} \qquad We \to +\infty; Re \to +\infty. \tag{I.17}$$

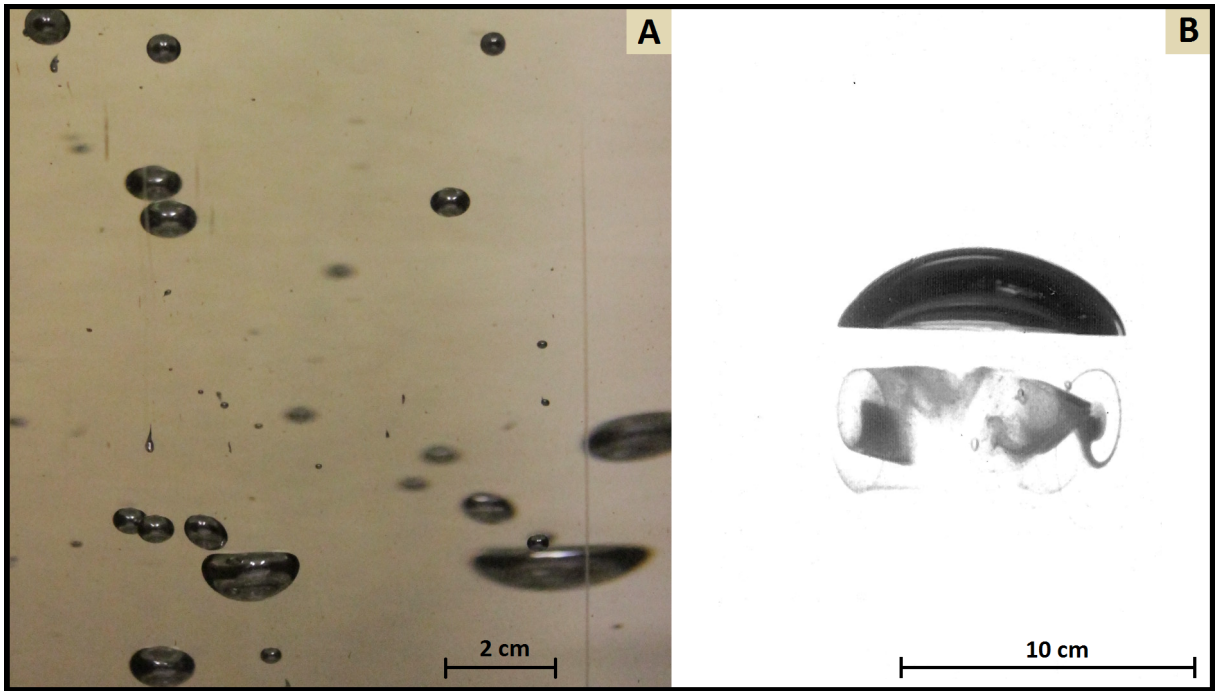

FIGURE I.7 – Panneau de gauche : gouttes de gallium liquide en chute libre dans du glycérol (extrait de **?**). Panneau de droite : bulle d'air en ascension libre dans un mélange d'eau/UCON oil. De très fines bulles issues du processus de formation de la bulle d'air matérialisent les courants de recirculation.

Cette tendance peut être corrigée avec le terme de Hadamard et Rybczynski (**?**, **?**) pour tenir compte de l'écoulement à l'intérieur de la goutte, mais comme il s'agit de l'ajout des effets visqueux, ce terme est très vite négligeable à haut Re :

$$Cd(Re) = \frac{8}{3} + \frac{12}{Re}.\left(\frac{\frac{2}{3} + \frac{1}{R_\mu}}{1 + \frac{1}{R_\mu}}\right) \qquad We \to +\infty; \quad Re \to +\infty. \tag{I.18}$$

Parallèlement, les fluides réels ayant une tension de surface finie, il est commun que la transition entre régime visqueux et régime inertiel (fonction de Re) soit concomitante avec une transition en nombre de Weber. Quand le nombre de Weber approche 1, les forces inertielles sont comparables à la tension de surface et la goutte ne peut rester sphérique. Elle prend généralement une forme d'ellipsoïde aplati puis de calotte ellipsoïdale ou sphérique (figure **??**) suivant le rapport de viscosité (**?**, **?**, **?**). Différentes correlations existent dans ce domaine pour lier l'excentricité de la goutte au nombre de Weber (**?**), et ensuite corriger le coefficient de trainée en fonction de ce paramètre géométrique (**?**). Néanmoins une déformation même peu importante conduit au décrochement de couches limites (**?**) de sorte qu'une valeur constante de Cd est rapidement atteinte. L'allure de $Cd(Re)$ contient donc généralement un minimum qui correspond au décrochement des couches limites (figure **??**).

Enfin, une dernière transition a lieu quand Re est entre 10 et 50 (**?**) pour les gouttes et bulles avec un R_μ assez haut : le cisaillement dans la couche limite de la calotte devient suffisamment important (**?**, **?**, **?**) pour étirer une "jupe" (figure **??**), c'est-à-dire un fin film de fluide étiré depuis la goutte qui figure la limite entre la couche limite décrochée et la bulle de recirculation du sillage. Le seuil qui détermine la formation de cette jupe semble

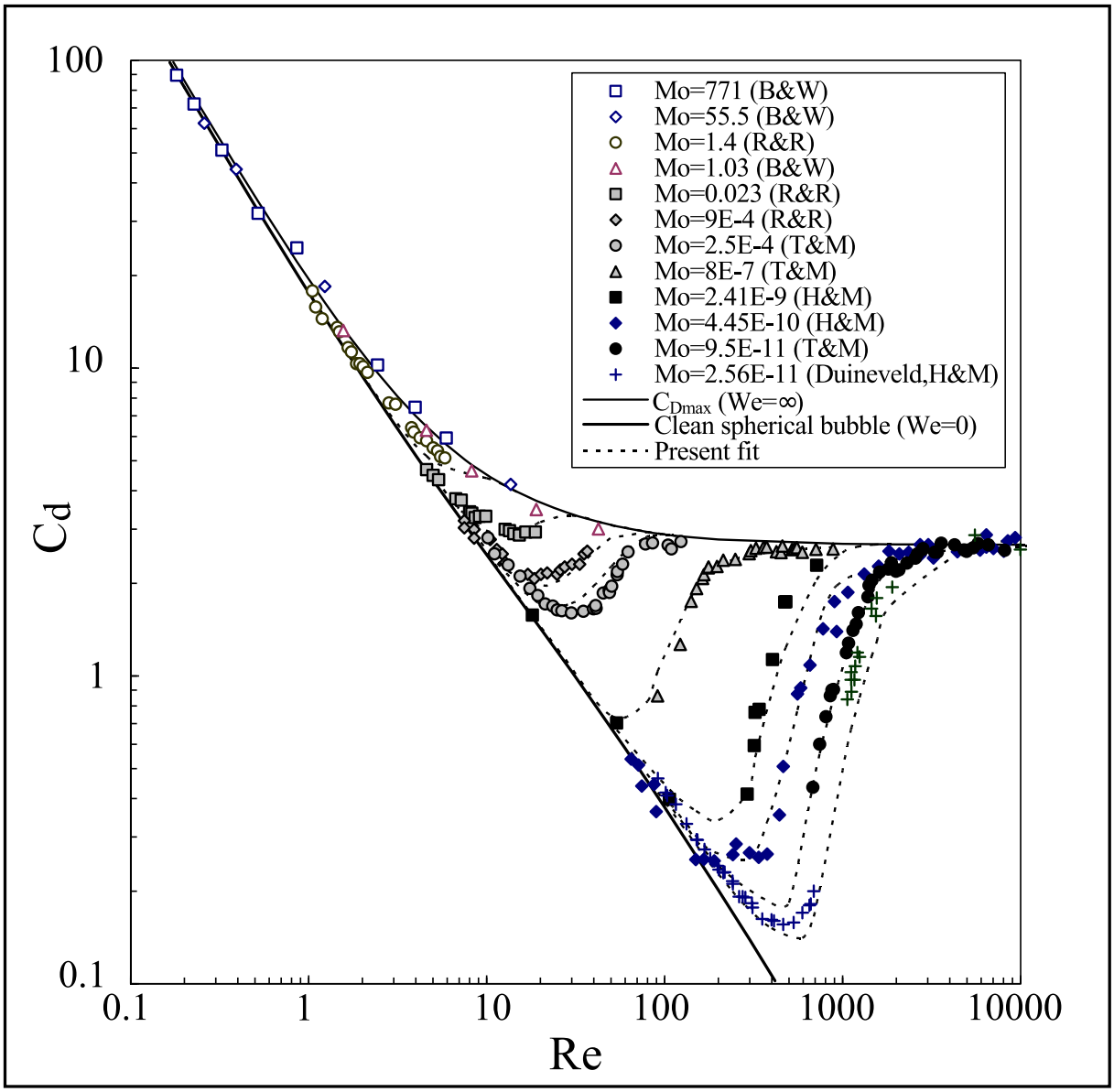

FIGURE I.8 – Graphe du coefficient de trainée Cd de gouttes en chute libre en fonction du nombre de Reynolds Re pour différents couples de fluides (le nombre de Morton est basé sur les grandeurs caractéristiques propres au fluide de la goutte) extrait de **?**.

être corrélé avec le rapport $\frac{We}{Re}$ (appelé le nombre capillaire) qui est donc le rapport entre les forces de viscosité et la tension de surface. Toutefois ce seuil reste aussi dépendant de Re (**?**).

D Stabilité des gouttes

La fragmentation des gouttes et bulles est pour les mêmes raisons que la vitesse terminale de chute un sujet sur lequel il existe une littérature massive. Des colonnes d'extraction aux sprays, la stabilité des gouttes est d'un intérêt industriel primordial (**?**) car la taille des fragments qui résultent de la fragmentation pilote la surface d'échange

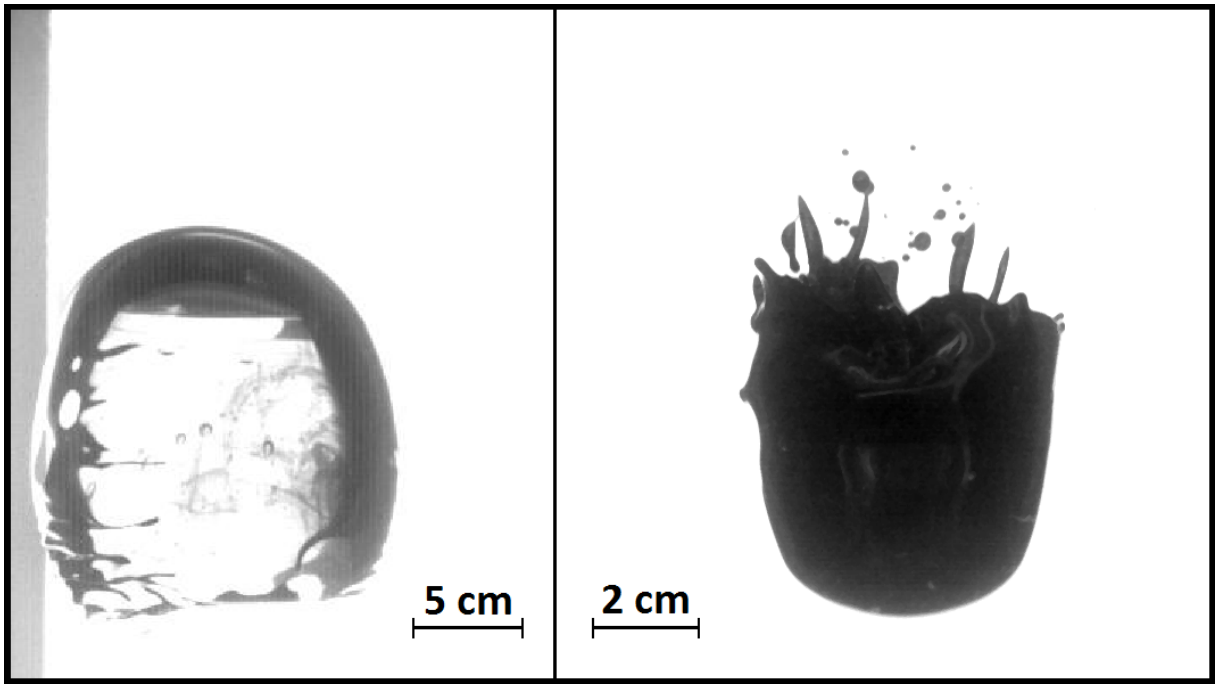

FIGURE I.9 – Panneau de gauche : bulle d'air en ascension libre dans un mélange d'eau/UCON oil. La bande grise est un objet derrière la cuve. Panneau de droite : goutte de galinstan liquide en chute libre dans un mélange d'eau/UCON oil. Dans les deux cas le nombre capillaire Ca est d'ordre 1 ce qui permet la formation d'une nappe d'air/galinstan étirée en arrière à la limite entre la bulle de recirculation et la couche limite décrochée. Le cisaillement qui est moteur de la formation de cette "jupe" provoque aussi des ondulations dans sa position moyenne et des amincissements locaux. Des trous peuvent ainsi apparaitre à cause de ces amincissements comme cela est visible dans le cas de la bulle d'air .

entre les deux fluides. Il en découle que le résultat de la fragmentation doit être connu dès l'instant où on veut estimer des temps d'évaporation dans des sprays ou des temps caractéristiques d'échanges entre deux phases dans les mélangeurs industriels (**?**). Ce faisant, dans les applications industrielles, la fragmentation est généralement très contrôlée, ce qui nous amène à la première difficulté pour comparer les résultats existants avec ceux qui vont être exposés dans ce manuscrit : dans le cas général abordé par la littérature, le mouvement du fluide qui va se fragmenter n'est pas une chute libre, c'est une injection. L'équilibre implicite entre les forces de flottabilité et l'inertie de l'écoulement n'est donc en général pas vérifié. Toutefois, certains mécanismes sont à l'œuvre quel que soit le rapport entre ces forces. Deux types de forces sont capables de déformer une goutte au point de la fragmenter, la pression et les forces visqueuses. Dans notre cas, les forces de viscosité seront sous dominantes vis-à-vis de la pression dynamique (régime inertiel). Dès lors, lorsque le nombre de Weber d'une goutte basé sur sa vitesse relative par rapport au fluide dans lequel elle évolue dépasse un certain seuil proche de 1, la tension de surface ne peut plus compenser la pression dynamique. Pour une vitesse donnée, la goutte se fragmente si son rayon dépasse un rayon critique (**?**) :

$$\frac{\rho.U^2 \cdot R_c}{\sigma} = We_c \quad \Leftrightarrow \quad R_c = \frac{\sigma}{\rho.U^2} \cdot We_c \tag{I.19}$$

En chute libre, la vitesse dépend de R, en prenant les équations (I.13) et (I.14), on obtient le rayon limite stable :

$$\frac{1}{Cd} \cdot \frac{\Delta\rho.g.R_c^2}{\sigma} = We_c \quad \Leftrightarrow \quad R_c = .\sqrt{\frac{\sigma}{\Delta\rho.g}}.Cd^{\frac{1}{2}}.We_c^{\frac{1}{2}} \tag{I.20}$$

On retrouve donc la longueur capillaire l_σ qui est utilisée pour estimer la taille des gouttes de fer liquide dans l'océan de magma lors de l'écoulement post-impact (cf. équation **??**). Ce rayon critique est confirmé par les expériences et des théories sur les gouttes d'eau dans l'air (**?**, **?**, **?**) pour lequel $We_c = 6$ et par des expériences sur des systèmes fluide-fluide (**?**, **?**) pour lequel il est reporté $We_c = 17$. Nous avons pu récemment confirmer cette dernière valeur sur des expériences faites avec du gallium dans du glycérol (**?**) pour lesquelles $9 < We_c < 22$. La longueur capillaire est donc généralement reconnue comme la limite de stabilité des gouttes en chute libre. Il est plus délicat de comparer les gouttes subissant des accélérations impulsionnelles. Néanmoins, qu'elle soient accélérées par des ondes de choc ou par un écoulement soudain, on peut définir un nombre de Bond ou un nombre de Weber défini par l'accélération calculée à partir de la trajectoire des gouttes. Dans ce dernier cas, l'accélération de la goutte est généralement proportionnelle à U/t car la goutte est accélérée de 0 à U. Comme la distance d'accélération est de quelques rayons, on a $t \sim U/R$, donc les seuils en nombre de Bond donnés dans la littérature équivalent généralement à un seuil en nombre de Weber (**?**). En fin de compte, un seuil $We_c \sim 10$ est reporté dans la littérature de façon assez consistante (**?**, **?**, **?**, **?**, **?**).

De façon plus systématique, R. Grace, T. Wairegi et J. Brophy ont repris les résultats de différents auteurs sur la stabilité de gouttes en chute libre, faisant ainsi la collection de donnés sur une grande variété de systèmes de fluides (**?**). Ils ont aussi complété ces résultats souvent effectués avec des systèmes de fluides ayant $R_\mu < 1$ avec des expériences sur différents systèmes de fluides avec $R_\mu > 1$ (figure **??**). En supposant que le seuil de stabilité correspond au seuil du taux de croissance positive d'une instabilité de Rayleigh-Taylor au front des gouttes, ils ont aussi obtenu une relation du type $R_{max} \simeq R_c = C_1.l_\sigma$, avec C_1 une constante de l'ordre de 1. Une bonne prédiction du rayon maximum est reportée mais elle est au prix d'une constante C_1 différente pour le cas $R_\mu > 1$ et $R_\mu < 1$.

Dès lors, il est important de constater que cette échelle de longueur l_σ ne peut-être utilisée que pour donner un ordre de grandeur de la taille limite des gouttes stables mais ne peut cacher la mécanique des fluides fine de la fragmentation. Malgré tout, si on se limite à raisonner en ordre de grandeur, il semble que le rapport entre la longueur capillaire et le rayon de la goutte soit un paramètre de contrôle majeur. La raison est à rechercher d'après la littérature dans le mécanisme de l'instabilité de Rayleigh-Taylor. En effet l_σ est aussi proportionnelle à la longueur d'onde de la perturbation qui est la plus instable vis-à-vis de ce mécanisme. Pour des gouttes d'eau dans l'air, ce problème est résolu en remarquant que la goutte s'aplatit pendant sa chute (**?**) et donc le rayon perpendiculaire à l'écoulement (et à la gravité) augmente, ce qui ouvre la voie à cette instabilité. Pour des bulles d'air dans l'eau, le seuil de stabilité est plus haut en nombre de Weber, il a donc été proposé que le rayon doit être sensiblement plus grand que l_σ (**?** , **?**), afin que l'instabilité ait le temps de grandir alors qu'elle est advectée vers l'arrière de la bulle. Dès lors, il semble

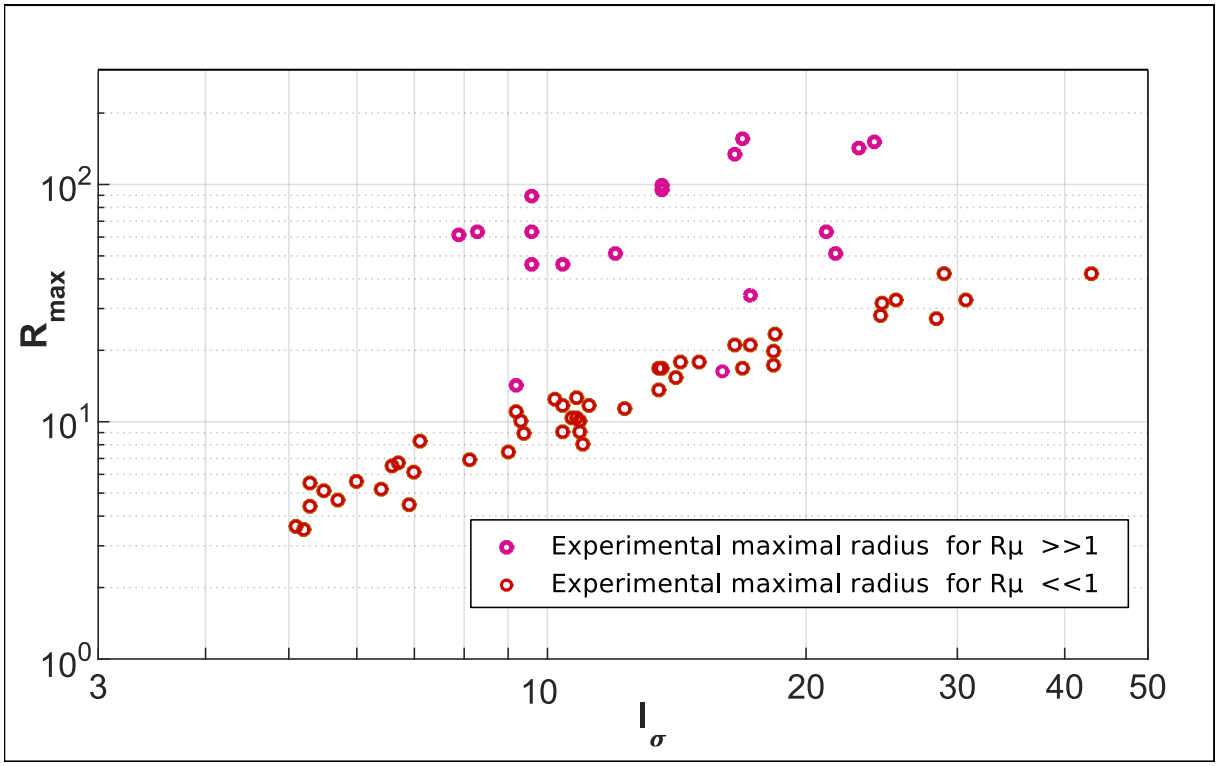

FIGURE I.10 – Graphe du rayon maximum de gouttes en chute libre en fonction de la longueur capillaire pour différents systèmes de fluides. Le rayon maximum des gouttes ayant $R_\mu \ll 1$ sont centrés sont proportionels á l_σ avec un coefficent de 0.9 tandis que celui des gouttes ayant $R_\mu \gg 1$sont proportionels á l_σ avec un coefficent de 5. Données issues de plusieurs études agrégées dans **?**).

raisonnable que R_μ et $\tilde{\rho}$, qui contrôlent la vitesse de l'interface goutte/milieu ambiant, soient des paramètres secondaires de la stabilité des gouttes.

L'influence du rapport de viscosité est peu étudiée dans la littérature. Bien souvent, la viscosité est prise en compte sous la forme du nombre d'Ohnesorge :

$$Oh = \frac{\mu_m}{\sqrt{\sigma.\rho_m.R}} \tag{I.21}$$

Il semble que ce soient essentiellement des raisons historiques qui ont focalisé l'attention générale, et bien souvent exclusive, sur le nombre d'Ohnesorge : de nombreuses études ont été menées sur la production d'aérosols par la fragmentation de gouttes de différents fluides dans l'air. En conséquence, le rapport de viscosité de ces études était généralement très inférieur à 1 et la viscosité intervient alors dans le volume de la goutte comme simple retardant à la dynamique de la fragmentation (**?**), quel que soit le mode de fragmentation. Ainsi, la litterature reporte une influence de Oh sur la valeur We_c à partir de $Oh > 0.1$ pour de nombreuses expériences (**?**, **?**, **?**, **?**) qui ont conduit les auteurs à avancer diverses corrélations expérimentales (figure **??**). En 1988, J. Kitscha et G. Kocamustafaogullari (**?**) ont proposé une théorie tenant compte d'un mécanisme mixte Rayleigh-Taylor/Kelvin-Helmholtz pour rechercher le seuil de stabilité des gouttes et bulles, mais l'effet de la viscosité était réintroduit de façon ad hoc via une constante dépendante de $\tilde{\rho}$ et Mo. Toutefois, il semblerait qu'aucune relation ne soit robuste pour $Oh > 1$ (**?**). Pour le cas

des bulles, la viscosité ayant un effet direct sur le nombre de Reynolds, et bien souvent sur le coefficient de trainée, son effet via le rapport de viscosité a souvent été masqué par son effet principal sur ces deux paramètres cruciaux.

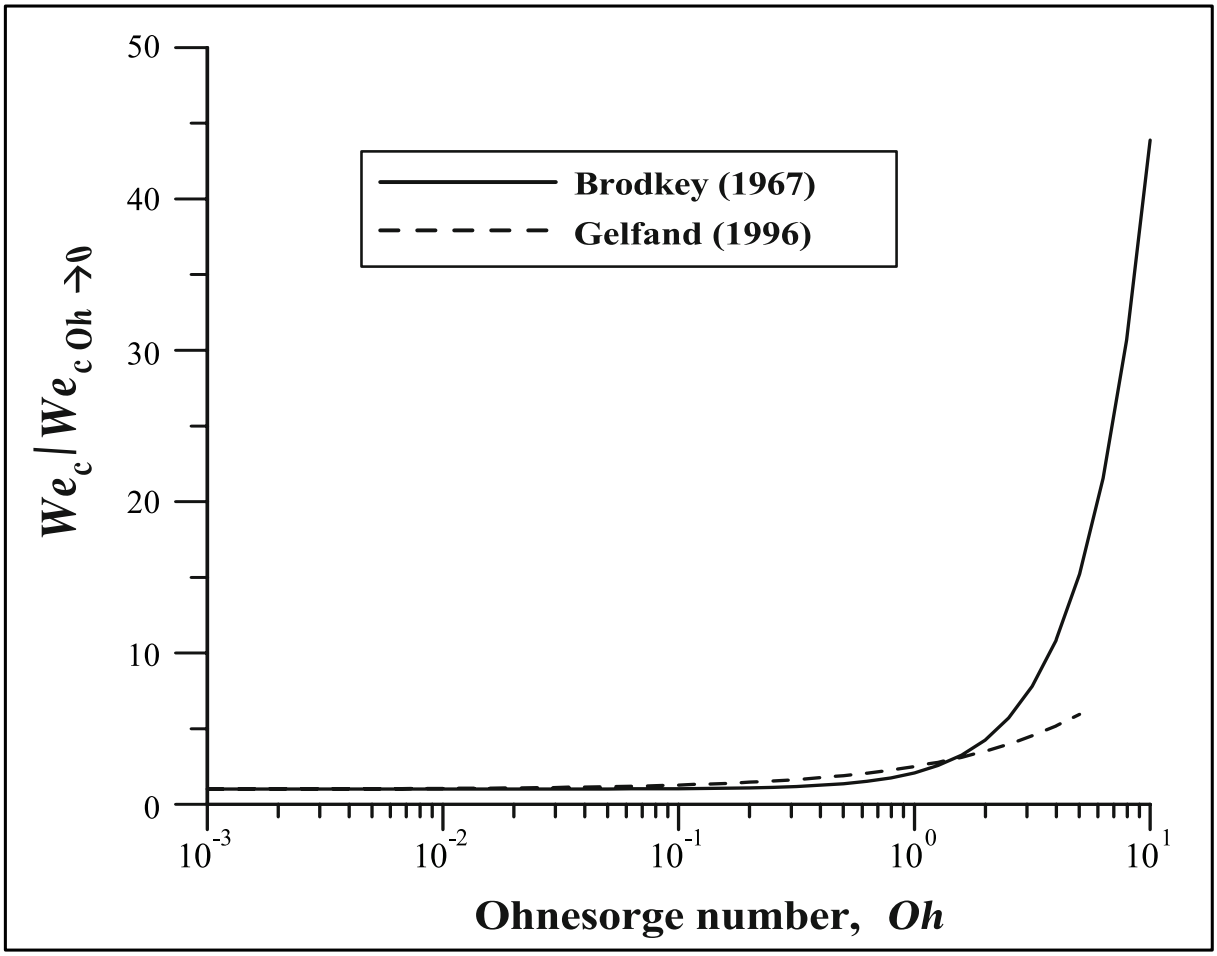

FIGURE I.11 – Graphe du rapport entre le nombre de Weber critique et le nombre de Weber critique pour une goutte ayant une viscosité nulle en fonction du nombre d'Ohnesorge relatif à la goutte (extrait de **?**).

Il faut noter que les récentes études ayant trait à l'effet du rapport de viscosité sur le seuil de stabilité ont apporté des éléments pouvant renouveler l'intérêt pour la question. Par exemple, Ohta et collègues (**?**) ont effectué des simulations de gouttes en chute libre pour des nombres de Bond $10 \leqslant Bo \leqslant 30$. Ayant fixé le nombre de Morton du fluide ambiant, les rapports de viscosité sont 50, 10, 0.52, 0.1 et 0.01, ce qui correspond à des nombres d'Ohnesorge d'environ 0.0018, 0.009, 0.17 0.9 et 9 pour le fluide de la goutte. Le rapport de densité est d'ordre 1 ($\tilde{\rho} = 0.65$ ou 0.77 suivant les simulations). Pour les rapports de viscosité les plus hauts, la vorticité tend à se concentrer dans la goutte plutôt qu'à l'extérieur et le seuil de stabilité est plus haut en nombre de Bond.

D'autre part, ces récentes études ont aussi permis de montrer comment $\tilde{\rho}$ et R_μ influent sur la déformation qui conduit à la fragmentation. La zoologie de ces modes de fragmentation est largement documentée dans la littérature sur les gouttes dans l'air (**?**, **?**,**?**, **?**, **?**). Ces différents modes de fragmentation existent dans différents domaines délimités

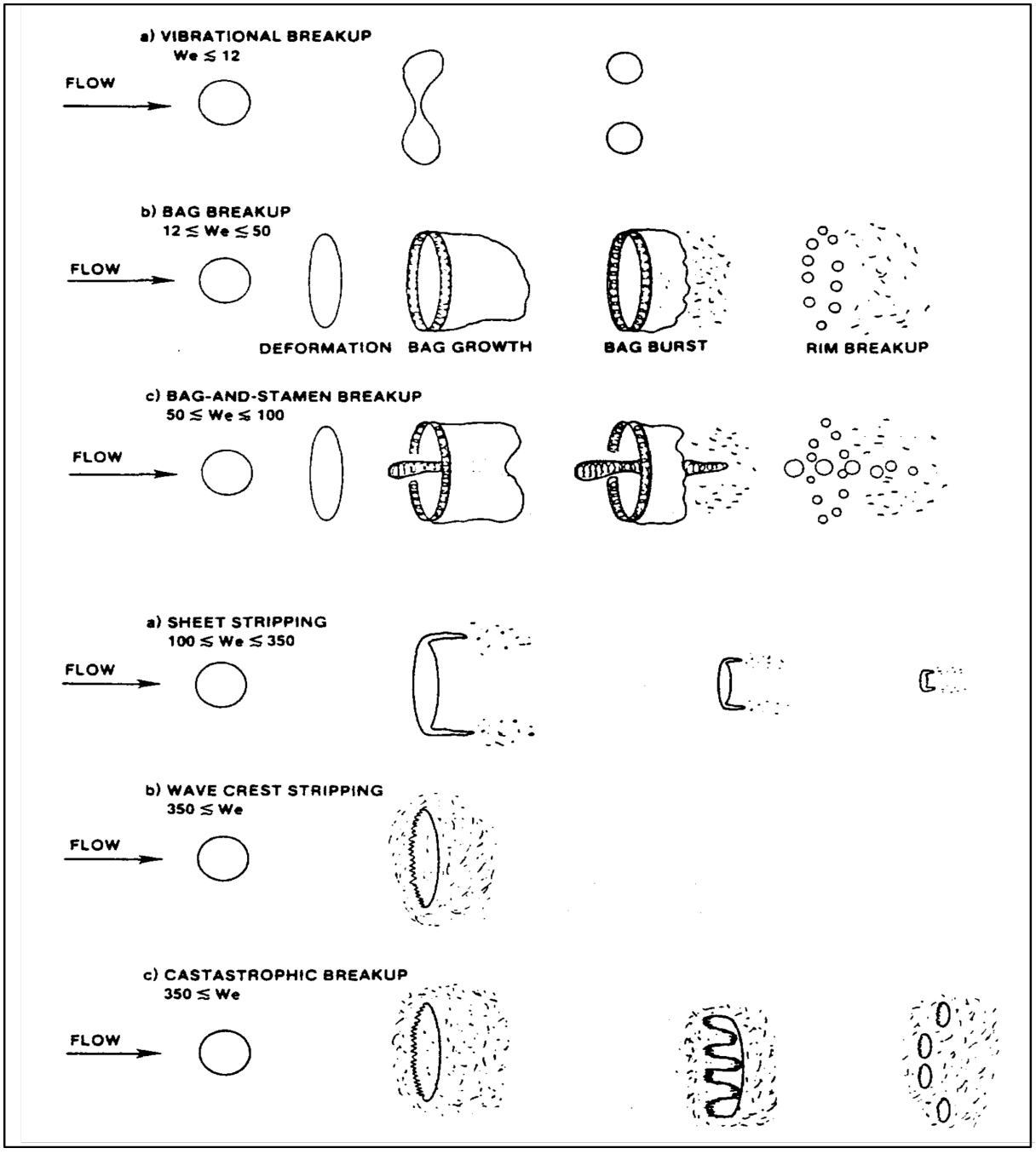

FIGURE I.12 – Schéma des différents modes de fragmentation observables lors de l'accélération soudaine d'une goutte d'eau par un écoulement gazeux pour des nombres de Weber croissants de haut en bas (extrait de **?**).

par des nombres de Weber critiques (figure **??**). De la même manière, les simulations de Kékesi et collègues en 2014 (**?**) montrent que les modes de fragmentation se diversifient si l'on fait varier le rapport de densité et le rapport de viscosité. Ils ont notamment identifié une limite entre des modes en sac classiquement rencontrés dans les gouttes d'eau en chute libre dans l'air, où le sac s'ouvre en étant soufflé vers l'aval de l'écoulement, et les modes en cisaillement, où le sac s'ouvre dans l'autre sens (figure **??**). Cette limite a été interprétée

comme délimitant deux domaines où le rapport entre deux temps caractéristiques est supérieur à 1 dans l'un et inférieur à 1 dans l'autre, chacun des deux temps caractéristiques étant attaché aux deux types de mode de fragmentation mentionnés précédemment. Ce ratio dépend des rapports de viscosité et de densité suivant la relation :

$$\frac{t_{shear}}{t_{bag}} = R_{\mu}^{-1}.\tilde{\rho}^{-\frac{1}{2}}.Re^{-\frac{1}{2}}. \tag{I.22}$$

t_{shear} désigne ici le temps caractéristique des modes de déformation dominés par le cisaillement, t_{bag} désigne le temps caractéristique des modes de déformation dominés par la déformation par la pression dynamique, conduisant à la fragmentation en sac. De même, S. Jain en 2018 (**?**) a conduit des simulations ayant pour but d'étudier l'influence du rapport de densité : le diagramme de régime montrant les différents modes de fragmentation semble confirmer cette tendance. M. K. Tripathi et collègues (**?**) ont eux aussi simulé des gouttes en chute libre en gardant tous les nombres adimensionnés égaux sauf le rapport de densité ; les différences dans les déformations entre les deux types de gouttes sont selon eux attribuables à la concentration de la vorticité dans la phase la moins dense. Des expériences récentes menées par M. Landeau et collègues en 2014 (**?**) ont montré que les modes de fragmentation dans le cas des écoulements post-impacts planétaires sont probablement plus ressemblants à ceux qui sont dominés par le cisaillement, les fluides utilisés pour ces expériences leur permettant d'atteindre le rapport de densité attendu et un des rapports de viscosité attendu pour le système fer liquide/magma.

En conclusion, la stabilité d'une goutte isolée peut paraitre loin des régimes à haut nombre de Weber et à haut nombre de Reynolds qui nous occupent, mais ce problème permet de connaitre comment vont s'organiser les forces aux échelles où la fragmentation va se produire.

E Fragmentation

1 Généralités

Dans le problème posé par les échanges de chaleur et d'éléments entre le fer liquide et le magma, la fragmentation du métal tient un rôle central en contrôlant la surface disponible pour les échanges (**?**, **?**). On se place dans la limite où un des deux fluides est dilué (ici le métal liquide) de sorte que la fragmentation ne produit que des entités isolées d'un fluide dans un autre sans changer radicalement les propriétés de ce dernier, par opposition avec les mousses et émulsions. Si la limite de stabilité a été utilisée pour déterminer une taille maximale de goutte et ainsi une surface minimale d'échange du fer liquide pendant sa chute, c'est le nombre de Weber qui fait le rapport entre l'énergie disponible pour la fragmentation et le gain d'énergie qu'implique de fabriquer une surface ayant une énergie unitaire de σ. Ainsi la condition $We_l \simeq 1$, où We_l est le nombre de Weber à l'échelle l, permet de définir un rayon typique en deçà duquel l'énergie cinétique de l'écoulement est plus petite que celle stockée dans la surface des gouttes et n'est donc pas suffisante pour former de nouvelles gouttes :

$$\frac{We_l}{We} = \frac{l}{R} \quad et \quad We_l \simeq 1 \qquad \Rightarrow \qquad l = R.We^{-1} \tag{I.23}$$

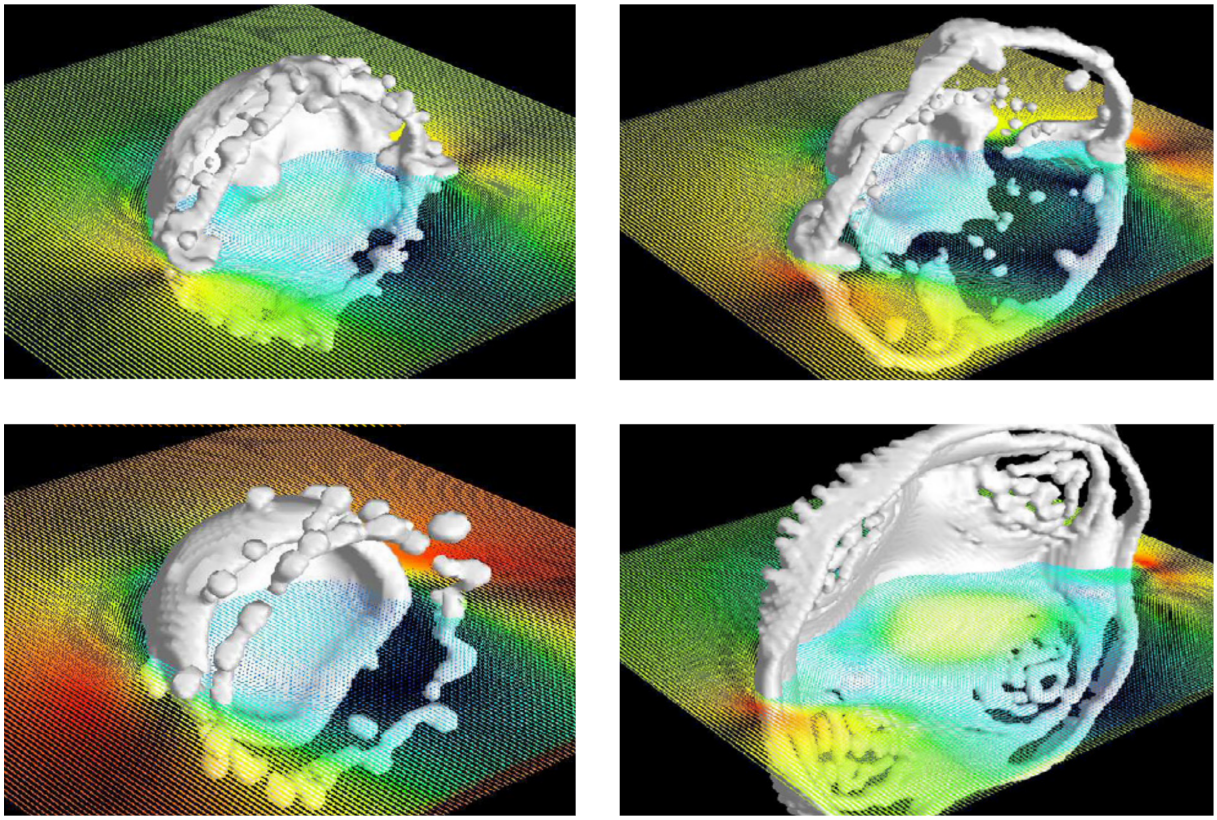

FIGURE I.13 – Graphe d'isocontours de densité pour différentes simulations 3D de gouttes de flottabilité non nulle maintenues dans un écoulement soumis à une gravité constante. Les 4 simulations sélectionnées sont faites à différents We, $\tilde{\rho}$ et R_μ montrant la diversitée des modes de fragmentation dans la zone de notre étude (extrait de **?**).

Cette échelle peut être considérée comme une limite physique car le rapport entre l'énergie cinétique de l'écoulement et l'énergie de surface est 1 quand les gouttes produites atteignent cette dimension. Le diamètre moyen des gouttes est donc généralement plus grande car une fraction seulement de l'énergie disponible peut être utilisée pour fragmenter. En effet, la fragmentation implique la formation de structures alongées (**?**). Cette déformation crée des gradients de vitesse, qui tendent à disparaitre quand deux entités sont créées au terme ultime de cette déformation. On reconnait alors un processus de collision purement visqueux (par opposition à une collision élastique) qui intervient à cause de la cohésion de la matière (*i.e.* la tension de surface), faisant de la fragmentation un phénomène intrinsèquement dissipatif, irréversible. De plus, dans notre contexte de fragmentation, deux particules des différents fluides doivent se rencontrer, et l'une doit communiquer sa vitesse à une autre, pour induire la déformation du métal liquide. Il s'agit là aussi d'une étape similaire à une collision purement visqueuse.

En conséquence, prédire le résultat de la fragmentation ne peut être fait sans prendre en compte précisément les mécanismes à l'œuvre. C'est pourquoi le résultat de la fragmentation de gouttes proches du seuil de l'instabilité ne nous intéressera pas ici ; il est trop loin des deux contextes de fragmentation qui peuvent intervenir. D'après notre expérience précédente (**?**), il est important de considérer à la fois la fragmentation à partir des grandes échelles, loin de la stabilité où la tension de surface agit encore, et la fragmentation aux

petites échelles, mais cette fois dans le contexte d'une turbulence développée. Il s'agit en fait de deux approches assez distinctes correspondant à des exigences théoriques de capacités prédictives différentes. La dernière approche consiste à ignorer l'influence du changement de topologie initial et le biais que la tension de surface pourrait produire sur la distribution de tailles résultant de cette première fragmentation. Le présupposé de cette méthode est que seul importe le résultat ultime d'une série supposée très grande d'évènements de fragmentation et coalescence de gouttes soumises aux déformations des mouvements turbulents du fluide ambiant. Cette approche est privilégiée pour les populations de gouttes dans les agitateurs industriels dont le temps de résidence doit être très supérieur à tous les autres temps dynamiques pour s'assurer de l'équilibration (généralement les temps diffusifs sont très supérieurs aux temps dynamiques, nous reviendrons sur ce régime car il caractérise aussi notre système). La taille caractéristique r_σ des fragments est donc fixée par un équilibre local entre la tension superficielle et les variations de pressions dynamiques produites par les mouvements turbulents à l'échelle r_σ (**?**, **?**). En supposant l'auto similarité de la turbulence mise en avant par Kolmogorov en 1941 (**?**), on peut obtenir les variations de vitesses typiques de la turbulence à n'importe quelle échelle. On procède en égalisant l'énergie cinétique volumique à toute échelle plus petite que l'échelle intégrale de l'écoulement :

$$\frac{U^2.U.R^2}{R^3} \simeq \frac{u^2.u.r_\sigma^2}{r_\sigma^3} \qquad \Leftrightarrow \qquad u \simeq U.\left(\frac{r_\sigma}{R}\right)^{\frac{1}{3}}. \tag{I.24}$$

u est ici l'ordre de grandeur des variations de vitesse à l'échelle r_σ. L'équilibre entre la tension de surface et la pression dynamique développée à l'échelle r_σ s'écrit donc :

$$We_{local} \simeq 1 \qquad \Leftrightarrow \qquad \rho_a.u^2 \simeq \sigma\frac{1}{r_\sigma} \qquad \Leftrightarrow \qquad r^{\frac{5}{3}} \simeq \frac{\sigma}{\rho_a.u^2}, \tag{I.25}$$

ce qui permet d'obtenir la célèbre loi d'échelle en -3/5 :

$$r_\sigma \simeq C_1.R.We^{-\frac{3}{5}} \tag{I.26}$$

avec C_1 une constante généralement d'ordre 10^1. Cette loi est généralement vérifiée (**?**, **?**, **?** , **?**, **?**, **?**), tant que l'auto-similarité de la turbulence n'est pas brisée par l'introduction d'une échelle spatiale caractéristique. Celle-ci peut être l'échelle de Kolmogorov $l_\nu = R.Re^{-\frac{3}{4}}$ où les forces de viscosité prennent le pas sur l'inertie des mouvements de plus petite échelle et les dissipent. Celle-ci peut aussi être l'échelle de taille des gouttes elle-même dans le cas d'un écoulement peu dilué.

Une complexité apparaît tout de même lorsque la viscosité des gouttes est suffisamment faible pour que les modes propres de vibrations des gouttes puissent stocker de l'énergie cinétique entre deux accélérations liées aux mouvements turbulents. Dans ce cas, un enchainement particulièrement favorable de mouvements en phase avec l'oscillation propre de la goutte peut constituer une excitation résonnante capable de faire se séparer la goutte en deux (le mode qui domine est quasi exclusivement le mode $n = 2$). Il en résulte que si les mouvements turbulents sont trop faibles pour fragmenter une goutte en un évènement, elle peut quand même fragmenter à cause d'une interaction prolongée avec la turbulence. On peut ainsi constater une réduction de la taille maximale des gouttes (**?**, **?**). Les mouvements d'oscillations de la forme globale se traduisent dans l'intérieur de la goutte par un écoulement laminaire, donc linéairement amorti, pour une large variété

d'applications (**?**). Si le forçage turbulent est relativement constant sur la trajectoire de la goutte, il faut simplement que les perturbations de vitesse soient proportionnellement plus fortes, d'un facteur indépendant de l'échelle, pour compenser la dissipation visqueuse. On constate donc que la loi d'échelle **??** peut toujours être appliquée (**?**) en modifiant la constante C_1. Ceci se fait donc au prix de supposer la turbulence homogène sur un temps caractéristique de l'ordre de quelques temps d'oscillations de la goutte et sur une distance correspondant au parcours moyen de la goutte dans ce même temps. Dans le cas contraire, le critère de fragmentation semble reposer sur la valeur du nombre de Weber (turbulent) de la goutte intégrée sur son parcours (**?**).

Malgré sa robustesse à prédire la taille moyenne des gouttes dont la fragmentation est dominée par les mouvements turbulents, la loi d'échelle **??** prédit seulement une échelle caractéristique et ne suffit donc pas à résumer une distribution de tailles de gouttes complète. Dans les agitateurs industriels, la taille caractéristique d'intérêt est bien souvent le rayon de Sauter (**?**, **?**), défini comme étant le rayon d'une goutte ayant le même rapport surface/volume qu'un ensemble de goutte dont les tailles obéissent à cette distribution. Cet intérêt se comprend si l'on prend le cas où la diffusion est le seul facteur limitant les transferts diffusifs. Comme la quantité de chaleur (ou de masse) qui diffuse par unité de temps est proportionnelle à la surface d'après la loi de Fourier (ou loi de Fick), et la quantité totale transférable est proportionnelle au volume, le temps caractéristique d'équilibration thermique (ou chimique) évolue donc linéairement avec le rapport surface sur volume. On nomme $n(r)$ la distribution de tailles de goutte en nombre de gouttes par unité de rayon. Si $N(r)$ est le nombre de goutte avec un rayon inférieur à r, $n(r)$ est défini comme suit ;

$$N(r+dr) - N(r) = n(r)dr \qquad \Leftrightarrow n(r) = \frac{dN}{dr}(r). \tag{I.27}$$

Le rayon de Sauter R_{32} est le rapport entre la surface totale de la distribution et le volume total de la distribution (à un facteur 1/3 près) :

$$R_{32} = \frac{\int_0^{+\infty} \; r^3.n(r)\; dr}{\int_0^{+\infty} \; r^2.n(r)\; dr} \tag{I.28}$$

De manière plus générale, on peut définir les diamètres caractéristiques de la distribution R_{mk} :

$$R_{mk} = \left(\frac{\int_0^{+\infty} \; r^m.n(r)\; dr}{\int_0^{+\infty} \; r^k.n(r)\; dr} \right)^{\frac{1}{m-k}} \tag{I.29}$$

Nous reviendrons dans le chapitre **??** sur la pertinence de l'emploi du rayon de Sauter. Néanmoins on peut d'ores et déjà constater que puisque le rayon moyen est défini comme R_{10}, il n'est pas *a priori* possible de relier le rayon moyen et le rayon de Sauter. C'est donc dans la perspective de pouvoir prédire les conditions de transferts diffusifs entre une phase dispersée en gouttes et un fluide agité de mouvements turbulents que des modèles statistiques d'évolution de population de goutte (PBM) ont été développés (**?**). Néanmoins, nous montrerons dans le chapitre **??** que la dilution dans notre cas rend la probabilité de collision des gouttes très faible. La dilution tend aussi à réduire les vitesses, ce qui rend aussi de multiples épisodes de fragmentation improbables.

2 Distributions issues de modèles

Le type d'approche que nous allons utiliser, par opposition aux approches d'évolution de population de gouttes, condisère l'étape initiale de fragmentation : elle suppose que la physique de l'écoulement ayant lieu au moment de la fragmentation détermine la distribution de taille de gouttes. Celle-ci reste figée une fois que les gouttes sont formées.

Distribution log-normale

Une des distributions les plus rencontrées dans la littérature (**?**, **?**, **?**, **?**, **?**) est la distribution log-normale. Le principe vient de Kolmogorov en 1941. Il s'agit d'une distribution fondée sur un scénario de pure fragmentation : la masse initiale de fluide de volume v_0 est fragmentée en m étapes (jusqu'à par exemple atteindre la taille limite des gouttes stables), chaque étape faisant se diviser une goutte d'un volume v_k en deux gouttes de volume v_{k+1} et v'_{k+1} respectivement. La conservation de la masse implique que $\mathrm{v}_{k+1} = \alpha_{k+1}.v_k$ et $\mathrm{v}'_{k+1} = (1-\alpha_{k+1}).\mathrm{v}_k$, avec α_{k+1} une fraction volumique pouvant prendre n'importe quelle valeur de 0 à 1. Au bout des m étapes, une goutte a un volume v_m qui vérifie la relation :

$$\mathrm{v}_m = \mathrm{v}_0 . \prod_{k=1}^{m} \alpha_k \tag{I.30}$$

En prenant le logarithme de cette expression :

$$\ln(\frac{\mathrm{v}_m}{\mathrm{v}_0}) = \sum_{k=1}^{m} \chi_k \qquad \text{où} \qquad \chi_k = ln(\alpha_k) \tag{I.31}$$

En supposant le nombre d'étapes de fragmentation très grand, et un processus sans mémoire et invariant suivant l'échelle, $\sum_{k=1}^{m} \chi_k$ est une somme de variables aléatoires indépendantes de même loi de probabilité. Si on nomme E et V respectivement l'espérance et la variance de la loi de probabilité suivie par les χ_k , $\sum_{k=1}^{m} \chi_k$ devrait suivre une loi normale avec une espérance de $m.E$ et un écart type de $m^{\frac{1}{2}}.\sqrt{V}$ d'après le théorème central limite. On obtient donc la loi de probabilité de v_m :

$$d\,\ln(\mathrm{v}_m) = \frac{d\mathrm{v}_m}{\mathrm{v}_m} \;\Rightarrow\; n(x = \frac{\mathrm{v}_m}{\mathrm{v}_0}) = \frac{1}{x.m^{\frac{1}{2}}.\sqrt{V}.\sqrt{2\pi}} . \exp\left(-\frac{1}{2}.\left(\frac{\ln(x) - m.E}{m^{\frac{1}{2}}.\sqrt{V}}\right)^2\right) \tag{I.32}$$

La distribution en rayons se déduit en remplaçant le volume d'intégration $d\mathrm{v}_m$ par $4\pi.r^2.dr$:

$$n(x = \frac{r}{r_0}) = \frac{\sqrt{8\pi}}{x.m^{\frac{1}{2}}.\sqrt{V}} . \exp\left(-\frac{1}{2}.\left(\frac{\ln(x^3) - m.E}{m^{\frac{1}{2}}.\sqrt{V}}\right)^2\right). \tag{I.33}$$

De la simplicité de ce scénario vient deux contraintes assez fortes. La première est que l'on suppose un processus répété un très grand nombre de fois m, et que l'on suppose que le nombre m d'étapes est relativement constant dans la population de gouttes finales. Ceci ne dépasse pas souvent le statut d'hypothèse de travail, tant la difficulté de vérifier l'arbre généalogique des gouttes est limitante dans le cadre des expériences. La deuxième implication est une implication très pratique, l'écart type de la distribution finale du

logarithme du volume est lié à son espérance par un facteur $m^{\frac{1}{2}}$. Puisqu'on a supposé une fragmentation binaire indépendante de l'échelle, E doit rester indépendant du nombre de Weber, mais il est tout à fait concevable que $m \simeq We^h$, avec $h > 0$. Dans ce cas, cela implique que la variance de la distribution finale du logarithme du volume est proportionnelle à $We^{\frac{1}{2h}}$. Dans le cas contraire, ce scénario de division binaire sans mémoire et invariant en échelle ne peut être que trop simple pour décrire les expériences. La vérification de cette dernière contrainte est bien souvent ignorée (**?**).

Formalisme de l'entropie maximum

Un autre grand type de distribution utilisant un scénario statistique simple est basé cette fois sur la maximisation de l'entropie associée à la distribution de la variable volume de gouttes. Elle existe sous une version continue et une version discontinue. Cette dernière considère la matière divisée en N_e blocs élémentaires de matière agrégés complètement au hasard en un ensemble de groupes composés de n_e éléments, n_e étant variable d'un groupe à l'autre. Chacun de ces groupes est donc censé représenter une goutte de taille définie : ils sont au nombre de k_n pour chaque taille de groupes n_e (**?**, **?**). L'intérêt de ce scénario est de pouvoir réinjecter une partie de la physique de façon assez naturelle (mais pas forcément suffisante) : la taille de l'élément fondamental, de l'a-tome, peut être prise comme une fraction de l'échelle à laquelle la tension de surface compense les forces qui tendent à déformer les gouttes. La théorie du dénombrement nous enseigne que toutes les répartitions des N_e atomes en K groupes ne sont pas équivalentes ; le fait de faire des groupes de façon totalement aléatoire produit des regroupements équivalents, ils ont donc plus de probabilité d'apparaitre. C'est en vérité un raisonnement analogue au théorème centrale limite mais au lieu de produire une moyenne et une variance, un degré de liberté de plus permet de produire une distribution complète. Le fait d'avoir une probabilité maximale équivaut à dire qu'ils ont une entropie maximale. Le nombre d'états $\Omega(k_n)$ produisant un ensemble k_n de groupes de façon équivalente s'exprime de la manière suivante :

$$\Omega(k_n) = \frac{K!}{\prod_{n_e=0}^{N_e} k_n!} \cdot \frac{N_e!}{\prod_{n_e=0}^{N_e} (n_e!)^{k_n}}. \tag{I.34}$$

Le terme de gauche vient du dénombrement des groupes ($K!$), où les groupes ayant un nombre de gouttes égal sont indiscernables ($k_n!$). Le terme de droite vient du dénombrement des gouttes ($N_e!$) où les gouttes sont indiscernables entre les groupes et à l'intérieur des groupes de même taille ($(n_e!)^{k_n}$). Deux contraintes s'appliquent sur cette relation de dénombrement, le nombre de groupes total et la conservation de la masse :

$$K = \sum_{k=0}^{N_e} k_n \qquad N_e = \sum_{k=0}^{N_e} k_n.n_e. \tag{I.35}$$

En faisant varier les k_n tout en respectant ces deux contraintes, on peut trouver un maximum au cardinal de l'ensemble k_n et ainsi trouver la distribution de tailles de goutte la plus probable. Celle-ci est la distribution de Poisson :

$$n(n_e) = \frac{k_n}{K} = \frac{\langle n_e \rangle^{n_e}}{n_e!}.e^{-\langle n_e \rangle} \qquad ; \qquad \langle n_e \rangle = \frac{N_e}{K}. \tag{I.36}$$

$\langle n_e \rangle$ est ici la taille moyenne des groupes d'atomes. Pour revenir à une vision continue de cette distribution, on doit adimensionner le rayon des gouttes par une échelle caractéristique correspondant à la taille d'un atome l_a, le lecteur attentif aura le choix de remplacer cette échelle par l_σ, r_σ ou toute autre échelle stabilisée par la tension de surface. Le volume d'intégration doit aussi être corrigé de la même manière que l'équation **??**, car il s'agit là aussi d'une distribution en volume.

$$n\left(x = \frac{r}{l_a}\right) = \frac{\left(\frac{\langle r \rangle}{l_a}\right)^{3x^3}}{\Gamma(x^3 - 1)} . e^{-\left(\frac{\langle r \rangle}{l_a}\right)^3} . \, 3x^2 \tag{I.37}$$

$\langle r \rangle$ est le rayon moyen, soit $\langle r \rangle = R_{10}$. Γ est la fonction Gamma, qui étend la factorielle aux réels positifs. Cette distribution semble rendre compte de certains cas où des particules avec peu d'inertie sont agitées sans possibité d'agrégation (**?**, **?**). Toutefois, il n'est pas étonnant que cette distribution ne soit pas le cas général : en effet descendre jusqu'à l'échelle de ce que l'on pourrait considérer comme atome de la fragmentation sans autre effet que le pur hasard revient à supposer que la tension de surface a une intensité nulle au-dessus de l'échelle de l'atome et une intensité infinie en-dessous. Cette séparation d'échelles n'est pas évidente et dans le cas général il faut considérer qu'à l'échelle où se passe la fragmentation, quelle qu'elle soit, la tension de surface est un acteur majeur.

La version continue de l'approche de l'entropie maximum ne profite pas de l'introduction "naturelle" de la physique via l'atome de fragmentation. C'est une approche quasiment totalement basée sur le concept d'information, comprendre loin de la microphysique de la fragmentation. On généralise alors la distribution à une distribution de tailles de vitesse, d'énergie cinétique, etc. L'entropie à maximiser est l'entropie de Shannon (**?**, **?**)

$$S = -k \sum_{\Omega} P_i ln(P_i), \tag{I.38}$$

où k est une constante, P_i est la probabilité de l'évènement numéroté i, et Ω est l'espace de tous les événements "volume", "énergie de surface", "quantité de mouvement", "énergie cinétique" (**?**). Une forme générale de distribution maximise S :

$$n = \exp\left(-\beta_0 - \beta_1 . r^3 - \beta_2 . r^2 - \beta_3 . r^3 . v - \beta_4 . r^3 . v^2\right). \tag{I.39}$$

Les constantes β doivent ensuite être déterminées en appliquant des contraintes physiques adéquates : on égalise les différents moments de la distribution avec la masse, la partition d'énergie de surface, d'énergie cinétique, etc. mesurées expérimentalement. Les distributions produites reviennent généralement à un fit de données sans applicabilité aux expériences faites dans d'autres conditions car cela revient à faire un modèle surparamétrisé (**?**).

Distributions issues de l'agrégation

Le dernier scénario part du fait que si la fragmentation s'arrête, c'est parce que la cascade vers les petites échelles fait passer le système d'un domaine où la tension de surface est sous-dominante à un domaine où c'est une force majeure. Dans ce cadre, le moment de la fragmentation est aussi l'occasion d'une grande quantité d'agrégation, qui donne en fait sa forme à la distribution de tailles de goutte (**?**). L'équation décrivant l'évolution d'une

concentration volumique de gouttes $\omega(\mathrm{v})$ caractérisées par leur volume v sous l'effet de la coalescence a été formulée par M. von Smoluchowski en 1917 :

$$\frac{\partial \omega(\mathrm{v},t)}{\partial t} = \frac{1}{2}.\int_0^{\mathrm{v}} K(\mathrm{v}-\mathrm{v}',\mathrm{v}').\omega(\mathrm{v}-\mathrm{v}',t).\omega(\mathrm{v}',t)\ d\mathrm{v}' \ -\omega(\mathrm{v},t).\int_0^{+\infty} K(\mathrm{v}',\mathrm{v}).\omega(\mathrm{v}',t)\ d\mathrm{v}'. \tag{I.40}$$

$K(\mathrm{v},\mathrm{v}')$ est appelé le kernel de coalescence, c'est la fréquence de coalescence, par unité de volume, de deux gouttes de volume v et v′ respectivement. La distribution de tailles étant dans ce contexte la simple normalisation de la concentration :

$$n(\mathrm{v},t) = \frac{\omega(\mathrm{v},t)}{N_{tot}} \qquad ; \qquad N_{tot} = \int_0^{+\infty} \omega(\mathrm{v},t)\ d\mathrm{v}. \tag{I.41}$$

La structure de l'équation de Smoluchowski fait que les distributions qui en résultent présentent pour des temps assez longs une même tendance asymptotique identique quel que soit le kernel de coagulation $K(\mathrm{v},\mathrm{v}')$ qui les fait évoluer. A cause de l'auto-convolution, elles ont un comportement asymptotique exponentiel (**?**, **?**).

On place nos réflexions au niveau du dernier changement de topologie que subit le fluide qui se fragmente. L'élément central de cette théorie est la structure allongée dans une seule direction à partir de laquelle les gouttes se forment (**?**) : le ligament (cf. figure **??**). On sait depuis les expériences de Plateau en 1873 que cette structure est instable et la minimisation de l'énergie de surface par la dynamique tend à former des gouttes. Lord Rayleigh a théorisé le mécanisme de cette instabilité en 1879 (**?**) et par là même donné le temps caractéristique de croissance de celle-ci. Un ligament initialement cylindrique de diamètre D voit croître une modulation sinusoïdale de son rayon conduisant ultimement à la formation de gouttes sur un temps caractéristique $T = \sqrt{\frac{\rho_m.D^3}{\sigma}}$. Ce temps est identique à celui nécessaire à une goutte reliée à une autre plus grande par un pont liquide pour se vider dans cette dernière. Ceci est inévitablement censé se produire lorsqu'un ligament présente des perturbations causées par les fluctuations naturelles de la turbulence. Une représentation utile à la réflexion sur le processus d'agrégation dans ce contexte est de voir les irrégularités, les "corrugations", des ligaments comme une suite de blobs en communication les uns avec les autres qui, par le jeu des pressions capillaires, vont se vider les uns dans les autres. Pendant cette dernière étape de changement de topologie que constitue la rupture du ligament, on a donc coexistence de fragmentation et coalescence, ce qui justifie l'emploi de l'équation Smoluchowski **??**. L'universalité de cette étape de fragmentation est illustrée sur la figure **??**.

Comme le ligament est un objet dont la dimension est proche de 1, le volume des individus définissables sur celui-ci est à peu près proportionnel à leur dimension linéaire (dans l'axe du ligament). En conséquence, l'équation de Smoluchowski peut en première approximation être écrite de manière à peu près équivalente en volume ou en rayon. De plus, cette équation fait apparaitre un terme d'auto-convolution (à gauche), qui est le terme central caractérisant la coalescence ; c'est ce terme qui fait évoluer la distribution à partir d'elle-même. En supposant une fréquence d'agrégation indépendante de la taille (soit $K(\mathrm{v},\mathrm{v}') = K$), la transformation de Laplace permet de reformuler l'équation d'évolution de la concentration $\omega(r,t)$:

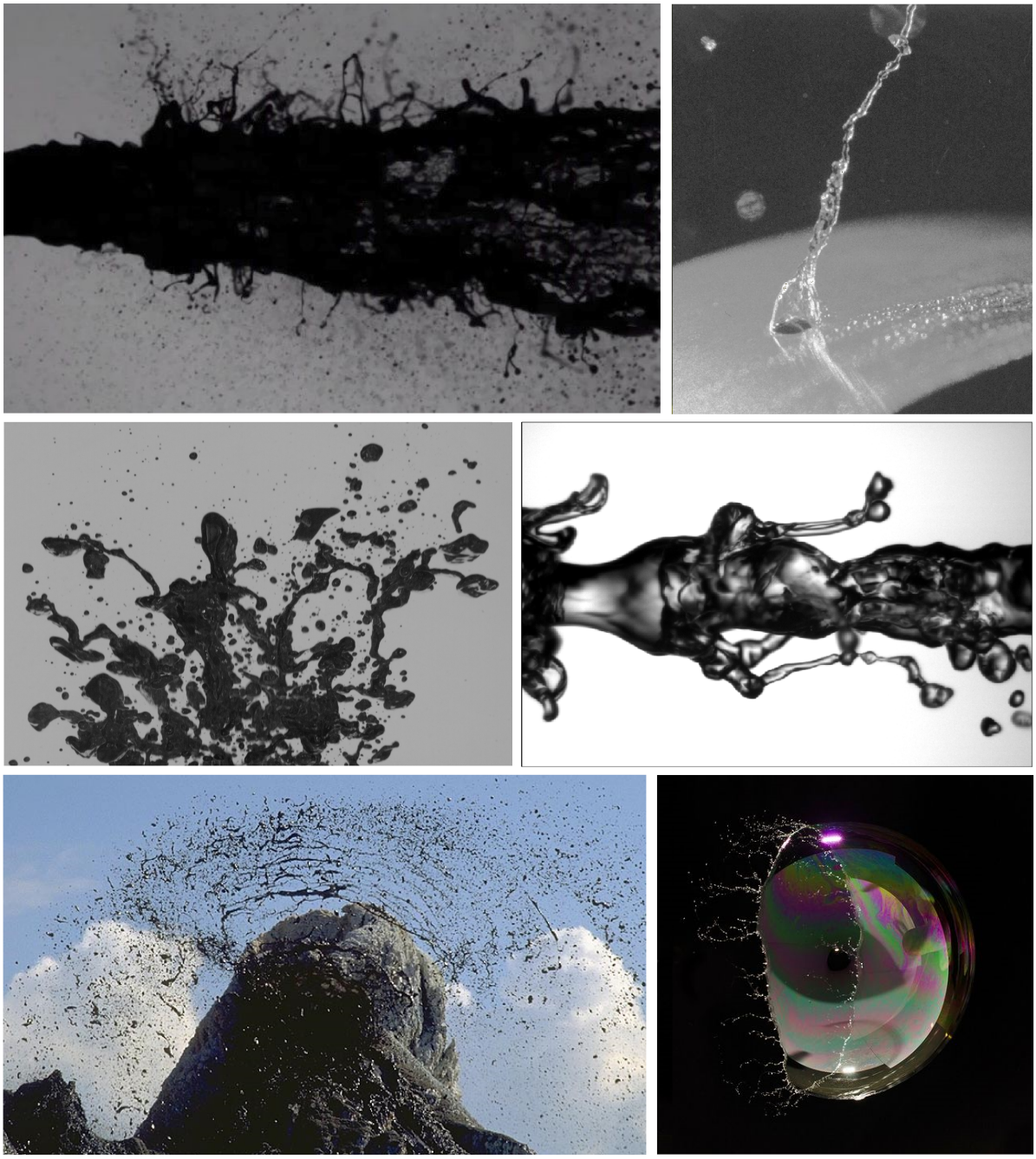

FIGURE I.14 – Photographies d'écoulements diphasiques au moment de la fragmentation de ligaments en gouttes. De gauche à droite et de bas en haut, images extraites de Lucas Weiss, de **?**, de la présente étude, de **?**, de Roby Carniel et Marco Fulle (SwissEduc), et Richard Heeks (site personnel).

$$\frac{\partial \breve{\omega}(r,t)}{\partial t} = -\ \breve{\omega}(r,t)\ .\ N_{tot}(t)^{\gamma-1}\ +\ \frac{1}{3\gamma-2}\ .\ \breve{\omega}(r,t)^{\gamma}, \tag{I.42}$$

où $\breve{\omega}(r,t)$ désigne la transformée de Laplace de la fonction $\omega(r,t)$. Le coefficient γ est le paramètre d'interaction qui détermine la possibilité d'agrégation. Il est lié à la dispersion

en taille des corrugations initiales des ligaments (**?**, **?**).

Finalement, on dimensionne l'équation **??** par le nombre courant de fragments afin de rechercher une fonction de probabilité issue d'un processus d'agrégation allant à son terme d'un point de vue statistique. Ceci est à comprendre en termes de forme de la fonction de probabilité, car il va sans dire que l'agrégation poursuivie jusqu'à l'infini reconstruit une masse unique. En d'autres termes, c'est une distribution dont la forme n'évolue pas malgré l'agrégation. Cette distribution suit une loi gamma d'ordre k (**?**), qui est une convolution de k exponentielles :

$$n\left(x = \frac{r}{\langle r \rangle}\right) = \frac{k^k}{\Gamma(k)} \, . \, x^{k-1}.e^{-kx} \qquad \text{avec} \qquad k = \frac{1}{1-\gamma}. \tag{I.43}$$

Γ est la fonction gamma d'ordre k. Ici aussi $\langle r \rangle$ est le rayon moyen :

$$\langle r \rangle = R_{10} = \frac{\int_0^{+\infty} \; r.\omega(r,t) \; dr}{N_{tot}(t)}. \tag{I.44}$$

On remarquera que la distribution finale est à la fois marquée par le processus d'agrégation qui donne la décroissance exponentielle à la distribution et par la géométrie initiale du ligament. Les corrugations initiales des ligaments déterminent l'ordre de la fonction gamma k via le paramètre d'interaction γ (**?**). La taille moyenne des gouttes est quant à elle une fonction non-triviale du diamètre moyen du ligament et du paramètre d'interaction (**?**) : lorsque celui-ci est proche de 1 (ceci correspond à un ligament presque lisse), l'agrégation est faible et le diamètre moyen est proportionnel au diamètre du ligament, le cas limite de non-interaction ($\gamma = 1$) étant le résultat du cas idéalisé de l'instabilité de Rayleigh-Plateau dans le cas d'une perturbation monochromatique (**?**). Lorsque le paramètre d'interaction est fort (ligament fortement corrugé), le diamètre moyen des gouttes tend à se rapprocher du diamètre sphérique correspondant au volume du ligament, car le nombre de gouttes produites est très petit et la valeur moyenne est alors marquée par la plus grosse goutte produite, qui draine la majorité du volume du ligament. Plus de détails sur la dynamique d'agrégation à l'échelle des ligaments peuvent être trouvés dans la revue de Eggers et Villermaux (**?**).

Cette distribution semble dans les faits être très adaptée pour les cas où une taille de ligaments particulière est sélectionnée par la dynamique de l'écoulement (**?**, **?**, **?**, **?**, **?**). Néanmoins, comme l'élément fondamental de ce scénario est le ligament fluide, une subtilité apparaît lorsque les diamètres caractéristiques des ligaments produits ne sont pas monodisperses, ou de façon équivalente lorsque la taille moyenne du ligament est très modulée dans sa longueur (**?**). Dans ce cas une application peu prudente de cette théorie peut mener à des interprétations précipitées (**?**). Dans le cas d'une modulation à grande échelle de la section transverse d'un ligament très long, Villermaux et Bossa en 2011 ont notamment trouvé que la distribution de tailles de goutte n'est pas une fonction gamma (**?**). Dans ce contexte, la dynamique d'agrégation laisse sa marque à la fois sur la distribution de tailles de ligament ainsi que sur le produit de la fragmentation de ceux-ci. Ils ont supposé que la distribution de tailles de ligament suit une loi gamma, car elle est produite par une dynamique d'agrégation à plus grande échelle. Ainsi, il est possible d'obtenir la distribution complète des tailles de goutte en intégrant le produit de la distribution de tailles de ligament avec la distribution du rapport taille de goutte sur taille de ligament (celui-ci fonctionne dans cette opération comme une probabilité conditionnelle) :

$$n\left(x=\frac{r}{\langle r\rangle}\right)=\frac{2m^m n^{\frac{m+n}{2}}\ (mx)^{\frac{n-m}{2}}\ x^{m-1}}{\Gamma(m)\Gamma(n)}\ .\ K_{m-n}(2\sqrt{mnx}). \tag{I.45}$$

K_{m-n} est une fonction de Bessel de 2ème espèce modifiée, de paramètre $m-n$, m est le paramètre associé aux corrugations de grande échelle produisant la distribution de tailles de ligament et n est associé aux corrugations de petite échelles pilotant la fragmentation des ligaments individuels. Les deux paramètres de cette distribution sont donc vérifiables expérimentalement (**?**). De manière générale, ce cadre d'interprétation invite donc à prêter attention à la dynamique des ligaments, qui peut même, le cas échéant, produire des distributions multimodales contenant plusieurs fonctions gamma (**?**).

En conclusion, la question des distributions de tailles de goutte, bien que foisonnante, doit être comprise dans le cadre plus général des modèles simplifiant la physique et ayant des prétentions à prédire les données pour des expériences réalisées dans des circonstances similaires ; de tels modèles ne peuvent se permettre d'introduire des paramètres surnuméraires, à moins de laisser la possibilité d'en vérifier la valeur autrement que par la seule inversion des données qu'ils visent à prédire (**?**). Ces paramètres doivent par ailleurs être cohérents vis-à-vis de la physique en question, mais ce n'est qu'une condition nécessaire.

F Ecoulement à grande échelle

1 Thermique turbulent

De même que les petites échelles de l'écoulement post-impact posent question sur le transfert diffusif, l'existence d'un écoulement à grande échelle est probablement déterminant sur la profondeur à laquelle le métal liquide peut s'équilibrer (**?**, **?**). En première approximation, la situation initiale de la chute d'une grande masse de métal liquide dans un océan de magma peut se rapprocher de ce qui est connu dans la littérature sous le nom de thermique turbulent (**?**, **?**, **?**). Un thermique turbulent est un écoulement qui se développe lorsqu'une masse de fluide est relâchée dans un autre fluide de densité différente dans des conditions telles que la viscosité peut être négligée (*i.e.* l'écoulement devient turbulent en un temps caractéristique proche du temps de chute libre de cette masse de fluide). Le nom et la première motivation viennent de l'étude des phénomènes atmosphériques de convection où celle-ci prend parfois la forme de masses d'air chaud, "les thermiques", se décrochant de la couche limite thermique au-dessus du sol et évoluant dans une atmosphère plus ou moins stratifiée (**?**). La théorie canonique de ce type d'écoulement est formellement basée sur l'intégration des équations de Navier-Stokes dans un certain volume.

Ce volume est généralement défini par une surface de contrôle sphérique enfermant initialement le fluide de densité différente. Cette dernière est grossièrement définie pendant l'évolution du thermique par la limite entre le fluide ambiant pur et le fluide dense dilué (la véritable forme de cette limite n'est sphérique qu'à l'ordre 1, mais c'est d'une importance secondaire). Dans sa chute, la turbulence va entrainer du fluide ambiant à travers cette surface de contrôle, mélanger celui-ci avec le fluide déjà contenu dans cette surface et faire ainsi croître le volume (*cf.* figure **??**). Si la forme de cette surface de contrôle est une véritable supposition, on comprend bien que le choix d'intégrer les équations de Navier-Stokes à la limite du fluide dilué répond à des exigences pratiques de prédiction de la position et de la dilution en fonction du temps du fluide "coloré" (dans certains contextes

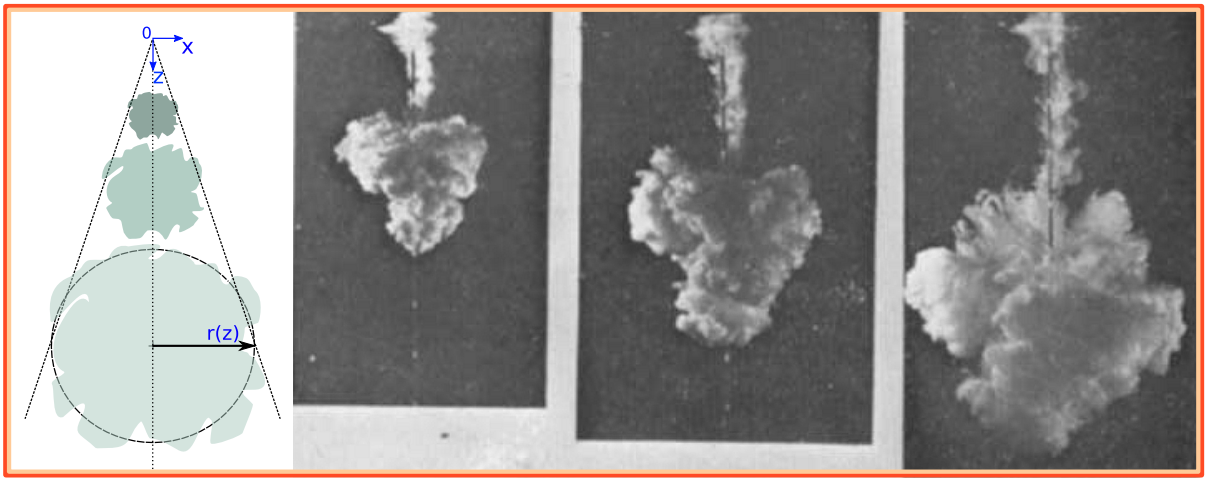

FIGURE I.15 – Panneau de gauche : Schéma d'un thermique turbulent. Panneau de droite : Photographies d'expérience de chute d'un fluide dense et miscible dans de l'eau. Les intervalles de temps sont constants. Extrait de **?**.

il pourrait même être contaminé). Ce n'est donc ni une véritable supposition ni un choix arbitraire mais implicitement une solution d'ordre 1 à problème plus général d'optimisation d'une estimation des valeurs de vitesse, dilution et position du fluide "coloré".

Plusieurs hypothèses permettent de donner aux équations intégrées de conservation de la masse et de Navier-Stokes une forme simple. Une liste détaillée est donnée par Escudier (**?**) mais nous aborderons un cas plus général, en particulier concernant la perte de quantité de mouvement dans la trainée du thermique (*i.e.* l'existence d'une force de trainée). Nous retiendrons :

1. le flux de masse entrainée à travers la surface de contrôle est proportionnelle au produit de son aire avec la vitesse typique de chute/d'ascension du thermique avec un coefficient de proportionnalité α (**?**).

2. le flux de masse entrainée à travers la surface de contrôle est associé à un flux de quantité de mouvement négligeable ou nul.

3. le fluide à l'intérieur de la surface de contrôle n'en sort pas et ne voit pas sa densité moyenne évoluer autrement que par dilution (l'excès de masse est conservé).

4. le thermique est sphérique et bien mélangé ; il est caractérisé par son rayon, la position de son centre et sa masse volumique moyenne (*cf.* figure **??**).

La spécificité du problème géophysique requiert que deux hypothèses fortes soient abandonnées par rapport au thermique classique. Dans notre cas le thermique peut avoir une vitesse initiale non-nulle et sa différence de densité par rapport au fluide ambiant n'est pas négligeable (non-Boussinesq). Lorsque les 4 hypothèses sus-citées sont vérifiées, on peut écrire les 3 équations permettant d'obtenir l'évolution en temps du rayon $r(t)$, de la masse volumique $\rho(t)$ et de l'altitude du thermique $z(t)$:

$$\begin{cases} \dfrac{d}{dt}\left[\rho.\dfrac{4}{3}\pi\ r^3\right] & = 4\pi r^2.\ \rho_a.\alpha|v| \\ \dfrac{d}{dt}\left[\ (\rho-\rho_a).\dfrac{4}{3}\pi\ r^3\right] & = 0 \\ \dfrac{d}{dt}\left[\ \left(\rho.\dfrac{4}{3}\pi\ r^3+\rho_a.k.\dfrac{4}{3}\pi r^3\right).v\ \right] & = (\rho-\rho_a).\frac{4}{3}\pi\ r^3.g\ -c_d.\pi r^2.\frac{1}{2}\rho_a v|v| \end{cases} \tag{I.46}$$

Ici k est le coefficient de masse ajoutée (**?**), rendant compte de l'instationnarité de l'écoulement associé à la dilution du thermique (de plus en plus de fluide doit être mis en mouvement afin de faire place à la masse grandissante du thermique). Le coefficient de trainée c_d n'a pas ici tout à fait le même statut que notre coefficient de trainée Cd défini comme nombre adimensionné quantifiant le rapport de la poussée d'Archimède sur l'inertie de l'écoulement. c_d est un paramètre *a priori* constant dont la fonction est de quantifier la quantité de mouvement perdue dans le sillage du thermique. Le Cd du thermique turbulent est quant à lui dépendant du temps. Quelques réorganisations permettent de saisir l'effet de chacun des termes. Comme $v = \frac{dz}{dt}$, la différence des 2 premières équations divisée par v donne :

$$\frac{dr}{dz} = \alpha. \tag{I.47}$$

En conséquence, α est aussi le coefficient d'expansion du thermique turbulent. Sa valeur est facilement accessible expérimentalement et il n'est donc pas dans les faits un véritable paramètre libre du modèle de thermique turbulent. Néanmoins, du fait de la forte approximation faite en supposant la surface de contrôle sphérique, il reste entaché d'indéterminations importantes à petite échelle de temps. Des valeurs allant typiquement de 0.35 à 0.2 jusqu'à 0.01 pour des cas limites (à la limite avec des cas où une théorie sur les vortex toroidaux serait peut-être plus adaptée) sont reportées par la littérature (**?**, **?**, **?**). En parallèle, l'utilisation des 2 premières équations permet d'expliciter le rôle de chacun des termes issus de la dérivée de l'impulsion dans la $3^{ème}$ équation :

$$(\rho+k\rho_a).\frac{4}{3}\pi r^3\ \frac{dv}{dt} = (\rho-\rho_a).\frac{4}{3}\pi\ r^3.g\ -\left(\frac{1}{2}c_d+4\alpha(1+k)\right).\pi r^2.\rho_a v|v| \tag{I.48}$$

On constate que le terme apporté par la trainée est indiscernable du terme de dilution : ils ont exactement la même influence. Dans le cas où les coefficients de trainée et de masse ajoutée sont nuls, on peut chercher une solutio auto-similaire au système d'équations **??** (**?**). Par la suite, nous préférons intégrer numériquement l'équation **??** afin d'avoir une réprésentation plus fidèle de la trajectoire des thermiques. Toutefois, il faut noter un résultat de ce modèle qui nous importera particulièrement par la suite : la profondeur du diapir croit asymptotiquement en fonction de la racine carrée du temps (**?**, **?**) :

$$z(t) \simeq R_0.\left(8\alpha^3\left(1+k+\frac{3}{16}\frac{c_d}{\alpha}\right)\right)^{-\frac{1}{4}}\ .\ \left(\frac{\frac{\Delta\rho}{\rho_a}g}{R_0}\right)^{\frac{1}{2}}\ .\ t^{\frac{1}{2}} \tag{I.49}$$

avec R_0 le rayon initial du thermique. La vitesse caractéristique apparaissant dans cette expression est encore une fois la vitesse de chute libre. Les équations du thermique accompagnées de l'hypothèse d'entrainement turbulent expliquent avec succès un grand nombre d'expériences de lâcher de masse de fluide plus ou moins dense que son environnement (**?**, **?**, **?**, **?**), de même que des expériences où le fluide diphasique est une suspension de bulles, particules fines ou gouttes (**?**, **?**, **?**, **?**, **?**, **?**, **?**). La question de la signification physique de ce modèle reste cependant encore entourée de flou. L'existence et le rôle des coefficients de masse ajoutée et de trainée dans les équations s'entendent bien car il s'agit d'un couplage entre le volume de fluide défini par la surface fermée et l'extérieur par l'intermédiaire de la pression (qui ont leurs homologues pour des objets plus simples, *i.e.* rigides). Le flux entrainé et la valeur relativement constante, pour une expérience donnée, du coefficient d'entrainement restent avant tout basés sur des arguments dimensionnels (**?**). En particulier, un lien étroit semble exister entre le coefficient d'entrainement et la circulation du vortex (**?**) subsistant au cœur du thermique turbulent (**?**, **?**).

2 Vortex toroïdal dense

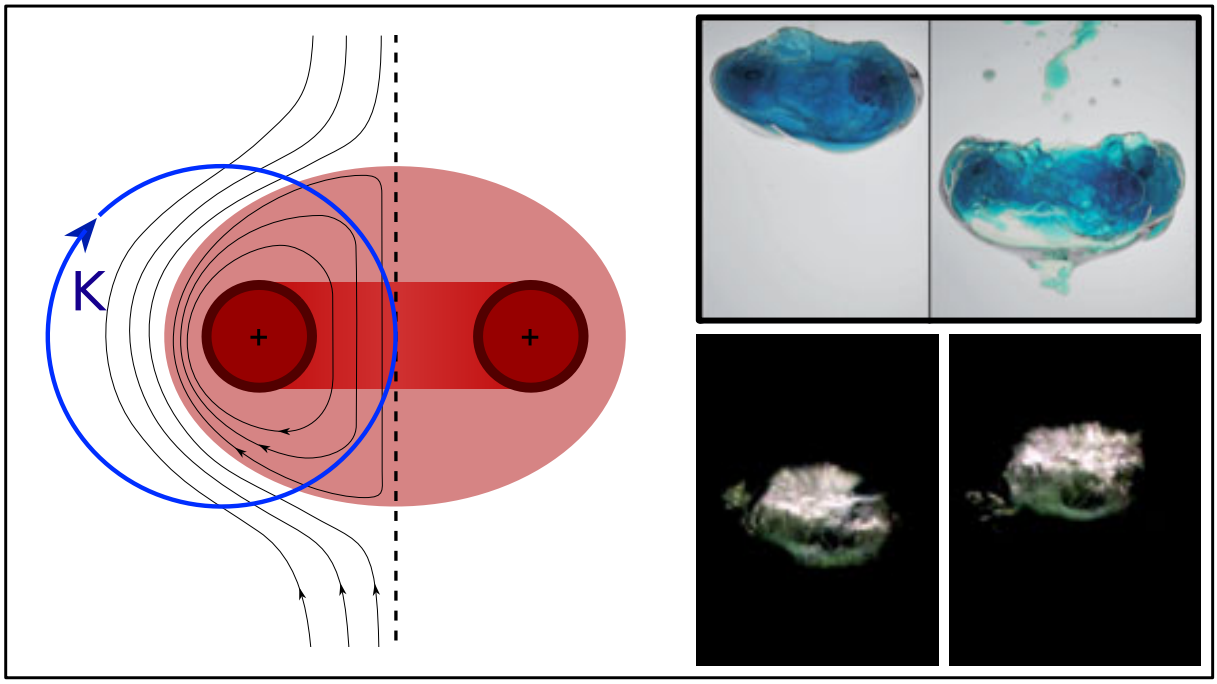

FIGURE I.16 – Paneau de gauche : schéma de vortex toroïdal dense. Des lignes de courant typiques sont superposées pour référence. Panneau de droite, encart supérieur : photo de vortex dense issu de la chute d'un fluide immiscible extraite de **?**. Encart inférieur : photo de vortex toroïdal dense issu du lâché d'une bulle d'air au fond d'un réservoir d'eau extraite de **?**.

De récentes expériences réalisées par M. Landeau (**?**) ont montré une corrélation entre le nombre de Richardson terminal (équivalent au coefficient de trainée du présent manuscrit) et le coefficient d'entrainement. Ces mesures étaient accompagnées d'observations montrant clairement une transition entre un régime où la masse de fluide dense prend une forme de

vortex toroïdal associé à un faible Cd et à un α proche de 0.05, et un régime plus typique de thermique turbulent (*cf.* fig **??**) associé à un Cd proche de 1 et un α autour de 0.2. Il est en effet plausible que la vorticité contenue dans le thermique turbulent modifie les conditions aux limites du thermique turbulent de telle manière que ce dernier voit à la fois sa trainée être réduite et simultanément rende plus difficile l'entrainement à travers la surface de contrôle. Ceci expliquerait la corrélation positive entre α et Cd mais comme cette vorticité n'était pas mesurée et que sa valeur n'était que qualitativement corrélée avec la cause de son introduction, le lien est resté manquant. L'idée d'un lien entre vorticité initiale et coefficient d'entrainement date pourtant de 1957 avec le modèle de vortex dense de Turner (**?**, **?**, **?**). La supposition de départ du modèle est que la vitesse de la masse de fluide dense est **auto-induite** par le vortex toroïdal contenu dans cette même masse. La circulation K est supposée constante sur un contour fermé passant par le centre de la région occupée par la masse et se bouclant dans le fluide extérieur. Comme la vitesse est induite, la conservation de la masse et de l'impulsion voit ce terme substitué par $c_v \frac{K}{r}$, où c_v est une constante positive :

$$\left\{ \begin{array}{rl} \dfrac{d}{dt}\left[\rho.\dfrac{4}{3}\pi\ r^3\right] & = 4\pi r^2.\ \rho_a.\alpha\ .\ \left|c_v\dfrac{K}{r}\right| \\ \dfrac{d}{dt}\left[\ (\rho-\rho_a)\,.\dfrac{4}{3}\pi\ r^3\right] & = 0 \\ \dfrac{d}{dt}\left[\rho.\dfrac{4}{3}\pi\ r^3.c_v\dfrac{K}{r}\right] & = (\rho-\rho_a)\,.\frac{4}{3}\pi\ r^3\ .\ g \end{array} \right. \tag{I.50}$$

De même que pour le thermique turbulent, on simplifie la première équation avec la différence de la première avec la deuxième, on obtient :

$$\left\{ \begin{array}{rl} \dfrac{dr}{dt} & = \alpha\ .\ \left|c_v\dfrac{K}{r}\right| \\ \dfrac{d}{dt}\left[\rho r^2\right] & = \dfrac{1}{c_v}\ .\ \dfrac{(\rho-\rho_a)\,R_0^3 g}{K} \end{array} \right. \tag{I.51}$$

L'approximation de Boussinesq (les variations temporelles de ρ sont négligeables vis-à-vis de celles de r^2) permet d'obtenir le rayon en fonction du temps

$$r(t)^2\ -\ R_0^2\ =\ \frac{1}{c_v}\frac{\Delta\rho R_0^3 g}{K}(t-t_0). \tag{I.52}$$

Il est toujours possible de redéfinir l'instant t_0 et le rayon R_0 de référence, on peut voir que même un vortex qui ne respecte pas initialement les approximations de Boussinesq tend à l'asymptote des temps longs vers la loi $r^2 \simeq t$. Comme on a $\dfrac{dz}{dt}\ =\ \left|c_v\dfrac{K}{r}\right|$, on retrouve :

$$\frac{dr}{dz}\ =\ \alpha\quad\text{avec}\qquad z(t)^2 \simeq t \tag{I.53}$$

En un mot, les vortex toiroïdaux ont les même contraintes dimensionnelles que les thermiques turbulents, et obéissent donc à des lois asymptotiques similaires. Ceci a justifié

une continuité entre les deux (**?**, **?**), et permet par la même occasion de produire une prédiction sur la constante α (**?**) dans le cas de l'approximation de Boussinesq :

$$\alpha \ = \frac{1}{c_v} \ \frac{\frac{\Delta\rho \ R_0^3 \ g}{\rho_a}}{K^2}. \tag{I.54}$$

De plus, dans le cas d'un simple thermique sans vitesse initiale, la vorticité est produite initialement par la poussée d'Archimède, de telle sorte que le rapport $\Delta\rho \ R_0^3 \ g/K^2.\rho_a$ est d'ordre 1, ce qui est cohérent avec les valeurs typiques de α (**?**, **?**).

Pour affiner ce modèle de vortex, une force aérodynamique analogue à l'effet Magnus (**?**) a été ajoutée. Elle tend à faire s'élargir le vortex turbulent dans la direction horizontale (**?**). Généralement, cela implique d'abandonner la description qui se base sur une surface de contrôle, ce qui réduit les capacités de prédiction de la dilution de la masse de fluide dense. Toutefois, dans ce cadre le bilan permet de donner une explication sensible à l'expansion du vortex via sa vorticité. On se place cette fois au niveau d'un élément d'épaisseur unitaire d'un tore de volume W, la conservation de la quantité de mouvement donne :

$$\frac{d}{dt} \ . \ \left[\rho \frac{W}{2\pi r}.\vec{v}\right] = \ \rho_a \ 2r \ \vec{K} \ \wedge \ \vec{v} \ + \ \frac{W}{2\pi r} \ . \ (\rho_a - \rho) \, \vec{g} \tag{I.55}$$

Dans le référentiel avançant à la vitesse induite du vortex, la composante horizontale (donc induisant une expansion latérale) de la force aérodynamique appelée force de Kutta-Joukowski compenserait la poussée d'Archimède (**?**, **?**, **?**). L'expansion des vortex toroïdaux d'air lors de leur remontée dans l'eau (*cf.* fig **??**) semble obéir à ce genre de dynamique (**?**). Toutefois, cette variante ne permet pas de comprendre comment de la masse peut s'ajouter au vortex turbulent, le coefficient α étant rajouté de façon *ad-hoc*, ou de la même manière que précédemment, ce qui fait coexister la théorie de l'induction de vitesse (caractéristique des écoulements laminaires) avec un entrainement turbulent.

G Transferts diffusifs

Au lecteur fatigué de ces lignes, il pourra sembler laconique bien que réconfortant d'aborder le problème des échanges diffusifs dans une forme aussi limitée que celle-qui va suivre. C'est encore une fois la contrainte d'un sujet vaste au possible, et très largement étudié, qui va nous conduire à limiter notre analyse des transferts diffusifs dès maintenant. La diffusion d'un scalaire (ici la température ou les compositions de différents éléments) dans un fluide en mouvement obéit à une équation d'advection-diffusion. Dans notre cas la température et la composition rétroagissent de façon négligeable sur l'écoulement (les variations de densité induites sont négligeables vis-à-vis de $\Delta\rho$), l'étude des transferts diffusifs se limite donc à l'ajout de l'équation d'advection-diffusion, qui s'écrit dans sa forme adimentionnée de la manière suivante

$$\frac{d\tilde{A}}{d\tilde{t}} \ + \ \left(\tilde{\vec{u}}.\nabla\right) \tilde{A} \ = \ \frac{1}{Pe}. \triangle \tilde{A} \tag{I.56}$$

avec $\tilde{A}$ la température ou concentration divisée par la concentration de référence, et Pe le nombre de Péclet :

$$Pe = \frac{uR}{D}. \tag{I.57}$$

D est le coefficient de diffusion que l'on notera lorsque le besoin de détailler les situations se fera sentir $D_{T/a}$ et $D_{C/a}$ pour le coefficient de diffusion dans le fluide ambiant de la température et de l'espèce chimique C respectivement, et $D_{T/m}$ et $D_{C/m}$ le coefficient de diffusion dans le métal liquide de la température et de l'espèce chimique C respectivement. Le nombre de Péclet compare l'intensité de l'advection à la diffusion. Dans notre cas, les coefficients de diffusion sont au plus de l'ordre de 10^{-6} $m^2.s^{-1}$, qui sont donc très inférieurs aux ordres de grandeur mis en jeux par l'advection (*cf.* partie 1). On peut alors restreindre une nouvelle fois nos considérations d'équilibration à des régimes à très grands nombres de Péclet, où la diffusion est asservie à la cinématique de l'écoulement. Une seconde subtilité doit être introduite à ce point : notre intérêt principal est l'équilibration des deux phases, or l'interphase entre ces deux phases est par définition une limite cinématique. L'intégrale de l'équation d'advection-diffusion sur cette interface permet de se rendre compte que c'est l'intégrale du gradient sur cette interface qui est responsable du passage du scalaire d'une phase à l'autre. Néanmoins, dans la limite des hauts Pe, ce sont les mouvements de fluide qui vont produire ces gradients. Proche de l'interface, on aura donc un équilibre entre gradient diffusif et advection. "Proche" est à comprendre littéralement, c'est une distance typique sur laquelle vont se construire les gradients et l'échelle typique de l'advection, car cette équation relaxe vers un équilibre local.

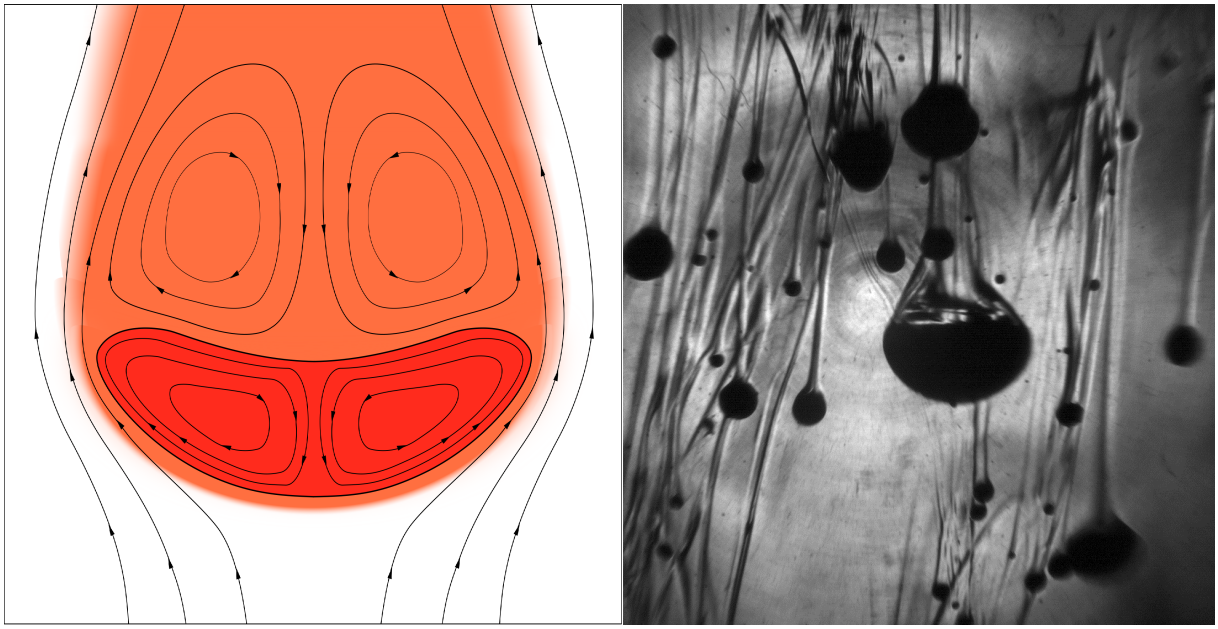

FIGURE I.17 – Panneau de gauche : schéma représentant une goutte en déséquilibre thermique avec le fluide dans lequelle elle chute. La couleur représente l'écart de température local par rapport à la température du liquide ambient. Panneau de droite : image extraite de vidéo en ombroscopie d'une expérience de chute de galinstan préalablement chauffé dans un mélange d'eau/UCON oil.

Plusieurs cadres de pensée ont été développés afin de déterminer la longueur typique du gradient. Pour les gouttes par exemple, on peut citer la théorie de pénétration du

gradient de Higbie (**?**), qui considère un gradient verrouillé par l'advection ce qui permet notamment de prédire le transfert à l'intérieur de gouttes qui oscillent (**?**, **?**). D'autre part, on peut aussi considérer que l'effet de l'advection est le renouvellement de la surface au niveau de l'interface entre les deux fluides (**?**). Ces deux théories sont en vérité compatibles et quasi-indiscernables si l'on fait attention où se situe la résistance à la diffusion. Pour les cas très simples comme la dissolution d'un gaz à partir d'une bulle de ce gaz pur dans l'eau, on sait que le gradient se construit par diffusion dans une couche limite advectée à la vitesse de chute de la goutte u sur une distance à peu près égale au rayon R. L'épaisseur l_A de la couche limite sur laquelle se construit le gradient vérifie l'équilibre entre advection et diffusion :

$$u \,.\, C \,.\, 2\pi R.l_A \;\simeq\; D.4\pi R^2 \frac{C}{l_A} \tag{I.58}$$

Ce qui donne

$$l_A \;=\; \sqrt{D\frac{R}{u}} = R \,.\, Pe^{-\frac{1}{2}}, \tag{I.59}$$

où $\frac{u}{R}$ est le temps d'advection de la goutte, mais aussi le temps de renouvellement de la surface. Un bilan global sur la goutte (*i.e.* implicitement une intégration de l'équation **??** dans le volume de la goutte) permet alors d'obtenir une loi d'échelle sur le temps caractéristique d'équilibration :

$$\frac{dVC}{dt} \;\simeq\; SD\frac{\Delta C}{l_A} \qquad \Longleftrightarrow \qquad \frac{dC}{dt} \;\simeq\; \frac{S}{V}\frac{1}{R}D \,.\, Pe^{\frac{1}{2}} \,.\, \Delta C. \tag{I.60}$$

ΔC est la différence entre la concentration en C à l'intérieur et à l'extérieur de la goutte, V et S sont respectivement le volume et la surface de la goutte. Bien que très simple, ce cas de figure fait apparaitre un temps caractéristique $\tau_{eq} \;=\; \frac{\frac{V}{S}.R}{D} Pe^{-\frac{1}{2}}$ qui montre que l'équilibration entre deux phases va être à la fois pilotée par la physique de la couche limite (ici donnant le terme en $R.Pe^{-\frac{1}{2}}$) et par le rapport surface sur volume de la goutte. C'est pourquoi beaucoup de modèles d'équilibration entre deux phases dans des réacteurs agitateurs se sont concentrés sur le diamètre de Sauter (**?**), qui de par sa définition est un diamètre très important pour l'estimation des échanges diffusifs (**?**, **?**).

En conclusion, si le cas particulier du transfert entre deux phases à haut nombre de Péclet peut paraitre simple au vu de la domination des termes d'advection, la contrainte de passer l'interface nous invite à considérer la cinématique de l'écoulement dans le détail, à toutes les échelles. En effet les petites échelles de l'écoulement (bien souvent, mais pas toujours, la turbulence) peuvent produire les gradients plus intense capables de transporter les scalaires à travers les interfaces mais toutes les échelles déforment l'interface. Et c'est pourquoi au vu de l'anticipation que consiste la formulation d'hypothèses sur les petites échelle de l'écoulement, notre exposé sur les transferts diffusifs entre métal et silicate pendant l'écoulement post-impact s'arrête ici.

Nous allons donc dans un premier temps analyser les expériences que nous avons faîtes avec un système de fluides analogues afin d'étudier la dynamique de l'écoulement post-impact avant et après la fragmentation. Nous testerons notamment les hypothèses relatives au thermique turbulent/vortex toroidal et les équations d'évolution qui en résultent. Nous étudierons aussi la fragmentation des gouttes, leur distribution de tailles et leur vitesse de

chute. Ceci nous permettra enfin de construire un ensemble d'hypothèses réalistes sur les petites échelles de l'écoulement. Ce faisant, nous analyserons plus en détail les expériences de mesure de température que nous avons conduites afin de quantifier les échanges diffusifs pendant l'écoulement post-impact et nous testerons les théories qui s'y rapportent.

Chapitre II

Experimental methods

This thesis reports an experimental study of the fall of a large amount of liquid iron initially sitting at the top of a deep magma ocean. The choice of approaching this flow via experiments appeared to us as the most promising given the very turbulent two phase flow that it implies. We designed an experiment aiming at reproducing a comparable flow, both in terms of initial condition and in terms of dynamical and diffusive regime.

A Choice of the system of analog fluids

The main characteristics of the geophysical system of fluids is its ratio of density $\tilde{\rho}$ and its surface tension. For planets we have simultaneously $\tilde{\rho} - 1 \sim 1$ and $\tilde{\rho} \sim 1$, the later condition being verified for most liquid systems. Several system of immiscible fluids allow to reach $\tilde{\rho} - 1 \sim 1$. In previous experiments (**?**), we have used gallium as an analog for the liquid iron and a mixture of water and glycerol for the magma ocean. We decided to improve on this system of fluids which had several drawbacks. Indeed gallium melts at 30 °C which makes it prone to freezing as soon as it touches the bottom of the tank, preventing easy recovery. The glycerol absorbs the moisture of the air which creates a low viscosity stable layer close to its surface.

Galinstan is a eutectic mixture of gallium, indium and tin. Its main physical constants are summarized in table **??**. It has replaced mercury in medical thermometers for the same reasons it interests us : it is non-toxic and liquid down to −19 °C (contrary to pure gallium). Its thermal diffusivity is large compared to its viscosity (its Prandtl number $Pr = \frac{\mu C_p}{\lambda}$ is smaller than 1) which means that momentum diffusion is slower that heat diffusion. Due to its metallic state, very different from the usual fluids, its molecular interactions with common fluids are weak and have a negligible effect on its surface energy σ. This chemistry of metals is also responsible for their strong cohesion thus their high σ. Taken together, the interfacial energy between galinstan and any other fluid of the lab with which it does not mix (*i.e* not a liquid metal) is generally its own surface tension, equal to 0.72 $J.m^{-2}$. One thing affects it interfacial properties, it reacts with the dioxygen of the air to form an oxide. The main consequence of the presence of this skin is the enhancement of its apparent wettability towards most solid surfaces. It also gives a surface viscosity as its ability to present surface waves is damped. The effect on the raw interfacial energy is unclear but in order to avoid any, and to avoid the aforementioned effects, the surface

of galinstan was cleaned by two methods. It stayed as much as possible under a layer of hydrochloric acid and approximately every hundred runs, the galinstan was filtered using a fine mesh of steel which is not prone to form amalgams with galinstan.

	iron	galinstan	silicate magma	UCON oil	water
density ρ (in $kg.m^{-3}$)	7800	6440	3500	1100	1000
dynamic viscosity μ (in $Pa.s$)	$10^{-3} - 10^{-1}$	$2.4 \cdot 10^{-3}$	$10^{-2} - 10^{3}$	$3 \cdot 10^{1}$	10^{-3}
thermal conductivity λ (in $J.s^{-1}.K^{-1}.m^{-1}$)	10^{2}	16.5	4	0.165	0.61
specific heat Cp (in $J.K^{-1}.kg^{-1}$)	$5 \cdot 10^{2}$	330	10^{3}	1900	4200
thermal diffusivity η (in $m^{2}.s^{-1}$)	$2.6 \cdot 10^{-5}$	$7.6 \cdot 10^{-6}$	$1.14 \cdot 10^{-6}$	$7.9 \cdot 10^{-8}$	$1.46 \cdot 10^{-7}$
Prandtl number Pr	$5 \cdot 10^{-3} - 10^{-1}$	$5 \cdot 10^{-3}$	$4 \cdot 10^{-1} - 10^{4}$	$1.1 \cdot 10^{5}$	6.9

TABLE II.1 – Table of the main physical constants of the fluids in the present study.

UCON^{TM} oil is a polymer of polyalkylene glycols made of monomers of ethylene and propylene oxides, silicate magma being a liquid made of short polymers of silicate ions with metallic ions in between. It mixes completely with water in a clear liquid whose viscosity can be buffered from water's viscosity (see table **??** for actual value) up to 32 000 times the one of water for pure UCON^{TM} oil, although the full range of viscosity accessible for this mixture was not used in the present study. The base mixture we used is already diluted at 50 % in weight with water. A few tens of percent of hydrochloric was also added to the mixture of UCON^{TM} oil and water in order to prevent the oxidation of the galinstan during its fall. For the mass fraction we have used, the mixture water/UCON oil evaporates, becoming more buoyant and maintaining a convection at the scale of the tank that contained it, resulting in inhomogeneities in the bulk of the ambient fluid. It was mixed vigorously at a different frequency depending on the requirement of the experiment. The density and the viscosity of the mixture of water and UCON^{TM} were measured for each mass fraction of UCON^{TM} of the mixture. This involved different techniques as more precise and more convenient methods were made available to us during the course of this thesis.

Taken together, galinstan and UCON^{TM} oil have a $\tilde{\rho}$ of about 6 which is higher than for liquid iron versus silicate magma (the value is closer to 2) ; however, it seems that the transition between regimes dominated by shear and dominated by dynamic pressure is higher (**?**, **?**). In our experiment, this high $\tilde{\rho}$ mostly allows us to reach higher velocities and thus higher Re and We. From the chemical point of view, the similarity of galinstan and UCON^{TM} oil with the fluid they are supposed to represent is also helpful when the fragmentation cascades down to very small scales. Indeed, this process can theoretically

produce very high or very low pressure. If the phases were too similar, that could result in chemical disequilibrium i.e the two phases could locally be more soluble in each other. That in turn could create gradients of the composition along the interface. This would in turn retroact on the fragmentation process via the dependency of the surface tension on composition (the Marangoni forces). Since the galinstan and the mixture water/UCON^{TM} oil are so dissimilar, they are unlikely to react with one another even at high capillary pressure.

B First experimental set-up

1 Description of the set-up

The first experiment consisted in a 70 cm high by 45 cm square-base transparent tank filled with the mixture of water and UCON^{TM} oil (cf. fig. **??**). The outside frame of the tank extended in an arm at the top of the tank. As an initial condition for the experiment we filled a balloon with a precisely weighted mass of galinstan (the precision of the scale was $\pm 1g$), and fixed it at the top of the tank. Because of the weight of the liquid metal, the balloon deformed in such a way that the typical depth of the center of mass of the liquid metal beneath the ambient fluid's surface was about 3 radii. At the beginning of the experiment the balloon was pierced, releasing in a few thousandths of second the galinstan as a spheroidal mass quasi unperturbed by the retraction of the balloon, with no initial momentum.

The piercing mechanism was made of two syringes linked by a tube, with a needle mounted on the extremity of the piston of the smaller syringe. At the bottom of the tank was a custom made square funnel and bottom reservoir, both made of expanded polystyrene ballasted with iron rods. A cork was made of a ballasted ping-pong ball in order to close the bottom of the reservoir which was linked to a hole at the bottom of the main tank. This liquid metal recovery system was made so that the galinstan would be funneled after its fall in the small reservoir in the most adiabatic way we could design. This is where a measure of its mean temperature after its fall was made. Since the reservoir and the funnel are inverted pyramids, the main surface of exchanges of the pond of liquid metal (the top one) was a square whose area was always proportional to the volume. Thus, the volume to surface ratio of importance for the timescale of thermal equilibration of this pond was always the same, giving this design a timescale of equilibration of the galinstan once its rests in the reservoir an approximately constant value. After each run of the experiment, the shape of the reservoir also insured that no galinstan could stay when the cork was unplugged.

At the back of the tank, a 120 cm high by 60 cm wide white LED panel allowed a uniform backlighting. For each run of the experiment, a high frequency black and white video camera (FASTCAM Mini) recorded the fall of the liquid metal at 1000 frames per second and with a field of view covering the entire depth of free fall of the galinstan (*cf* fig. **??**).

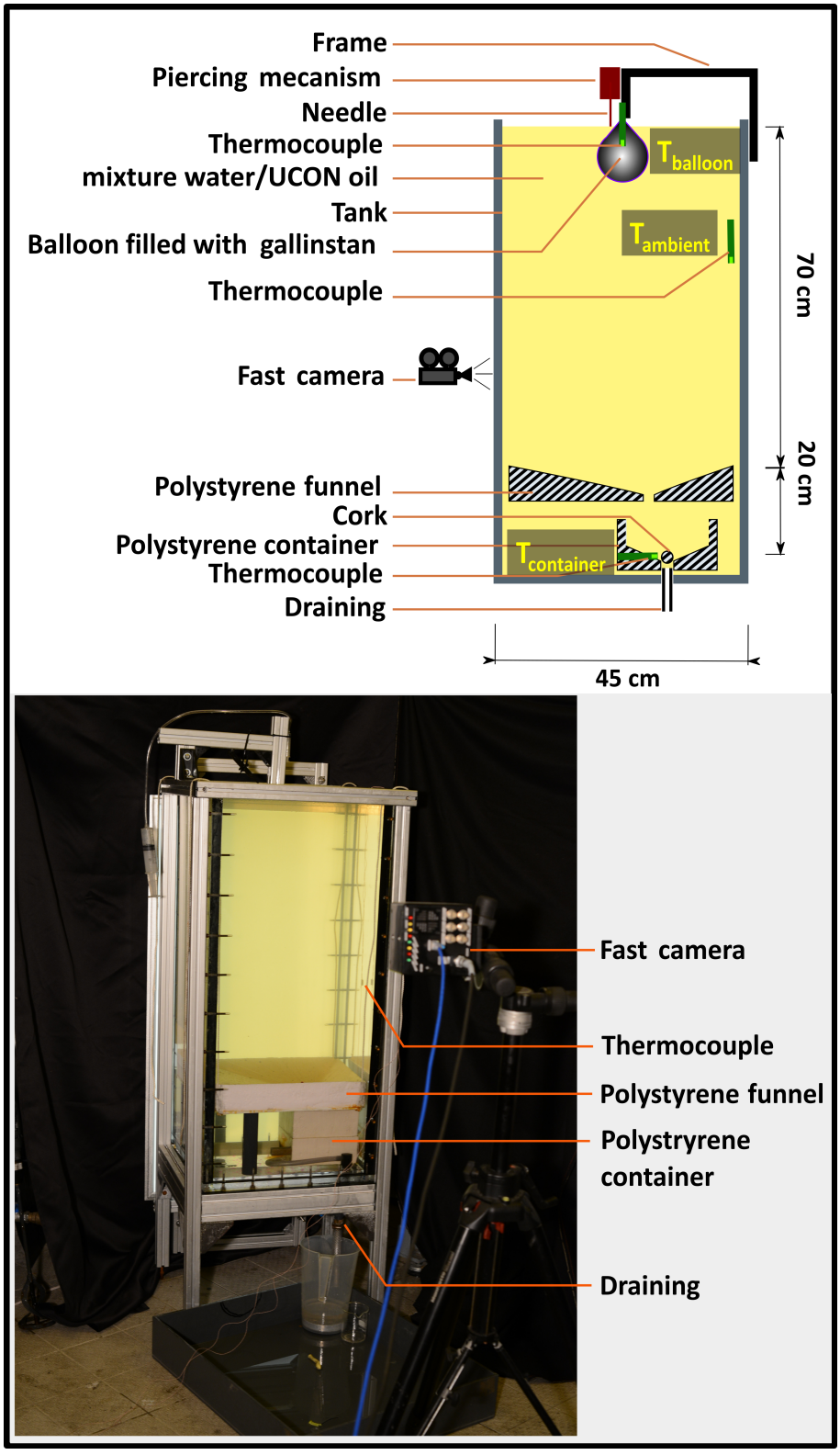

FIGURE II.1 – Top panel : Schematic of the first experimental apparatus. Bottom panel : Photo of the first experimental apparatus.

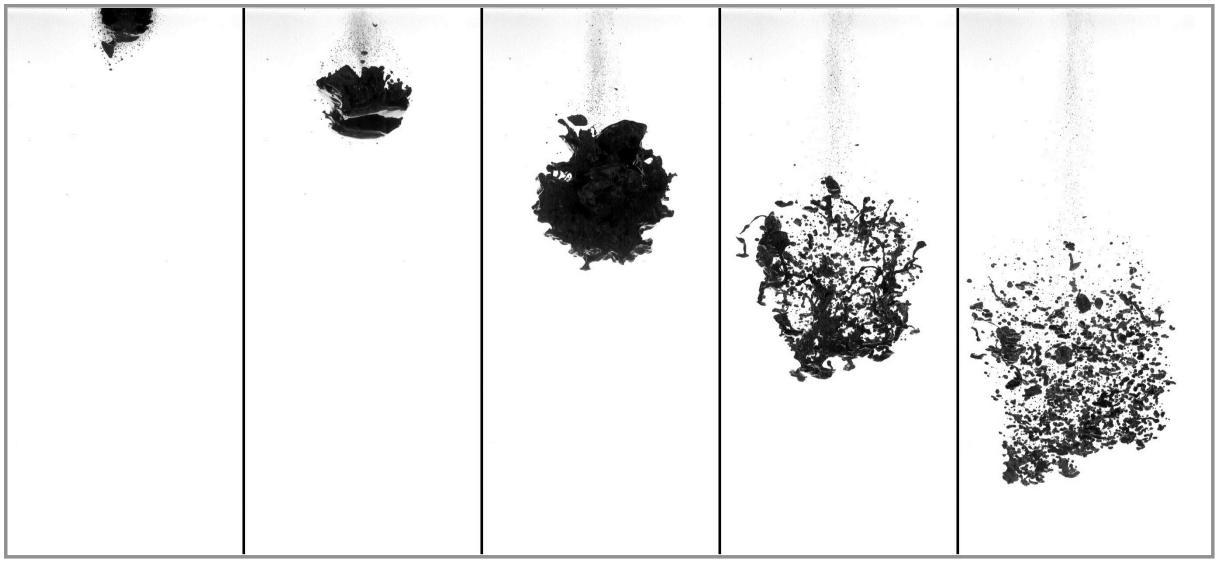

FIGURE II.2 – Series of photos extracted from the video of the fall of a $0.031m$ radius diapir of galinstan falling in water. The metal appears mainly in very dark shade of grey except from a few reflections on the interface prior to breakup. The time interval between snapshots is around $0.12\ s$.

2 Metrology

Measures based on video analysis

The videos of the experiments were treated using Matlab with both built-in routines and custom ones that we briefly explain here.

The intensity levels in the videos that were backlit are, despite some reflections on the surface of the liquid metal, mostly split between black and white. That is why for most of the video processing, the images are binarized using a threshold on the level of renormalized intensity around 0.5. We use the binarized images to compute the position of the center of mass of the black pixels (*cf* fig **??**, center panel) which we assimilate to the position of the center of mass of the galinstan in the plane perpendicular to the line of sight (the assumption being that the projection of the center of mass is the same as the center of mass of the projection). We also use the binarized images to compute the root mean square of the distance between the pixels and the center of the black pixels that we assimilate to radius of the region occupied by the gallium (in order to connect with the idea of the turbulent thermal). The choice of the power to use for the averaging of the distance (formally the particular moment of the distribution of distances as defined for the distribution of radii in chapter **??**) is somewhat arbitrary. A power 2 with respect to the distance is more suited to the part of the fall where breakup of the galinstan has not occurred because it contains a correction that is the equivalent of supposing spherical geometry. When the liquid metal is broken up in a dense cloud of droplets, partial superposition of the drops is expected to affect the distance computed as a standard deviation. We see this as unavoidable as the galinstan opacity implies superposition and saturation, hence information is lost with the projection.

Three more variables of interest are extracted from the binarized images.

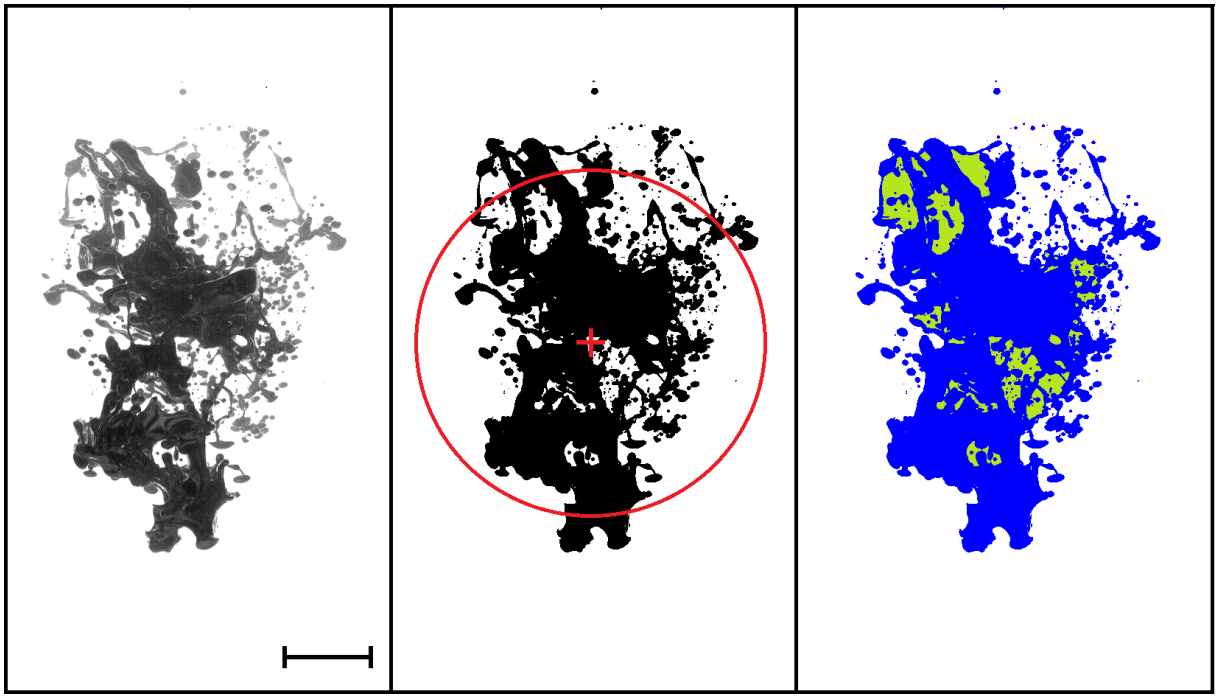

FIGURE II.3 – Images showing the different pieces of information extracted from the videos made with the large framing. Left : raw snapshot from the experimental video. Middle : binarized image with the barycenter of the black pixels (called the center of mass) and the circle with a radius having the value of the mean distance between the black pixels and the center of mass. Right : binarized image colorized in blue in the regions of black pixels that do not touch the side of the frame (connected components) and in green the regions of white pixels enclosed in the connected components assimilated to the holes in the liquid metal sheet.

— The cumulative quantity of black pixels,

— The number of black pixels regions independent from each other that are not linked to the border of the images, the "connected component" (cf fig. **??**, blue regions in the right panel),

— The cumulative quantity of white pixels enclosed in the black pixel regions (cf fig. **??**, green regions in the right panel).

The regions that are counted via the later criterion correspond, at the moment of the breakup, to holes in the stretched liquid metal sheets (cf. fig. **??**). Later in the fall, this criterion identifies regions that are spaces between overlapping droplets. All variables are counted for each frame giving access to their full time series and allowing the calculus of derivatives. Of particular interest will be the falling speed of the liquid metal and the expansion rate of the width of the spherical region it occupies.

Measures of the mean temperature of the liquid metal

In order to quantify the heat exchanged between the liquid metal and the ambient fluid during its fall, we heated galinstan before each experiment through the balloon wall with a warm water bath. The typical difference of temperature with the room and the mixture of

water and UCON^{TM} reached by the galinstan was +15 °C. This value was a compromise in order to have a good noise over signal ratio for temperature measurements, while trying not to affect too much the viscosity of the ambient fluid in the thermal boundary layers. The viscosity of the mixture water and UCON^{TM} is indeed quite sensitive to temperature. For the two highest viscosity ratio where the mixture's viscosity is the most sensitive to the temperature, an increase of +15 °C produces a decrease of viscosity of about 50 %.

Once heated to the desired temperature, the balloon filled with galinstan was placed on its support and popped within ten seconds. We used 3 thermocouples of type N (from the company TC direct) to record time series of the temperature in the balloon, in the tank, and in the bottom reservoir (cf. fig. **??**). Each thermocouple was coated with glue in order to prevent the galinstan to diffuse into the particular alloy of the junction. This in theory reduces the temporal resolution attainable with the thermocouple but we did not need an extreme resolution and were mainly limited by the recording of the temperature via National Instruments acquisition cards. These recordings were made at 2 Hz.

The thermocouple in the balloon was placed during its filling and before closing it. It was placed in such a way that with the stretching of the balloon under the weight of the galinstan the volume of measure of the thermocouple (on the order of a few cubic millimeter) was approximately at the position of the center of the mass of galinstan, which sometimes led to accidental breakup of the balloon when it was not stretched under its own weight. In the few seconds before the popping of the balloon, the temperature inside decreased as it entered the colder ambient fluid (cf. fig. **??**). Because of the central position of the thermocouple, the good conductivity and the expected strong convection inside the balloon, we assumed that the temperature recorded was the mean temperature of the galinstan up until it starts to fall. The second thermocouple was placed at about one centimeter of the side of the tank in order to record the temperature of the ambient fluid outside of the expected thermal boundary layer (the temperature of the room was not well controlled). A few minutes before each run, the ambient fluid was agitated in order to homogenize temperature. The third thermocouple was put in the deepest part of the bottom reservoir, a few millimeters above the side once again in order not to be in any thermal boundary layer. When the liquid metal reached this reservoir, its residual momentum was enough to mix completely the temperature, giving access to the mean temperature of the galinstan after its fall and fragmentation. When staying in the reservoir, galinstan cooled down slowly with a nearly exponential decrease of the temperature as a function of time (cf. fig. **??**). This trend allowed us to extrapolate the temperature of the liquid metal just when it arrived, before it had the time to mix. A second empirical correction was also made to correct for the exchanges of heat made while the liquid metal was pouring from the funnel to the top reservoir by gently pouring heated liquid metal on the funnel, and simultaneously recording the temperature in the funnel and in the bottom reservoir (the measure of the temperature of the galinstan at the level of the funnel for an actual experiment was impossible as the liquid metal arrives too discontinuously).

As galinstan exchanges heat with the ambient fluid when it falls and fragments proportionally to its initial difference of temperature, no raw temperature will be presented or discuss in the following discussion. We will always discuss a non-dimensional final temperature difference :

$$T^* = \frac{T_{final} - T_{ambient}}{T_{initial} - T_{ambient}} \tag{II.1}$$

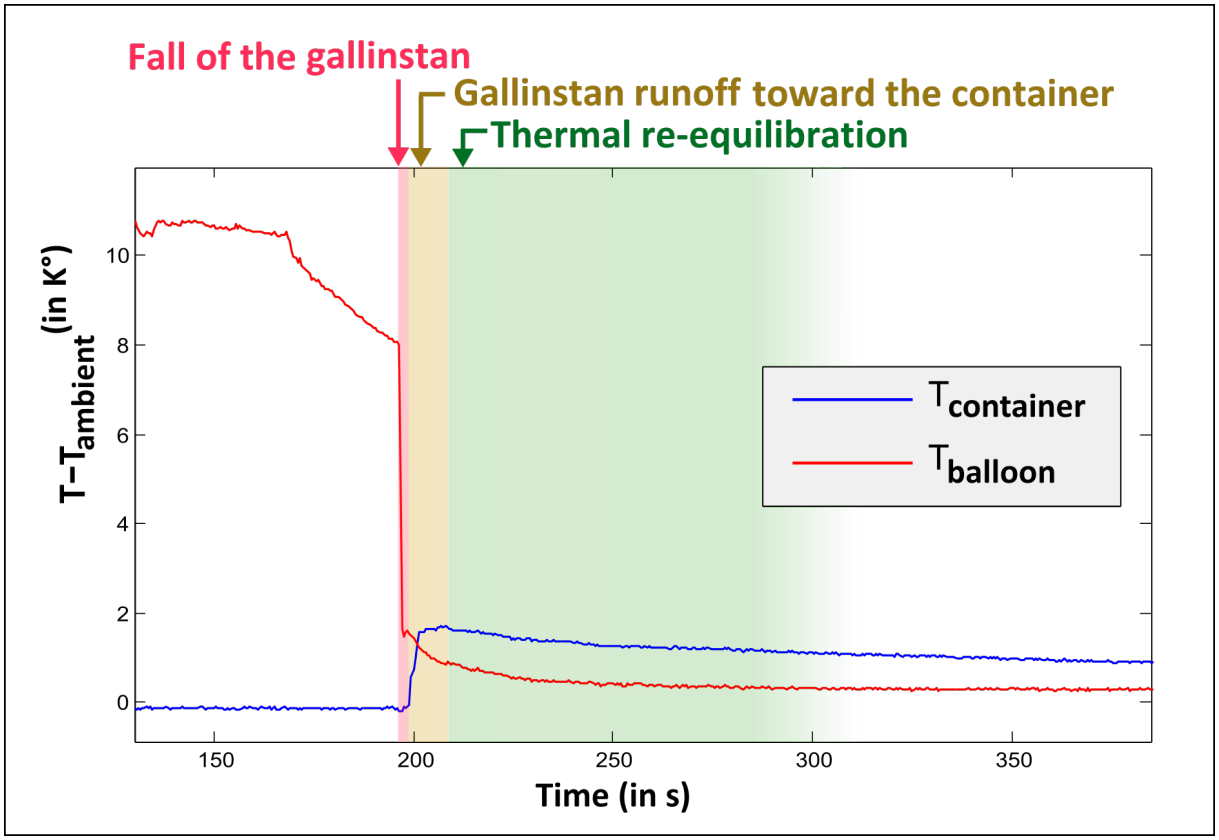

FIGURE II.4 – Graph of the difference of temperature of the thermocouples in the bottom reservoir (in blue) and in the balloon (in red) with the temperature of the thermocouple in the ambient fluid. Different zones of each time series show clear ruptures indicating the start of the fall of the liquid metal and the arrival of the liquid metal in the bottom reservoir.

T_{final} is the corrected final temperature of the galinstan, $T_{initial}$ is the initial temperature of the galinstan (the temperature recorded by the first thermocouple before the slope break, *i.e* the start of the fall) and $T_{ambient}$ is the temperature of the mixture of water and UCON^{TM}. We will also speak in terms of degree of equilibration X :

$$X = 1 - T^* \tag{II.2}$$

C Second experimental set-up

1 Description of the set-up

A number of problems arose from the campaign of measurements on the first experimental setup. One of the goals of this first campaign was the measure of the distribution of drop sizes. Unfortunately the depth of fall of the first setup was not large enough to produce a stable well sampled distribution of droplets. Therefore, in order to resolve this technical problem and a few other scientific problems discovered in the first campaign such as the speed of fall of the diapir before breakup, we decided to reproduce the analog

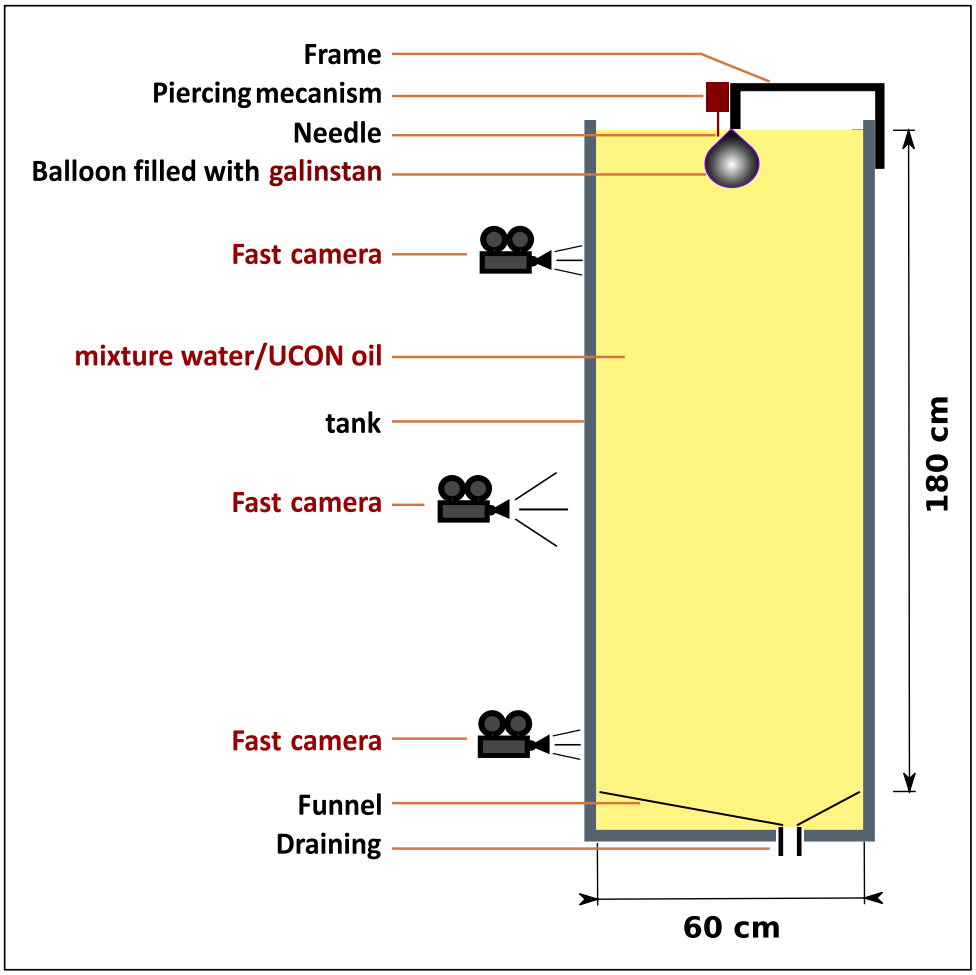

FIGURE II.5 – Schematic of the second experimental apparatus

flow with the same initial conditions in a 1.5 wider and 3 times taller tank (200 cm high and 60 cm wide, see fig. **??** and **??**).

As this height of fall would leave too much time for the galinstan to exchange heat with the mixture of water and UCON^{TM}, we did not intend to measure temperatures because the final difference would have a ratio noise/signal too high. The bottom reservoir was not necessary anymore so it left space for even more height of fall. This led to a height of fall roughly 4 times larger in the second setup than in the first one. In addition, this height of fall gave us the opportunity to film more precisely selected parts of the fall of the galinstan. We used mainly three types of framing (see fig. **??**) :

1. a large scale framing where all the fall and evolution of the galinstan could be followed,
2. a close-up on the top of the tank to investigate the trajectory of the falling mass prior to breakup,
3. a close-up at the bottom of the tank to measure distribution of sizes and vibrations of droplets.

Since each position of the camera excluded the other ones, there is no correspondence among the set of video produced during the second campaign of experiments, for each

FIGURE II.6 – Photo of the second experimental apparatus. The writer of these lines posed to give an idea of the scale.

video one experimental run had to be made.

As for the different framings, different lighting have been used, adapted to the measures planned. The videos with the large scale framing and zoom on the bottom were backlit using the same type of LED panel as in the first set, but two panels had to be spliced vertically. The videos with the zoom on the top of the experiment were lit with two spots on the side of the tank.

2 Metrology

Measures based on video analysis

The routine that we have developed on Matlab for the treatment of the videos made with the first experimental set-up was used again in order to produce comparable data. Only the videos with the large scale framing underwent this treatment.

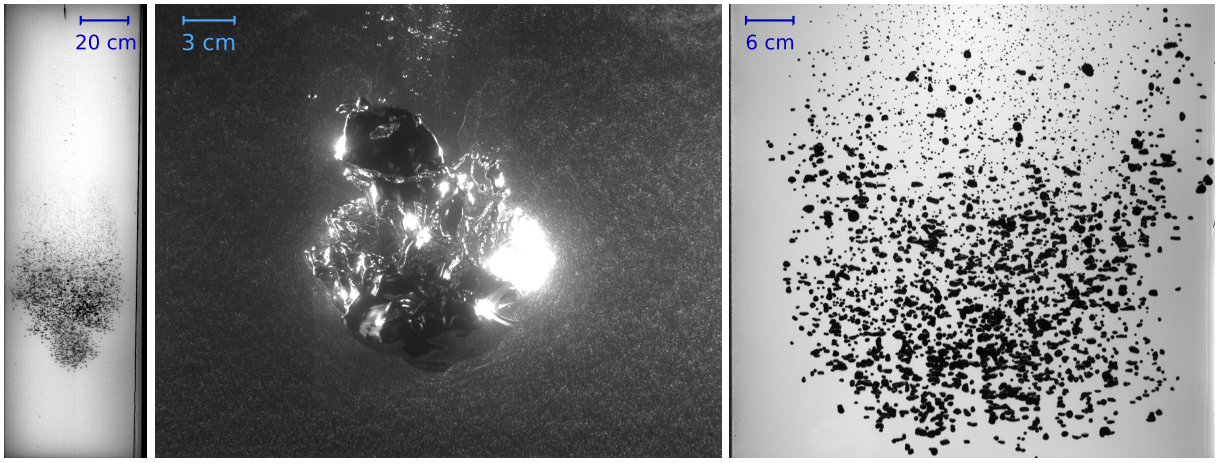

FIGURE II.7 – Snapshots extracted from different videos sampling all the framings used to film the experiments made with the second setup. This compilation concerns only the framings where data extraction from the videos were performed.

Pseudo-PIV based on a plane of particles

Modern PIV technique is based on the lighting of tracer particles via a laser sheet that can be static, or for some PIV in volume, is scanning the entire domain. The idea being that since tracers particles are uniformly spread in the volume one must know where the light is in order to know where the measure is being done. Since the surface of the galinstan is presenting specular reflections, it was not possible to implement a rigorous PIV technique in our setup. We then reused an old method that relies on knowing where the PIV particles are rather than where the light is. This technique involves deposing a curtain of very thin bubbles (their terminal speed must be very small compared to the typical speed of the flow) in a plane containing the trajectory of the center of mass of the falling galinstan. We proceeded by electrolyzing the mixture of water and UCON^{TM} with an electrode at the very top of the tank and another one made with a platinum wire stretched across the middle of a plastic frame fitted for the inner dimensions of the tank. By applying a large voltage between the electrodes while sliding the frame down or up (cf. fig. **??** center and fig. **??**), we were able to set up a curtain of bubbles in the middle of the tank, right in the path of the liquid metal. Since the conductivity of the mixture of water and UCON^{TM} is a function of the mass fraction, several parameters had to be adjusted in order to produce the desired bubble density and mean diameter : the problem depends on the wettability of the ambient fluid and the bubble gaz with respect to the platinum, which were unknown to us. The voltage, the sweep speed of the plastic frame and the quantity of hydrochloric acid were then adjusted by trial and error.

This technique has been used for a long time in order to study the flow around droplets (**?**,**?**, **?**), but was closer to PTV as computation of the trajectory and velocities was done by hand. With available massive computational ressources, we choose to set-up this technique as a pseudo-PIV with denser bubble curtains. Consequently, each pair of consecutive frames was treated using the PIV software DPIV-Soft 2010 on Matlab (**?**).

Obviously, pixels that represent liquid metal should not be used for the PIV, as the velocity computed would be influenced by both the local speed of the fluid and the changing orientation of the interface. However, the images made with bubble curtains contained

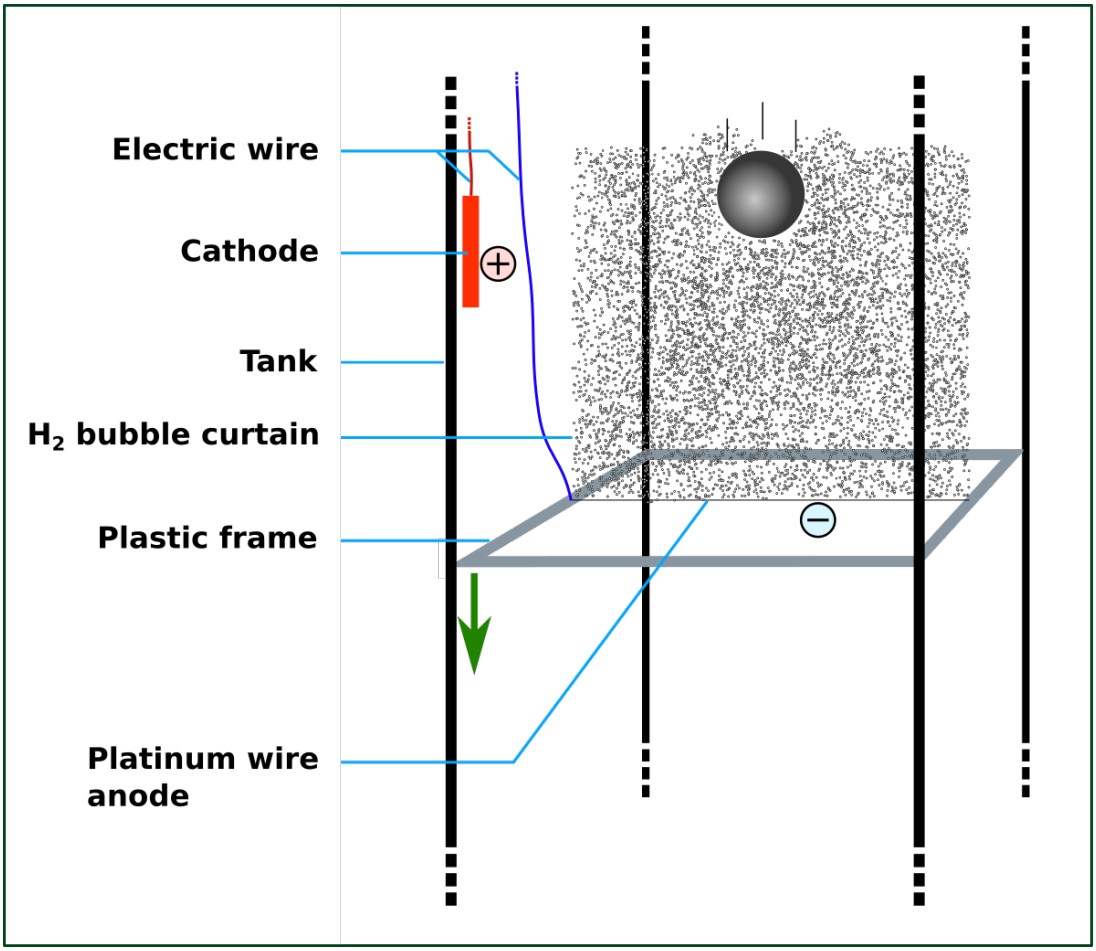

FIGURE II.8 – Schematic of the sliding frame holding the platinum wire that we used to depose a curtain of thin H_2 bubbles by electrolysis. The plane of bubbles was positioned in the middle of the tank in order to contain the trajectory of the diapir of galinstan prior to its breakup.

regions of all intensities and nearly all scales (cf. fig. **??**). Consequently, we found no simple automatic procedure to reliably detect the limits between the liquid metal and the ambient fluid. Contours of the liquid metal were then computed by hand using a custom routine that recorded 30 points to approximate the interface on a dozen of frames regularly spaced in every experimental video. Since DPIV-Soft 2010 was not able to implement a mask for the zone inside the interface given the sparse data the manual procedure was able to retrieve, the full computation was made and the spurious velocity were discarded a posteriori.

At this point, our goal in setting up this technique can be more precisely stated. The measures gathered with this method allow us to compute the center of mass and the radius as a function of time for the pixels inside the manually computed contour (since there is no hole in it, this technique is equivalent to the one previously laid out). But more importantly, it also enables the integration of the mass flux and the impulse flux passing through the contour (cf. fig. **??**) which, under the approximation of axisymmetry, closes the balance of forces. This has a direct application in testing the validity of the turbulent thermal model for the first part of the fall of the galinstan.

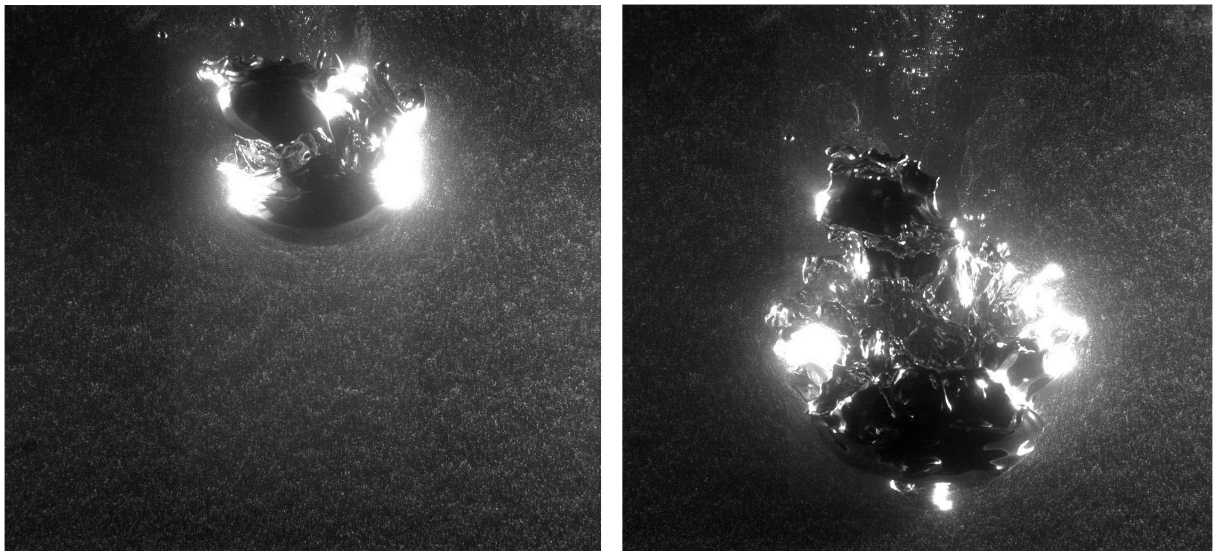

FIGURE II.9 – Snapshots extracted from the video of the fall of a $0.031m$ radius diapir of galinstan. The H_2 bubbles allow to trace the velocity field in the proximity of the diapir but the curtain contains zones of higher and lower intensity. The liquid metal is also presenting a lot of light reflection giving rise to zones of all levels of luminosity at all length scales.

The use for our flow of a curtain of bubbles as a basis for PIV constitutes a stretch of the method previously used on strictly axisymmetric structures (**?**). However, strict axisymmetry has limited interest to us since it is almost synonymous to stable drops. It is worth noting that we have limited our field of study with this technique to the first part of the fall so that the flow would not be far from axisymmetric. We did not expect this to be a decent approximation after the full breakup of the liquid metal, and significant departure from axisymmetry by particularly energetic structures even before breakup was expected. A technical objection could be made in the fact that with the same curtain of droplets two camera could have made possible the full computation of the 3D velocity vectors with their accurate positions. This would be a significant improvement only if the velocities perpendicular to the plane passing by the supposed axis of symmetry were not negligible, i.e. the flow was truly 3D. In such cases the integration of the flux on a contour instead of on a surface would have been meaningless anyway rendering the improvement useless. Nevertheless, videos made with a bubble curtain show a nearly axisymmetric flow and computations based on the analysis of these videos have been done with this assumption.

Geometry of the drops

i) Radii

Videos of the experiment made with the large scale framing and the zoom on the bottom of the tank were treated by a custom Matlab routine. This routine, actually developed on the first setup, is a limited-tracking and drop counting algorithm that processes raw experimental videos into a list of all the radii of the drops counted in the videos as a function of time accompanied by two films : one exposing the raw result of the criterion

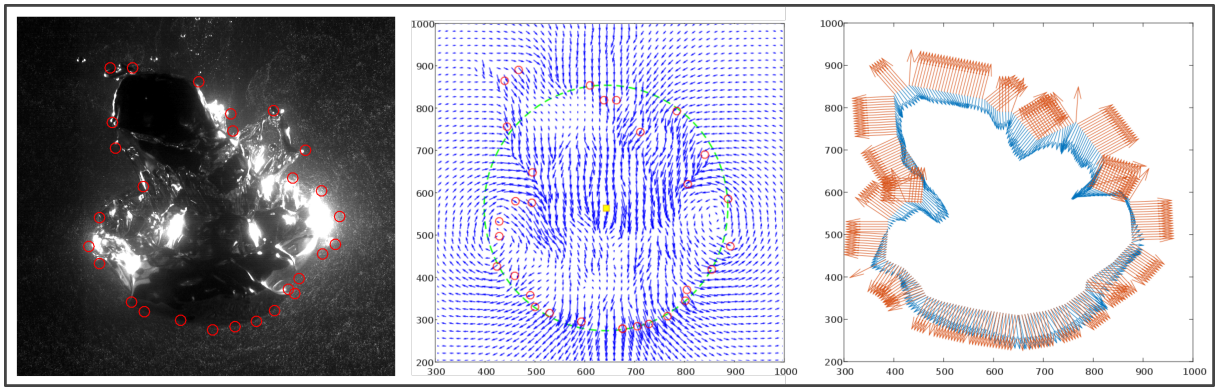

FIGURE II.10 – Images showing the processing for the videos made with side lighting and a curtain of bubbles. Left : snapshot of a video where manually retrieved points (red circles) defining the contour of the diapir were superimposed. Middle : velocity field computed using PIV technique on the videos made with the bubble curtain. Superimposed are the manually retrieved contour (red circles), the center of mass of the zone inside the manually retrieved contour (yellow dot) and the circle with a radius equivalent to the spherical radius of this zone (green line). Right : plot of the local normal to the contour (brown arrows) and ambient fluid velocities (blues arrows) plotted on the manually defined contour. Both quantities are integrated in order to produce the mass and impulse flux as a function of time.

used to identify individual drops, the other one exposing the full method with partial tracking of the particles.

This algorithm has been constructed in order to produce distributions of radii of the droplets as a function of time while minimizing the possible statistical bias due to the loss of information that drop superpositions represent. The principle is to track particles to previous or following frames where they are not superimposed. On the binarized images extracted from the videos, the connected components are listed. One by one, a criterion based on the shape of the polygon that each connected component is defining allows a first sorting between drops and non-drops. Among the non-drops connected components, many of them are superpositions of 2 or 3 drops. For these structures, the program constructs 3 dimension space-time diagram, where the speed of the structure has been substracted, by superposing the sub images containing it in the third dimension. Connected components are again looked for in order to identify the initial structure and the "branches" it is connected to through time. Then 2D (constant-time) slices of this connected component are inspected to find the one with the most "branches". The sub image found with this procedure is once again put to the test of the criterion on the connected components in order to count the branches as drops, or non-drops if an ambiguity remains (cf fig.**??**). For the videos detailing the full process, every structure that is tested with the criterion is colored. They are colored in green if they are identified as drops by the first test, they are colored in blue if the tracking is used on them and they are colored in red if neither of the tests identify them as a drop (cf fig. **??**). These videos can then be used to refine the thresholds composing the criterion.

The aforementioned criterion is composed of three Boolean that must be simultaneously verified. These Booleans are themselves based on a threshold with respect to a particular

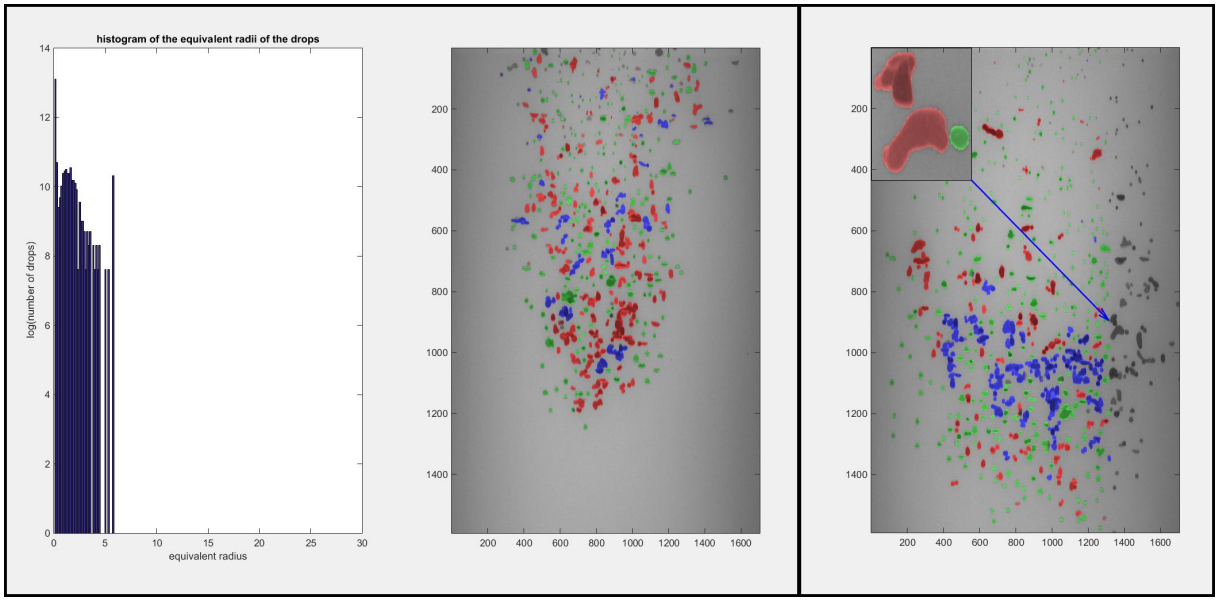

FIGURE II.11 – Snapshots of the videos summarizing the sorting performed by the drop count algorithm. Left panel : Histogram of the radius of droplets measured on the adjacent image and snapshot of the experimental video where drops are colored in green if they are count directly, blue if the tracking method has been used to retrieve better views of the same drop and successfully counted at least one drop, and red if not. Right panel : example of a colored snapshot where a sub image has been colored. It presents the best image found by the tracking of an object that is not considered as a drop in order to make every count of drop resulting from the tracking explicit. It is colored with the same convention as the main image.

variable. The first one gauges the horizontal symmetry of the structure by making the normalized product of the sub-image with its symmetric. The second one is the aspect ratio of the bounding box of the structure (drops are always flattened by the cross flow hence they always have an aspect ratio above 1). The third one is called the solidity and is the ratio of the area of a connected component over the area of the convex polygon that bounds it.

Since the drops are more and more deformed as they get bigger, with shapes varying as a function of viscosity ratio R_μ, the question of which radius was the most relevant to us and to compare with the literature had not an obvious answer to us. Thus, we have decided to compute three different measures of the drops that have their own interest and uncertainties :

— The horizontal dimension of the connected component that we assimilate to the radius perpendicular to the flow. We will call it the cross flow radius.

— The radius of the disk having the same surface area as the connected component. This is the classical way to compute drop radii. We will call it the spherical radius.

— The radius deduced from the calculus of the volume of the drop using the complete shape of the connected component, assuming axisymmetry. We will call it the integrated radius.

For the videos made with the large scale framing, all the drops are visible in one frame so this process alone is enough to produce a full distribution of the droplet sizes, although it is limited by a resolution that is unfortunately quite close to the typical size of the droplets (the mean resolution is around $1.5 \cdot 10^{-3}\ m.px^{-1}$). For the videos made with the zoom at the bottom of the video, the resolution is much better (the mean resolution is around $0.32 \cdot 10^{-3}\ m.px^{-1}$), but the totality of the drops is never visible in one frame. Furthermore, the drops are passing in the field of view as they fall. Since this depth represents a late stage of the cloud of droplets evolution, the drops do not have a collective speed and instead fall with a speed close to their terminal velocity. This means that one must aggregate the data from several images to produce a distribution. Since the drops are falling at different speeds, a bias is easily introduced because drops will be counted too many times or too few depending on their speed and the analysis frequency. This effect was corrected by measuring the falling speed of the drops as a function of their radius using a PTV routine. These speeds are then used to renormalize the counting of the drops that is made with a frequency of analysis much higher that the frequency of passing of the drop in the field of view.

The data produced by this method are saved in a different file for each video, the stacking is done only when the data are plotted in order to solve problems of time offsets between videos for the videos made with the large scale framing and to renormalize the counts in the histogram by taking into account the falling speed of the drops for the videos made with the zoom on the bottom.

ii) Frequencies and amplitudes of droplet vibrations

For low viscosity contrast (R_μ close to unity) droplets presented oscillations. Thereupon, we have adapted a particle tracking velocimetry program on Matlab written by Nicholas T. Ouellette and Douglas H. Kelley (**?**) in order to follow drops as they fall and record their shape.

For this analysis, we treat the videos filmed with a zoom on the bottom of the tank because of the need for spatial resolution, in order to have well defined shapes. The shape of the drops was computed as a contour of arbitrary intensity level on the raw images (non-binarized) increasing even more the resolution. These contours are transformed into a polar coordinate system centered on the drop and then juxtaposed as a space-time diagram (cf. fig. **??**). Finally, a 2D Fourier transform of these space-time diagrams is applied in order to identify the leading modes with their amplitudes and their periods. In addition, the PTV program records the instantaneous speed of the drop.

iii) Static forms of droplets

A similar method has been systematically applied to stable drops with the aim of recording their static shape. The main difference between the two modifications of the PTV program of Ouellette and Kelley being that for this one the contour is not analyzed all along the track but averaged over a small window that is the closest to the center of the frame, in order to minimize the distortion and parallax errors. The contour and its

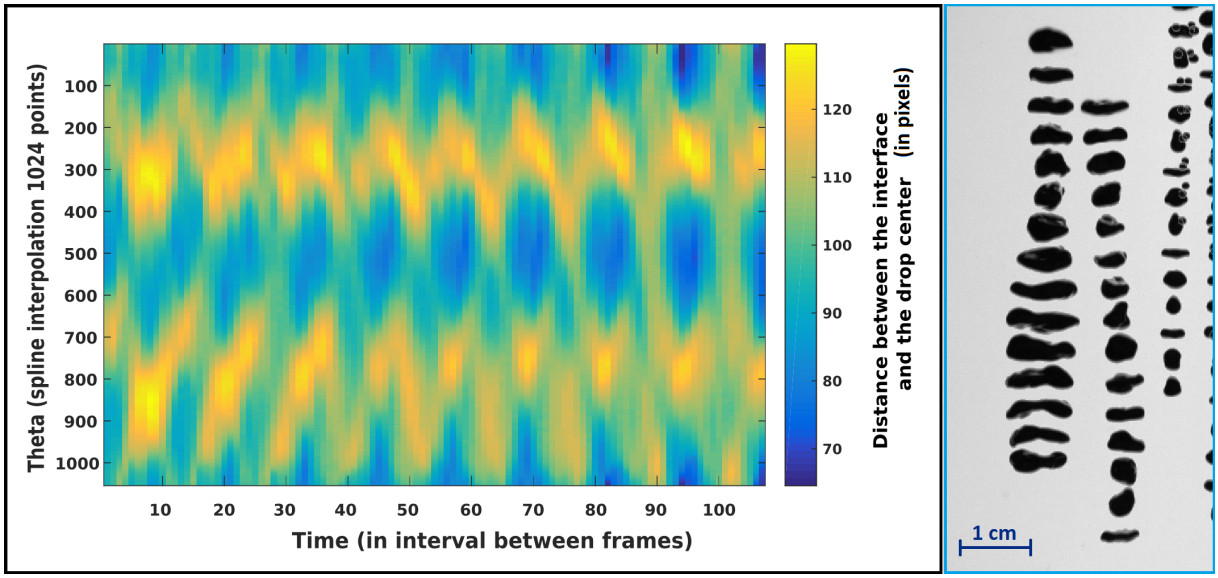

FIGURE II.12 – Left panel : color plot of the space time diagram of a drop contour. Right panel : superposition of snapshots extracted from the video of an experiment zoomed on the bottom of the tank. In this experiment, a 0.019 m radius galinstan diapir was released in pure water.

Fourier decomposition are then saved for each drop along with their speed, which allows averaging among drops before plotting.

Shadowgraphy

When trying to minimize the distortion and parallax errors, we have tried to implement an imaging technique close to the Schlieren method as it makes parallel rays that would solve both of these problems. Formally, the idea was to construct a telecentric objective and an adapted lighting. The set-up of this imaging technique consisted in two 40 cm wide Fresnel lenses on each side of the tank. At the focal point of the first lens a bright LED spot with a diaphragm was placed. Across the tank, at the focal point of the second lens, the diaphragm of the video camera was placed. Unfortunately, the quality of the optical system tank-lenses was not good enough to have simultaneously a wide field a view and a good focus. In consequence, the sampling of droplets that could be analyzed was unsatisfying.

However, this was the occasion to implement a Schlieren method (cf. fig. **??**). The top of the tank was fitted with a heating system for the balloon and the liquid metal was heated prior to the experiments filmed with this apparatus, as for the first experiment. The altitude of the lenses was a compromise between the residual heat of the drops and the spread of the cloud of droplets in order to avoid superposition as much as we could as well as having a difference of refractive index resulting from the difference in temperature that would produce noticeable patterns.

Measurements of the typical length scale of the temperature gradient in the trail of these drops were attempted, but these are not very reliable as they were done be estimating the length of the intensity perturbation with the eye.

Moreover, the difference between a shadowgraphy imaging and a Schlieren imaging

FIGURE II.13 – Snapshot of a video made with a Schlieren optical setup of the fall of a 0.031 m radius diapir of galinstan in a mixture of water and UCON oil. The liquid metal has been heated before the experiment. The thermal boundary layers around the drops appear darker or brighter because they slightly deflect the initially parallel light rays. The imperfections of our optical system do not allow the region to appear in consistent shades of grey for the same conditions but they appear distinct from the local background.

is the ability to substract rays that are deviated by their passage in zones of different refractive index : in a proper system of shadowgraphy they are not substracted therefore the difference of intensity with respect to the background intensity is related to the integrated Laplacian of the refractive index in the line of sight. On the contrary in Schlieren imaging, it is related to the integrated directional derivative of the refractive index whose direction is selected by the substracting device. Since we could not improve the quality of our optic system enough, the rays were not entirely parallel therefore the substracting device had not a entirely reliable substracting effect. The resulting setup was somewhat intermediate between shadowgraphy and Schlieren imaging. In conclusion, we are not able to say with precision how much of the local variations of intensity are related to the gradient or to the Laplacian of the refractive index.

D Exploration of the parameter space

As stated in the introduction, the real values of the parameters for planetary applications are unattainable by the experiments. The idea of our approach is classical in studying geophysical problems. Starting in the right dynamical and diffusive regime, a parametric study should allow us to understand how the forces interplay and what consequences this has on the diffusive exchanges. In doing so, one must sort out what is the physics that is only relevant for the analog flow in the laboratory, and what can be extrapolated to the original problem, the post impact flow in our case.

In our study, we have independently varied the initial mass of galinstan we put in the balloon and the mass fraction of UCON oil in the ambient fluid in order to vary the Re, We and R_μ which are, as previously stated, the main parameters of our problem. We have targeted 4 mass fractions in order to produce 4 viscosities in the ambient fluid. As the volumes of fluid used in the second setup were quite important, we did not correct these mass fractions to exactly match the mass fractions used in the first setup. Nevertheless for both setups the four viscosities were on the order of 10^0, 10^{-1}, 10^{-2} and $10^{-3} Pa.s$ which corresponds to R_μ of 500, 50, 5 and 0.5 respectively.

As previously mentioned, the initial masses of galinstan were precisely weighted but also grouped around 5 classes ; $75g$, $175g$, $395g$, $805g$ and $1615g$. The 5 classes were not used simultaneously : the 4 smallest classes were aimed at in the first setup and the 4 largest in the second setup. This was done mostly for technical reasons. In the first setup the more mass was put in the balloon the more the balloon deformed. In consequence, the thermocouple in the balloon was less and less likely to record a temperature relevant for the whole mass of galinstan because the thermocouple tended to be in the very top of the mass of liquid metal. In addition, due to the small dimension of the first setup, the class 1615 g would have been prone to wall effects very soon in the fall which may have rendered the interpretations for this class confusing compared to the other ones. For the second setup, our focus was in the statistics of the flow, particularly in the statistics of droplet sizes. Thence, for each class of mass and for each viscosity, we have done as many experimental runs as necessary to count at least 4000 events (i.e. measure 4000 radii). This meant doubling the number of runs each time a smaller class is added to the scope of the study, as these classes are roughly produced by dividing the mass of the next upper one by 2. Adding the smallest class of initial mass to the measures made on the second setup would have been too costly in time.

When converted in terms of initial spherical radius, the masses defining the classes are initial spheroids of $1.4 \cdot 10^{-2}$ m, $1.87 \cdot 10^{-2}$ m, $2.5 \cdot 10^{-2}$ m, $3.1 \cdot 10^{-2}$ m and $3.9 \cdot 10^{-2}$ m. Then, taking the Newtonian scaling for terminal speed **??** as a characteristic velocity, one can define a priori values for the Reynolds and Weber numbers with the initial radii and viscosities previously mentioned :

$$Re = \frac{(\rho_a.\Delta\rho.g)^{\frac{1}{2}}.R^{\frac{3}{2}}}{\mu_a} \quad ; \quad We = Bo = \frac{\Delta\rho.g.R^2}{\sigma} \tag{II.3}$$

This gives a complete set of a priory parameters for our problem. The (Re,We) and (Re,R_μ) planes of the space of parameters are show in figure **??** with the corresponding zones screened in the case of impactors at the time of terrestrial planet accretion and the zones screened by our first and second experimental setups. In both the geophysical case

and our experiment, the width of these regions is due to the range of initial size of the liquid metal diapir. To the best of our knowledge, our analog system is in the right region of the parameter space (i.e. it is both in the relevant dynamical regime and fulfills the condition $Pe \gg 1$).

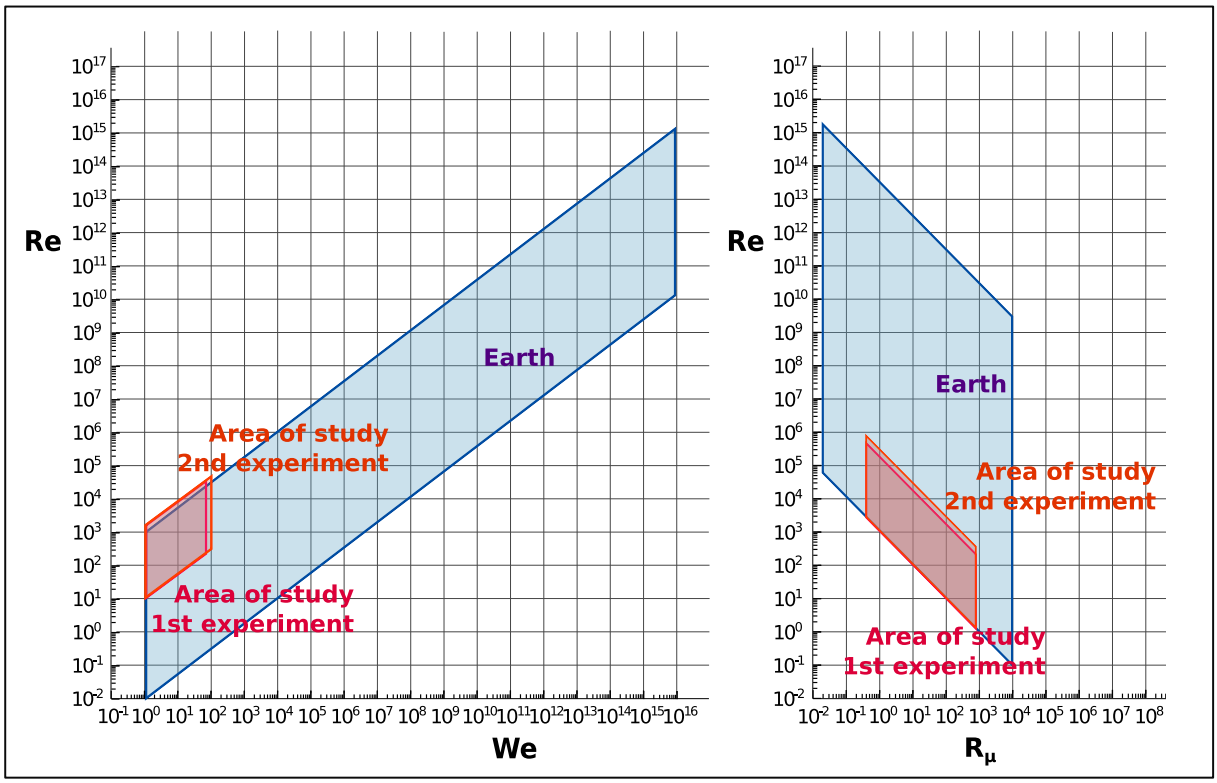

FIGURE II.14 – Planes (Re,We) and (Re,R_μ) of the space of parameters relevant for the present study. The slope in the (Re,We) plane is due to the assumption of a Newtonian scaling for the velocity. The distance between parameters for planetary impacts and the one we can reach via experiments makes necessary the search for an asymptotic regime in Re and We.

E Simulated data

The limiting possibility of tracking superposition of droplets back or forward to a position where the drops could be measured has led us to use synthetic data in order to probe if the superposition combined with the counting algorithm was giving a bias to the distribution.

Obviously, a full investigation of this problem would imply either having a 3D scanning method to have the full experimental distribution or reproducing the full 3D flow by integrating the Navier-Stokes equations in both fluids. One could then measure the full distribution and compare them to the distributions that the projected field of the phase variable would give. A 3D scanning method was not available to us and 3D simulations are way out of the scope of this study. Thus, we have made a supposition to simplify this problem as the experiment is supposed to answer the question of the true form of the distribution of sizes.

The most discriminating criterion to exclude shapes that are not a unique drop is the criterion of the solidity of the shape. Since it is the ratio of the total area over the area of the convex hull of the shape, it is in fact a criterion on the area of the concave parts of the shape. In the simple case of the superposition of two spherical drops, this area is a function of their distance but also of their respective radii. For non spherical droplets, the concave parts have an area that is a non trivial function of their position. Therefore, we made the hypothesis that the bias due to the illegitimate counts of superposing drops is a function of the actual drops shape and of their distribution of sizes. In doing so we also consider the drops to be approximately randomly distributed in a cloud of droplet of a known size. Thus, we have produced synthetic experimental video with distribution of sizes that could be arbitrarily defined. Our procedure to produce synthetic data is as follow :

The raw data to simulate are the binary videos. A well-defined binary image of a realistic drop was chosen as reference for the shapes of all the drops. Using any specified function as the distribution in its dimensional form (as long as its verifies the classical hypothesis for probability functions of discrete variables), the program randomly selects a drop size that is used to scale down the model image with the same ratio meter per pixels as in the experimental images. The randomly selected drop sizes are recorded and integrated in order to have the total volume of the drop catalog created. This process stops when the volume represented by the randomly selected drop sizes is equal to the volume specified, which is set to the volume corresponding to one class of masses. Then the initial position of the drop is randomly selected. The distribution of the initial positions is a Gaussian with a standard deviation equal to the radius corresponding to the class of mass simulated. The norm of the speed vector is also randomly selected via a Gaussian function centered on the Newtonian scaling for the terminal speed of the diapir of the class of mass selected. Finally, the orientation of the velocity vector of the drops is randomly selected so that the mean orientation is vertical and points towards the bottom. The standard deviation for the angle of the velocity vector with respect to the vertical is a typical value for the arctangent of the coefficient α of the turbulent thermal (the value of 0.1925 rad was chosen), as $\alpha = \frac{dr}{dz}$ if the cloud of drop falls as a thermal. A last subtlety is introduced : the trajectories of the drops if computed as described before are straight which renders our process of tracking useless and is not very realistic. Therefore, a horizontal oscillatory motion is superimposed to the straight trajectory with a period of a few advection times for the drop and an amplitude equal to a fraction of the radius.

The making of the video from that point is just superposing the images of the drops according to their size and their position corresponding to the number of the frame in the video. The same algorithm as for experimental videos is then used to treat the synthetic videos with experimental results in chapter **??** section B 3.

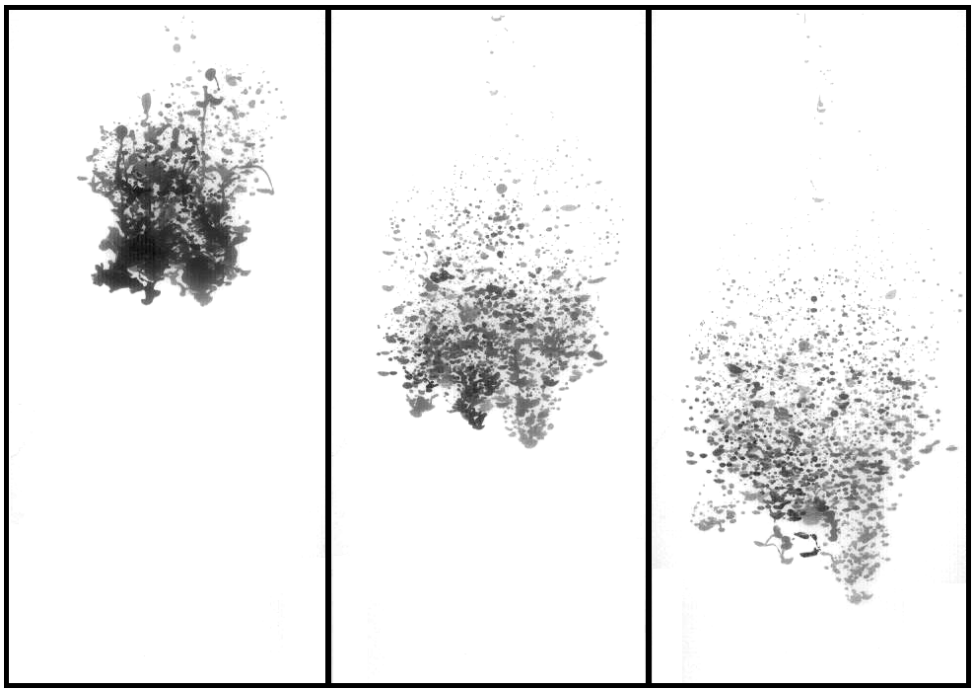

FIGURE II.15 – Snapshot of the video of the fall of a $0.039m$ diapir of liquid metal falling in a mixture of water and UCON oil. In this experiment $Re = 358$, $We = 76$ and $R_\mu = 80$.

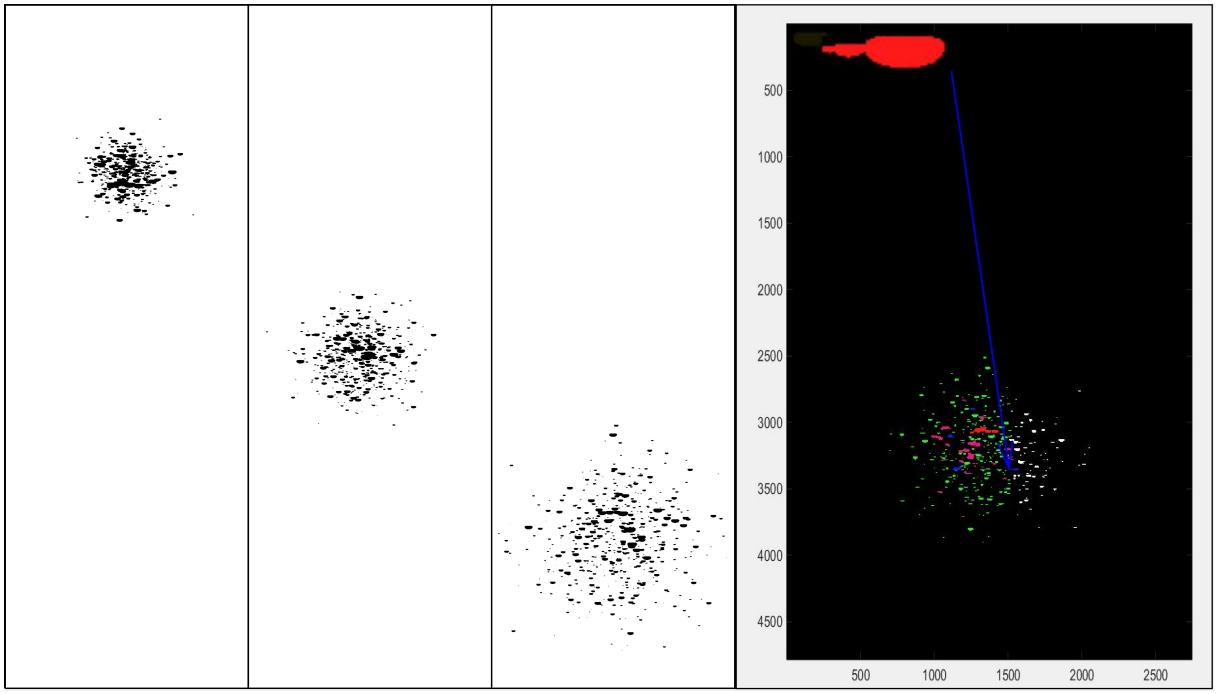

FIGURE II.16 – Left panel : snapshot of a video created by computer reproducing the metric calibration, the mean diameter and the total mass of a typical experimental run with the constraint of a specified distribution of sizes for drops. The mass reproduced here corresponds to an initial radius of 0.039 m. Right panel : snapshot of the video summarizing the drop counting process for the simulated experimental video with a zoom on one rejected pattern on the top left.

Chapitre III

Large scale dynamics

After the retraction of the balloon, the galinstan initially released as a spheroid starts to fall and deforms. For sufficiently large diapirs (the ones that are above the critical radius), this deformation is not stopped by surface tension and unstable structures are formed, from which breakup occurs within a distance that is of the order of a few radii of the initial mass of galinstan. From that point, the cloud of droplets continues its descent until it reaches the bottom.

A Fragmentation regimes

Our smallest class of initial mass of liquid metal does not produce a Weber number that is far from criticality ($We \simeq 10$). Thus, we have observed different fragmentation regimes as we increased the Weber number of the flow in a way that is quite similar to the regimes of fragmentation for droplets of water (**?**). Their domains of existence are an interval in Weber number. In details, the way that breakup unfolds is more similar to the regimes that are reported by M. Landeau and colleagues in 2014 (**?**) but a significant transition can be observed in our experiments when changing the viscosity ratio.

We have observed several fragmentation regimes depending on the initial radius of the diapir and on the viscosity of the ambient fluid. For the smallest diapirs except in the highest viscosity contrast, breakup generally occurs with what appears to be a "vibrational" breakup mode : the droplets flatten because dynamic pressure is not compensated by surface tension to a point that surface tension develops non axisymmetric perturbations of the form of the droplet that tends to select a preferential direction of elongation. From that point, flattening in the horizontal direction becomes elongation, up until the droplet becomes Rayleigh-Plateau unstable (**?**). This regime is named vibrational breakup because for droplets below the critical radius, the response to the dynamic pressure is oscillatory flattening, while over the critical radius, the formalism being strictly the same, the response grows exponentially in time (for complete development of this approach see **?** and **?**). This regime can also be found in numerical simulations, although not always called "vibrational" (**?**).

For the smallest diapirs in the highest viscosity contrast, the diapirs are stable and takes the form of an ellipsoid cap (cf. fig. **??**). This means that the critical radius is influenced by the viscosity of the ambient fluid. This may be due to the fact that the ratio

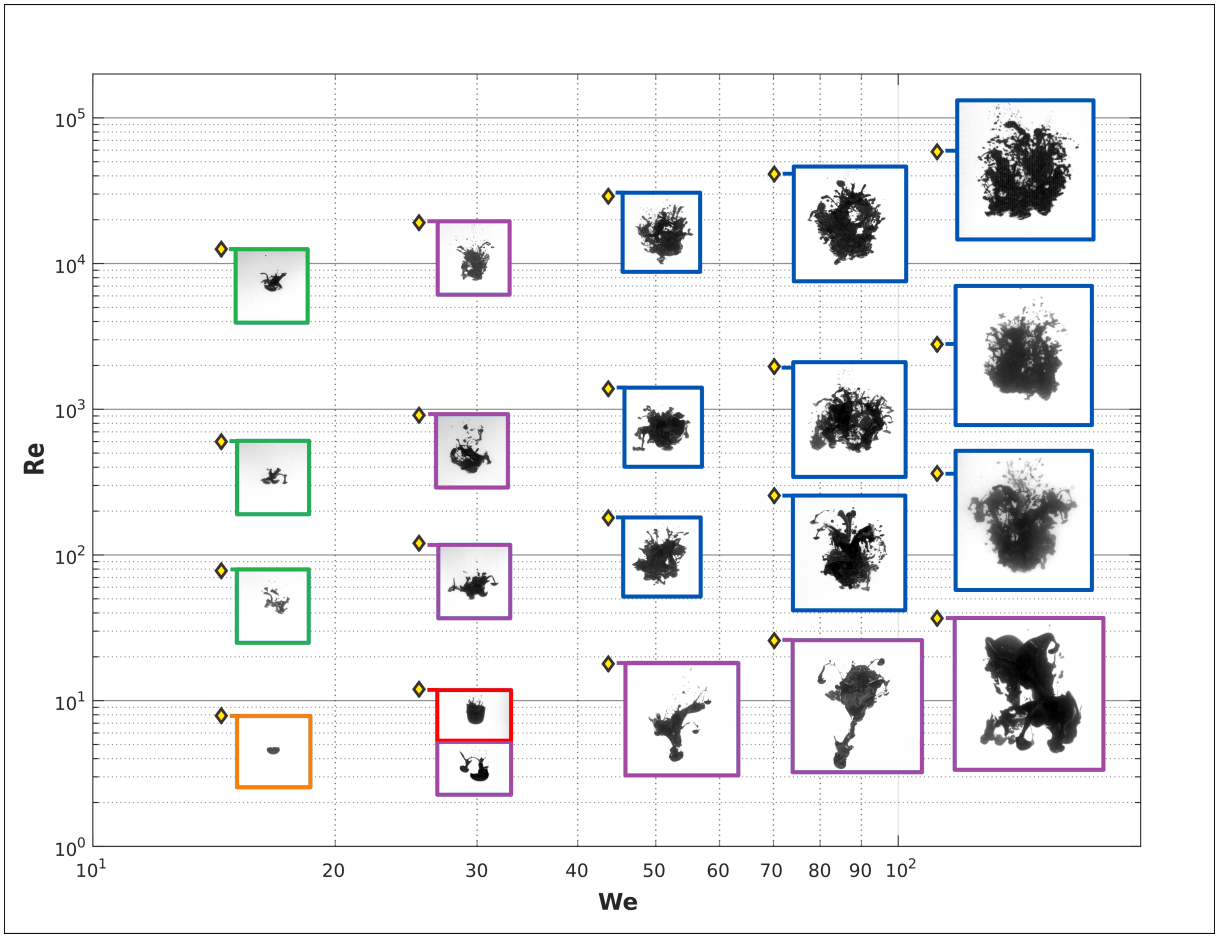

FIGURE III.1 – Deformation and breakup regimes in the Re and We plan of the space of parameters. The snapshots are extracted from the respective videos of the experiments near the moment of breakup. Framed in blue are the diapirs that undergo turbulent breakups, in violet are the diapirs that undergo Rayleigh-Taylor breakup, in green are diapirs that undergo the vibrational breakup, in red is the skirted cap and in orange the stable ellipsoidal cap.

of viscosity increases the recirculations inside the drop. This could prevent the drop to flatten too much as it is the case for vibrational breakup and could give less time for the RT instabilities to grow (**?**). We did not vary Re independently from R_μ while keeping the main control parameter concerning the stability of droplet constant (the Weber number We). Therefore we cannot assert with absolute certainty which one of these parameters is postponing the destabilization of the drops but since the main effect of Reynolds number in this area of the space of parameters has more to do with stretching structures on the side, we suggest that the viscosity ratio is the parameter that controls this increase in maximum stable radius.

A small ambiguity resides in the description of the mode of breakup of the smallest diapir. The fact that it is purely vibrational can be disputed as a smooth transition with the Rayleigh-Taylor regime is very probable (**?**, **?**). Indeed this very regime seems to predominate for the same ratios of viscosity and for the second smallest diapirs. In this regime, perturbations of the interface appear at the leading front, provoked by what

resembles to Rayleigh-Taylor instability. Sometimes structures elongated by the shear stress on the side of the diapir would also see their tip destabilized by RT mechanism while the rest of these scales or ligaments would be drained back into the main mass of galinstan.

The regime characterized by the Rayleigh-Taylor instability is also the best to qualify how the 4 biggest classes of diapirs with the highest viscosity ratio break-up. However, for the smallest of these, that is to say the second smallest class of diapir overall, it is not clear if the breakup is provoked by a random perturbation or if the retraction of the balloon has to do with it. Indeed in approximately 30% of the experimental runs in these conditions, the diapir stayed mostly whole and developed an unsteady skirt as can be seen for very large air bubbles in water (**?**). In the other runs, it broke up according to the above-mentioned fashion. Since this particular radius implies apriori Weber numbers of 22, this behavior is not a surprise as is it close to criticality. Therefore, the small perturbation from the bursting of the balloon can indeed be the cause of the breakup of the liquid metal mass. As this uncertainty in the stability of the diapir could not be observed in any other case, we do not expect a larger influence of the retraction of the balloons for the other cases. The formation of a skirt at the rear of a drop happens when its speed makes the ratio of the Weber number over the Reynolds number higher than a threshold of order one (**?**, **?**). This ratio is widely known in the literature as the capillary number Ca which is the ratio of viscous forces over surface tension :

$$Ca = \frac{\mu_a U}{\sigma} \tag{III.1}$$

For the typical conditions where skirts can be observed, the capillary number is around 2. It is higher for the larger diapir falling in the same ambient fluid (the one that have the highest viscosity) but the overall instability of the diapir itself seems to prevent the developement of a full skirt. As these conditions are very close to criticality, we do no expect the skirted drops to be of any relevance for the geophysical case.

The last regime that concerns the 3 biggest classes of diapir falling in the ambient fluids with the 3 smallest viscosity ratios is the turbulent breakup. As noted previously, the transition into this regime can also appear smooth but as the diapirs become larger, the liquid metal is more and more stretched on the side and re-entrained at the rear of the diapir. The strong shear on the side of the diapir also produces horizontal undulations of the interface between galinstan and mixture of water and UCON oil that are most likely the result of Kelvin-Helmholtz instability. These undulations evolve in very stretched structures though they rarely detach from the main diapir. This behavior seems to be found in 3D simulations for similar parameters (**?**). From what we can see in the videos, at the moment of breakup, the liquid metal has become a very stretched thin sheet, wrapped around itself in a toroidal geometry. Along its fall, the liquid metal stays in a region that has roughly a spheroidal shape (the aspect ratio is about one). Once the sheet has thinned enough, the breakup occurs quite rapidly compared to the large scale advection. The fragmentation proceeds in steps classical for films (**?**) ; First this thin sheet is pierced randomly, the liquid metal then retracts from these holes. Measures of the speed of hole opening allow to estimate the thickness of the sheet at the moment of breakup via the formula of the Taylor-Culik speed u_{tl-ck} (**?**, **?**) :

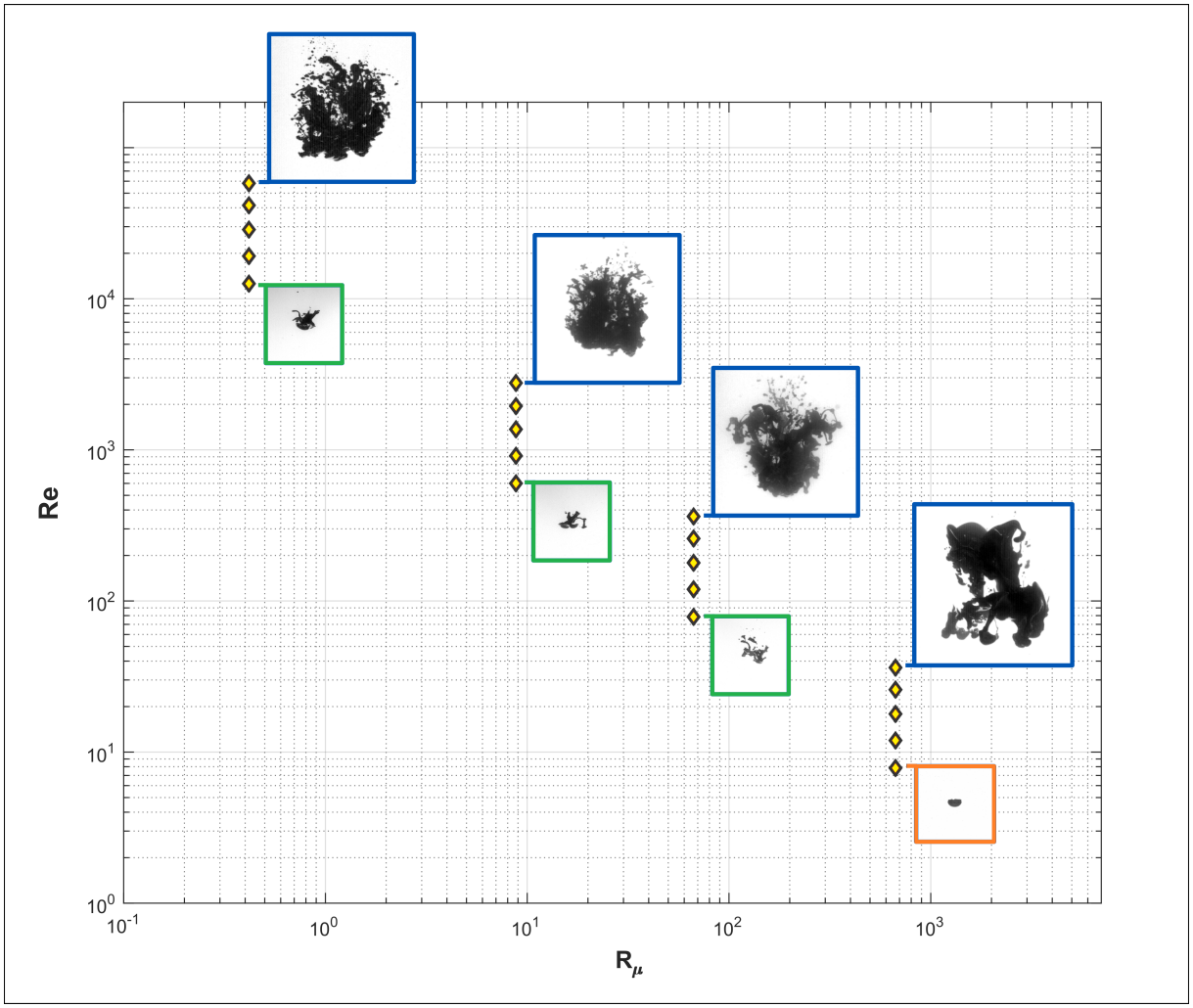

FIGURE III.2 – Deformation and breakup regimes in the Re and R_μ plane of the space of parameters. Red diamonds indicate the location the experiments. Framed in blue are the diapirs that undergo turbulent breakups, in green are the diapirs that undergo the vibrational breakup and in orange is the stable ellipsoidal cap.

$$u_{tl-ck} = \sqrt{2\frac{\sigma}{h\rho_m}} \tag{III.2}$$

h here is the film thickness. For every ratio and every size of diapir, the speed is approximately the same (in terms of orders of magnitude) and around 2 $m.s^{-1}$. This makes an average thickness of $5.5 \cdot 10^{-5}$ m. Ultimately, the result of these retractions is the formation of a lattice of ligaments where growing holes meet. These ligaments are for their huge majority already unstable to the Rayleigh-Plateau mechanism as soon as they form, as their aspect ratio is way above the threshold (**?**). They then rapidly breakup (again within a fraction of the advection time) in droplets (cf. fig. **??**).

These regimes seem coherent with the study of M. Landeau and colleagues in 2014 (**?**). In their study, they do not really qualify this high Reynolds high Weber regime differently from the one closer to criticality. This may be due to a lower density ratio that blurs the limits of these regimes. Additionally the proximity of the initial release position of the

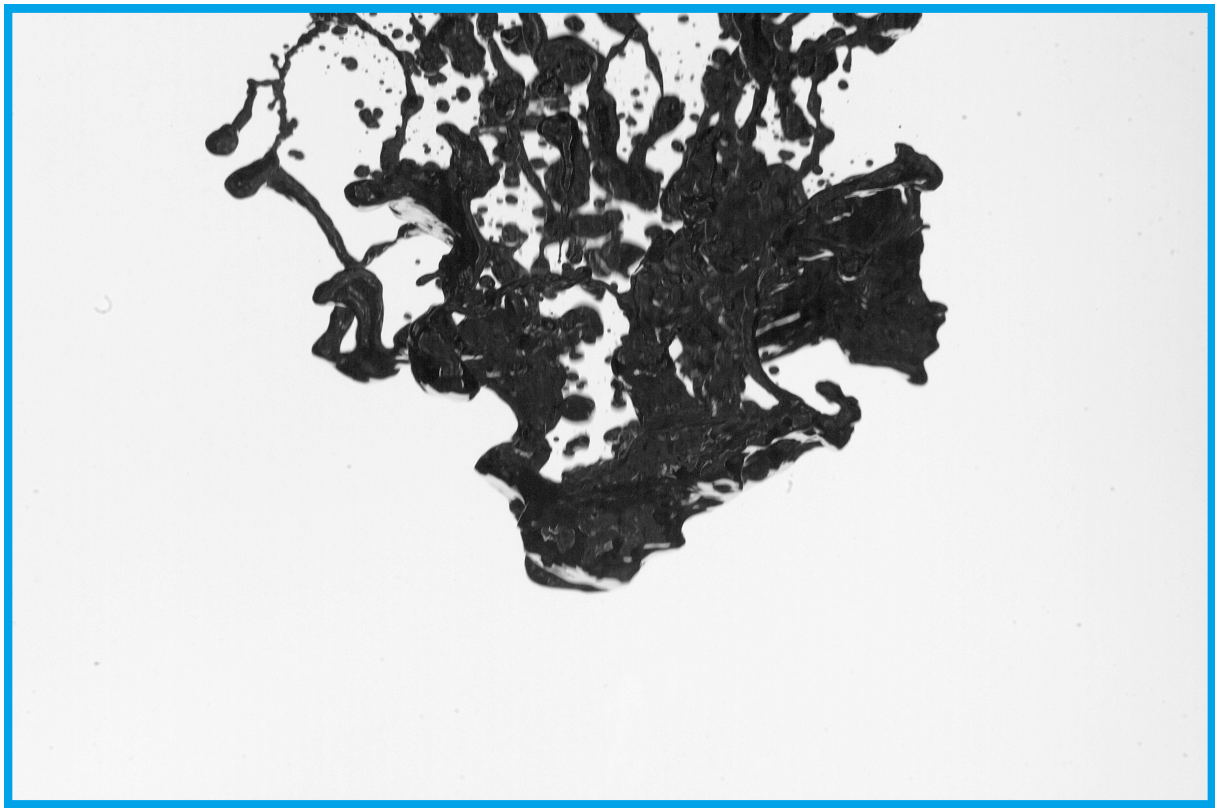

FIGURE III.3 – Snapshot of a video of a 0.024 m diapir of galinstan falling in water. This exemplifies the turbulent fragmentation at an advanced stage where the liquid metal sheet retracted to a network of unstable ligaments.

buoyant immiscible fluid to the free surface also produced a regime much more dominated by the presence of a vortex ring. In the present study the initial position of the diapir of galinstan with respect to the free surface is inbetween the configurations studied by Landeau and colleagues, although the comparison is only indirect since their release of the buoyant fluid is different from ours. Nevertheless, observations of our experimental videos suggest that there is probably a toroidal vortex in the diapir as it falls. The regime of fragmentation that we call turbulent is also consistent with their, although they attribute the main mechanism of fragmentation to Raleigh-Taylor instability. M. Hadj Achour also performed experiments with liquid metal in the same range of Weber number by making it fall in water, hence with comparable ratio of viscosity (**?**). Despite making their drops of liquid metal fall in the air and then impacting in water, they report similar regime of fragmentation that they call bag fragmentation (the bag is in their case oriented in the same way as in our experiment, downstream, which is opposite to free falling droplets of water in the air). From the description and the schematics of the high speed photograph of the work of Yang and Yang (**?**), it seems that they have observed the same regime as we describe, but we could not find the original high speed photography to confirm.

Finally, we also identify this regime with what the numerical simulations have called "backward-facing bag" breakup (**?**, **?**), "shear" or "rim-shear" breakup (**?**) as the main characteristics of sheet piercing and minor RT instabilities are also present there.

B Evolution of the radius as a function of the depth

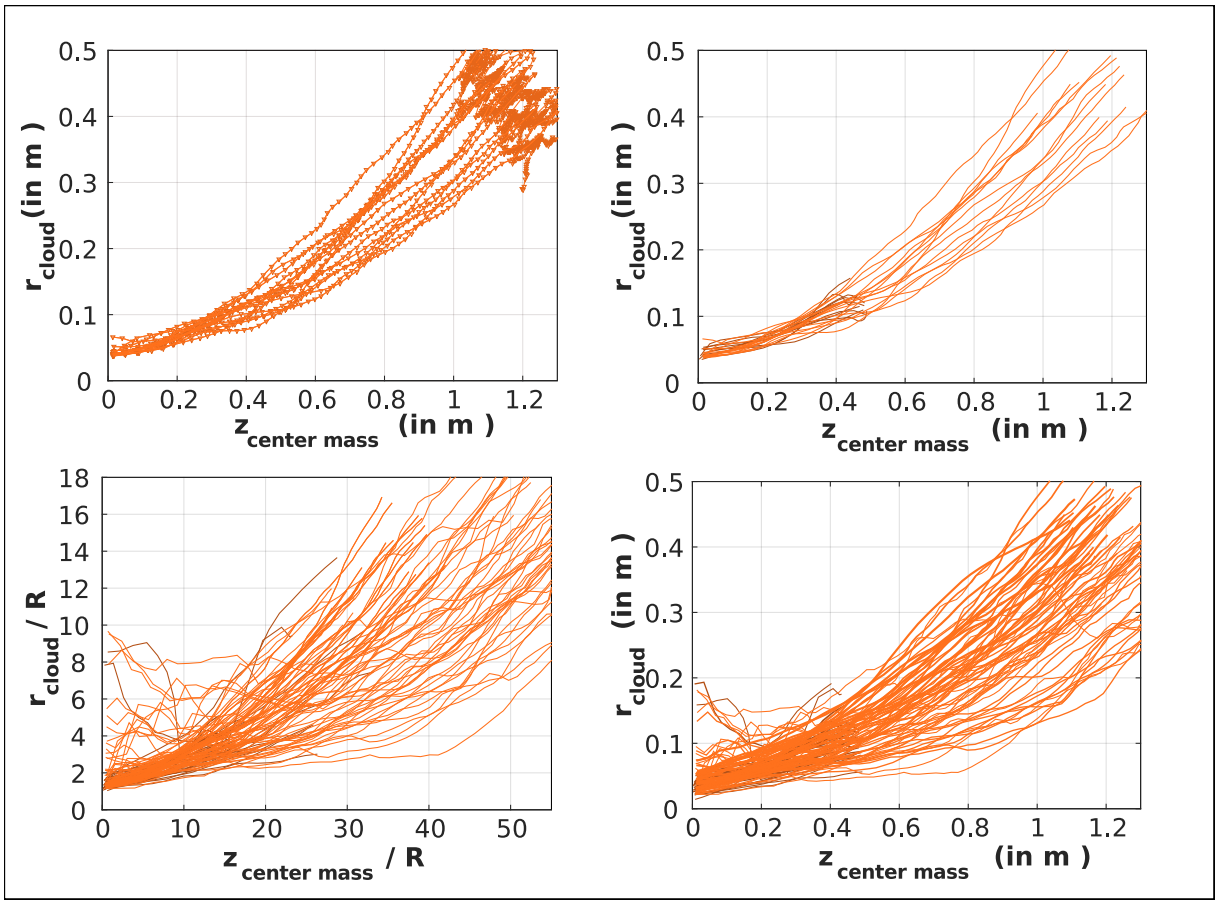

FIGURE III.4 – Graph of the radius of the region occupied by the liquid metal as a function of the depth of its center of mass for the experiments made at $R_\mu = 700$. The tracks from the first setup are in darker shade than the second setup. Top left panel : all experiments made with a 0.031 m radius diapir of galinstan in the second setups. Top right panel : all experiments made with a 0.031 m radius diapir of galinstan in the two setups. Bottom right panel : all experiments in the two setups. Bottom left panel : radius as a function of depth non dimensionalized by the initial radius of the diapir. The same plots are made for the other viscosity ratios in figure **??**, **??** and **??**.

The radii of the region of black pixels computed with the method described in the chapter **??** are shown in figure **??**, **??**, **??** and **??**. As a reference for the interpretation of the data, the top left panel of each of these figures show the sampling as well as the part of the track that is spurious because the liquid metal starts to leave the field of view. The top right panel shows for a selected set of parameters (the initial radius for all the track is 0.031 m) how the runs from the first and second experimental setups superimpose. This is especially important to see finite domain effects. The bottom right panel shows the tracks from all experiments in order to see the spread of the data. The bottom left panel shows the same data rescaled by the initial radius of the gallium diapir.

These curves exhibit two trends for the expansion of the region occupied by the liquid metal. The first is an expansion relatively linear and comparable in amplitude for the

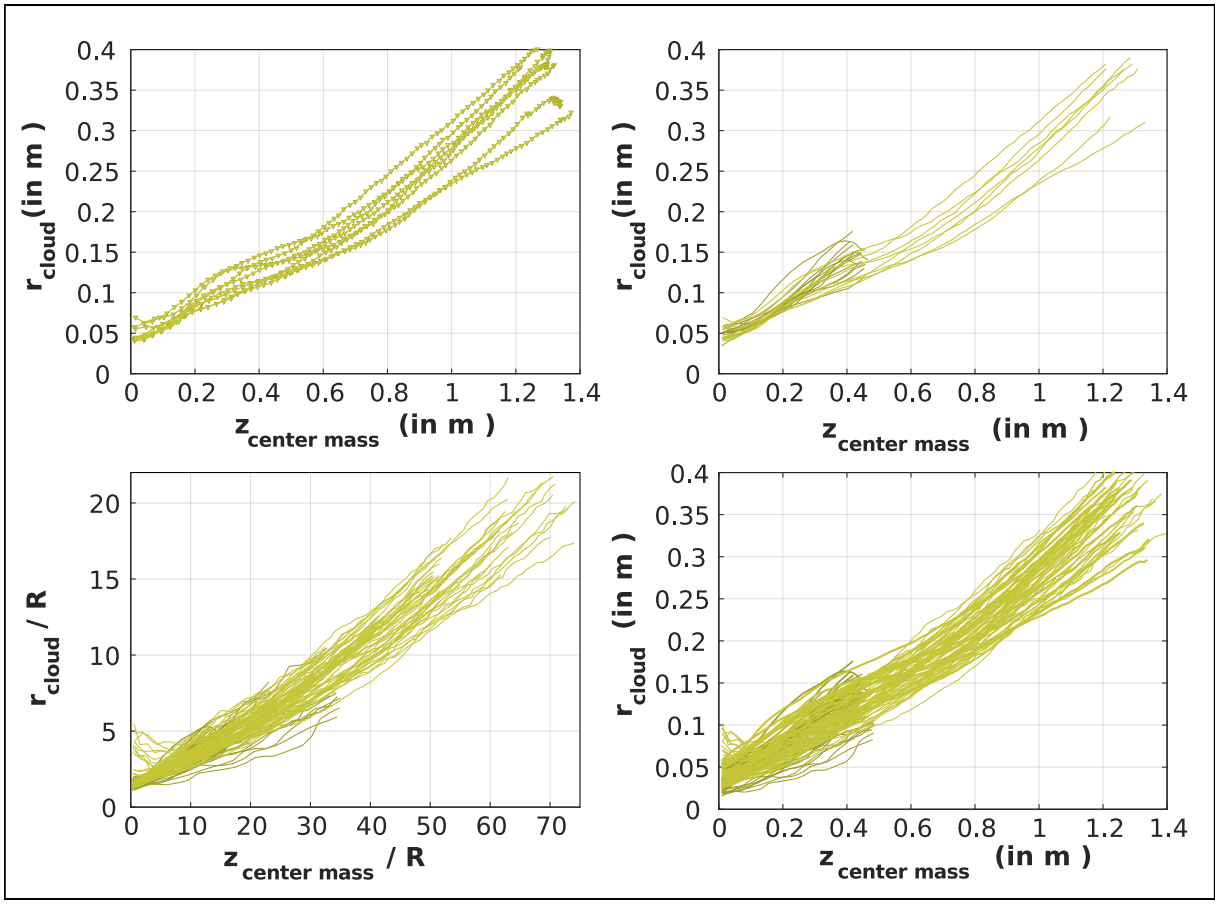

FIGURE III.5 – Graph of the radius of the region occupied by the liquid metal as a function of the depth of its center of mass for all experiments made at $R_\mu = 70$. The tracks from the first setup are in darker shade than the second setup.

three lowest viscosity ratio (cf. fig. **??** for $R_\mu = 70$, fig. **??** for $R_\mu = 8$, fig. **??** for $R_\mu = 0.4$) and approximately half its value for the highest viscosity ratio (cf. fig. **??** $R_\mu = 700$). Since this phase is spanning from $\tilde{z}_{centermass} = 0$ to $\tilde{z}_{centermass} \simeq 10 - 20$, this phase is dominated by the deformation that leads to fragmentation. Indeed qualitatively, breakup happens within a few radii, which we will confirm later with other measurements. In similar experiments (**?**), a value of 6 to 8 initial radii is reported for the breakup distance. The fact that expansion is smaller quantitatively for $R_\mu = 700$ also confirms our observation of a different fragmentation regime.

For the second part of the fall, the expansion at each viscosity ratio presents a different slope ; the higher the viscosity, the higher the slope. As this phase clearly extends up until the lowest part of the fall, we see this as the mark of the dynamic of the cloud of droplets as they fall independently from each other. If the droplets don't interact significantly during their fall, an apparent expansion, mostly vertical, appears from these different speeds. With the same sample of droplets of various sizes, different viscosities can produce different spreads because of the hierarchy of terminal velocity depending on the Reynolds number of the drops (cf fig **??**). Knowing the distribution of size of droplets should allow to predict the expansion in this regime.

These two trends are further confirmed by the analysis of the derivative of the radius

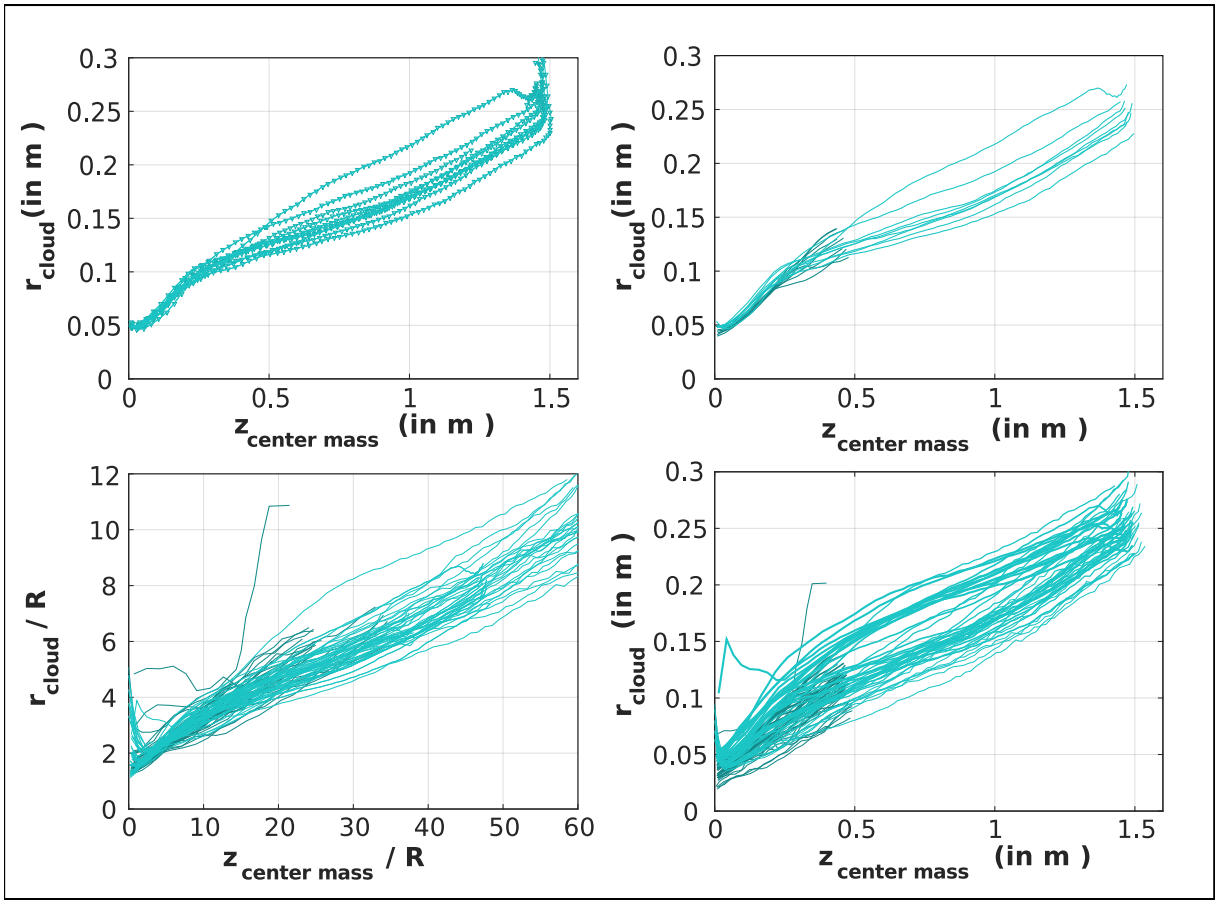

FIGURE III.6 – Graph of the radius of the region occupied by the liquid metal as a function of the depth of its center of mass for all experiments made at $R_\mu = 8$. The tracks from the first setup are in darker shade than the second setup.

of the region occupied by the liquid metal as a function of depth (cf fig. **??** up to $\frac{z}{R} \simeq 15$). For the three lowest viscosity ratios, this derivative is almost constant at a value of approximately 0.19. Noting that the liquid metal is unbroken at this stage, this constant derivative is compatible with the description of the fall of the liquid metal as a turbulent thermal as it was developed in several studies (**?**, **?**, **?**, **?**). As a matter of fact, the value of 0.19 is quite typical for turbulent thermal (**?**, **?**, **?**). In our case, the relatively constant derivative of the radius as a function of depth would imply that entrainment of fluid is indeed proportional to the surface of the region occupied by the galinstan at a given time, in agreement with the hypothesis developed in **?**. For drops in free fall, such trend for the deformation of the buoyant fluid is also common (**?**) **?**) although when just above stability (i.e subject to vibrational breakup) initial deformation would be exponential in time (**?**). This would result in an approximatly exponential trend in radius as a function of depth (see the following section about the constant falling speed).

An exponential trend could be argued for the most viscous case ($R_\mu = 0.4$) rather consistently for all radii, even though the biggest ones are far from stability. Thus, we interpret this differently. This trend is most likely the mark of successive divisions rather than vibrational deformation, as these divisions appear to result from Rayleigh-Taylor instabilities. At each division, the dividing droplet must collect a certain amount of

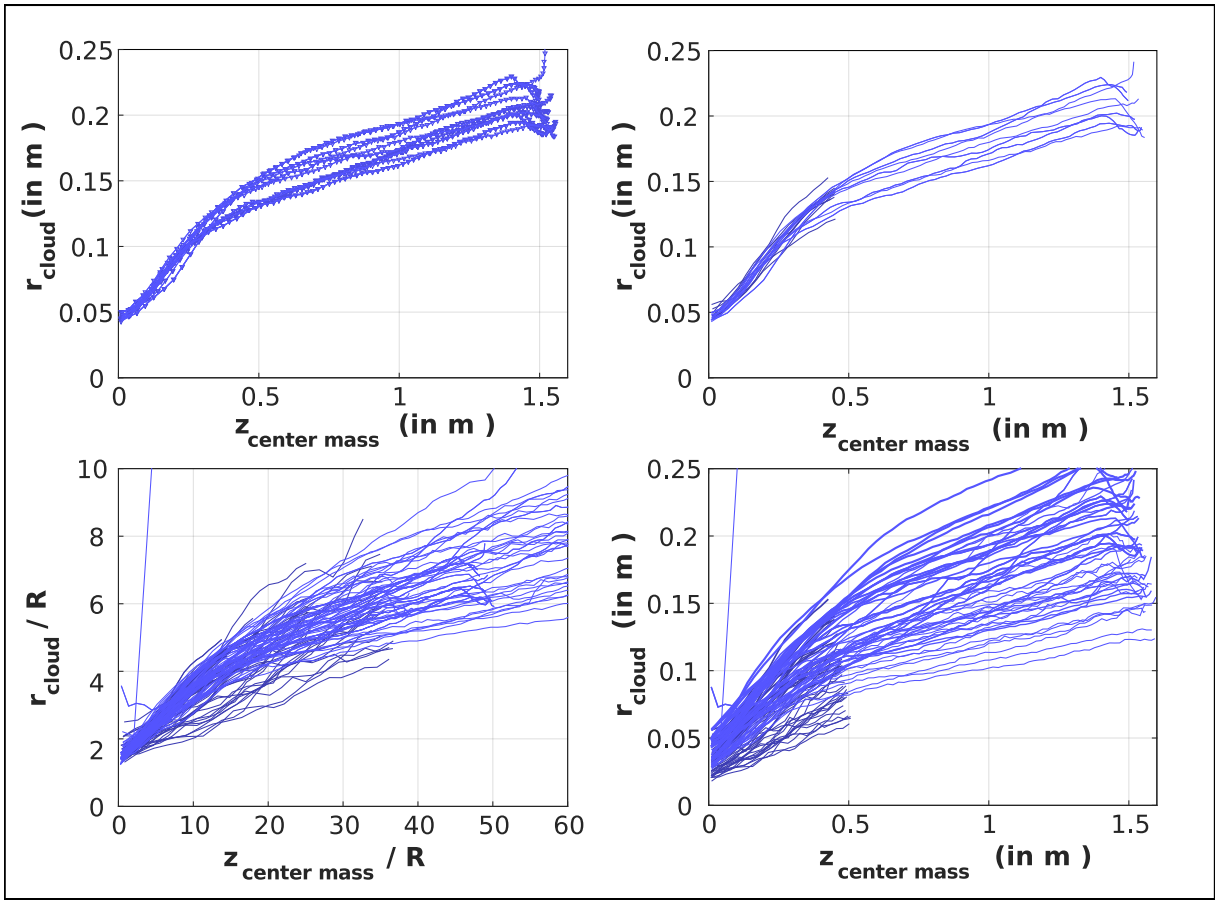

FIGURE III.7 – Graph of the radius of the region occupied by the liquid metal as a function of the depth of its center of mass for all experiments made at $R_\mu = 0.4$. The tracks from the first setup are in darker shade than the second setup.

mass from the stretched structures that it is in communication with in order to attain several unstable lengths l_σ in order to fragment. For each division to be completed, a time proportional to the time of growth of the Rayleigh-Taylor instability is required. Several steps of fragmentation according to this mechanism could then produce a radius (or more precisely a lateral expansion) evolving exponentially as a function of depth.

Alternatively, a similarity with the bag-breakup regime could be made for which the characteristic dimension of the bag is evolving proportionally to the square of the time (**?**). This is due to dynamic pressure at the front of the drop blowing the water droplets into a bag. In our case, the buoyant pressure indeed balances the dynamic pressure. Since it is purely pressure effect in both scenario, discerning between the two by how they scale with the parameters of our problem is impossible without having some fine measurements of the velocity field near the interface. The variability in the data does not allow a great confidence in the functional form either, so the observations lead us to favor the scenario of multi-stage Rayleigh-Taylor breakup to explain this trend. This scenario is compatible with a the breakup as envisioned by Kolmogorov and therefore suggests a log-normal distribution of the drop sizes.

To conclude, the first part of the fall of the liquid metal is characterized by a dilution of the liquid metal that scales with the initial radius of the diapir and therefore indicate a

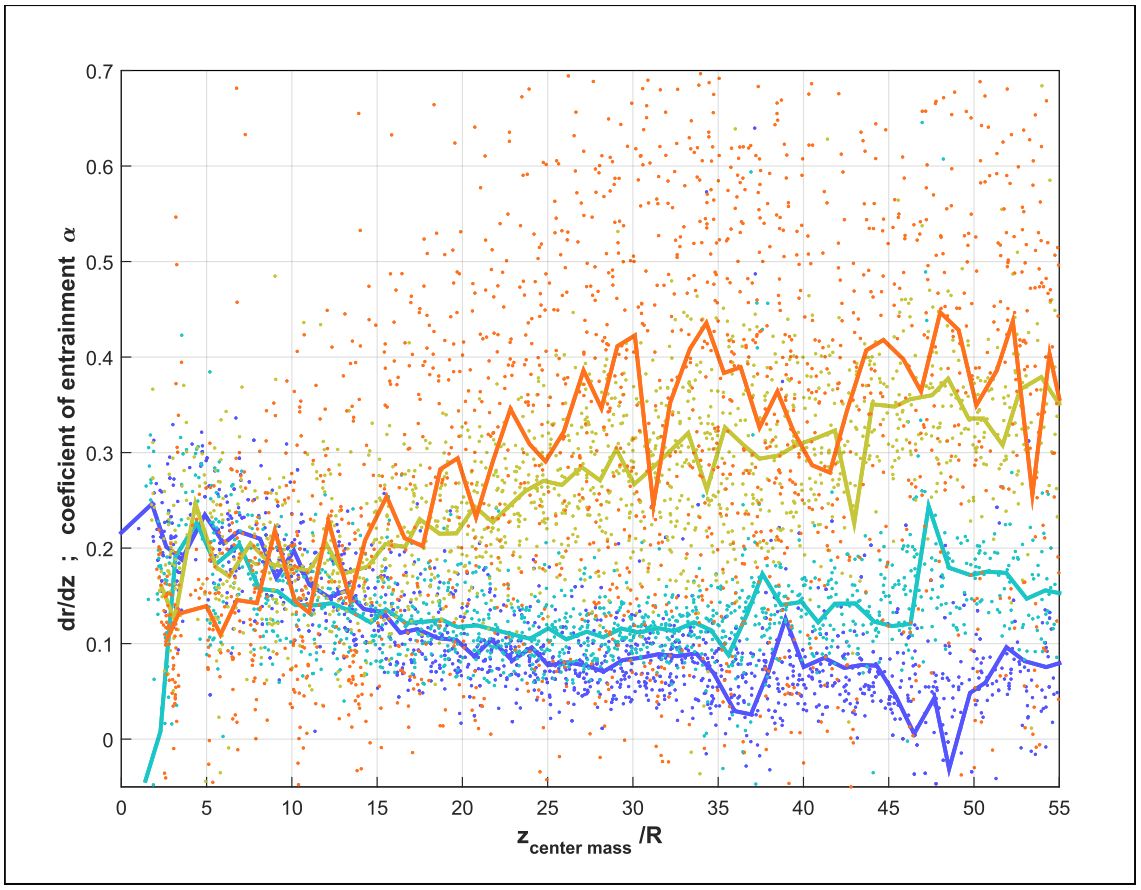

FIGURE III.8 – Graph of the derivative of the radius of the region occupied by the liquid metal as a function of the depth of its center of mass stacked between all experiments made with the same viscosity ratio. The dots are the instantaneous values and the solid lines are the window averaged values. In red are the aggregated data for $R_\mu = 700$, in yellow for $R_\mu = 70$, in cyan for $R_\mu = 8$ and in marine blue for $R_\mu = 0.4$.

collective behavior. For the three lowest viscosity ratios, the dilution suggests qualitatively and quantitatively that the liquid metal evolves as a thermal. In a broader view, it is important to see the value of the expansion coefficient as a strong constraint for any model aiming at explaining the fall of the liquid metal since the mode of deformation and breakup that takes place in this region of the parameters space is most likely to be the relevant one for post impact flows.

C Kinematic of the diapir's center of mass

The location of the center of mass of the diapir, approximated as the one of the black pixels in the experimental videos, is shown in figure **??** as a function of time for all four viscosity ratios. Since the diapir is initially released in a position where it just starts to appear in the image (because of the frame of the experiment), a depth of no more than $2R$ is missing from the videos. The two parts of the fall are again visible in both dimensional and dimensionless tracks. The second part of the tracks collapses much more in their dimensional form than non-dimensionalized by the Newtonian speed that characterizes the

large scale flow. In contrast, this scaling for the speed is much more adapted for the first part of the fall. This seems to confirm the tendency of the droplets to fall independently from each others, as a rain, in the last part of the fall, and therefore to "forget" the previous speed of the large scale flow.

Although variability between experiments is relatively important, the center of mass position as a function of time exhibits an approximately linear trend before breakup. The speed of the fall being almost constant, the Newtonian speed scaling can be tested by computing the drag coefficient with the speed averaged between $z_{centermass} = 3R$ and $z_{centermass} = 10R$. This interval is chosen in order to avoid the initial phase of acceleration in free fall. The resulting drag coefficients are shown as a function of the Weber number in figure **??** and as a function of the Reynolds number in figure **??**. The drag coefficient does not seem to depend on Re. This means that we have indeed reached the regime where inertia is balancing buoyancy for the initial falling speed of the diapir, as it is classical for drops of water falling in the air (**?**, **?**). In addition, the drag coefficient also seems to plateau with respect to We.

This trend tends to confirm what the data on $\frac{dr}{dz}$ shows (cf. fig. **??**) about the large scale deformation. The diapir deforms by entrainment of ambient fluid inside its boundaries, in a very similar way to turbulent thermals in miscible fluids. At the same time, its fall is independent of the Weber number and follows a simple balance of inertia against buoyancy. Therefore, we see this regime of deformation as only weakly influenced by surface tension (**?**) and it is likely that we have reached the ultimate regime of deformation at least for the three lowest viscosity ratios. This may not be the case for the highest viscosity ratio as the deformation and fragmentation appear to be limited by surface tension as the viscosity is slowing deformation.

To specify the kinematic of the center of mass of the diapir, the first part of the fall is plotted in figure **??** for the experiments of the two setups, along with the quantity of black pixels in order to relate the speed of fall with the approximate time of breakup. It is to be noted that from counting and direct observations of the films, this quantity is growing up until the moment of breakup, where holes in the film are retracting very fast, making a "kink" and even a slight decrease. This allows to define a window for the time of breakup (cf. fig. **??** and the next section for a more precise definition of what we will define as breakup time). The non-dimensional speed averaged among all runs appears to be approximately constant, except for the highest viscosity ratio, with a value of $\left(\frac{8}{3Cd}\right)^{-\frac{1}{2}}$ (by definition of the drag coefficient, here equal to about 4).

If the magnitude of this speed and its scaling with buoyancy are not surprising, the apparent constant trend is very surprising. For a rigid or weakly deformable object, such a straightforward balance with the initial dimension of the diapir is to be expected since this dimension does not vary greatly and saturates. Here by the time the diapir breaks up, its cross flow dimension has been multiplied by 3 to 4 hence the area of its cross flow section by 9 to 16. More precisely, as the Weber number of the flow grows, the surface tension has less and less importance and the diapir is expected to fall as a turbulent thermal (**?**, **?**, **?**, **?**) and not as a rigid body as the constant speed suggests. In the turbulent thermal theory, the apparent radius increase implies an increase of the effect of the drag (the drag coefficient is supposed constant). In addition, it also implies a gain of mass via the (measurable) turbulent entrainment. Combined, these effects would act toward the speeding down of the diapir. The quantitative aspect of these constraints can be compared

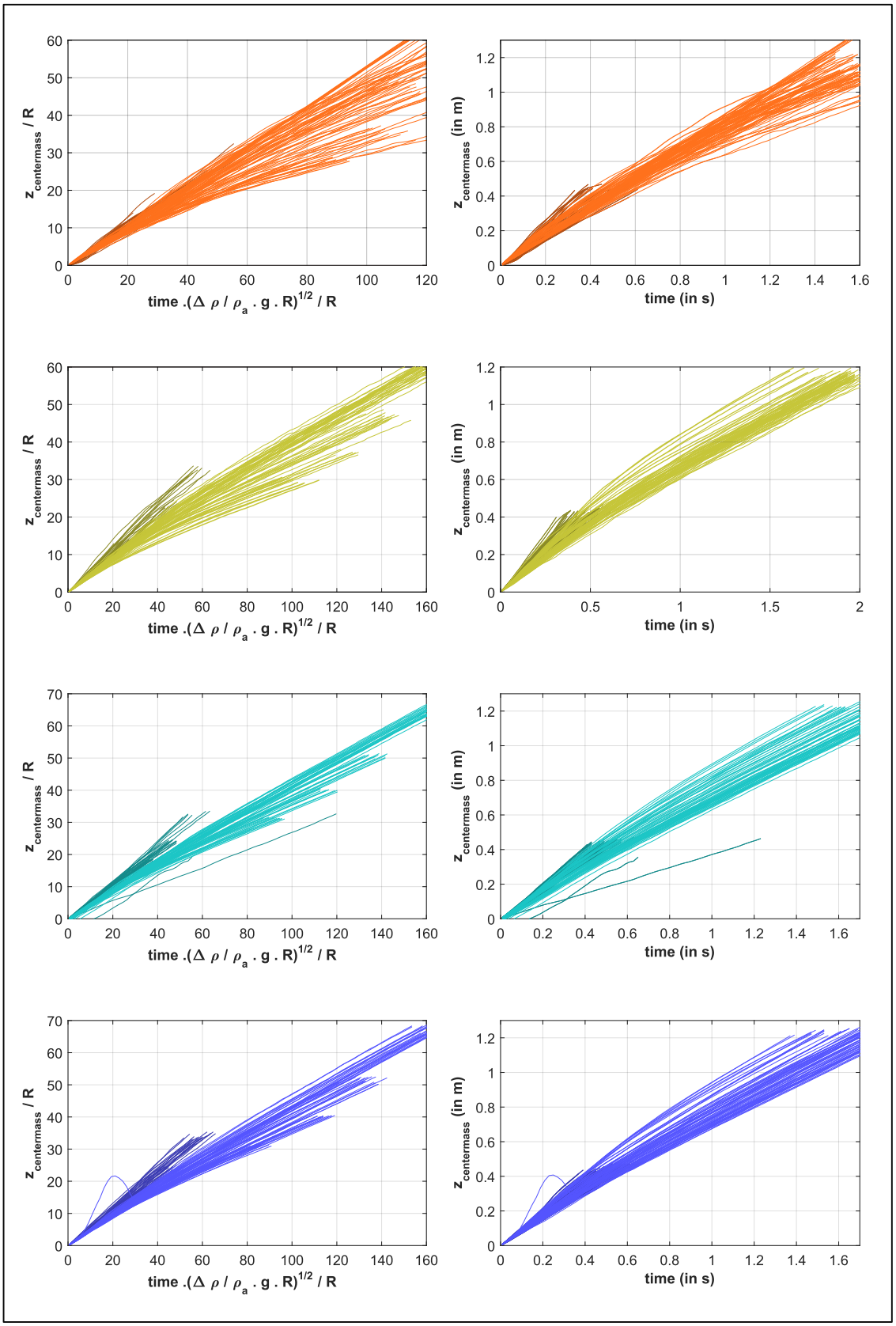

FIGURE III.9 – Graph of the center of mass position as a function of time for all experiments

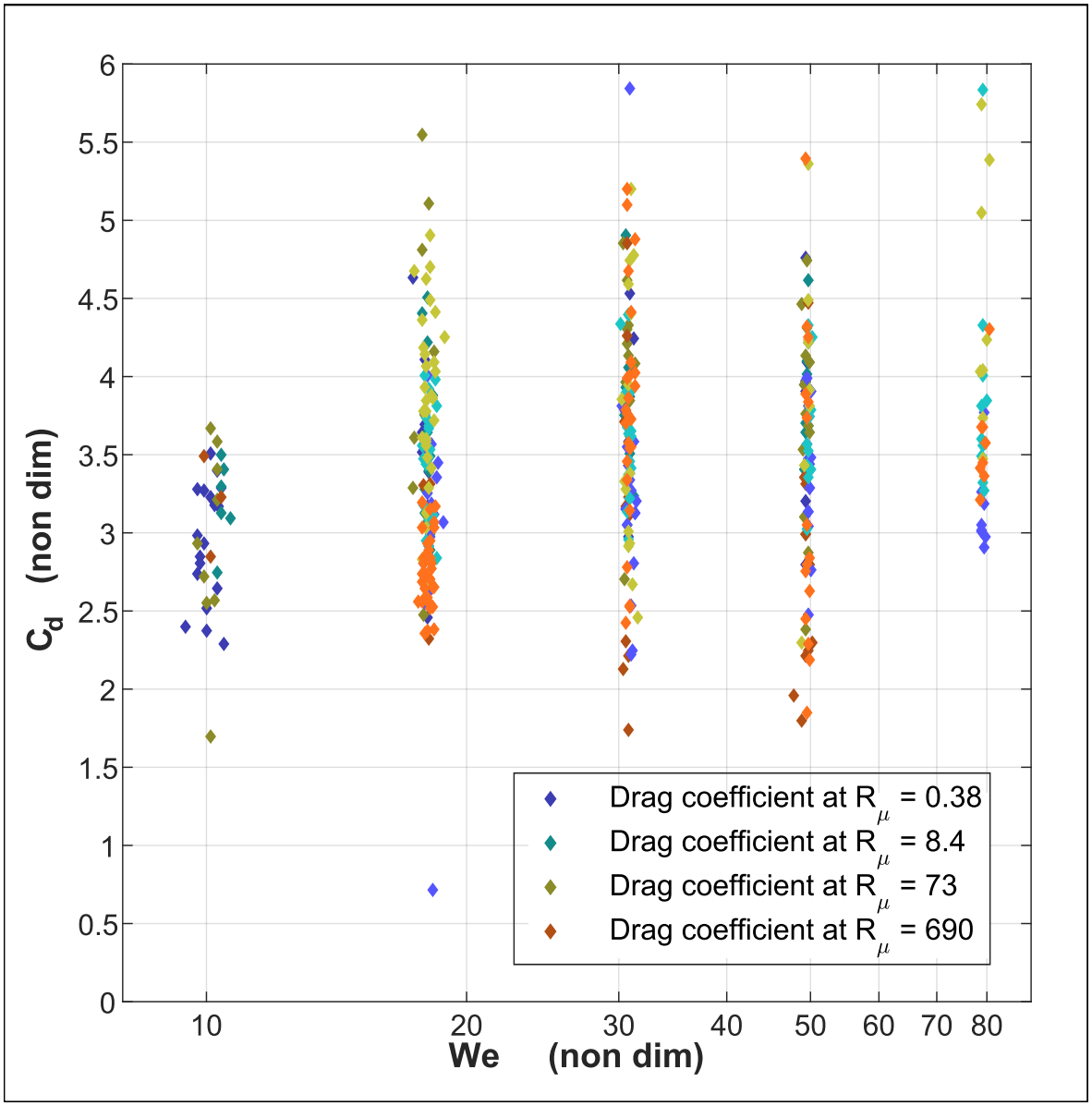

FIGURE III.10 – Graph of the drag coefficient as a function of the Weber number for all experiments made with the first and the second setups. Dark colors are experiments made with the first setup and light colors are experiments made with the second setup.

against the data in the form of the full integration of equation **??** (see dotted lines in fig. **??**).

Fully integrated, this equation gives all the phases of the fall of a turbulent thermal from rest (i.e does not contain only the asymptotic behavior). A constant coefficient of entrainment is assumed (that we set to a value of $\alpha = 0.19$ in agreement with our observations) as well as constant added mass k and constant drag coefficient cd. In that case, cd is not meant to represent all inertial effects, contrary to Cd. It is the classical drag coefficient of an object with a constant mass that parametrizes the result of the integration of the dynamic pressure over the surface of control. Therefore it cannot be constrained with the experimental values of the drag coefficient which is encompassing

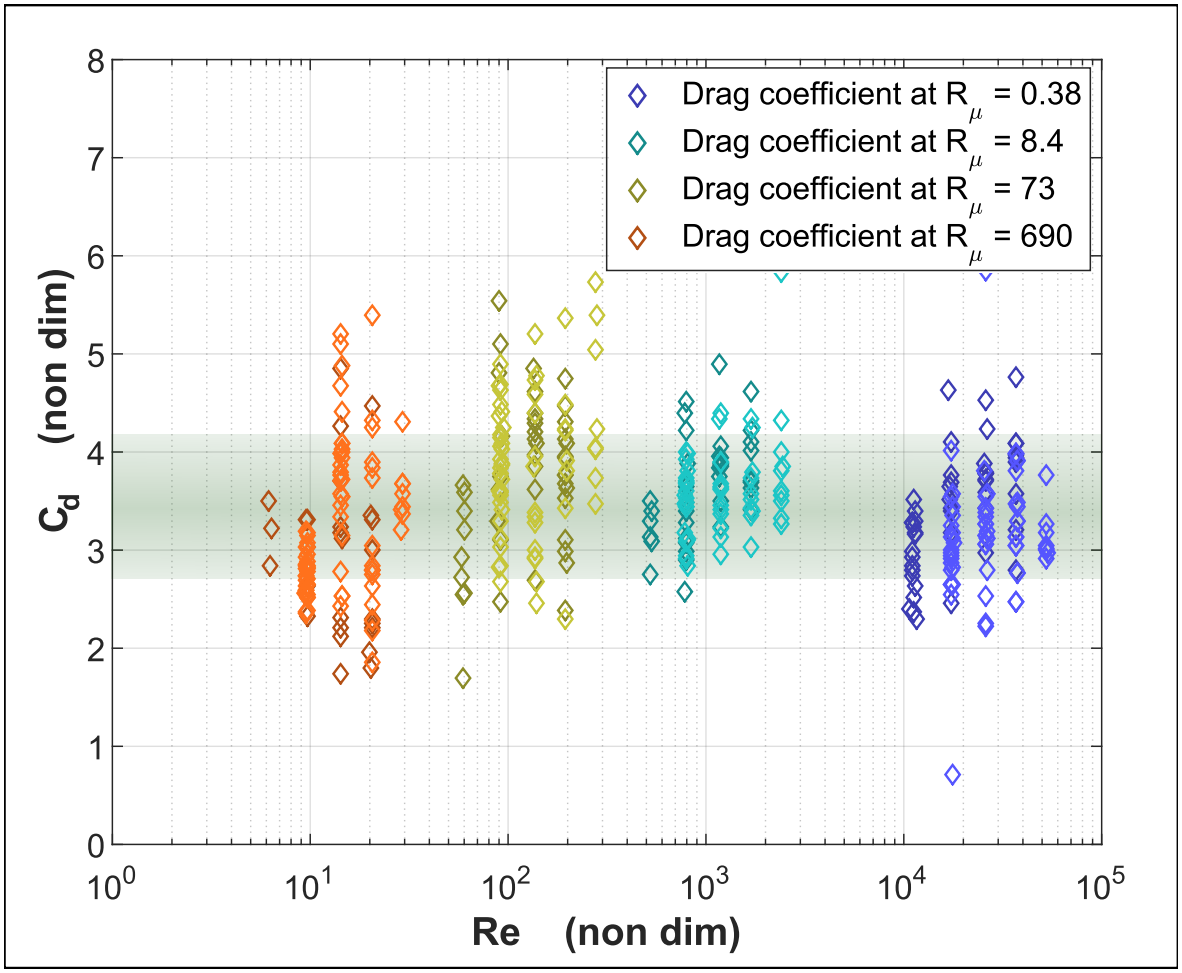

FIGURE III.11 – Graph of the drag coefficient as a function of the Reynolds number for all experiments made with the first and the second setups. Dark colors are experiments made with the first setup and light colors are experiments made with the second setup.

all inertial effects. Thus, we have varied cd and k in order to produce the best fit with our data. In addition, we were not able to measure the coefficient of entrainment from $\tilde{z}_{centermass} = 0$ to $\tilde{z}_{centermass} = 3$ as the diapirs are in their initial position not entirely in the field of view. We then decided to include an additional parameter, a radius lag $\frac{\Delta R}{R}$, from which the equation is integrated, to account for the fact that the model of a turbulent thermal may not be verified as soon as the diapir is freed from the balloon. This can also be seen as an initial dilution. We performed several integrations with either a ΔR equal to zero and an initial speed close to zero or on the contrary, allowing a ΔR different from zero (but never larger than two initial radii, which would set us in the part of the fall near or during the breakup) and an initial speed as measured in the experiment. The best fit produced by these two types of integration are shown in figure **??**.

Although they sit in the experimental variability, we do not consider them as satisfying for two reasons. The first one is that the theory fits the best the experiments made in the first setup with the highest R_μ, for which we consider the hypothesis of turbulent entrainment the less likely to be true (the value for the coefficient of entrainement does not even match the experimental derivative $\frac{dr}{dz}$ for this R_μ). The second is that the typical

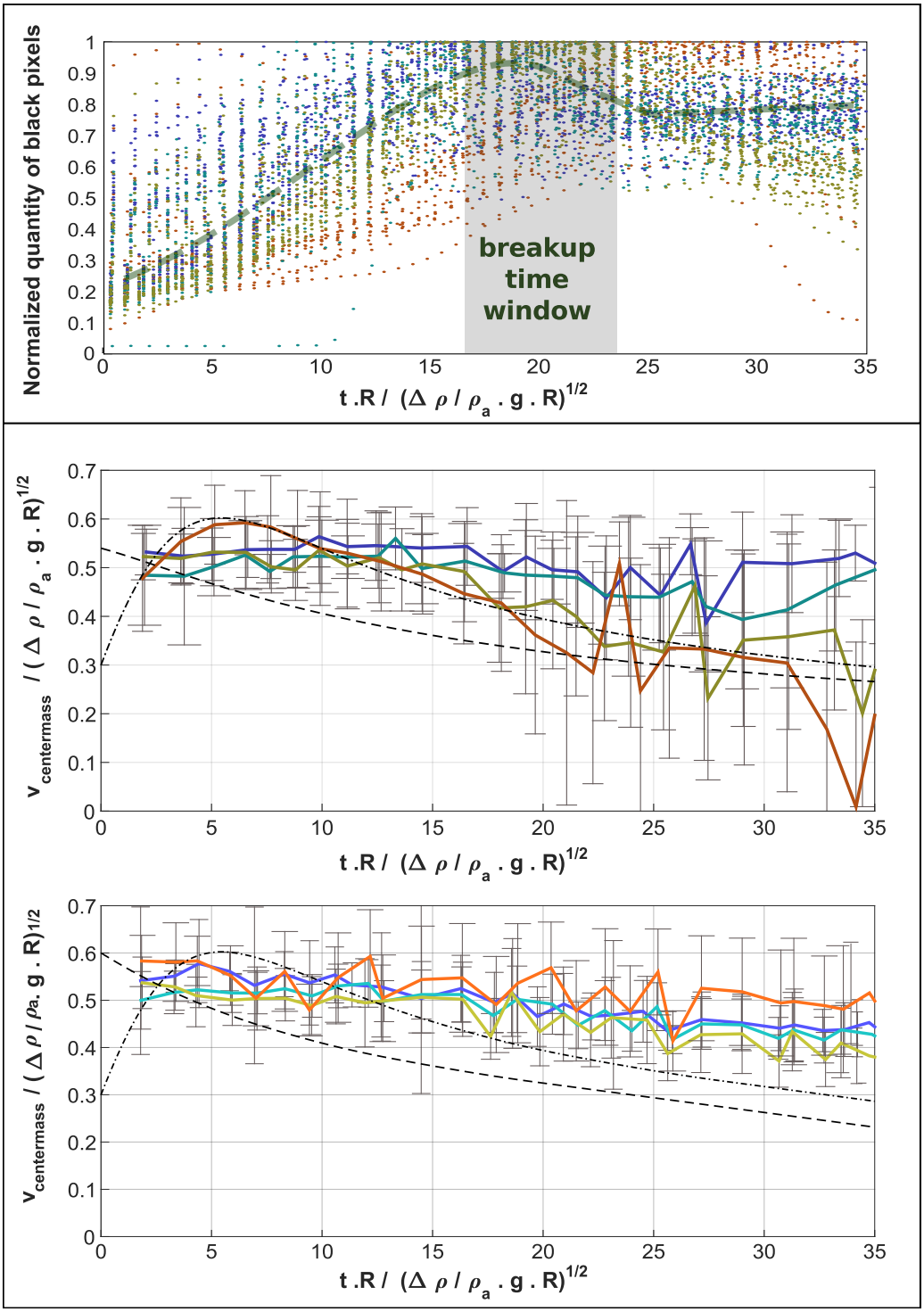

FIGURE III.12 – Top panel : graph of the sliding window average quantity of black pixels as a function of time. The local decrease of this quantity indicates an advanced stage for the breakup. Bottom panel : graph of the vertical speed of the diapir as a function of time stacked between all the experiments made at the same viscosity ratio. The dashed line and dash and dotted line correspond to the integration of the turbulent thermal equation with and without an initial dilution.

error made by the theory predicting the speed in the interval between the start of the experiment and the breakup is about 20 %. For the data to be that imprecise, the center of mass of the black pixels has to be misplaced to a problematic extent. More precisely, its depth is changing by about 10 radii before breakup. With an error of 20 %, this estimation of the center of mass of the diapir considered as a thermal would need to be wrong by about one initial radius or more. This value is large but it is conceivable owing to bias that could affect the difference between the altitude of the center of mass of black pixels and the altitude of the actual center of mass. For example, very stretched structures of liquid metal could lead to the misplacement of the center of mass compared to what is actually the thermal, as well as the unequal vertical distribution of liquid metal in the black region (i.e. settling of drops, thicker liquid metal sheet etc). Yet, from our observation these errors would put the actual center of mass even deeper for the same time, potentially giving a greater speed and consequently a higher error between theory and measurements.

Let us assume then that the data is reliable and the problem is the theory. The interest for this very first part of the fall is uncommon. We could not find any specific theory about this first part, apart from the free fall and negligible drag part (**?**). From the time scale of acceleration with no drag, this phase takes place in the range $\tilde{z}_{centermass} = 0$ to $\tilde{z}_{centermass} = 3$. One could assume the entrainment hypothesis illegitimate. However if the turbulent entrainment appears to be a strong assumption in general, in our case it paradoxically implies a fairly simple flow. Since we focus on the part of the fall before the breakup, the flow can't cross the bottom or the sides of the "inverted bag" we are seeing when galinstan is falling in the ambient fluid with the three lowest viscosities. Despite this fact, the liquid metal sheet is enclosing a region of space wider and wider, by entraining fluid in the rear. Therefore, negating the entrainment hypothesis, which is to say the entrained fluid does not fall with the liquid metal from now on but departs from the region occupied by it (the technical term of this outflow through the surface of control is detrainment) is in fact not a conservative hypothesis due to the complexity of the flow it implies (cf. fig. **??**). Unsupported by the experiments filmed with the large scale framing, the hypothesis of a detrainment quasi equal to entrainment needs measurements of the velocity field on the surface of control near the diapir to be supported. An alternative explanation to this excessive falling speed of the diapir is that the momentum flux carried by the entrained fluid is not negligible as it is generally supposed, which also requires measurements of the velocity field near the diapir. It is important to note that these two explanations are not mutually exclusive. We will come back to these hypotheses in chapter **??**.

Concerning the last part of the fall, the point we have made about entrainment is stronger when the galinstan is unbroken, but judging by the center of mass position as a function time, this regime dominated by the inertia of the initial mass of liquid metal and some type of entrainment extends to about 30 to 40 dynamical time or 15 to 20 initial radius in depth. Thus the discrepencies in how the entrainment proceeds concerns the diapir when it falls as a tubulent thermal, which last until the dynamics transition from a large scale flow dominated by collective effects to drops falling independently from each other. As this transition is between a flow dominated by collective effects to a rain, the transition should be described by the Rouse number $\mathcal{R}$ rising to a value of order one, which is to be linked to the sizes of the drops (see chapter **??** for detailed analysis).

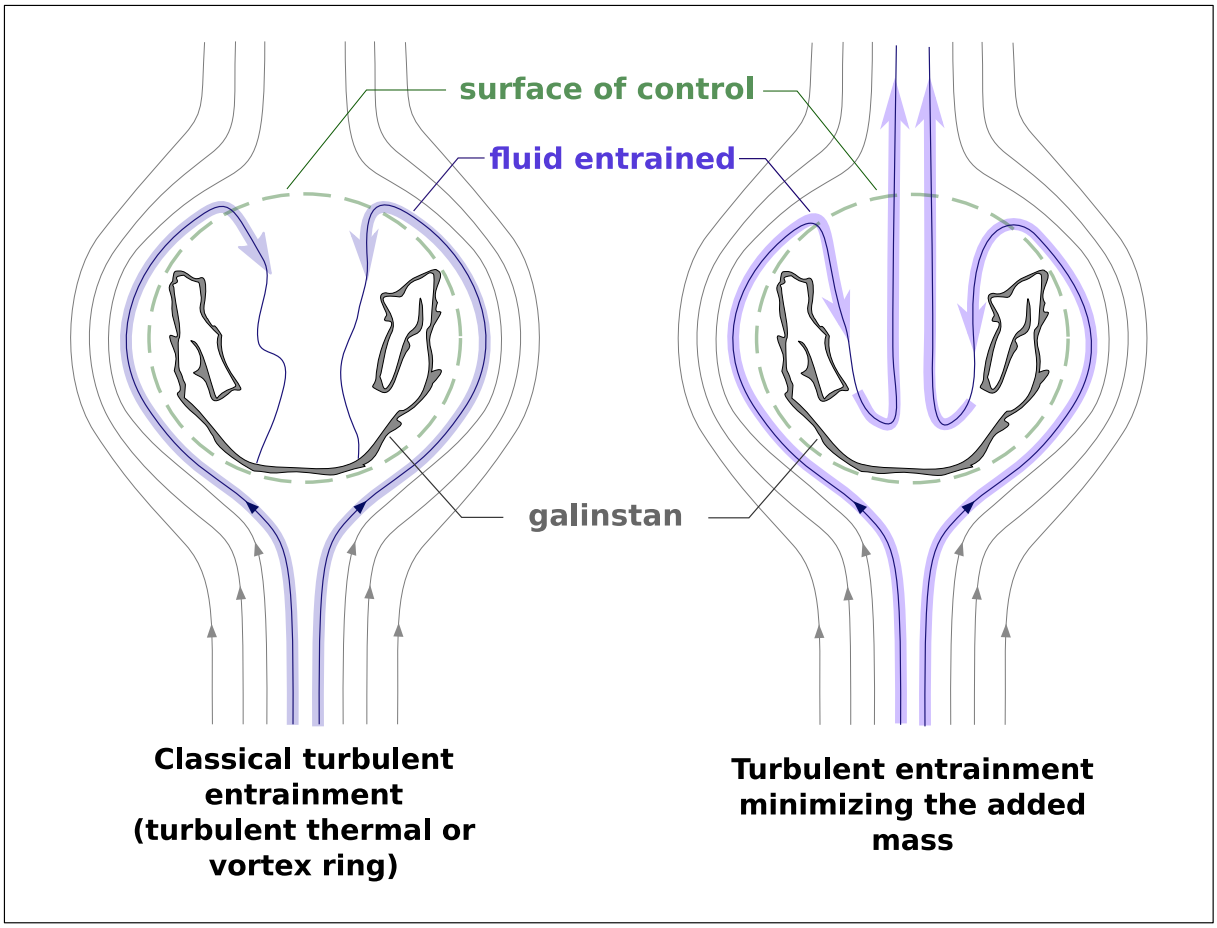

FIGURE III.13 – Interpretative schematic of a classical turbulent thermal/vortex ring in the context of the fall of an initially spheroidal mass of immiscible buoyant fluid (left) and an hypothetical structure resulting from the same initial condition that would minimize the added mass (right).

D Breakup distance

Since it is interesting for the discussion about the turbulent entrainment to know when breakup has occurred (galinstan being in an "inverted bag" state and unequivocally diluted prior to that event), we aimed at building a breakup criterion based on the continuity of the liquid metal film. In a broader context, breakup is commonly defined as the moment when holes appear in the buoyant liquid (**?**, **?**). In practice, we have supposed that breakup happens when the product of a positive power of three quantities is maximum. These three quantities are the quantity of black pixels, the opposite of its derivative with respect to time, and the quantity of white pixels enclosed in black pixels regions (cf. fig. **??**). The product in question should be maximum when the diapir's extension is large and holes have formed in the liquid metal sheet and are opening.

The results given by this criterion for the experiment of the first setup being rather robust with respect to the choice of the actual power of the 3 quantities, we have computed the breakup distances for each experiment as shown in figure **??**. However, this criterion did not reproduced these results for the videos of the second setup (cf fig **??**, top panel).

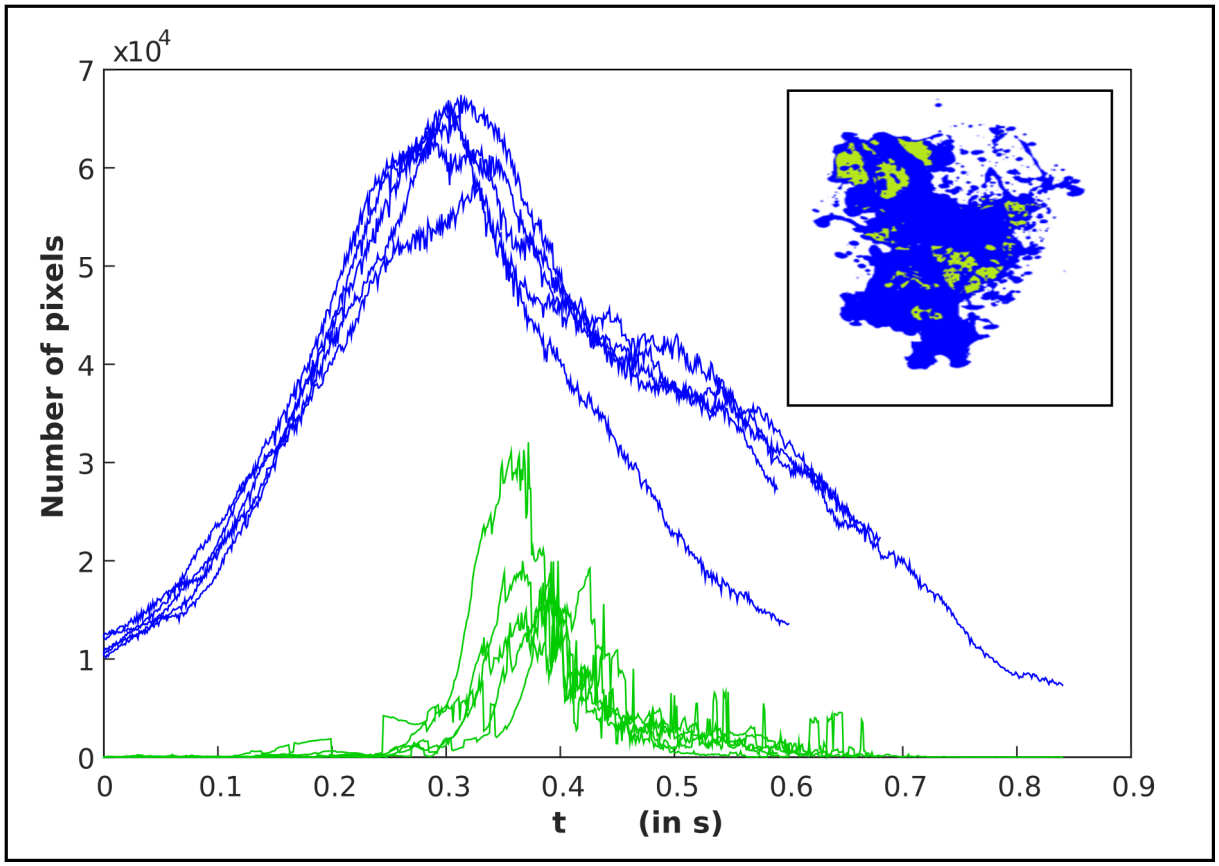

FIGURE III.14 – Graph of the quantity of black black pixels (blue line) and white pixels enclosed in a region of black pixels (green line) for 5 experiments as a function of time. Insert : Snapshot extracted from the video of an experiment of the fall of a galinstan diapir in a mixture of water and UCON oil colored in accordance with the definition of the plotted variables.

We interpret this as an effect of the limited resolution of the videos of the second setup. For the second setup, filming an height 3 times larger meant dividing the resolution by 3. This had a big effect on the noise of the three quantities included in the criterion because they are all proportional to the projected surface of the diapir, which implied that the signal over noise ratio is multiplied by at least 9. The proxy for holes is the quantity of white pixels in regions enclosed in a black pixels region which can appear in dense clouds of droplets. It is likely that this is the quantity that underestimated the breakup length.

Thus we have resorted to use a different criterion for the videos of the second setup. The time series of the number of connected components approximate well the time series of the number of drops and show a sharp increase near the time of breakup. We deduced a breakup length from the number of connected components in the images, in a similar way to **?**. These results are presented for all experiments of the second setup in figure **??** in the bottom panel. Although they are recovered differently for the two experiments, the breakup lengths are consistent both qualitatively and quantitatively. Excluding the breakup lengths for the highest R_μ which is probably higher due to the different mode of breakup, the values of the breakup lengths are not significantly affected by Re, and seem to get closer to about 10 initial radii as We increases. With such consistency, we

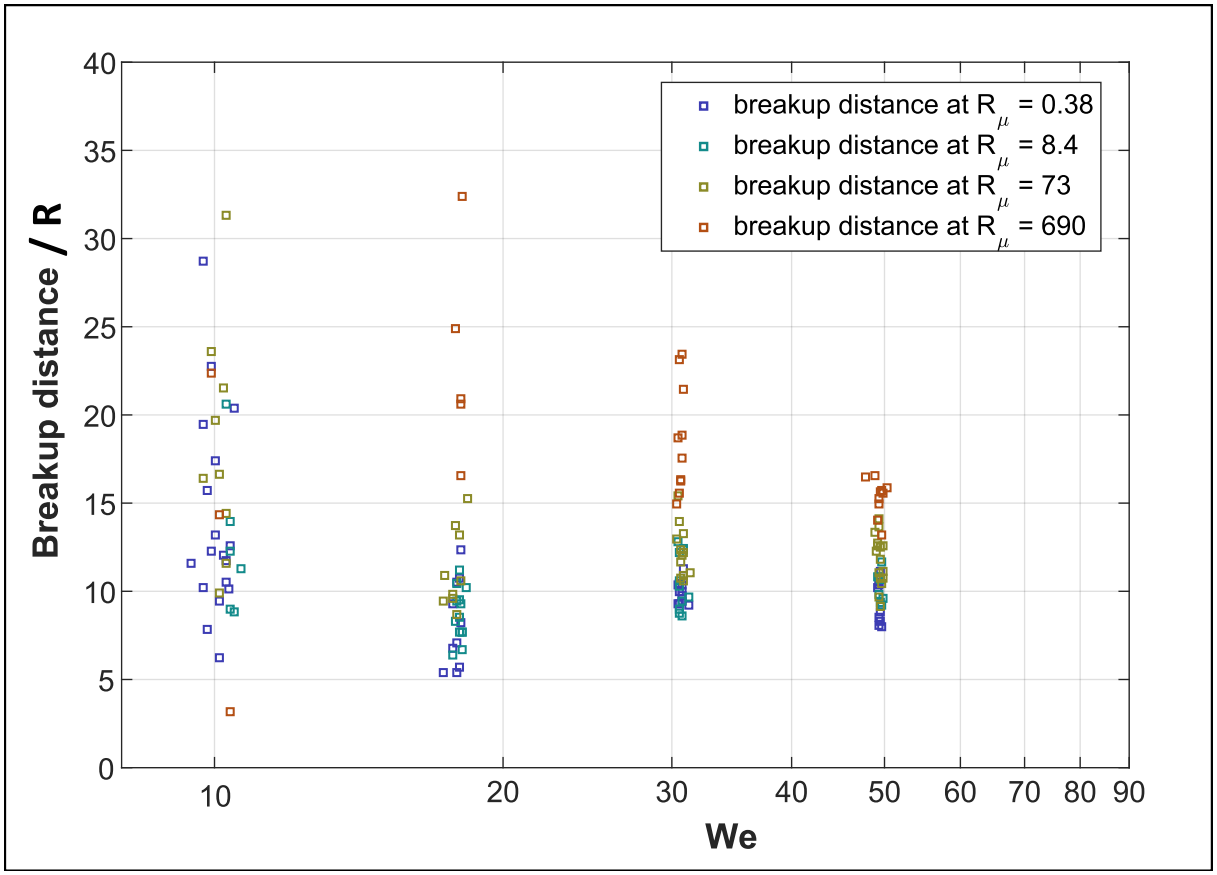

FIGURE III.15 – Graph of the breakup distance as a function of the Weber number for all the experiments made with the first setup. The breakup distances are here computed with the composite criterion based on topological variables.

argue that the breakup length l_{bk} is likely to have an approximately constant value for asymptotically large value of We and Re, and thus for the post impact flow :

$$l_{bk} = C_{bk}.R \tag{III.3}$$

C_{bk} is a constant approximately equal to 10. This implies that the breakup time t_{bk} is simply proportional to the large scale advection time $t_{bk} = C_{bk}.\frac{R}{U}$.

This scaling is quite classical in the literature (**?**, **?**, **?**, **?**) and is mostly interpreted as an acceleration time scale due to the aerodynamic forces. Indeed, from continuity of the pressure at the front interface of the drop, the dynamic pressure at the front induces a velocity in the liquid metal proportional to $\tilde{\rho}$ which gives a time scale t_{bag} (based on the initial radius of the diapir) :

$$t_{bag} = \sqrt{\tilde{\rho}}.\frac{R}{U} \tag{III.4}$$

This time scale represents the time it takes for the frontal interface of an inviscid drop to meet with its rear interface. In a broader sense, the thinning of the metal sheet at the front of the diapir scales with the large advection time scale, just like the apparent radius of the diapir does. Supposing that the liquid metal pierce when a critical thickness is attained, the breakup could be seen as crossing a threshold in the dilution of the liquid

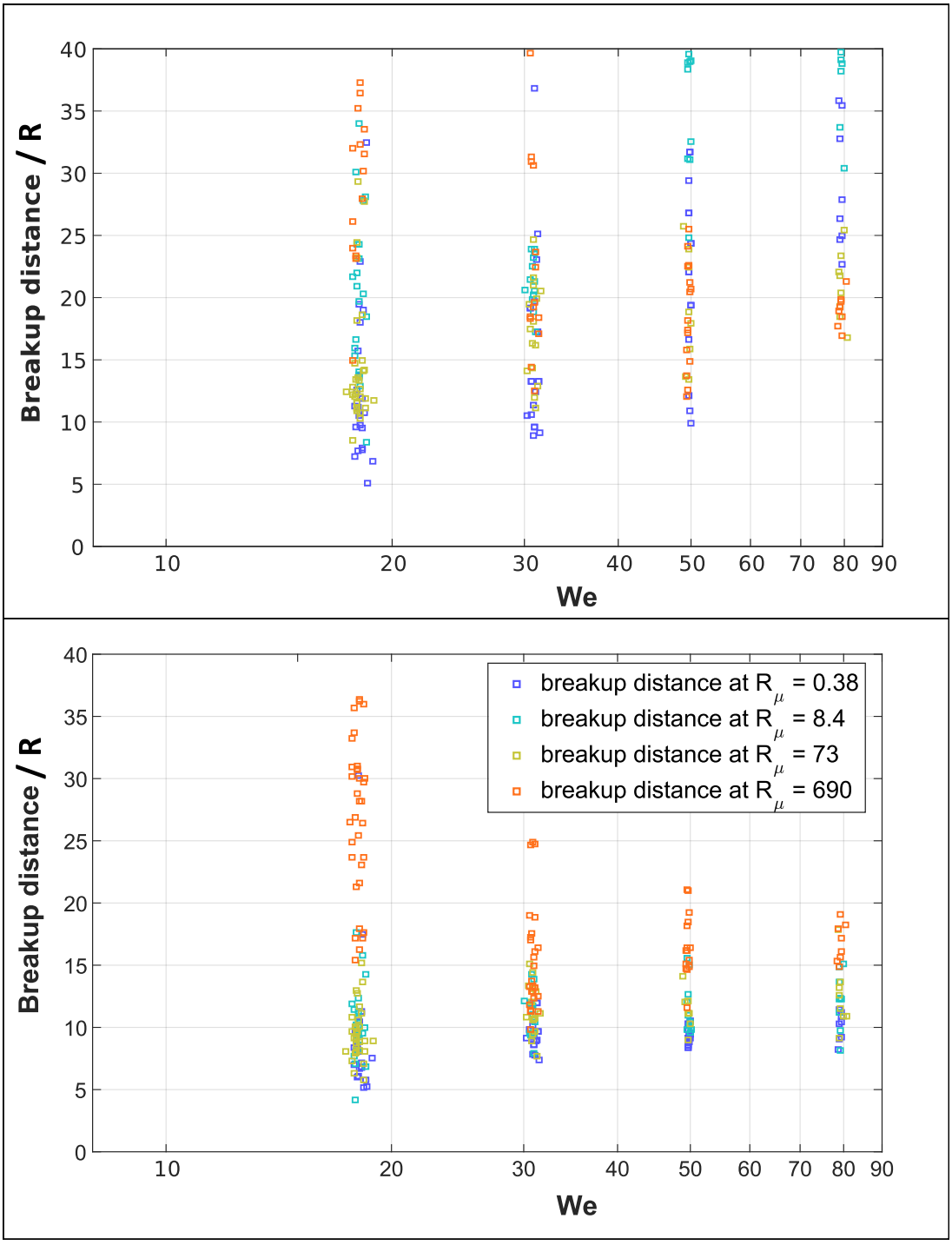

FIGURE III.16 – Graph of the breakup distance as a function of the Weber number for all the experiments made with the second setup. Top panel : the breakup distances are here computed with the composite criterion based on topological variables. Bottom panel : the breakup distances are here computed with the criterion based on the initial increase of the number of drops and its time scale in a similar way to **?**.

metal. However, the physics of the spontaneous piercing of liquid sheets being still poorly understood, the typical thickness of the galinstan at breakup (around $50 \cdot 10^{-6}$ m) does not

support a critical thickness independent of the dynamics. Indeed for the critical thickness to be independent of the dynamics (in the absence of surfactant), its is believed that the pressure fluctuations due to thermal agitation have to overcome surface tension (**?**). It would probably yields a thinner film because temperature fluctuations can only act at very small scales.

Since we do not vary the density ratio, we cannot verify if the time scale for aerobreakup t_{bag} is the correct one for us. As a matter of fact, any time proportional to the large scale advection time scale (provided that the coefficient has a value close to 10) would provide a good fitting of our data. Anyhow, the factor $\sqrt{\tilde{\rho}}$ indeed corrects in the right direction the length scale found in our experiment and in the experiment of M. Landeau and colleagues (**?**), for which they find $C_{bk} = 6$, for experiments with $\tilde{\rho} = 2$. For the breakup mode that is in our view the most relevant for the post impact flow, our combined data support then a scaling for the breakup length that is :

$$l_{bk} \;=\; 4\sqrt{\tilde{\rho}}\;.\;R \tag{III.5}$$

In conclusion, we have observed the large scale dynamics of the fall of a mass of liquid metal in a viscous fluid. It exhibits a dilution as a function of depth similar to the one of miscible flows known as turbulent thermals. Its speed is also comparable to turbulent thermals but evolves somewhat differently, in apparent contradiction with the entrainment of fluid inside the diapir. We will then proceed to investigate more precisely how the entrainment is affecting the trajectory of the diapir.

Chapitre IV

Dynamics of the flow prior to breakup

We examine here the data recovered from the analysis of the videos made with side lighting and a curtain of H_2 bubbles. As mentioned in the chapter **??**, we were not able to produce any reliable detection method of the interface based on levels of intensity, gradient of intensity or length scale hierarchy in the different zones. We resorted to pinpoint the interface by hand on a dozen of frames per films using 30 points. The low temporal resolution led us to not smooth the derivatives with spline interpolations for this data as this would mean loosing too much information. In order to test if such method could give satisfactory results, we have computed variables in the same way we have done for the images made with back lighting. This time the black pixels are the one enclosed by the pinpoint interface. The radius as a function of depth of the center of mass is shown on figure **??**. The increased resolution on the very first part of the fall allows us to see a phase of deformation where the apparent radius of the diapir is decreasing. Hence we have non dimensionalized the radius and the depth of center of mass with the minimal radius in order to collapse all the data. As it the case for the large scale data, the radius indeed seems to evolve linearly with depth. This implies a constant entrainment coefficient.

This is confirmed by the derivative of the radius as a function of depth shown in figure **??**. Here the derivative is approximately constant at a value of 0.2 which is entirely consistent with the previous data. It is one more argument in favor of the conservative hypothesis of a constant entrainment coefficient.

The fact that the radius of the sphere that has the same projected area evolves as expected means that the surface of the projected area should also have a comparable evolution. However, that is not the surface where we integrate the velocities. As the local nature of the velocity field imposes us to integrate the mass and impulsion fluxes locally, we also need to verify how the surface where we integrate relates to the equivalent surface of the spheroid supposed for the turbulent thermal. Strictly speaking, we are integrating on very small portions of the hand-drawn contour which correspond to half truncated cones. This is equivalent to supposing axisymmetry for the two sides of the diapir as if it was two separate runs and taking the average of the two values for the integrated surface, mass flux, and impulsion flux. The integrated surface is shown on figure **??**. One can clearly see that experiments have a large variation in the surface between runs and an approximately quadratic trend with respect to the depth. Once re-scaled by the surface of the sphere of the same radius, the quadratic trend seems to be largely due to the expansion of the diapir. Thus the surface of the equivalent sphere approximates the integrated surface via

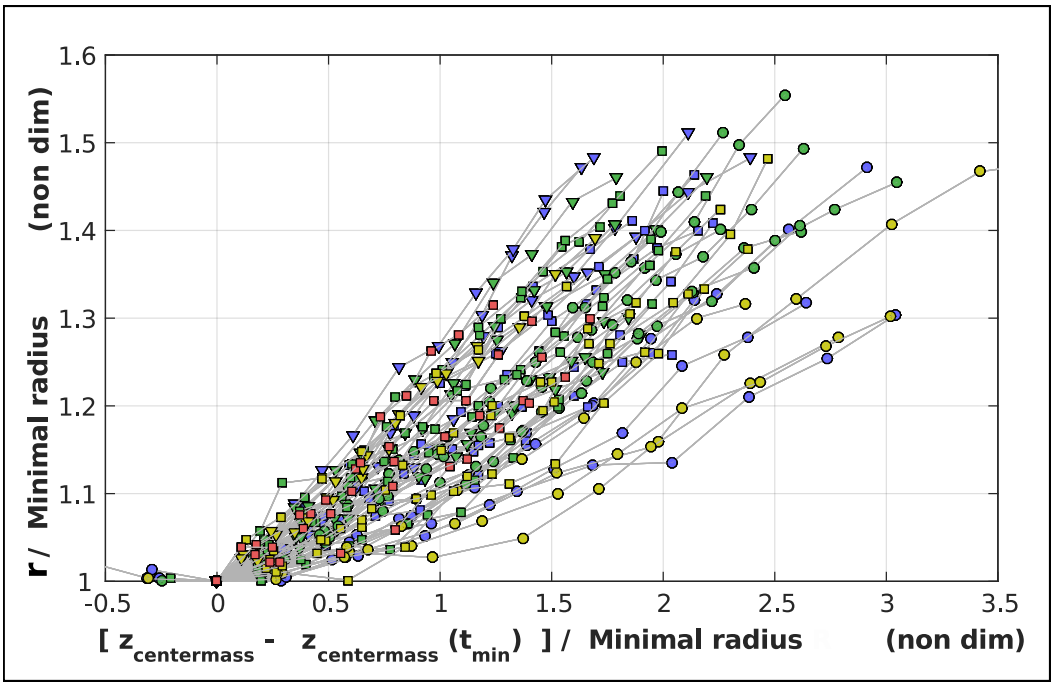

FIGURE IV.1 – Graph of the radius of the region occupied by the liquid metal as a function of the depth of the center of mass. The start of the analysis is close to the end of the initial phase of deformation that happens just after the release of the liquid. Since turbulent entrainment is not necessarily associated with deformation at this stage, we have non dimensionalized the radius and the depth by the minimal radius for each experiment and shifted the depth accordingly.

a constant of 1.2, but a slight increase in their ratio is visible. This is most certainly due to the increasing convolution of the interface as it gets stretched, and thus increases compared to its spherical equivalent. In addition, it could even be a sign that the interface is becoming fractal in nature as suggested in the study of Deguen and colleagues in 2014 (**?**) but since our method for recovering the interface is very crude, the data to support such a claim would need a prohibitive amount of time to recover.

The depth of the center of mass (cf. fig. **??**) also shows comparable results to the ones found in the videos with the large scale framing. It roughly evolves linearly with time as seen in figure **??** where the depth is compared to the one given by a simple theory of terminal velocity of an object with $Cd = 3.8$ (cf. chapter **??**). In order to compare with the turbulent thermal theory, a time integration of the equations **??** was performed. The radius computed in the first image of each video and the measured speed was used as initial conditions. The black curve is made by integrating with a value for $\frac{\Delta R}{R}$ equal to its experimental value averaged among all runs. The two white lines are done with a value for $\frac{\Delta R}{R}$ equal to its experimental average plus or minus the standard deviation. One can see that even if the theory doesn't depart too much from experiments, the actual trend exhibited by the experiments does not seem to be well reproduced. In conclusion, if taken alone, this data would not be enough to confirm departure from the turbulent thermal theory. Nonetheless, it is consistent with the experiments filmed with the large scale framing, making an aggregate of 488 experimental runs supporting this idea, or 378

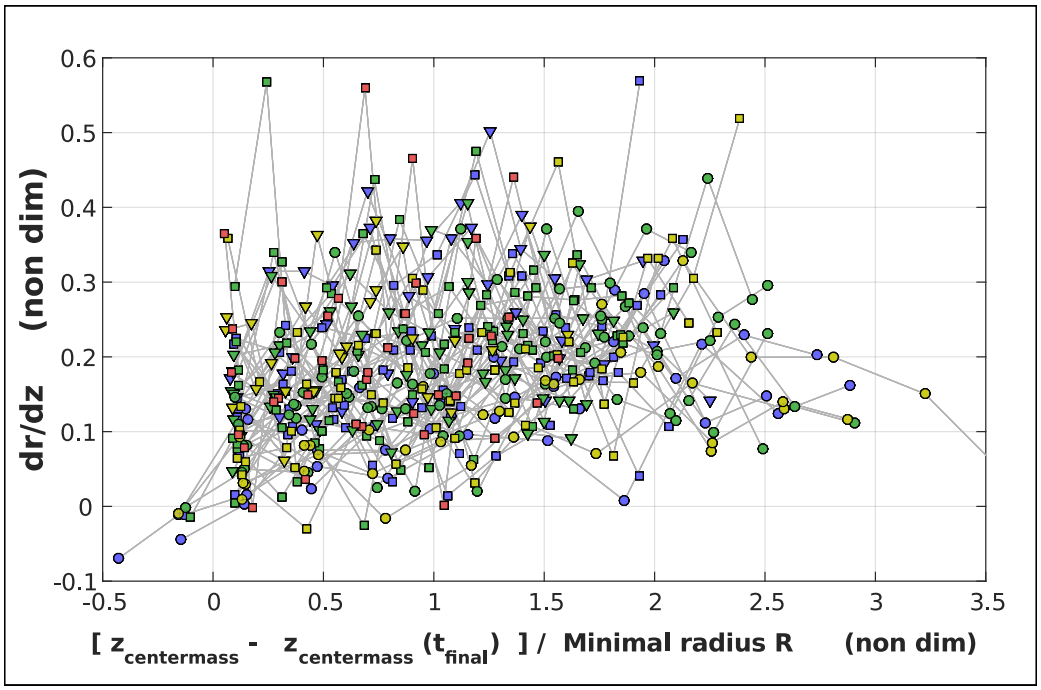

FIGURE IV.2 – Graph of the derivative of the radius of the region occupied by the liquid metal as a function of the depth of the center of mass for all experiments.

if one excludes the experiments made at $R_\mu \simeq 700$ for which additional complexities could be argued.

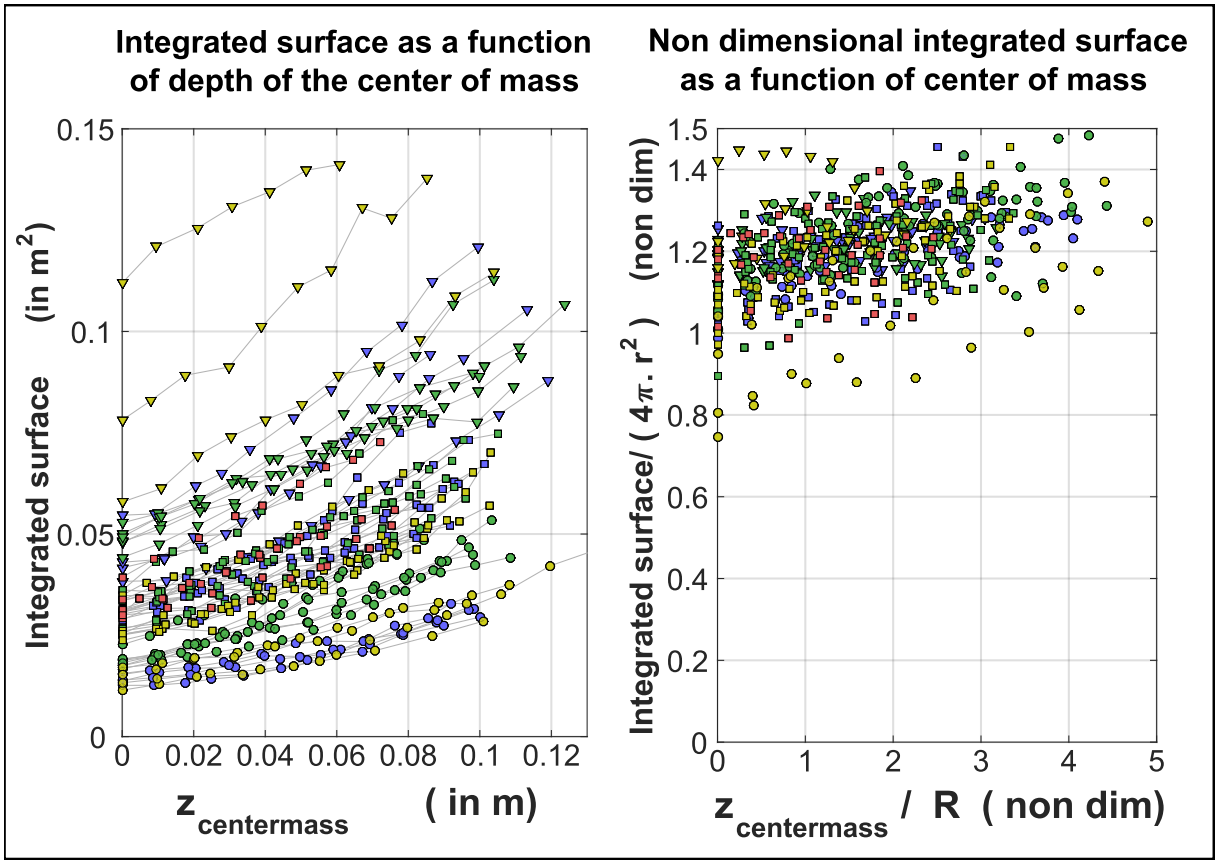

FIGURE IV.3 – Graph of the integrated semi-axisymetric surface as a function of the depth of the center of mass for all experiments. Left panel : dimensional surface. Right panel : surface non-dimensionalized by the surface of a sphere with the same local radius.

In order to compute the mass fluxes across the interface, both the local speed of the ambient fluid and the one of the interface have to be known. As previously stated, we retrieve the speed of the ambient fluid from PIV treatment. As we only need the speed of the interface perpendicular to itself, the roughness of the 30 points approximation allowed to estimate this speed rather easily. The displacement of the interface between two frames is measured by intersecting the local perpendicular of the interface computed from a given image with the interface of the following image. The mass fluxes can then be integrated along the contour. Figure **??** displays the evolution of the initial mass calculated with the apparent radius in the first frame together with the mass entrained into the diapir calculated from the integration of the mass fluxes in each image. As its ratio with the mass calculated with the apparent radius stays around 1 for all times, we can say with reasonable confidence that our computation of the mass fluxes is quite satisfactory since there is no loss or gain of mass.

As a consequence of this fact and the linear increase of the diapir's radius as a function of depth, the mass entrained in the diapir is rapidly reaching a regime where it is proportional to the speed of the diapir and its surface area, as seen in figure **??**. The coefficient of proportionality is the coefficient of entrainment which as a value between 0.15 and 0.2 (cf. chapter **??**). This is exactly the Morton hypothesis for thermals.

By the end of the video, the mass gained by entrainment of fluid inside the diapir

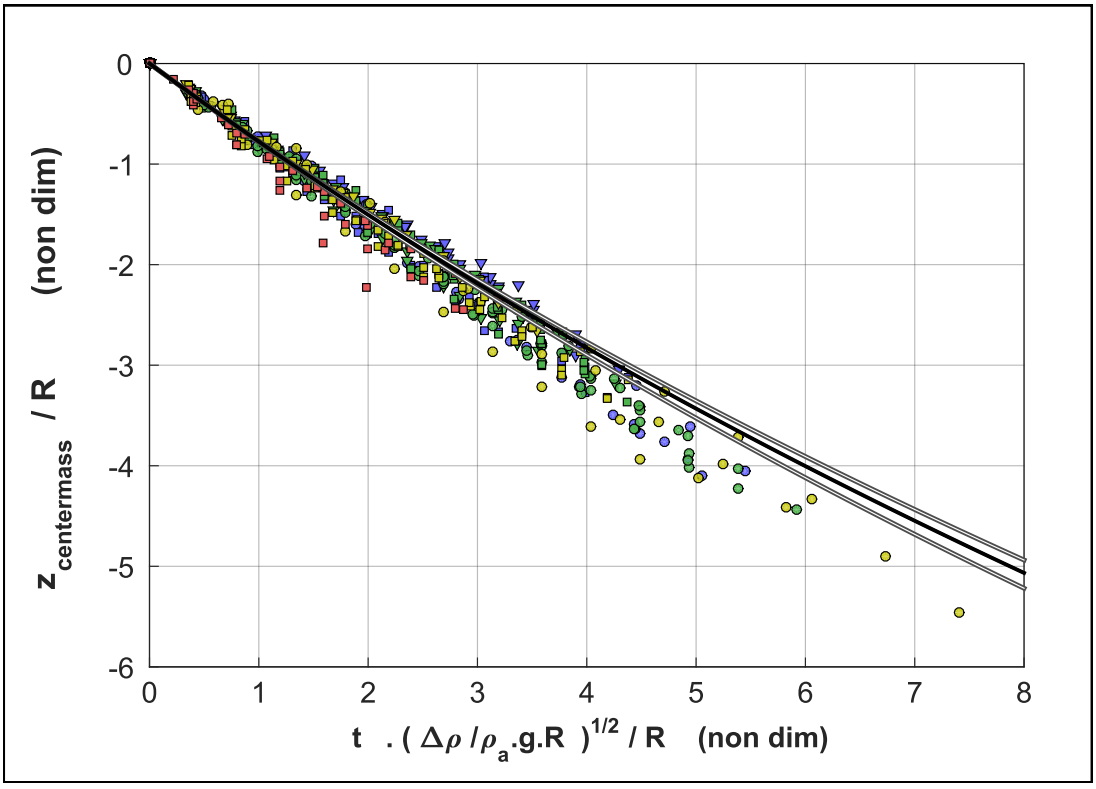

FIGURE IV.4 – Graph of the depth of the center of mass as a function of time for all experiments (Markers). Superimposed on this figure are the predictions produced by the integration of the turbulent thermal equation with a shift in measured initial radius at the beginning of the analysis compared to the actual initial radius of the diapir. The black line correspond to a shift equal to the mean measured shift and the black and white lines corresponds to a shift equal to the mean measured shift plus or minus its standard deviation.

amounts to 60 to 80 % of the apparent mass in the first frame (cf. fig. **??**). Since the momentum has to be distributed among all the mass and buoyancy corresponds to a comparatively lower acceleration as mass increases, the diapir is supposed to decelerate when entraining ambient fluid. This explains why the trajectory should be affected according to the classical Morton model shown on figure **??**.

Concerning the impulsion flux, it was computed by integrating the product of the mass flux on small elements of the contour with the local velocity in the reference frame of the laboratory. We reported on figure **??** the norm of this vector as a function of time. Although the ratio of signal over noise is around one, we can see that the impulsion flux is only slightly increasing from 0.1 to 0.2 times the buoyancy. This is a significant break from the classical turbulent thermal hypothesis which generally assumes that the impulsion flux is negligible compared to all other forces, but it is still smaller than them.

In order to see more precisely what effect can be produced by the impulsion flux, we have computed the corresponding average vector in figure **??**. As expected the momentum flux is equivalent to a downward force. It is also important to notice that the norm of this average across time is now under 0.2 time the buoyancy for the majority of the cases. Similarly, we have computed momentum flux non dimensonnalized by all the inertial terms

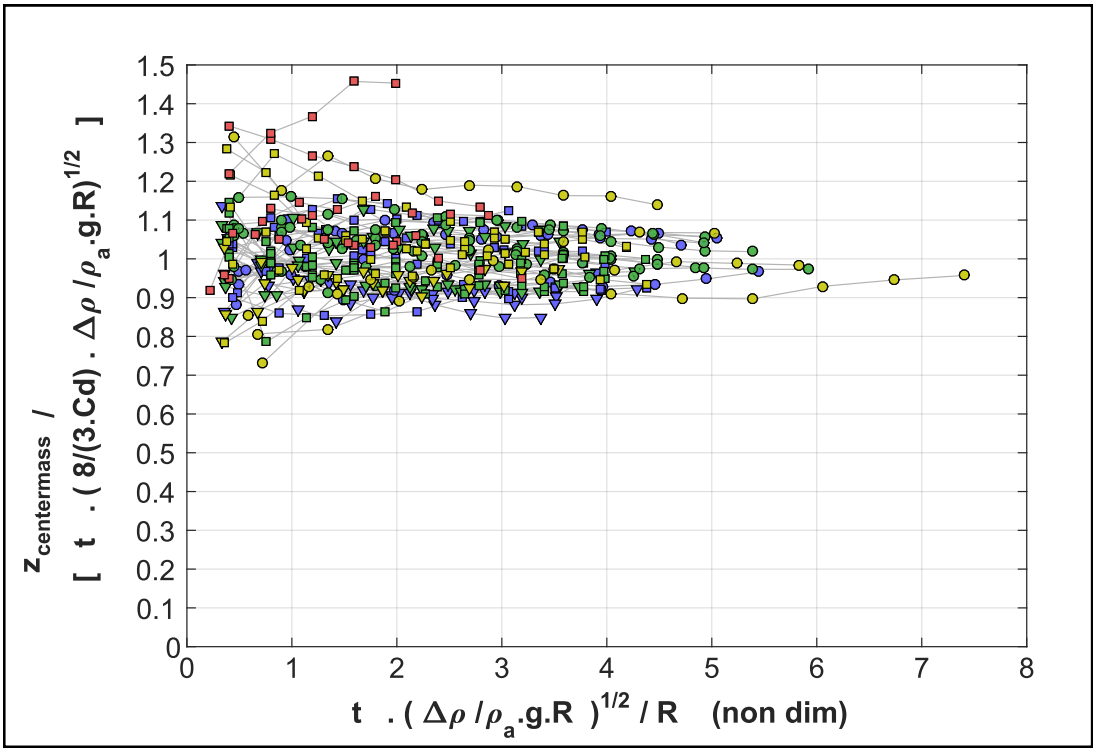

FIGURE IV.5 – Graph of the depth of the center of mass non-dimensionalized by the prediction of a constant speed as a function of time.

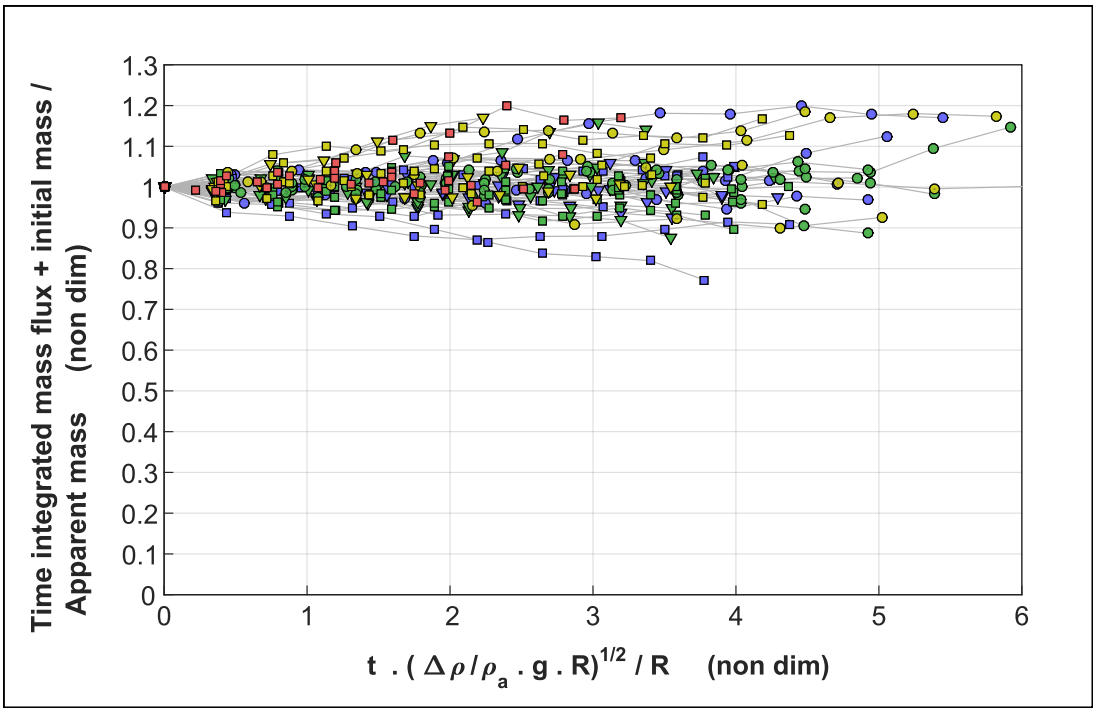

FIGURE IV.6 – Graph of the time-integrated mass added with the initial mass non-dimensionalized by the mass calculated from the apparent radius as a function of time

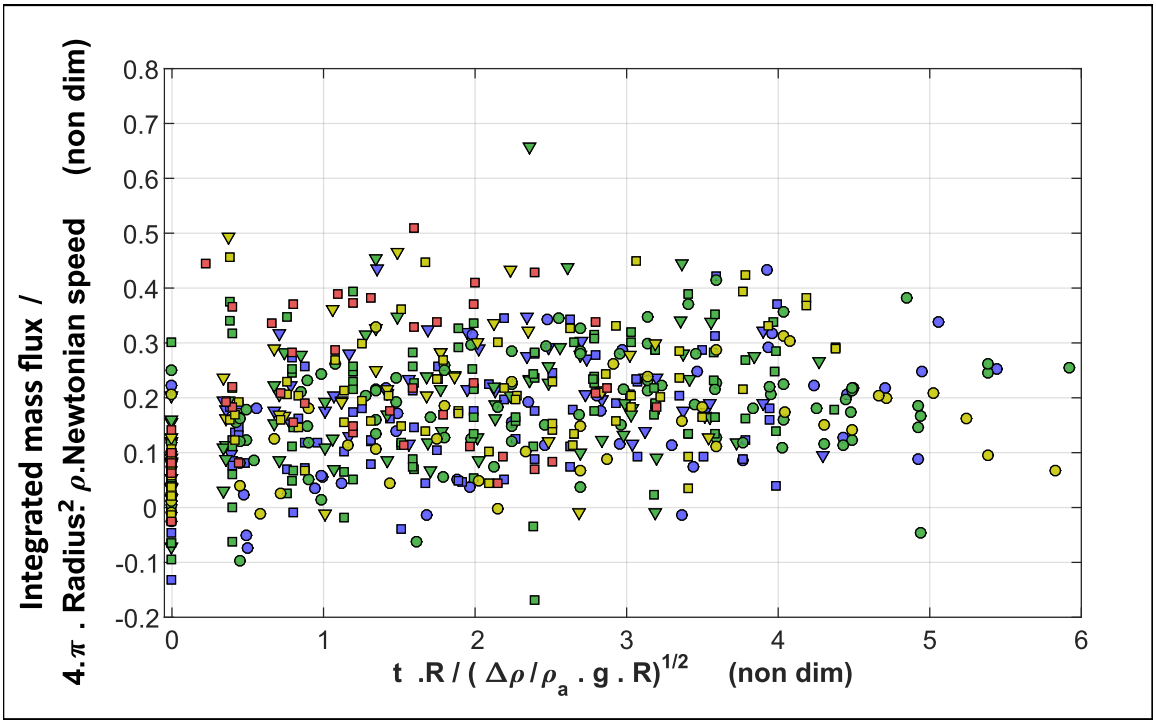

FIGURE IV.7 – Graph of the integrated mass flux non-dimensionalized by the scaling of the mass flux as assumed by the turbulent thermal theory as a function of time for all experiments.

(with the apparent radius in the first frame and $k = 0.5$, $Cd = 0.5$). The impulsion flux is close to 0.3 times the inertial terms.

This plot also shows a clear bias for the right direction. Two main explanations can be proposed for this fact ; either the breakup of the balloon induced a non-negligible rupture of symmetry that has consequences on the flow, or this bias is an artifact of the measurement method probably due to our asymmetric lighting condition. Indeed the two projectors used for the lighting of the bubble curtain were not the same. Since we did not have the chance to control for the coherence of every velocity field given by the PIV processing before computing the present results, it is possible that some zones in the images are not lit enough to produce reliable velocities. This can be supported by the fact that the subhorizontal vectors seem to be mostly related to the videos made at $R_\mu = 8$ which is incidentally the viscosity ratio where the mixture of UCON oil and water yielded the thinnest H_2 bubbles. Alternatively, if the hypothesis of a true symmetry breaking of the flow by the initial condition is true, one can expect that this symmetry breaking to have for consequence the production of an horizontal acceleration correlated to the horizontal impulsion flux. This is not the case has we will see in figure **??**. We will then favor the hypothesis that the impulsion fluxes the closest to the horizontal are wrongly computed by our image analysis procedure.

In any case, as can be seen with the histogram of the orientation of the average impulsion flux (cf **??**), the orientation is mainly pointing in the same direction as gravity. The histogram of the norm of the impulsion flux also gives a definitive comparison of its relative intensity compared to buoyancy. From this data, it is clear that the impulsion flux should not be expected to exceed a value of $0.2g$ in the interval probed during these

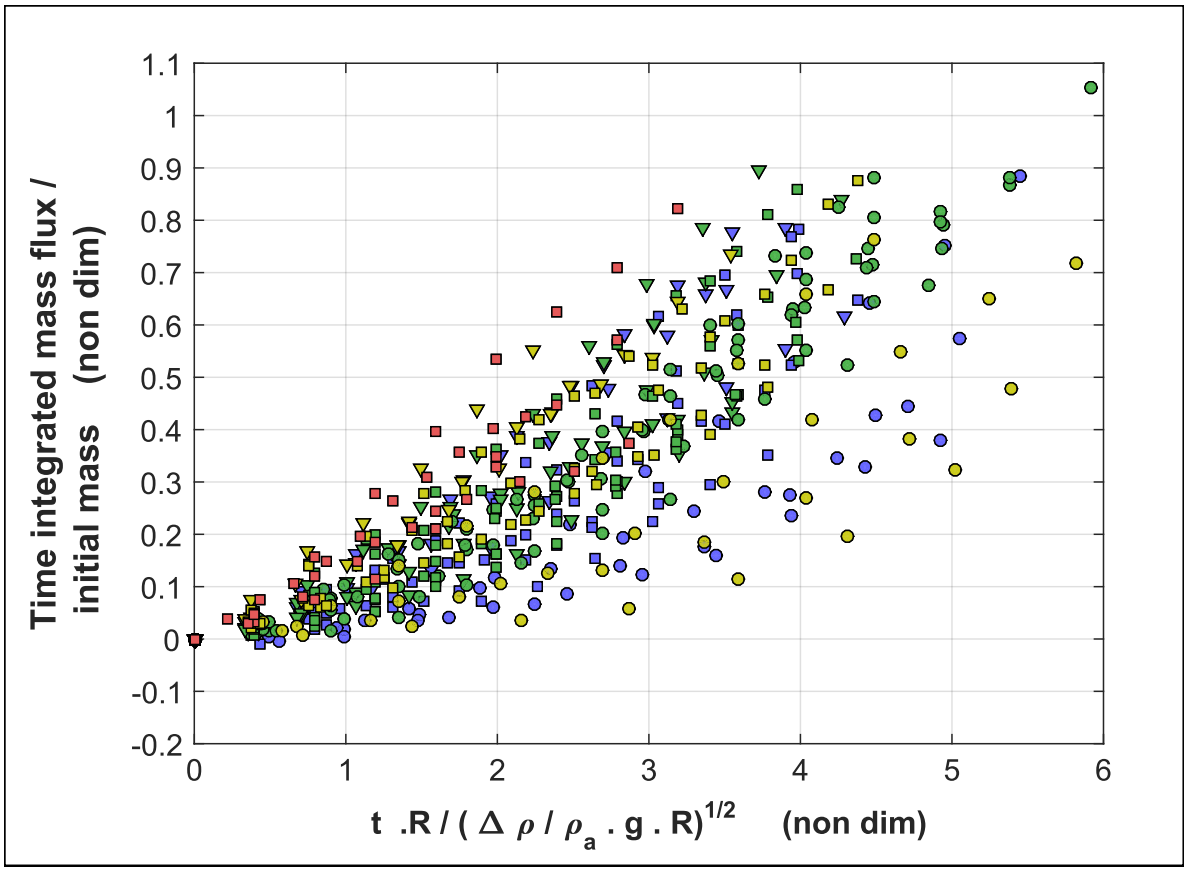

FIGURE IV.8 – Graph of the non-dimensional mass flux integrated in time as a function of time for all experiments.

experiments. In fact, its mean value is closer to $0.13g$.

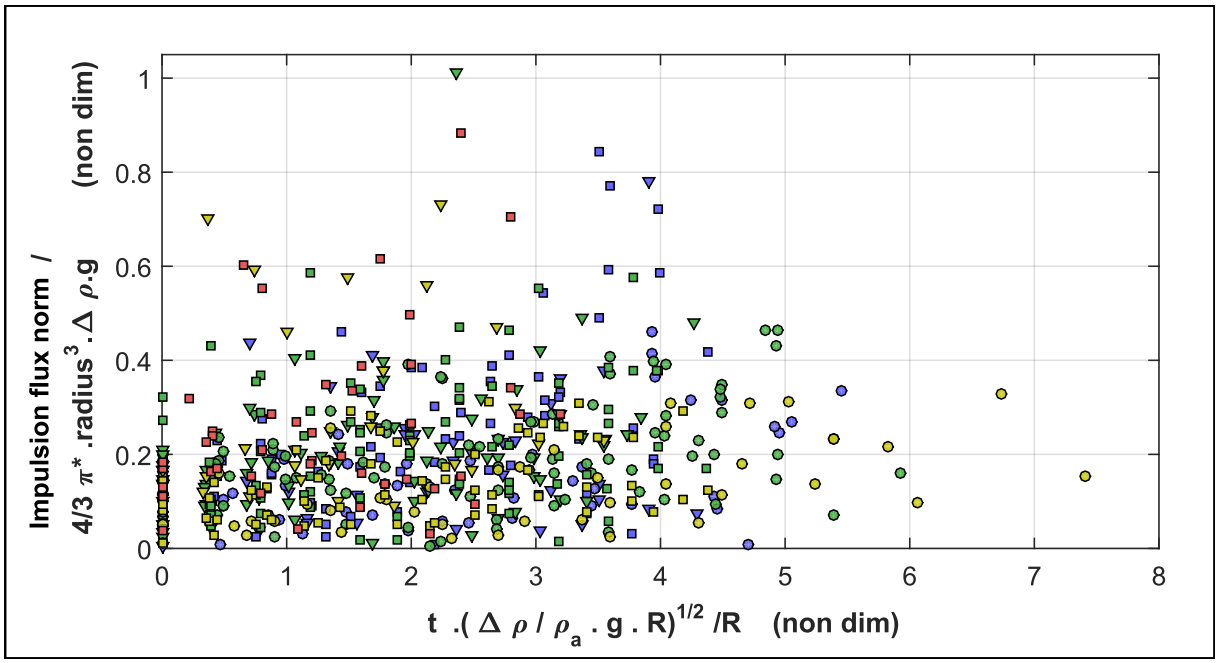

FIGURE IV.9 – Graph of the impulsion flux norm non dimensionnalized by the buoyancy of the diapir as a function of time for all experiments

This low value brings the question of closing the force balance with the buoyancy, the inertial terms included in the turbulent thermal model and the impulsion flux as we measured it

. As a first step, we have colored the experimental tracks with a criterion on the angle of the average impulse flux with respect to the gravity vector (cf. fig. **??**). Roughly splitting the data into two even groups, we cannot see a systematic trend linked to the direction of the impulsion flux. This is for us the sign that the impulse flux that are oriented in an horizontal fashion are an artifact of the measurement. More precisely, we have computed the average horizontal acceleration for each run from the depth of the center of mass (cf. fig **??**) by a three point method. The average horizontal acceleration does not seem to have any correlation with the horizontal impulsion flux. Beside, its average among all experiments has a value close to 0 contrary to the horizontal impulsion flux. Therefore we argue that the horizontal acceleration is due to random symmetry breaking caused by turbulence. Concerning the horizontal impulsion flux, we conclude that its asymmetry is due to our lighting method on top of random fluctuations that may be caused by the lighting or the turbulence.

At this point the main problem of closing the vertical force balance stays unsolved. Two hypotheses were explored. The first one is based on an assumption that our method underestimates the impulsion flux. Therefore, we have plotted the vertical acceleration as a function of the impulsion to see if the vertical acceleration can be a product of the sole vertical impulse flux. The other hypothesis is that the balance force can be closed by just including the impulse flux in addition to the buoyancy and the inertial forces. Thus we have plotted the vertical acceleration as a function of the resulting force in order to see if any small observable acceleration can be linked to it. As can be seen on the bottom panels

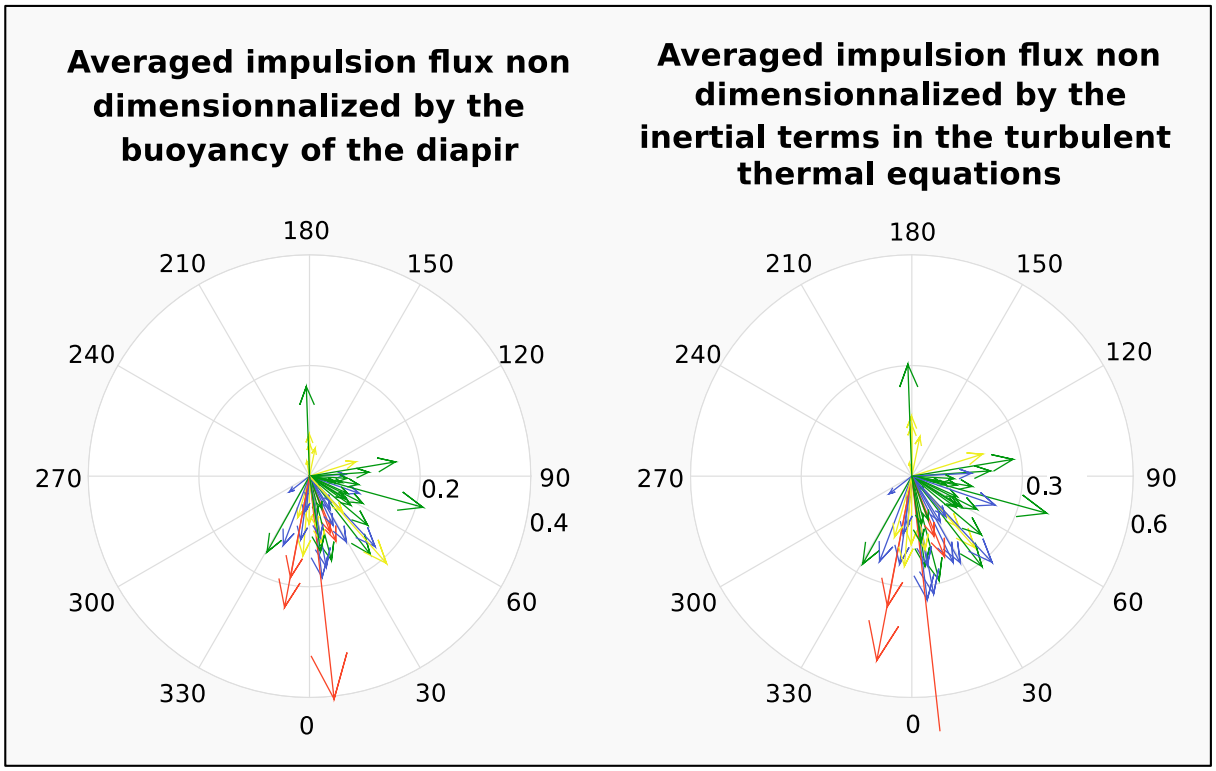

FIGURE IV.10 – Polar graph of the time-averaged impulsion flux for all experimental runs. Left panel : averaged impulsion flux non-dimensionalized by the buoyancy of the diapir. Right panel : averaged impulsion flux non-dimensionalized by the inertial forces arising from the turbulent thermal equations.

on figure **??**, neither of the hypotheses has credible support from the data. Nevertheless, it is important to notice that the balance of forces has mostly values below $-2m.s^{-2}$ while the vertical acceleration have mostly values above $-2m.s^{-2}$. Despite the level of noise present in our data, we believe this distribution indicates a missing force in the force balance beside the impulsion flux we have measured.

The problem this missing force (or unexplained acceleration) is posing relates as much to its magnitude as to its time dependency. We have shown that the impulse flux could not match in magnitude the unexplained part of the acceleration. Had it been the case, an acceleration close to zero throughout the whole depth of these experiments would have needed the impulse flux to match the evolution in time of the inertial forces that scale with r^2 (the speed being constant). Alternatively, if the impulse flux as we measure it is correct, the balance can still be reached if the friction experienced by the diapir is not entirely parametrized by our current expression of the inertial forces where all coefficients are constant. More precisely, since this parametrization makes a term growing with r^2 , the missing part would have to be decreasing in the same manner.

An elephant in the room must be addressed here. It is likely that a redefinition of the surface of control needed for the turbulent thermal or vortex ring theories with the streamlines would lead to a more compatible acceleration record. Putting aside the self-consistency of this approach, it is of limited interest for us as the main benefit of the turbulent thermal theory is to assess the dilution in a simple way. Redefining the surface of

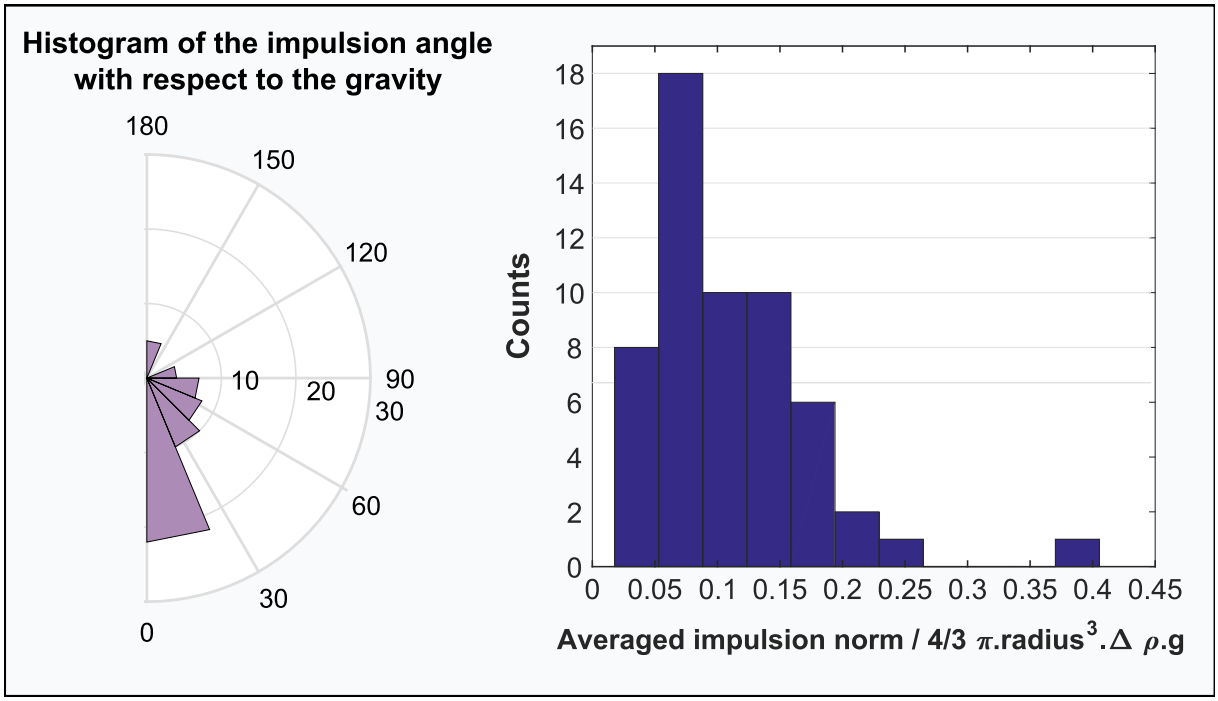

FIGURE IV.11 – Histograms of the impulsion flux. Left panel : polar histogram of the angle with respect to the gravity. Right panel : histogram of the impulsion flux norm non-dimensionalized by the buoyancy of the diapir.

control more broadly would undermine this benefit. Therefore we introduce an additional complexity to the balance of forces that is in our view relevant for the fall of the diapir as observed in the experimental video. We propose that the diapir is submitted to a vorticity dependent drag. Starting from rest with no vorticity and ending up as a vortex ring after the breakup, the diapir would experience a decreasing drag coefficient as it spins up in the phase of its fall following its initial acceleration and prior to its breakup.

Several arguments support such a scenario. Time dependent drag forces are typical of the buildup of a viscous layer during acceleration (**?**), or more generally of the development of unsteadiness of the trajectory of the bubble (**?**). However, since ambient fluid is entrained from the rear of the diapir, viscous layers are most likely entirely entrained into the diapir rendering the loss of momentum in these layers null. We can see this by comparing the volume flux that is entrained v_1 compared to the volume flux of the viscous boundary layers v_2 :

$$\frac{dv_1}{dt} = 4\pi r^2 \,.\, \alpha v \quad ; \quad \frac{dv_2}{dt} = 2\pi r \,.\, \sqrt{\frac{\mu_a r}{\rho_a v}} \,.\, v \tag{IV.1}$$

Hence the ratio of the two flux is approximately :

$$\frac{\frac{dv_1}{dt}}{\frac{dv_2}{dt}} = 2\alpha . Re^{\frac{1}{2}} \tag{IV.2}$$

The volume entrained being larger than the viscous boundary layers when $Re > 10$, those are probably entrained as they form in our experiments. In addition, we do not find any clear dependence of the trajectory of the diapir on the Reynolds number prior

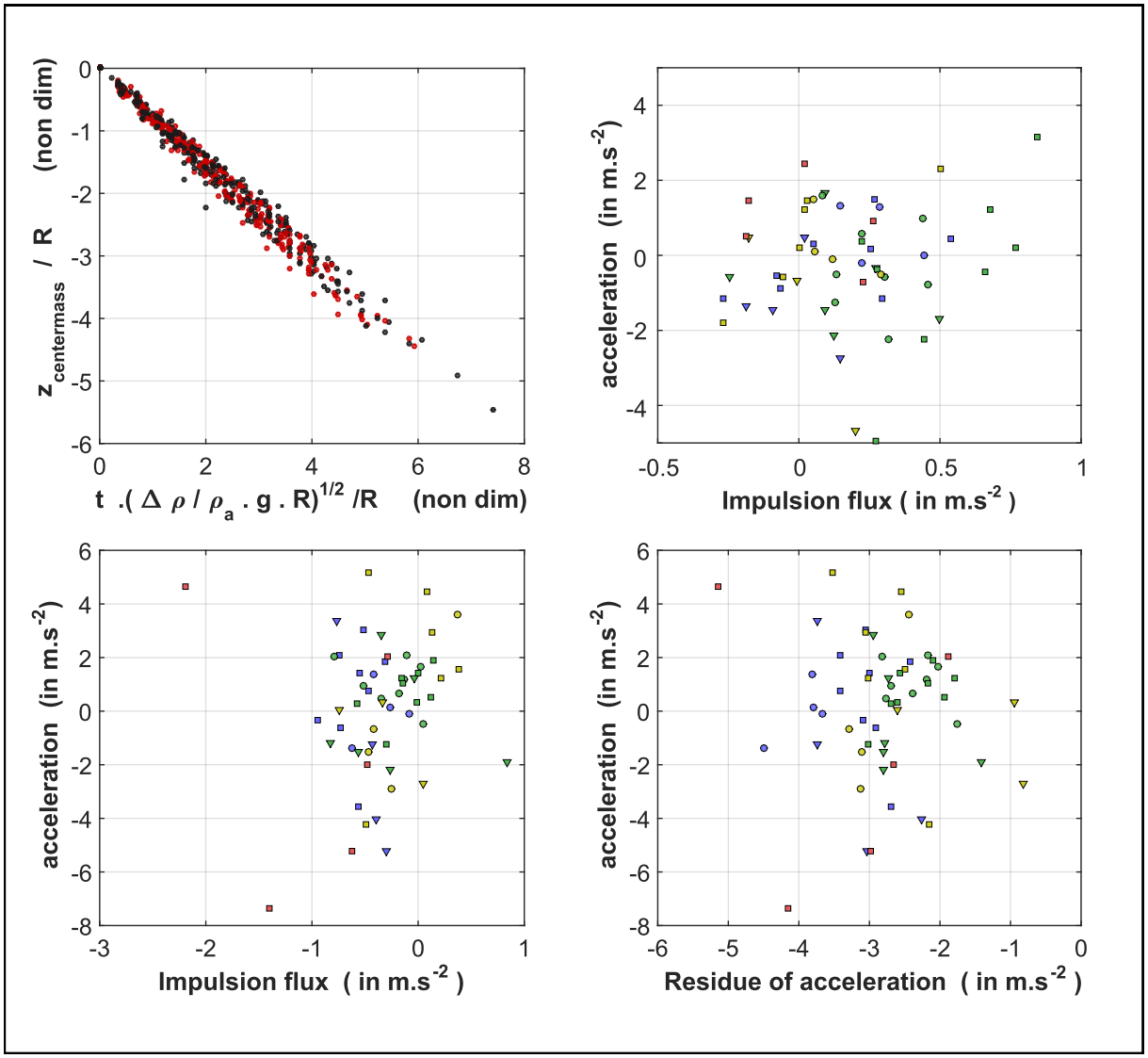

FIGURE IV.12 – Top left panel : depth of the center of mass as a function of time colored according to the angle of the averaged impulsion flux with respect to gravity. In red are the experiments with an angle superior to 40 degrees and in black the experiments with an angle inferior to 40 degrees. Top right panel : horizontal mean acceleration as a function of the horizontal mean impulsion flux. Bottom left panel : vertical mean acceleration as a function of the mean vertical impulsion flux. Bottom right panel : vertical mean acceleration as a function of the mean acceleration due to the sum of the buoyancy, inertial term from the turbulent thermal and impulsion flux.

to breakup. Therefore we do not favor a mechanism involving viscosity as the source of the time dependence since any transfer of impulsion to the boundary layer is not a loss. On another note, we can also consider surface tension effects as a source for this force, as entraining fluid inside the diapir of liquid metal creates surface. This implies to work against the capillary force and would create an over pressure behind the diapir. But since the ratio of the inertial forces over the capillary pressure is the Weber number, this force would be negligible or at least fading as we increase the initial radius. In consequence, the

best candidate is a still an undetermined inertial force.

The inertia of the buoyant fluid and the inertia of the ambient fluid are generally considered coupled, but they can be coupled in at least two different ways. For overdamped droplets, the outside flow drives the inside flow which undergoes viscous dissipation. As a result of this driving, similar boundary conditions can be applied on the surface of such drops as on rigid objects. The droplets simply have a non zero slip velocity at their surface. Thus, similar scalings for the drag coefficient, particularly at high Re can be recovered for drops (**?**, **?**). For classical vortex rings of miscible fluids, no drag is usually needed in order to explain their trajectory (**?**). Generally, the formalism used in this case boils down to the Biot-Savart induction of velocity of the vortex on itself (**?**) ; in this case the outside flow does not need to drive the inside flow. The other way to see it would be that when there is an annular vorticity, it is necessarily accompanied by an annular region of low pressure. In the presence of a velocity in the far field, this low pressure allows in fact to bend the streamlines and effectively produces a region where purely irrotational inviscid flow solutions can be applied when Re becomes large enough. The limit between the region of low pressure/vorticity would naturally be our surface of control (**?**). As a natural consequence of the irrotational potential flow outside and at the boundary of the region of interest, the aerodynamical drag force is essentially zero (**?**, **?**). Viewing the effect of rotation as primarily affecting the surrounding pressure is interesting for two reasons. First, it allows to conceive its effect even when a strong turbulence is superimposed on top of the annular vorticity, where obvious cautions can be invoked in using the Biot-Savart induction equation. What's more, this is also a way to follow its effect when going from a regime dominated by the rotation where Biot-Savart can be used in a straight-forward manner to a regime where organized rotation is fading in front of turbulence. To summarize, we think that as the diapir is spinning up, the pressure field in the proximity of its boundary shifts from a vertical dipole to a more symmetric distribution dominated by a torus of low pressure (as represented in fig. **??**).

From now on, let us assume that the integral of the dynamic pressure over the surface of control scales as the inertia of the outside flow minus the part that is regularized by the inertia of the flow inside the fluid particle. Thus we hypothesize that the drag force Fd that results from the pressure integration on the surface of control (which is the dominant term of the drag force in our regime) can be expressed as :

$$Fd \sim \left(\rho_a \,.\, v^2 - \rho \,.\, \frac{K^2}{r^2}\right) \,.\, \pi r^2 \tag{IV.3}$$

Here ρ is the mean density of the fluid particle. In consequence, the drag coefficient writes :

$$c_d = c_{dK}\left(1 - \frac{\rho.K^2}{\rho_a.v^2.r^2}\right) \tag{IV.4}$$

cd_k is a coefficient of the order of one. This expression has the property to make a bridge from an initially irrotational fluid particle (for example a drop of water falling in the air) to a vortex ring where the circulation is $K \simeq v.r$.

In addition, one also has to address how vorticity can be re-introduced in a reasoning aiming at encompassing the irrotationnal potential limit. Indeed, when we consider a fluid particle moving in an ambient fluid, both inviscid and homogeneous in density, no

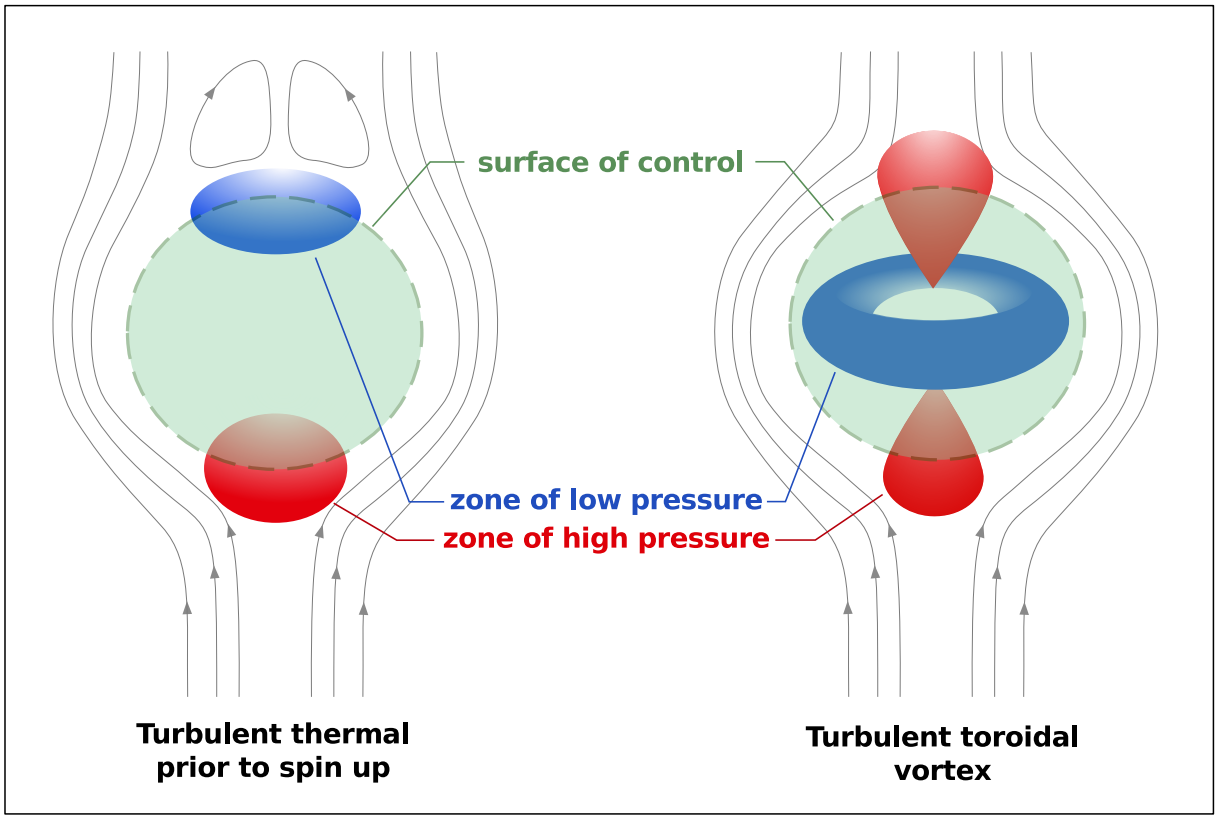

FIGURE IV.13 – Schematic of the hypothetical pressure field structure in and around the turbulent thermal before and after the spin up phase.

vorticity can be produced. However, viscosity can play an important role at small scale without changing the overall balance of forces at large scale. In our case, the strong shear near the interface creates instabilities that entrain the ambient fluid inside and generally intermingle the two fluids. This process produces smaller and smaller scales up to a point where the local velocity gradients are regularized by viscosity. In addition, such zones where fluids are effectively coupled by viscosity present inhomogeneity. This implies that there are zones of strong density gradient where baroclinic production of vorticity is most likely to occur.

The idea of the inherent baroclinic character of the initial condition of the miscible turbulent thermal and the inevitable production of vorticity was put forward early in the study of the subject (**?**, **?**). However, the fact that the ambient fluid is entrained at the rear of the diapir because of the non penetration of the liquid metal film sets a length scale at which the fluid is entrained which is typically a fraction of the radius. Assuming that the vorticity arises simply from the mixing of the ambient fluid with the diapir, this length scale sets a scale for the azimuthal angular momentum that is gained by entrainment equal to $v.\frac{r}{2}$. We also assume that the relevant part of the vorticity is the azimuthal one for reasons of symmetry. As this direction is stretched, it is more convenient to reason on the circulation around a contour following the surface of control and reconnecting via the axis of symmetry. The fourth turbulent thermal equation is then the conservation of angular momentum for a fluid containing important density inhomogeneities :

$$\frac{d\left[\rho.\frac{4}{3}\pi r^3.K\right]}{dt} \;=\; 4\pi r^2.\rho_a.\alpha|v|\;.\;v.\frac{r}{2} \tag{IV.5}$$

The complete system of equations for the evolution of two phases turbulent thermal then becomes :

$$\begin{cases} \dfrac{d}{dt}\left[\rho.\dfrac{4}{3}\pi\ r^3\right] & = 4\pi r^2.\ \rho_a.\alpha|v| \\ \dfrac{d}{dt}\left[\ (\rho-\rho_a).\dfrac{4}{3}\pi\ r^3\right] & = 0 \\ \dfrac{d}{dt}\left[\rho.\dfrac{4}{3}\pi r^3.K\right] & = 2\pi r^3.\rho_a.\alpha v|v| \\ \dfrac{d}{dt}\left[\ \left(\rho.\dfrac{4}{3}\pi\ r^3+\rho_a.k.\dfrac{4}{3}\pi r^3\right).v\ \right] & = (\rho-\rho_a).\frac{4}{3}\pi\ r^3.g-c_{dK}\left(1\ -\ \frac{\rho.K^2}{\rho_a.v^2.r^2}\right).\pi r^2.\frac{1}{2}\rho_a v|v| \end{cases} \tag{IV.6}$$

To test the abilities of this model compared to the classical turbulent thermal, we have performed integration in time similar to the one shown in chapter **??**. The fit provided by our toroidal vortex model is slightly better than the turbulent thermal one. The decrease in speed is indeed less steep and the maximum speed near the start is lower but the results are not entirely satisfactory (cf. purple line in fig. **??** and **??**). We have also tried to treat the coefficient of added mass k with the same dependence as the drag coefficient cd to take into account the fact that a modification in the geometry of the pressure field could also affect the coefficient of added mass (otherwise constrained by geometry). This was not sufficient to bridge the gap between data and theory. However, the left difference might indeed be explained by a non-trivial distribution of mass inside the region occupied by the liquid metal evolving as it falls. In the absence of data to support this assertion we think our interpretations must stop here.

Concerning the result of the theory by itself, the small effect it has can be seen as the principal reason why this effect has not been investigated previously in the literature on the turbulent thermal. This is reinforced by the fact that miscible thermals undergo entrainment on all sides. The corresponding typical length scale for the angular momentum related to the entrained mass would then be smaller, hence a smaller resulting circulation. In addition, as can be seen when developing the equation of evolution of angular momentum, this effect is bound to saturate :

$$\frac{dK}{dt} \;=\; \frac{3}{2}\frac{\rho_a}{\rho}\alpha v|v| \;-\; K\frac{\alpha}{3}.\frac{|v|}{r} \tag{IV.7}$$

The time scale of spin up being initially proportional to $\tilde{\rho}$, it is indeed no surprise that this effect can be overlooked. It can easily be mixed with the initial phase of acceleration/reorganization that a thermal initially goes through, during which it is still unclear that proper entrainment has begun. In our case, the very high $\tilde{\rho}$ is barely enough to provoke a modification on the same level as the experimental variability. It is also

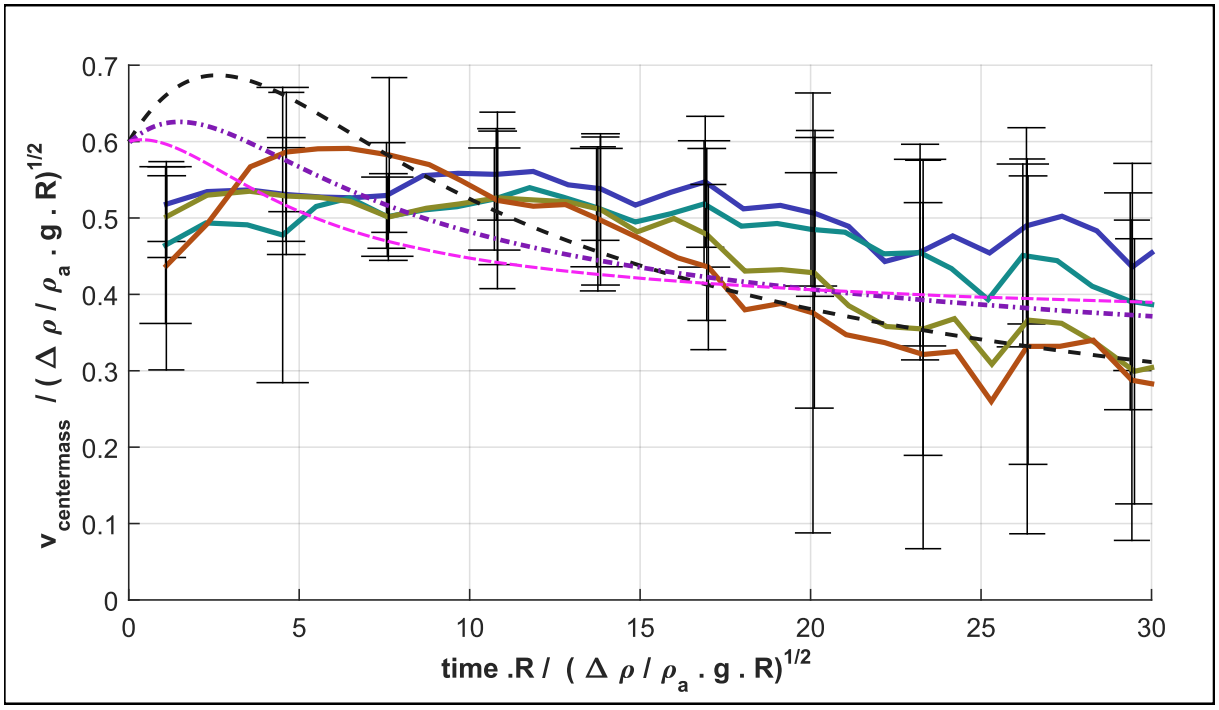

FIGURE IV.14 – Graph of the superimposed non dimensionnal velocities for all experiments made with the first setup. The predictions from the classical turbulent thermal model (dashed black line) and the thermal in spin up phase for similar parameters are superimposed (colored lines). In purple dashed dotted line is the solution for the thermal in spin up phase is computed with only vorticity dependent drag coefficient. In pink dashed line is the solution for the thermal in spin up phase is computed with a vorticity dependent drag coefficient and coefficient of added mass.

interesting to compare our experiment with the one of M. Landeau and colleagues (**?**). In their experiments, the density ratio $\tilde{\rho}$ is around 2 and they do not find any sensible departure from the turbulent thermal model. However an interesting phenomenon is observed which seems related to the rotation stored in the azimuthal direction. They noticed that the overall aspect of the diapir (toroidal vortex or turbulent blob) is linked to the initial position with respect to the free surface where the buoyant fluid is released. The diapir has an aspect closer to a toroidal vortex as it is released close to the surface. They also linked the coefficient of entrainment to the shalow release of the buoyant fluid, α being smaller when the buoyant fluid is released close to the surface. The entrainment coefficient for a buoyant toroidal vortex is indeed smaller (**?**) than for a classical thermal. In our view, the vorticity created by their release mechanism in addition to the finite depth of the initial position is creating an important vorticity that is able to bypass a potential spinup phase. In consequence, the large vorticity affects the entrainment coefficient without necessarily affecting the large scale behavior of the diapir because in that case the vorticity produced is small compared to the already existing one and therefore stays almost constant (cf chapter **??**).

Finally, it is important to acknowledge that previous experiments by Yang and Yang in 1989 have used somewhat successfully the turbulent thermal model in the case of similar and higher $\tilde{\rho}$ (**?**). However, their drops of liquid metal were accelerated by a shock wave,

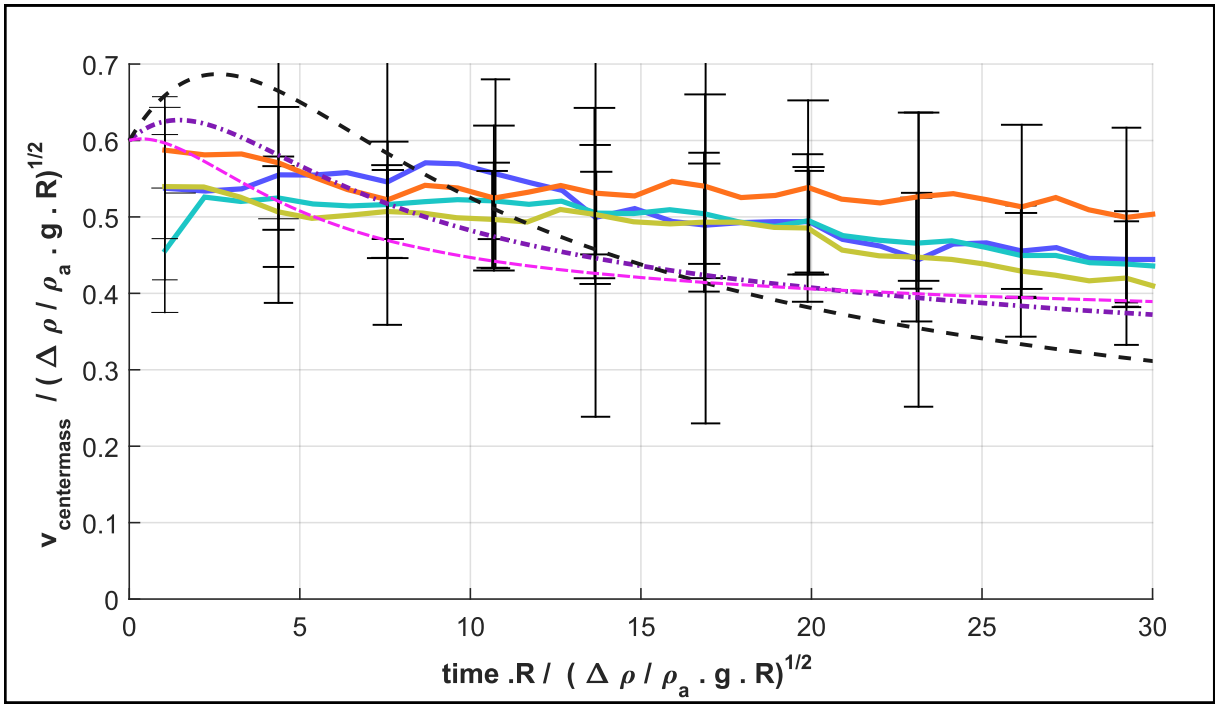

FIGURE IV.15 – Graph of the superimposed non dimensionnal velocities for all experiments made with the second setup. The predictions from the classical turbulent thermal model (dashed black line) and the thermal in spin up phase for similar parameters are superimposed (colored lines). In purple dashed dotted line is the solution for the thermal in spin up phase is computed with only vorticity dependent drag coefficient. In pink dashed line is the solution for the thermal in spin up phase is computed with a vorticity dependent drag coefficient and coefficient of added mass.

rendering the inertial effects dominant compared to buoyant effects.

In conclusion, we have constrained the value of the expansion of the diapir and linked it to the measured mass entrained. We also measured a non-negligible impulse flux associated with the mass entrained in the region occupied by the diapir. This constitutes a small break from the turbulent thermal equations that could not explain the discrepancies in the measured trajectories of the diapirs. These discrepancies could not be explained solely by a circulation dependent coefficient of drag either. Additional measurements investigating the repartition of the liquid metal and the difference of pressure between the front and the rear of the diapir may be needed to fully understand its trajectory prior to breakup.

Chapitre V

The divided state

A Settling speed of the droplets

The measures of average settling velocities by the modified PTV program were done in a window extending from a depth of 1.25 m to 1.75 m below the surface of the mixture water/UCON oil. This represents a depth of fall of $64R$ to $90R$ for the smallest diapirs and $29R$ to $41R$ for the largest. In first approximation, we assumed that the drops transition from collective to individual settling around the time when expansion of the cloud of droplets becomes viscosity dependent. From figure **??**, **??**, **??** and **??** we know that this transition happens somewhere between $20R$ and $30R$. The measures shown here should then be relevant for the "rain" part of the fall of the liquid iron in the magma ocean where individual behavior of the droplets are expected.

The raw measures for $R_\mu = 700$ are presented in figure **??**. The first issue encountered in interpreting these datas can already be seen for the integrated radii (bottom graph). This is the radius obtained by integrating the true shape of the droplets assuming axisymmetry. While initially supposed to represent the most faithfully the volume of each droplet, it maximizes the ratio noise/signal. In the following, we will then compute a compound radius that approximate well the size of the droplet while having a low noise/signal ratio. It is the spherical radius of the volume of the ellipsoid defined by the two axes of each droplets. Unfortunately, the program we have used did not record the height of the drops. Hence, the ellipsoidal radius will be computed with the following formula :

$$r_{ell} \;=\; r_{crossflow}^{\frac{1}{3}} \cdot r_{spherical}^{\frac{2}{3}} \tag{V.1}$$

$r_{crossflow}$ is half the horizontal extent of the droplet and $r_{spherical}$ is the radius of the circle that has the same area as the one projected by the drop. For an ellipsoidal drop, $r_{spherical}$ is the square root of the cross flow radius times the height of the drop. Therefore these exponents are taken so as to approximately compute the volume of an ellipsoid that has the cross flow radius as two of its semi-axis and the height of the drop as the last one.

An important characteristic of these data is the tendency for the drops to have a rather precise trend for the lowest bound of their velocity as a function of the radius. The highest bound however seem to be approximately constant. This is most likely due to the fact that this higher bound is in fact set by the fastest drops (i.e. the biggest ones). From observation it is indeed not rare to see a small drop trailing behind a bigger one, sucked by

the relatively lower pressure in the wake. This suggests an effect of random encounters and short range interaction of small groups of drops in opposition to variations of speed due to the average effect produced by surrounding drops (hindered settling). After breakup, the radius of the cloud is generally close to 3 times the initial radius of the liquid metal mass (cf. fig. **??**, **??**, **??** and **??**). This implies a volume fraction of ambient fluid ϕ inside the region occupied by the liquid metal equal to 0.963 and larger as the cloud of droplets gets more and more diluted. For such high volume fraction of the ambient fluid, the hindered settling of the drops by the others is easily parametrized with this very variable. The ratio of the settling velocity of a particle in an ambient fluid that is laden with the same type of particles over its settling velocity taken alone in an infinite domain R_U (**?**, **?**,**?**) is written as follows :

$$R_U \;=\; \phi^q \tag{V.2}$$

q is an exponent containing further complexities that can depend on the Reynolds number but has a value generally lower than 5 (**?**, **?**,**?**). This implies that the hindering effect of an homogeneous spread of particles should produce an average value of R_U never lower than 0.82. This general hindering effect cannot explain the large variations of settling velocities.

The computation of the actual drag coefficient of the drop Cd_d as a function of their Reynolds number Re_d allows to be more precise on the influence of the drops on each other settling speeds (cf. fig. **??**). A large amount of drops are distributed near the main curve of the settling speed of drops falling alone in an infinite media at moderate Reynolds (**?**). At Reynolds larger than 10^2, the drops stay in between this curve and the limit drag coefficient calculated for drops with a spherical cap shape at asymptotically large Re (**?**), coherent with the fact that drops are for this limit oblate spheroids, in between a sphere and a spheroidal cap.

A lot of drops can be found below the above mentioned relationship. They are the ones with a higher speed than their free fall would normally imply. It happens primary to small drops, especially for the 3 lowest viscosity ratios where the drops have moderate Reynolds number. This is coherent with our interpretation for these high speeds in this range of Re : in the wake of big droplets, inertial effects produce a gradient of pressure pulling smaller drops in the wake while the turbulence is nonexistent or not strong enough to produce fluctuations that would free them from this force.

Concerning the droplets having a drag coefficient larger than expected, resuspension by the residual turbulence can explain the spread. Alternatively, one could assume that these droplets have their velocities correctly measured but have their radius overestimated by superposition and/or limitation of resolution.

For an easier read of the plot $Cd = f(Re)$, it is useful to consider particular characteristics that help to discriminate between the different effects that drops are submitted to. First are the constant velocity characteristics, which have the following equation :

$$Cd \;=\; Re \cdot \frac{8}{3}\frac{\rho_a^2 U^3}{\mu_a \Delta\rho g} \qquad \Leftrightarrow \qquad Cd \;=\; Re \cdot \frac{Mo}{Ca^3} \tag{V.3}$$

If one supposes that the speed of the drop is correctly measured but that its radius is overestimated because of resolution, intersecting these characteristics with the actual physical curve $Cd = f(Re)$ can be used to retrieve the real radius. For most of these drops,

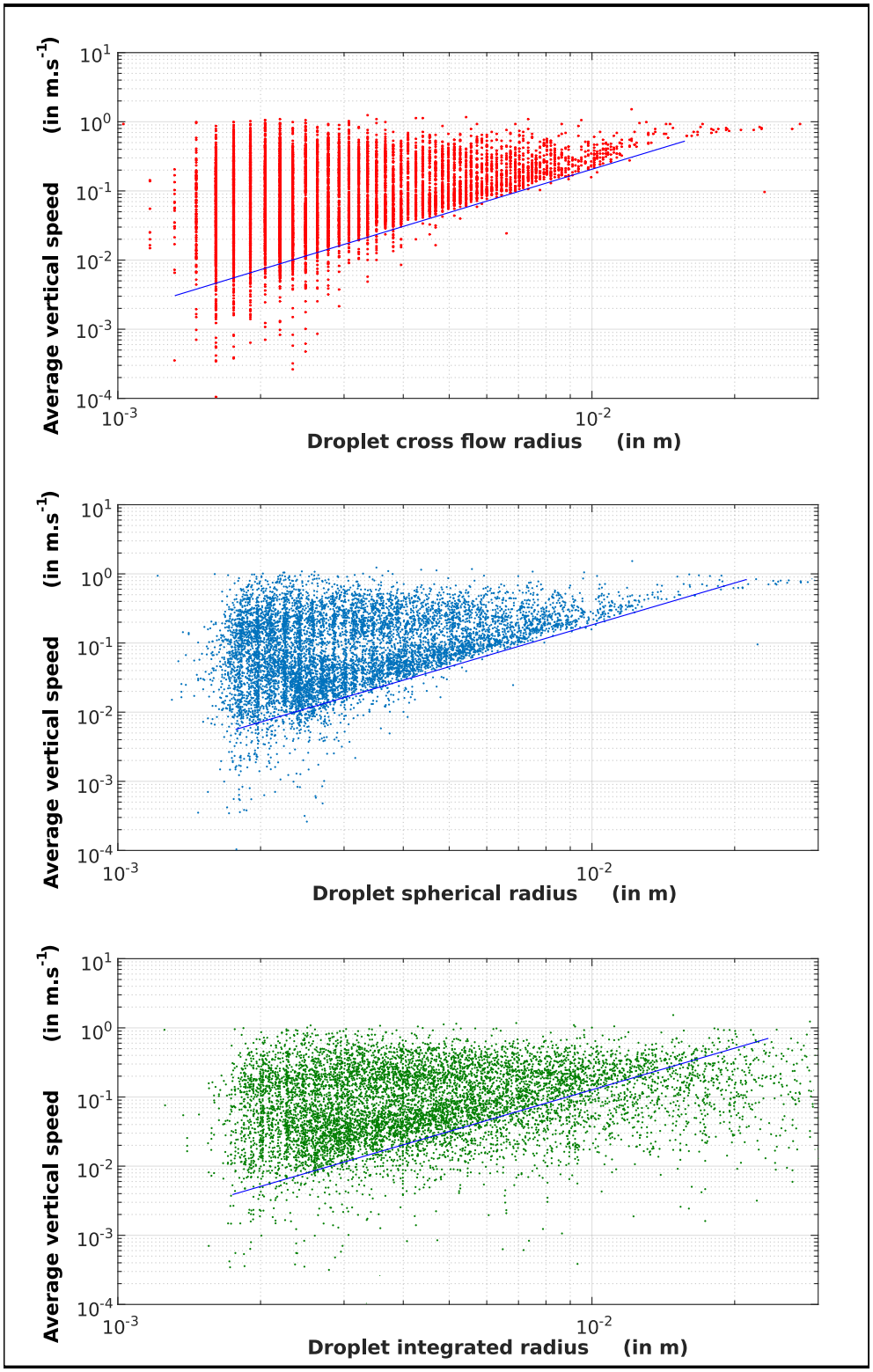

FIGURE V.1 – Graph of the average speed of the droplets as a function of their radius for the cross flow radius (top panel), for the spherical equivalent radius (middle panel) and for the integrated radius (bottom panel). The blue line represents the Stokes scaling for terminal velocity.

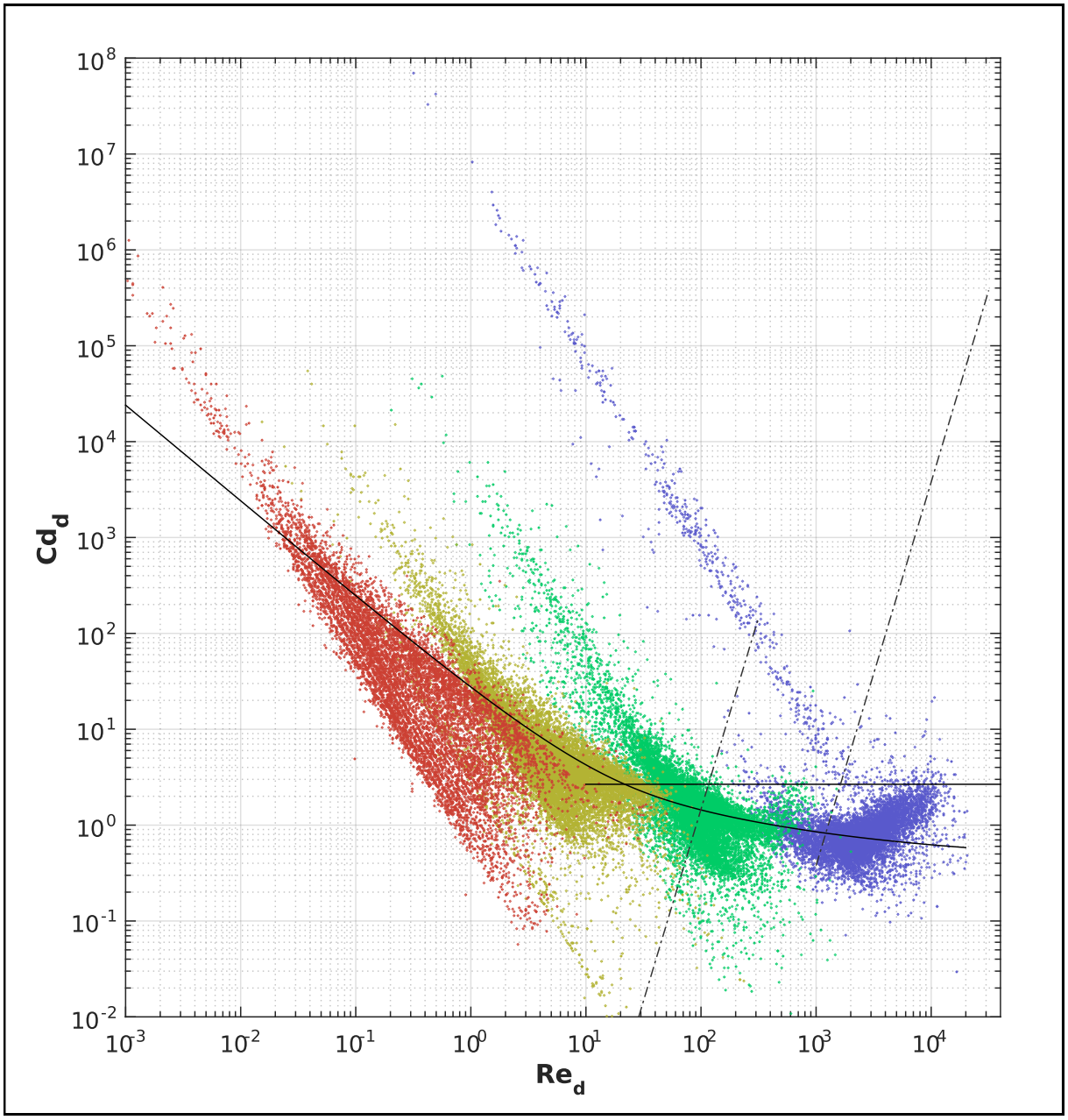

FIGURE V.2 – Graph of the drag coefficient Cd_d as a function of the droplet Reynolds number Re_d for all ratios of viscosity. The solid black curve is the relationship given by **?**. The horizontal solid black line is the asymptotic value of Cd for spherical caps given by **?**. The dash and dotted lines are the characteristics given by the condition $Cd = Re^4 \cdot \frac{8}{3} Mo$ for $R_\mu = 0.4$ and $R_\mu = 8$.

this would correspond to a radius much smaller than the measurement errors can produce, except for the smallest droplets for which such errors are possible. We conclude then that these high drag coefficients for small drops are mostly due to re-suspension.

However, for $R_\mu = 8$ and $R_\mu = 0.4$, a very wide excursion is noticeable. These anomalies have a slope of -2. It is the same slope as the constant radii characteristics :

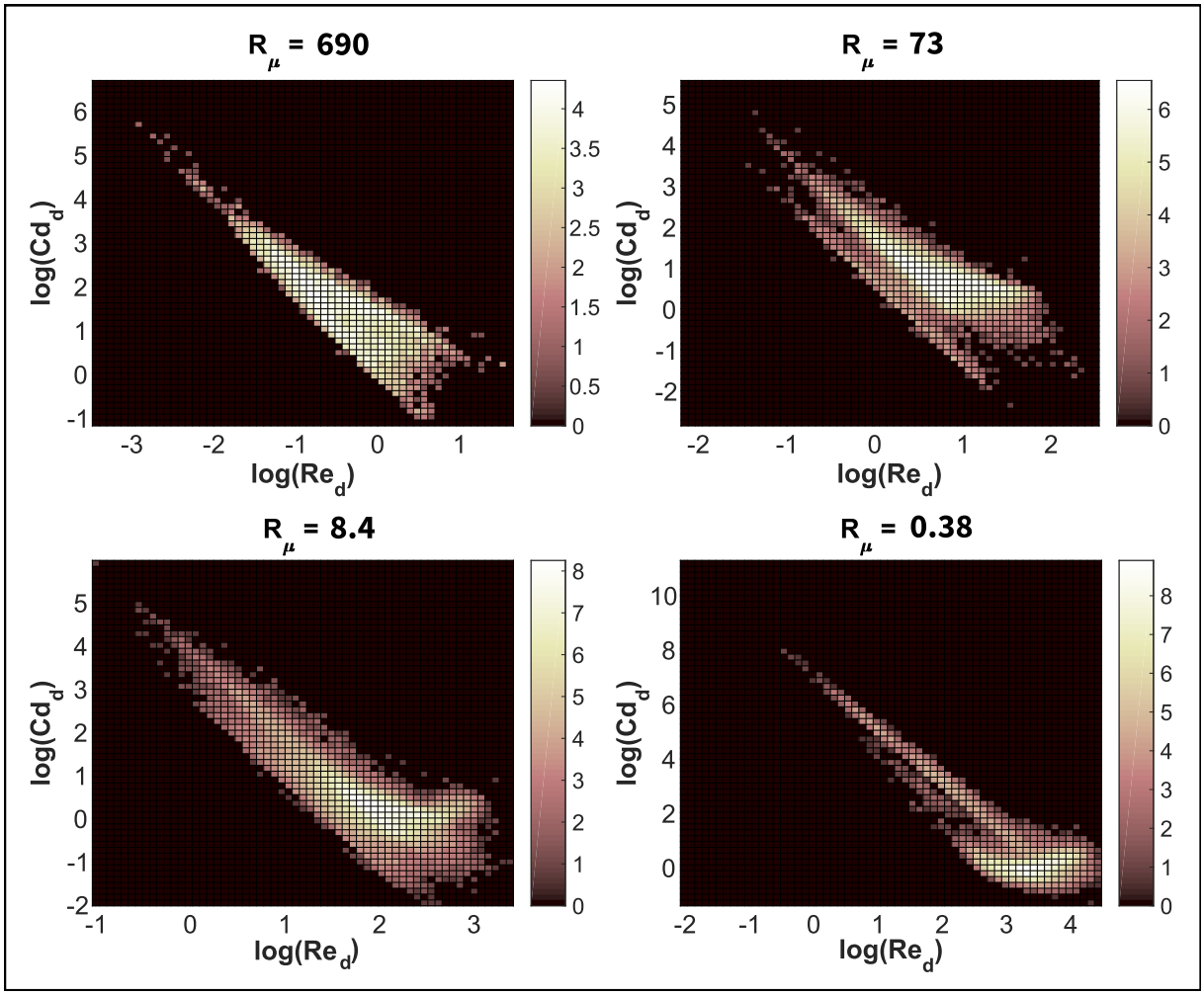

FIGURE V.3 – 2D histograms of the logarithm of the drag coefficient and of the logarithm of the Reynolds number plotted in a color scale set on the logarithm of the number of occurrences.

$$Cd \;=\; Re^{-2} \cdot \frac{8}{3} \frac{\Delta \rho g R^3 \rho_a}{\mu_a} \qquad \Leftrightarrow \qquad Cd \;=\; Re^{-2} \cdot Ar \tag{V.4}$$

Ar here is the dimensionless number known as the Archimedes number. Therefore these streaks actually corresponds to a narrow band in terms of radius. They contain events that have a characteristic radius but can also have a wide range of Cd. In our experiment, antibubbles (**?**, **?**, **?**) of galinstan are naturally created at around the same time as drops (cf. fig. **??**). With their mean density very close to the density of the ambient fluid, they settle down at a very low speed, often lower than the smallest drops. Hence they would appear on this plot with very high drag coefficient, because of the assumption of a density equal to ρ_m. Despite their high Cd, they are unlikely to be the ones figured on the streak since they seem to be rather distributed in size, with a mean radius generally higher than the drops.

In regards to the fact that this streak is present primarily when the viscosity of the ambient fluid is low enough for the drops to present oscillations, we argue that these drops

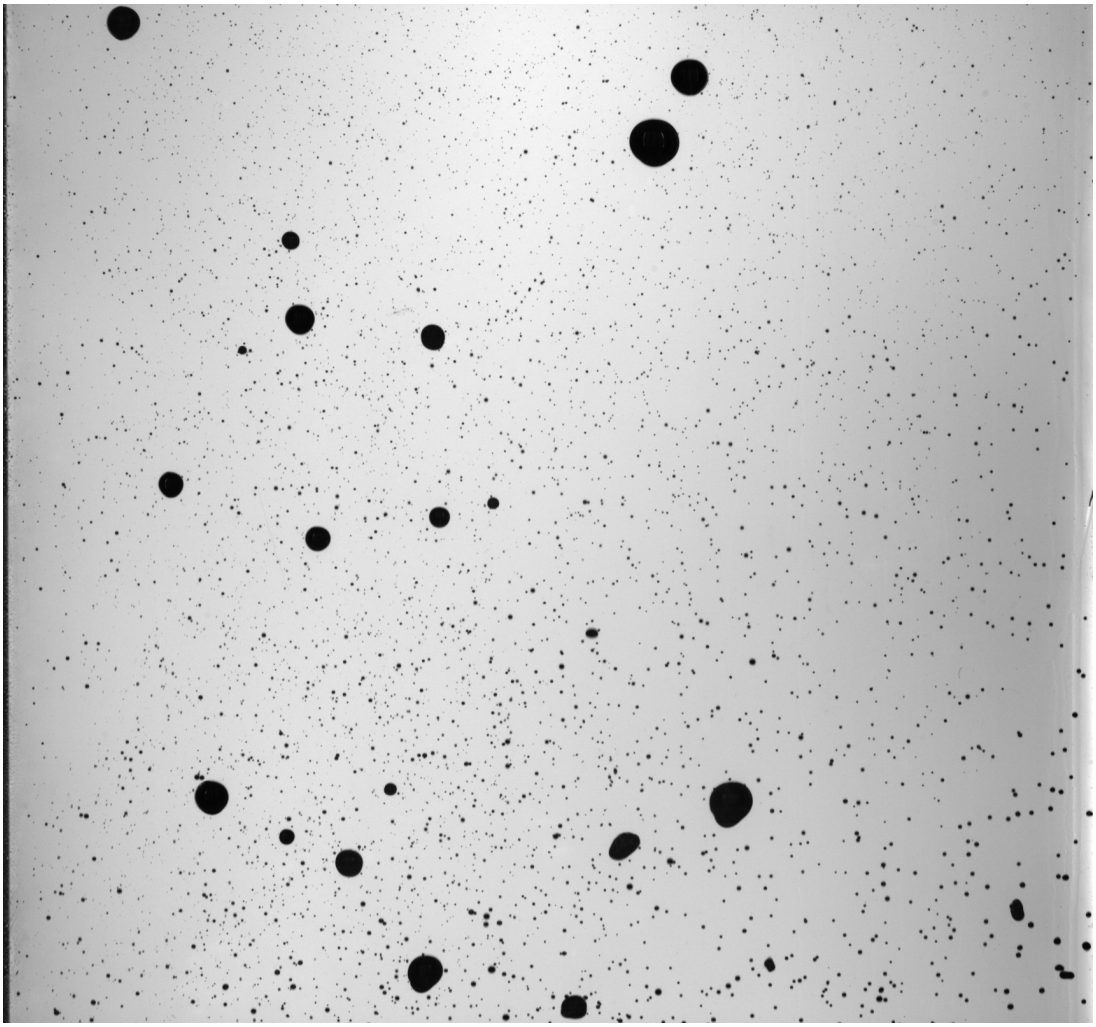

FIGURE V.4 – Snapshot of a video zoomed on the bottom of the tank of the fall of a 0.0389 m radius diapir of galinstan. At this level the drops have different times of arrival because they have traveled at their terminal speed. The smallest drops arrive the last, together with the antibubbles of galinstan (Every big structure on this snapshot is an antibubble).

are the one for which their natural falling speed and their first eigenmode of oscillation can resonate. This resonance is in our mind able to produce extreme deformation, dissipation hence extreme drag coefficient. We take for the scale of the frequency f of this eigenmode the inverse of a capillary time scale :

$$f \;=\; \sqrt{\frac{\sigma}{\rho_m R^3}} \tag{V.5}$$

The condition for resonance is to have a period of oscillation equal to the time scale of advection at the scale of the droplet :

$$\frac{f.R}{U} \;\simeq 1 \qquad \Leftrightarrow \qquad \sqrt{\frac{\sigma}{\rho_m U^2 R}} \;\simeq\; 1 \tag{V.6}$$

We recognize here the Weber number based on the density of the liquid metal. This

condition can also be transformed in a characteristic in the space (Cd,Re) which respect the following equation :

$$Cd \;=\; Re^4 \cdot \frac{8}{3} Mo\tilde{\rho}^3 R_\mu^4 \tag{V.7}$$

When plotted for the two lowest viscosity ratios, these lines intersect with the scaling for rigid spheres near where the abnormal streaks themselves would intersect it. This means that drops of this characteristic radius, when falling at their expected speed, are close to the condition of resonance and therefore subject to huge deformation when perturbed. This may be the explanation for the presence of these streaks.

Lastly, the 2 lowest viscosity ratios also exhibit an increasing trend in the highest Re. This is even more visible in the histogram of the logarithm of Cd and Re (cf. fig. **??**). This trend makes the bridge between the drag for sphere and the drag for spheroidal cap and shows the increase of the Cd due to the detachment of the boundary layers also observed for rigid spheres. Since the characteristic lines $We = 1$ that are plotted in figure **??** are based on the density of the drops, the same lines for the actual Weber number would be slightly to the right due to the factor 6 in density. Therefore, these lines also show the proximity of this detachment with the location in the plane (Cd,Re) where the Weber number is close to unity. The correlation between departure from the spherical shape ($We \sim 1$) and boundary layer detachment is indeed rather common in drops and bubbles (**?**).

B Distribution of sizes

1 Mean radii

The mean radius R_{10} of the droplets is particularly important in order to compare the distribution of sizes. Indeed drops formed in the same context but with different Weber numbers generally exhibit a comparable distribution of sizes when the radii are rescaled by R_{10} (**?**). In the broader context of the post impact flow, knowing the evolution of R_{10} as a function of We, Re and R_μ is therefore crucial to extrapolate our results to the planetary scale.

For each experiment, the mean measured radius R_{10} was computed on the fraction of droplet radii that is below a cutoff radius of about $2cm$. From observations of the videos the objects that have a size superior to $2cm$ are not stable drops and should be discarded as the average measure is marginally dependent on the presence of these events in the counting (an overestimation on the order of 10 % can be produced when including this fraction).

For the videos made at large scale, the sample considered is the simple collection of drops measured in an interval of 100 frames before the moment where the maximum number of droplets is measured. This allows the drops superposing to have more chances to be measured and smoothes the histograms. The mean ellipsoidal radii r_{ell} of the drops for the experiment filmed with the large scale framing are shown in figure **??**. The average radii seem to be weakly dependent on the viscosity ratio but more importantly, they are nearly constant with respect to the initial radius at a value of 0.0018 m . This value is close to the resolution of these films (0.00136 $m.pixels^{-1}$). Since the average drop has a

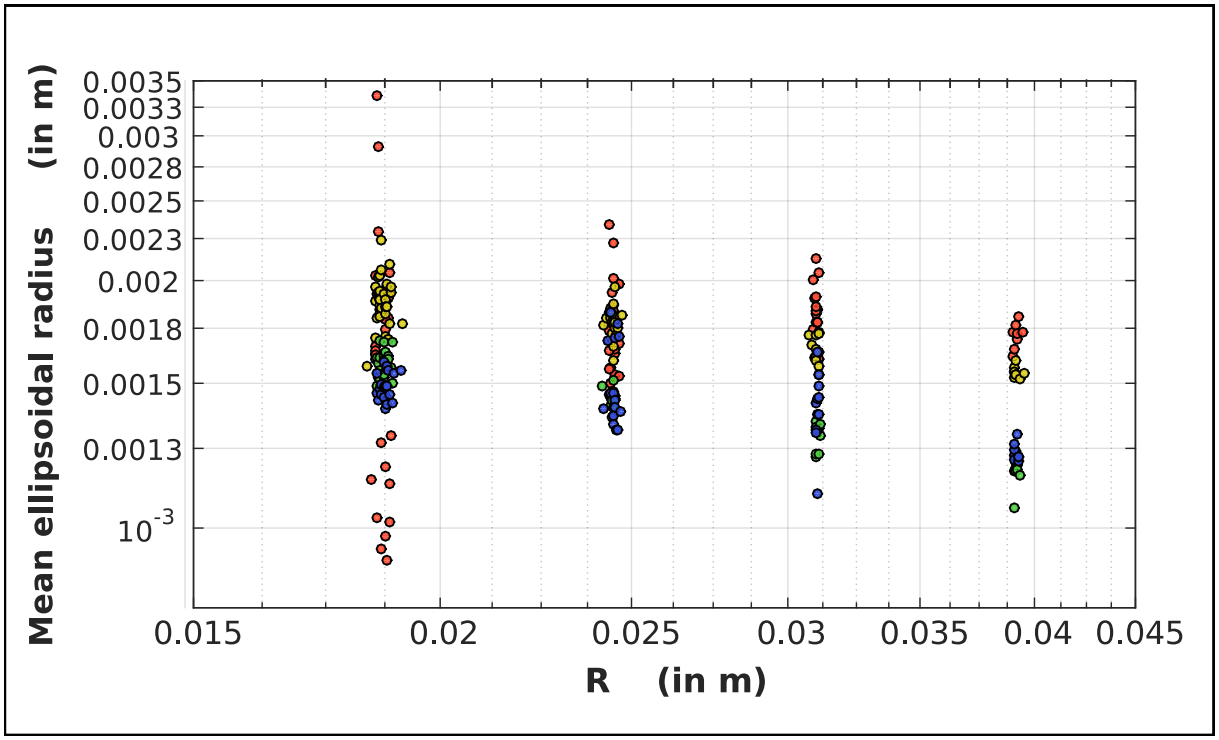

FIGURE V.5 – Graph of the mean ellipsoidal radius measured on the videos made with a large scale framing as a function of the initial radius for all viscosity ratios.

diameter of little more than two pixels, we consider these average radii as spurious in terms of absolute value. Yet, we argue that they are related to the average radius of the top fraction of droplets. In that framework, the higher average radius for the highest R_μ would imply that either the real mean droplet radius or the standard deviation of the droplet radius is higher for a higher viscosity ratio. This would confirm the observations made during the present study and our previous observations on a similar system (**?**).

Concerning the videos zoomed on the bottom of the tank, the droplets are passing through the field of vision and are generally already partially sorted because of their different falling speed. The making of the histogram and the computation of the average radius requires the counting over the whole span of the experimental video. In addition each count of droplets has to be re-normalized by their speed to account for the increased probability to count droplets when they are slower than the others. This was done by interpolating for each experimental film and each type of radius a relationship $v = f(r)$ with a polynomial of degree 3. This allowed to smooth the experimental relationships $v = f(r)$ while keeping their variations among runs. The mean radius for each experiment is presented in figure **??**. Unfortunately we were not able to produce a sufficiently large amount of data to provide a quantitative trend for the ratio of viscosity. A decreasing trend is however identifiable for the mean radius as a function of the initial radius of the diapir :

$$R_{ell10} \simeq R^{-0.985} \tag{V.8}$$

This is in stark contrast with the capillary length scale usually taken as an estimation of the size of droplets in the case of the post impact flow (its value is constant at $l_\sigma \simeq 3{\cdot}10^{-3}\ m$

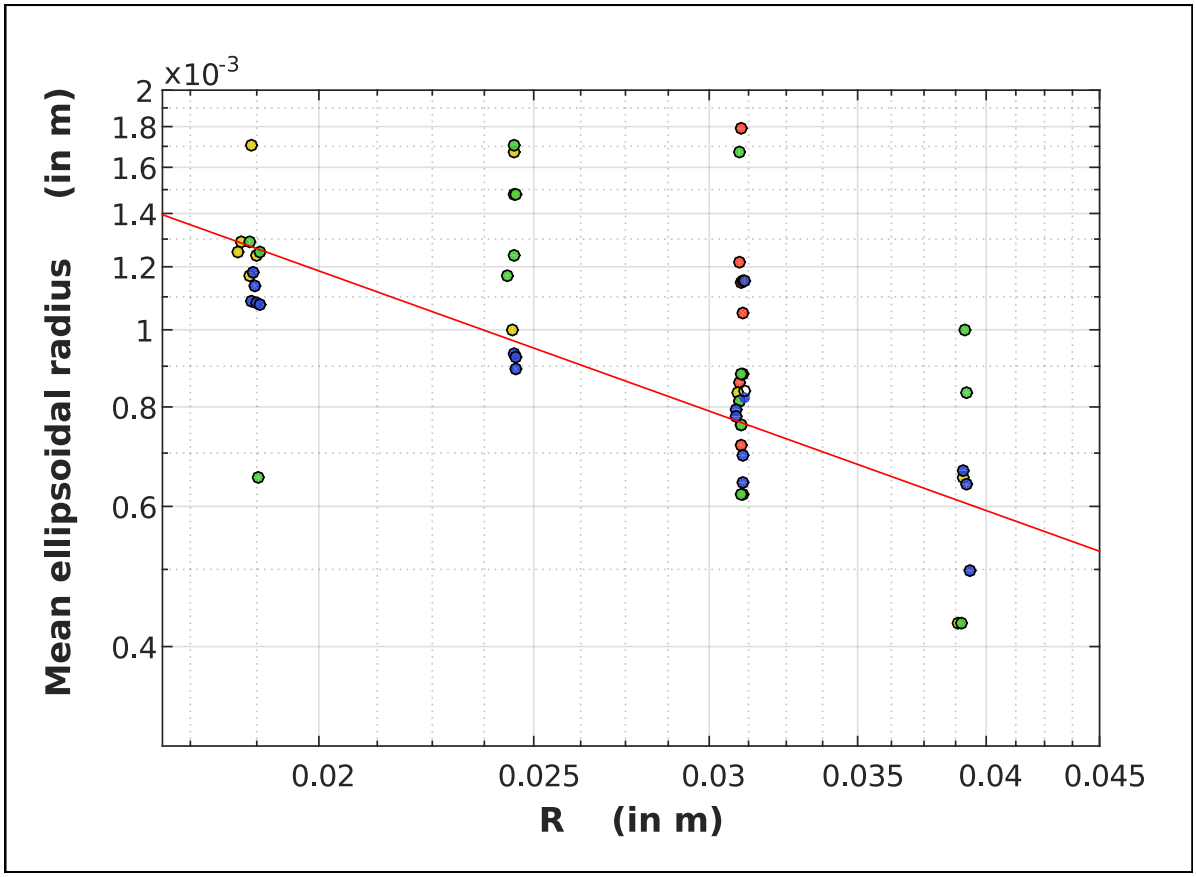

FIGURE V.6 – Graph of the mean ellipsoidal radius measured on the videos made with a zoom on the bottom of the tank as a function of the initial radius for all viscosity ratios. The red line represents the equation $R_{ell10} = 1.2 \cdot R^{-0.985}$.

in our experiment).

In our study we have varied two parameters when at least four non dimensional numbers (Re, We, R_μ and $\tilde{\rho}$) are direct inputs of the overarching problem of fragmentation of a liquid metal falling freely in an immiscible fluid with a different viscosity. Consequently a direct regression from the data to scaling laws of the mean radius as a function of the dimensionless numbers is unreasonable. Despite the reduction of information, taking into account additional observations can point towards the most probable physical scenario.

From the videos we have analyzed we know that the interface between the galinstan and the mixture of water and UCON oil is deformed by undulations that are likely to be Kelvin-Helmholtz instabilities. Additional videos were made in order to film the fall of the diapir from the top to see what is happening to these structures as they are engulfed in the diapir. Because of the reflection of light on the liquid metal clear static shots are still uneasy to interpret (cf. fig. **??**, bottom right pannel). The overall films however suggest that the long sheets created by Kelvin-Helmholtz instabilities undergo transverse modulation that leads to the formation of ligaments (cf. fig. **??**). These kinds of structures are also present in numerical simulation (**?**, **?**). Assuming the surface tension is limiting the growth of the KH instability, the maximum growing wave length λ_{KH} writes ;

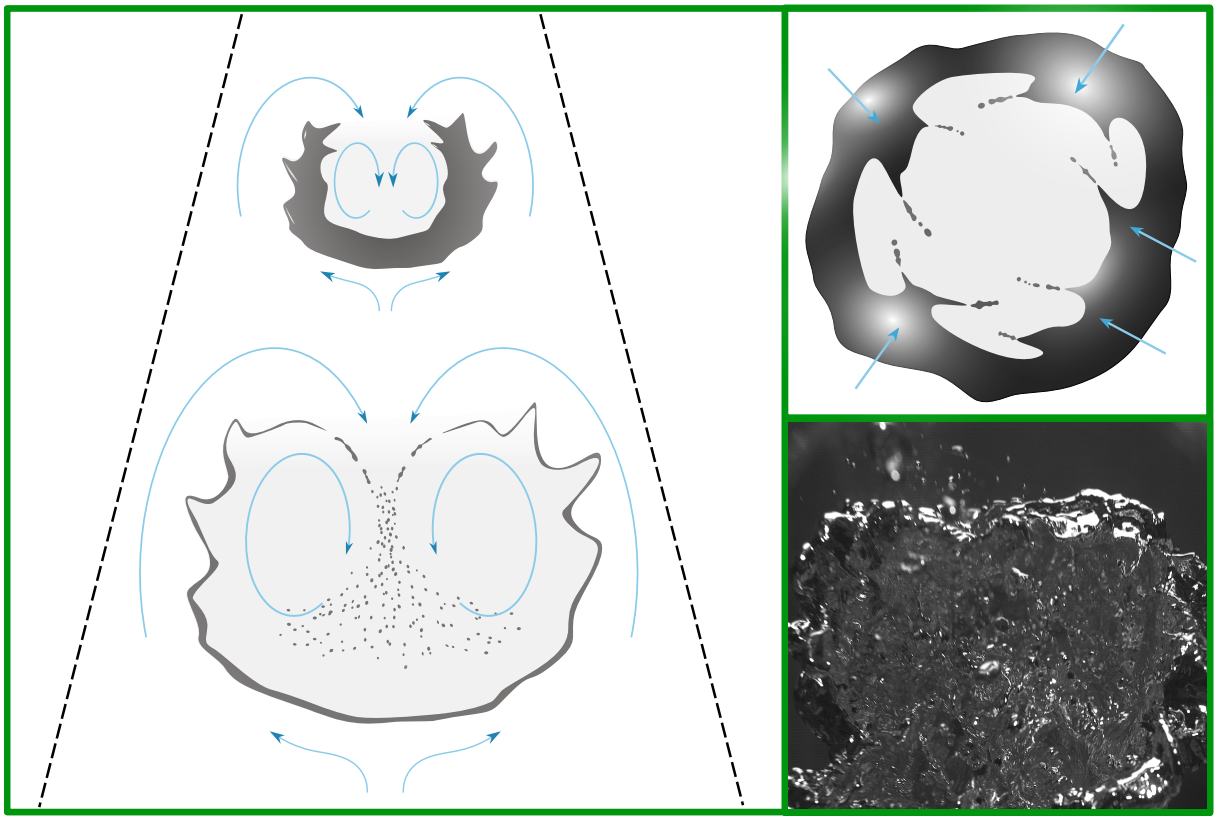

FIGURE V.7 – Interpretative schematic of the videos of the fall of a diapir of galinstan in water from the side. Top right panel : viewed from the top These schematics are based on observations of a few films of falling diapirs viewed from the top. Bottom right panel : Snapshot extracted from the video of the fall of a $0.031m$ radius diapir of galinstan in water viewed from the top at an angle close to 30 degrees from the vertical.

$$\lambda_{KH} \simeq \frac{\sigma\left(\rho_a + \rho_m\right)}{U^2.\rho_m\rho_a} \tag{V.9}$$

The breakup seems to occur on the rear of the diapir as the stretching rate appears to become more intense. This growing stretching rate is coherent with a flow that is in average to a toroidal vortex as fluid entrained would form at this location a downwelling that would correspond to an intense radial stretching. This quasi-static zone of breakup means that the speed of retraction is close to the local speed. As we have shown in section IV, the typical speed of this influx is a fraction of the large scale speed. Thus, equalizing these two speeds sets the thickness h of the liquid metal sheet :

$$\sqrt{\frac{\sigma}{\rho_m h}} \simeq U \qquad \Leftrightarrow \qquad h = \frac{\sigma}{\rho_m U^2} \tag{V.10}$$

The volume per unit length of the ligament is the one collected over one wave length of the KH instability by the retraction of the sheet. The typical radius of the ligament r_{lig} is then :

$$r_{lig} \simeq \sqrt{\lambda_{KH}.h} \qquad \Leftrightarrow \qquad r_{lig} \simeq R \,.\, \sqrt{\frac{\rho_a\left(\rho_a+\rho_m\right)}{\rho_m^2}}.We^{-1} \tag{V.11}$$

Since the ligaments are unstable as soon as they are created, they fragment and the created droplets have a mean radius close to the radius of the parent ligament (**?**). As a consequence of the two previous assumptions, their radii scale with We^{-1}. In our special case where the speed of the diapir obeys the Newtonian scaling ($U \simeq R^{\frac{1}{2}}$), We is proportional to R^2. In consequence, the scaling **??** seems to fit the data in a satisfactory manner, although the corrective term $\sqrt{\frac{\rho_a(\rho_a+\rho_m)}{\rho_m^2}}$ is giving a value 2 times lower than where the minimal value for the mean radius seems to sit. Given the spread of the data, a scaling with a slope slightly less steep is still possible. The closest one can find in the literature is related to the striping of droplets from the crest of undulations provoked by KH instabilities (see **?** for details). The analysis leads to the following relation for the mean radius :

$$R_{10} \;=\; R \,.\, We^{-\frac{1}{3}}.Re^{-\frac{2}{3}}.R_\mu^{-\frac{2}{3}} \tag{V.12}$$

This scaling would give a mean radius on the order of $10^{-7}m$ to $10^{-6}m$, which seems unreasonable according to observations of the most resolved films. In conclusion, the mean radius of the droplets formed by the fragmentation of a mass of liquid metal released without initial velocity in a viscous fluid seems to be best approximated by :

$$R_{10} \;=\; C_{mean}\; R \,.\, \frac{\left(1+\tilde{\rho}\right)^{\frac{1}{2}}}{\tilde{\rho}} \,.\, We^{-1} \tag{V.13}$$

C_{mean} is a constant approximately equal to 2.7.

2 Shape of the distribution

The histograms of the drops radii were computed alongside with the mean radii of each run so as to non-dimensionalize the measured radii by their average. The counts of droplets are then stacked among all experiments performed at identical target parameters to produce a single distribution as a function of the non-dimensional radius of the droplets. In addition, the histograms of the radii measured on the videos zoomed on the bottom of the tank were also constructed by renormalizing the counts of the droplets by their speed. Histograms of all the measured radii were constructed (cf. fig. **??**). Similarly to the data of the speed of droplets, the integrated radius shows greater levels of noise. Therefore we present the histograms of both the integrated radius and the ellipsoidal radius to identify the most accurate distribution.

Finally, since the mean radii measured on the video made with a large scale framing are not reliable, the parameters of the best fit for each theoretical distribution were first found on the histogram made with the data retrieved from the videos zoomed on the bottom of the tank. Then the same parameters were taken for the theoretical distributions, and the histograms made with the data retrieved from the videos made with the large scale framing were translated towards higher values of the non-dimensional radius. This was done in order to correct for the fact that the radii were normalized by an overestimated

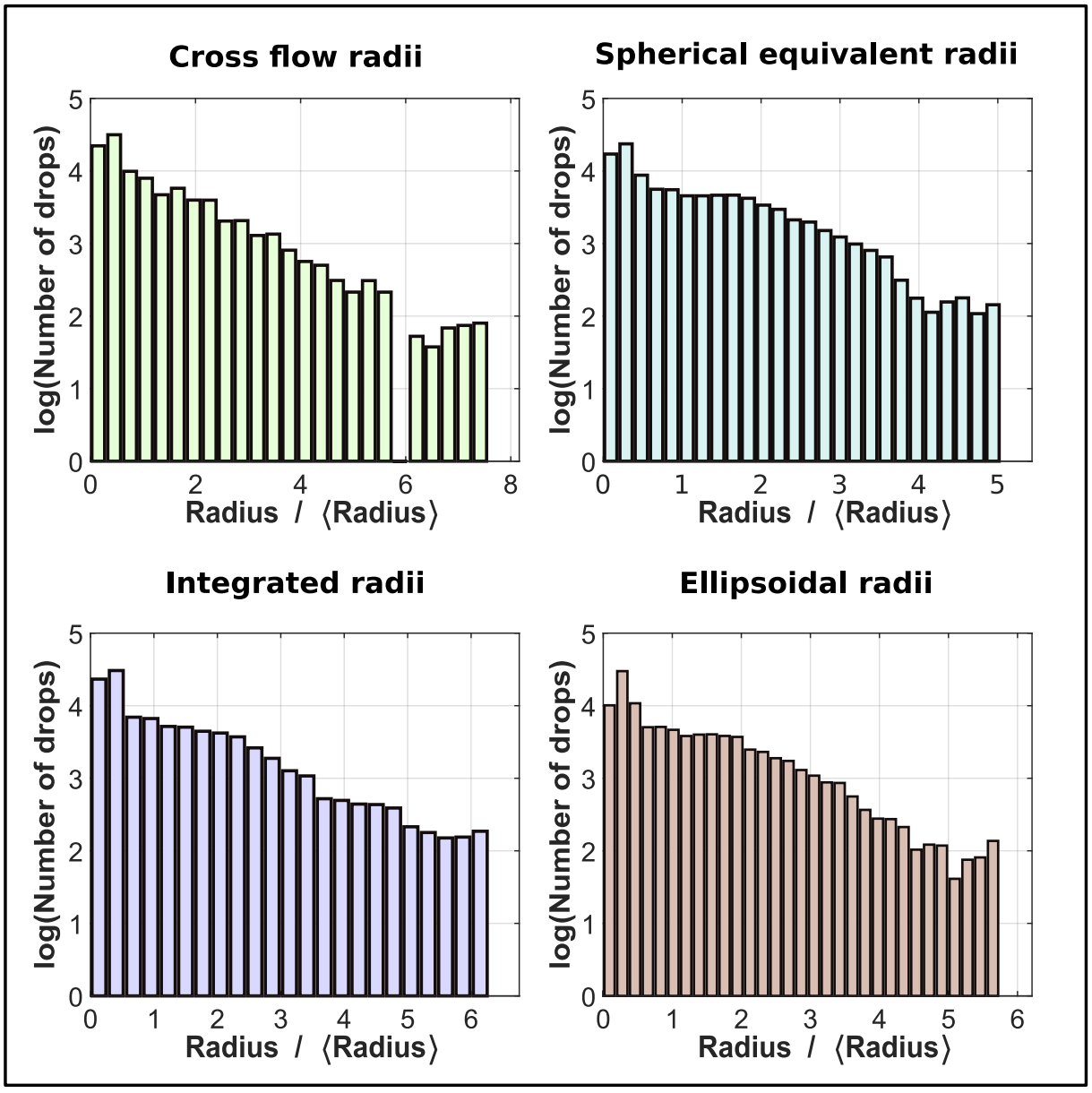

FIGURE V.8 – Histograms of all measured radii stacked between all experiments made at $R_\mu = 700$ and with a diapir of liquid metal with an initial radius of $R = 0.031\ m$. Exceptionally, colors have no particular meaning.

value of the mean radius. This secondary fit was made in accordance with the probable ratio between the overestimation of the mean radius and their other experimental value calculated with the videos zoomed in the bottom the tank. However, the non-convergence of the mean is also compromising the absolute value of the frequencies of droplets (the non-convergence of the mean could be due to non-counting of the smallest droplets instead of errors on the measures of their radius). Therefore, the theoretical distributions and experimental histograms were also normalized to provide probability distribution functions of the particular interval of radius for which spatial resolution is a lesser issue. This is essentially providing a comparison between the local slope of the experimental histograms and the theoretical distribution.

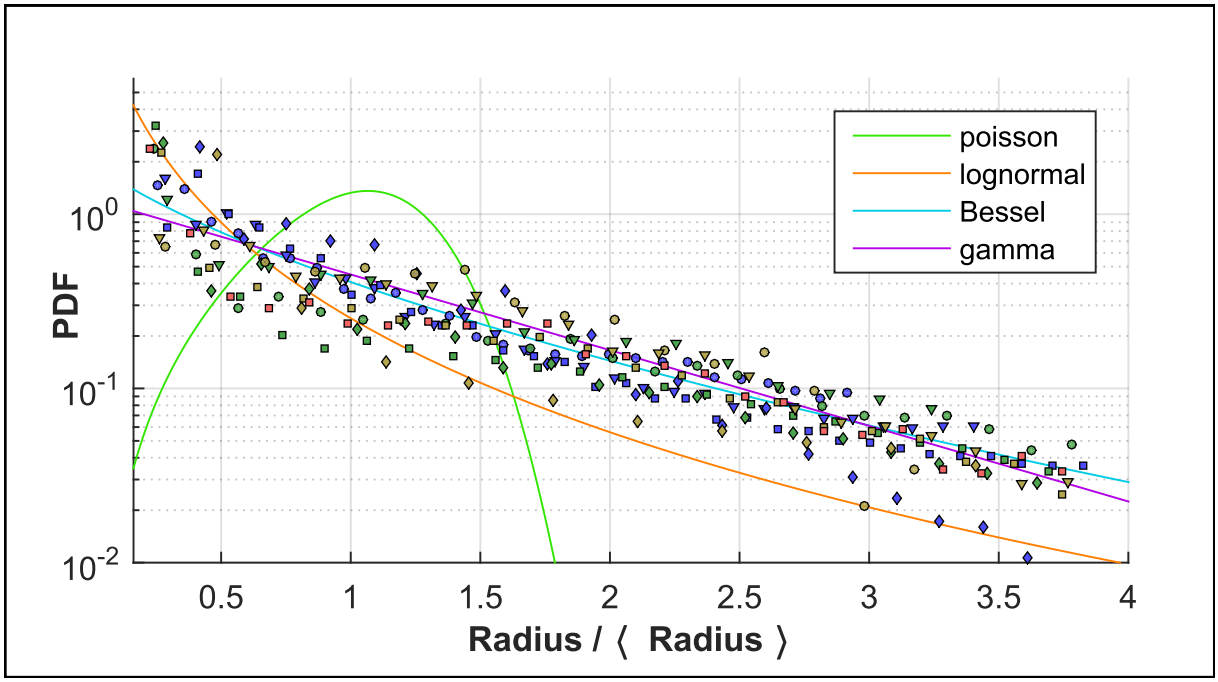

FIGURE V.9 – Histograms of the non-dimensional ellipsoidal radius of droplets measured on the videos zoomed on the bottom of the tank. The histograms were produced after stacking the counts for identical target experimental conditions. The different markers represent the initial sizes of the diapirs ; circles correspond to $R = 0.0186\ m$, triangles correspond to $R = 0.024\ m$, squares correspond to $R = 0.031\ m$ and diamonds correspond to $R = 0.039\ m$. Classical theoretical distributions are superposed for reference.

The histograms and theoretical distributions are found in figures **??**, **??**, **??** and **??**. The best fit for the complete set of data is the distribution constructed with the modified Bessel function of the second kind with parameters $m = 1$ and $n = 3$. Yet, the gamma distribution with a parameter of $k = 1$, which is in fact an exponential, provides a fit almost as good. This is in part due to the fact that the parameter k of the gamma distribution is related to the corrugations of the ligaments. The value of 1 for k is actually the asymptotic limit for very highly corrugated ligaments (**?**). These ligaments produce the distribution the most spread in terms of radius as large corrugations implies that aggregation is pushed to its limit and is able to produce bigger drops. The fact that this limit distribution still has a slope too steep to fit the experiments means that only one process of aggregation is certainly insufficient to explain the quantity of large drops. In all likelihood, the initial sizes of the ligaments are themselves distributed (**?**, **?**). Indeed when interpreting the data with the modified Bessel function, the value of 3 for n is also suggesting fairly corrugated ligaments, and the value of 1 for m also points to a fairly wide distribution of ligament cross-sections, close to an exponential (**?**, **?**). The log-normal distribution, while compatible with the expansion of the diapir for the highest R_μ (cf. chapter **??**), is not providing a good fit overall.

An important thing to notice and a hindrance to the interpretation is the fact that the distributions can have slightly different slopes depending on the parameters of the experiments. We attribute this to secondary "modes" of the distribution : small parts of the diapir fragment as a result of Rayleigh Taylor instabilities on the scales peeled from

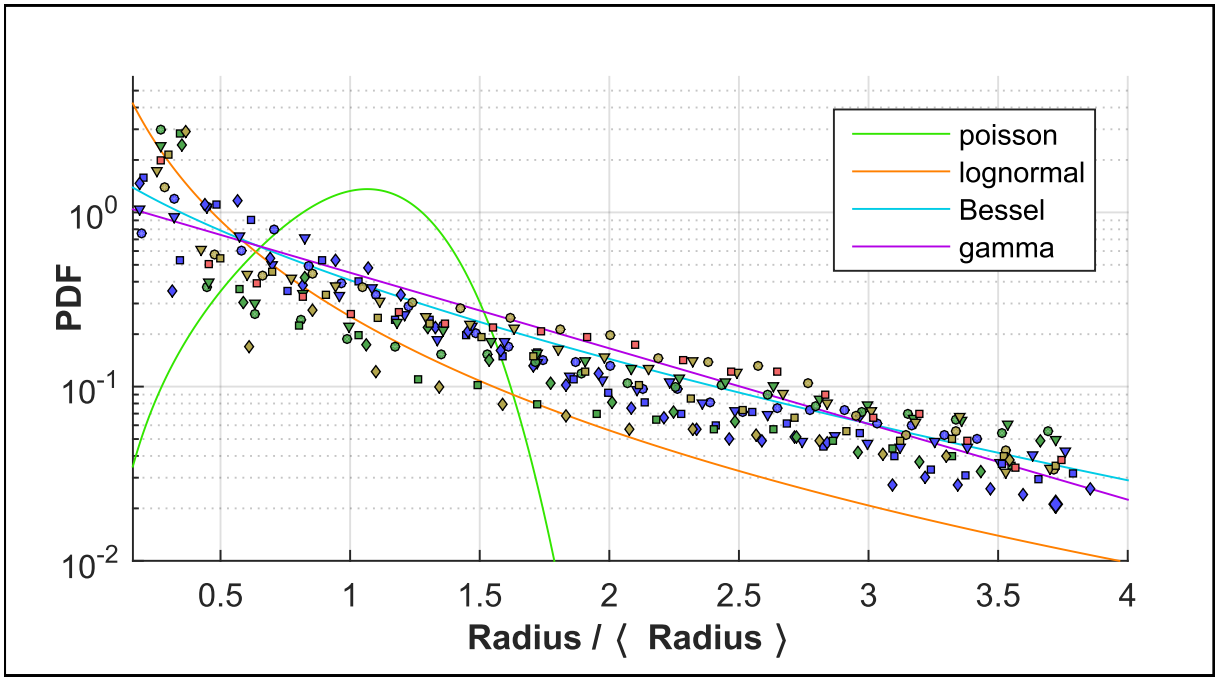

FIGURE V.10 – Histograms of the integrated radius of droplets measured on the videos zoomed on the bottom of the tank. The histograms were produced after stacking the counts for identical target experimental conditions. The different markers represent the initial sizes of the diapirs ; circles correspond to $R = 0.0186\ m$, triangles correspond to $R = 0.024\ m$, squares correspond to $R = 0.031\ m$ and diamonds correspond to $R = 0.039\ m$. Classical theoretical distributions are superposed for reference.

the main mass of galinstan as it falls. This produces small amounts of droplets that may not obey the main distribution but tend to broaden the experimental histograms since the drops are counted the same way irrespective of the way they are formed. Indeed the product of these RT instabilities is most likely to be of the order of $l_\sigma \simeq 3 \cdot 10^{-3}\ m$ which is higher than the measured mean radius. This is particularly true for the highest R_μ. The calculus of the higher moments of the distribution which are of great interest for the problem of diffusive exchanges is then subject to caution. A way to improve the data would be to track back the droplets to the structure where they originate. The distribution of sizes of ligaments is in fact needed to definitely confirm the necessity of a distribution based on a Bessel function (**?**). This tracking could also give an estimation of the participation of these secondary modes, if any, and could definitely rule out the scenario of breakup that supports the log-normal distribution.

For the distribution based on the Bessel function, we have computed the Sauter radius R_{32} and the volume mean radius R_{43}, that is to say the average radius when the drops of a single radius are weighted by the volume fraction they represent in the distribution instead of their numbers :

$$\frac{R_{32}}{R_{10}} = 2.2 \quad ; \quad \frac{R_{43}}{R_{10}} = 2.92 \tag{V.14}$$

These characteristic radii can then be used to calculate the long term and short term equilibration time scale as we will explain in chapter **??**

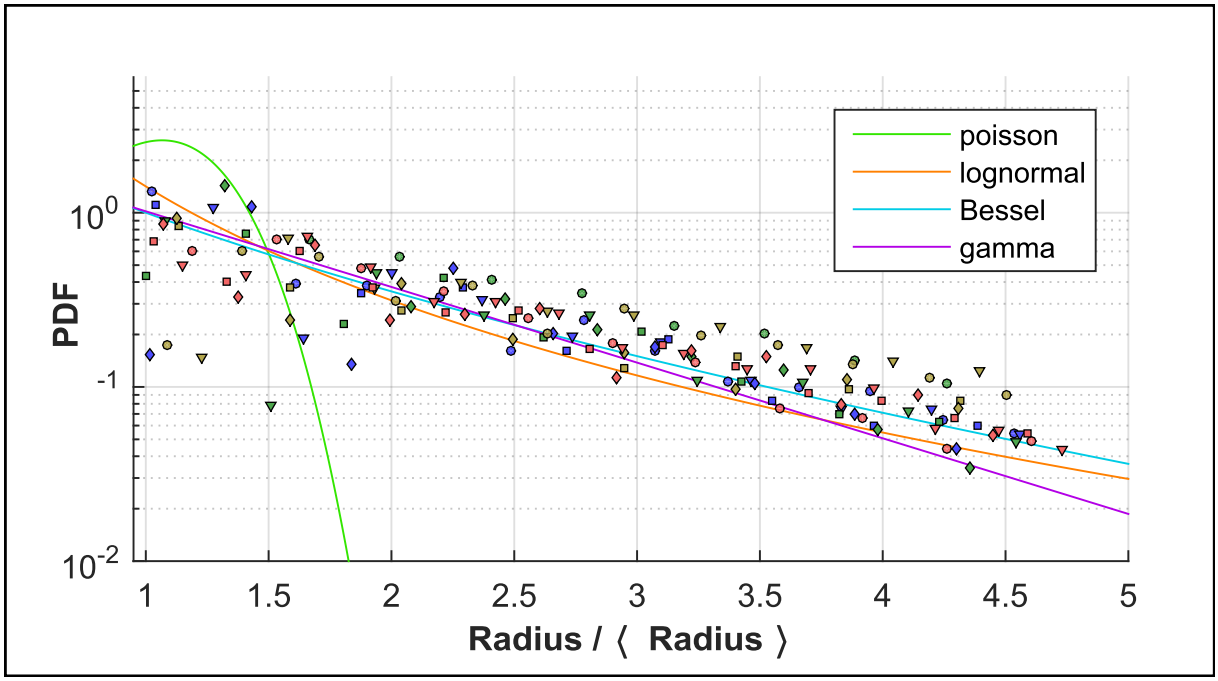

FIGURE V.11 – Histograms of the non-dimensional ellipsoidal radius of droplets in the interval $[1; 5]$ measured on the videos made with a large scale framing. The histograms were produced after stacking the counts for identical target experimental conditions. The different markers represent the initial sizes of the diapirs ; circles correspond to $R = 0.0186\ m$, triangles correspond to $R = 0.024\ m$, squares correspond to $R = 0.031\ m$ and diamonds correspond to $R = 0.039\ m$. Classical theoretical distributions are superposed for reference with a shift corresponding to the expected ratio between the mean radius measured on the videos made with a large scale framing and the one zoomed at the bottom of the tank.

3 Bias of the method

We have produced synthetic videos mimicking the experimental videos in order to assess the bias introduced by our counting algorithm in the experimental histograms. Since our biggest concern was drops overlapping and feeding the count of bigger drops, we have focused our investigation on the effect it could have on the slope of the distribution of sizes of the droplets. Nevertheless, simulating directly the binarized images has led to low resolution effects that are strongly affecting the integrated radii, that is why we only present the results for the cross flow radii.

If overlapping was a primordial factor, one could expect that it would take the role of a "numerical aggregation" and would therefore lower the slope of the distribution for big drops (**?**). We will focus here on videos constructed using 2 gamma distributions, one with a parameter $k = 10$ and one with $k = 2$. We did not produced a set of videos with the parameters found in the experiments because of time constraints in the making of simulated data. We have constructed histograms from the synthetic video the same way we have done for the videos made with the large scale framing. However, we increased the resolution in order to test the effects of overlapping without it intersecting with effects of very low resolution. Because of the time cost of producing the synthetic videos in large amounts (3 times the quantity of actual experimental video) the resolution was merely 2

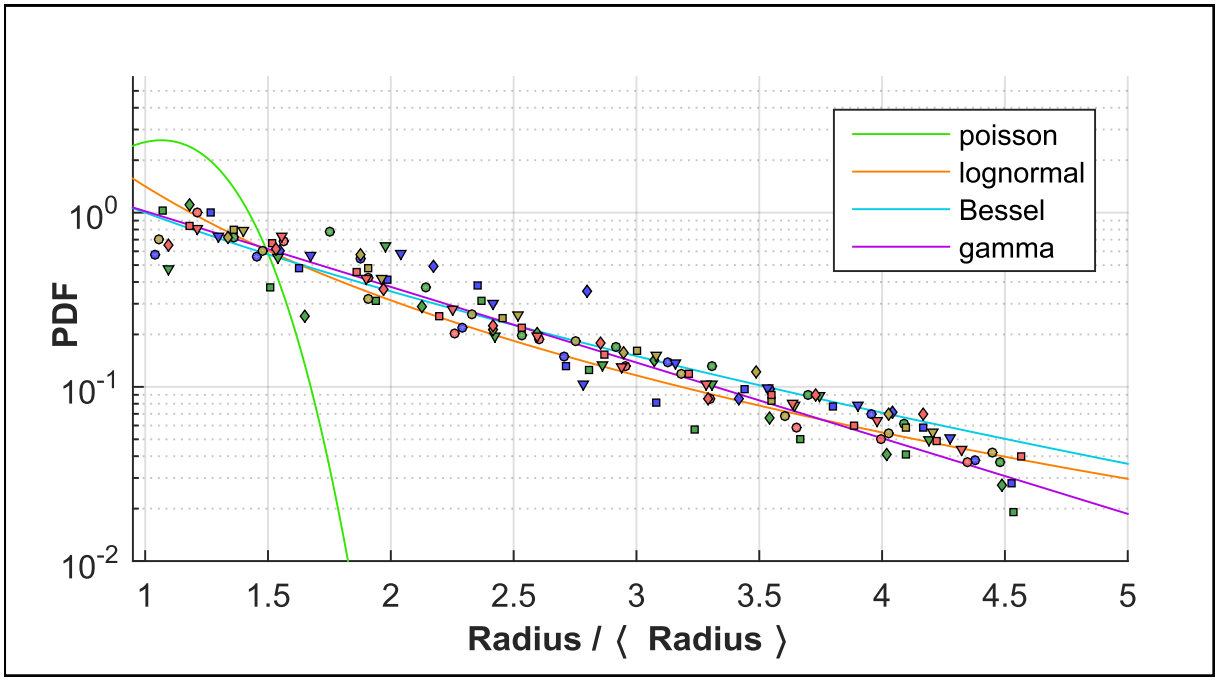

FIGURE V.12 – Histograms of the non-dimensional integrated radius of droplets in the interval $[1; 5]$ measured on the videos made with a large scale framing. The histograms were produced after stacking the counts for identical target experimental conditions. The different markers represent the initial sizes of the diapirs ; circles correspond to $R = 0.0186\ m$, triangles correspond to $R = 0.024\ m$, squares correspond to $R = 0.031\ m$ and diamonds correspond to $R = 0.039\ m$. Classical theoretical distributions are superposed for reference with a shift corresponding to the expected ratio between the mean radius measured on the videos made with a large scale framing and the one zoomed at the bottom of the tank.

times larger. In consequence, pixelisation effects are still present.

Both the distribution used to draw randomly the drops and the histogram from the videos analysis are reported on figure **??** for $k = 10$ and on figure **??** for $k = 2$. In the case of the sharp gamma distribution ($k = 10$), the expected effect is visible for the droplets having a radius 2 times the mean radius and larger. It is even stronger for videos aimed at simulating experiments made with the largest mass of galinstan. The slope of the probability density function for big drops is even lower. With this effect of the dilution of drops, we argue that overlapping is indeed a big obstacle when experimentally investigating the distribution of droplets sizes. However, this seems confined to narrow distributions as the gamma distribution with $k = 2$ was recovered rather accurately by our counting algorithm (cf. fig. **??**). In our experiments, the density of drops in the region they occupy is quite inhomogeneous. In addition, the drops are roughly sorted in size. Consequently, one could argue that the problem of superposition is mainly due to it affecting drops that are densely packed, which could be drops of a particular size (or range of sizes). Yet, the drops are sorted vertically and the density of droplets is approximately radial. Therefore the local density should not be correlated with the size to a point where counts of big drops are affected by superposition. In conclusion, given the overall slope of the experimental distributions (around 1), we argue that they are unbiased by the superposition of droplets.

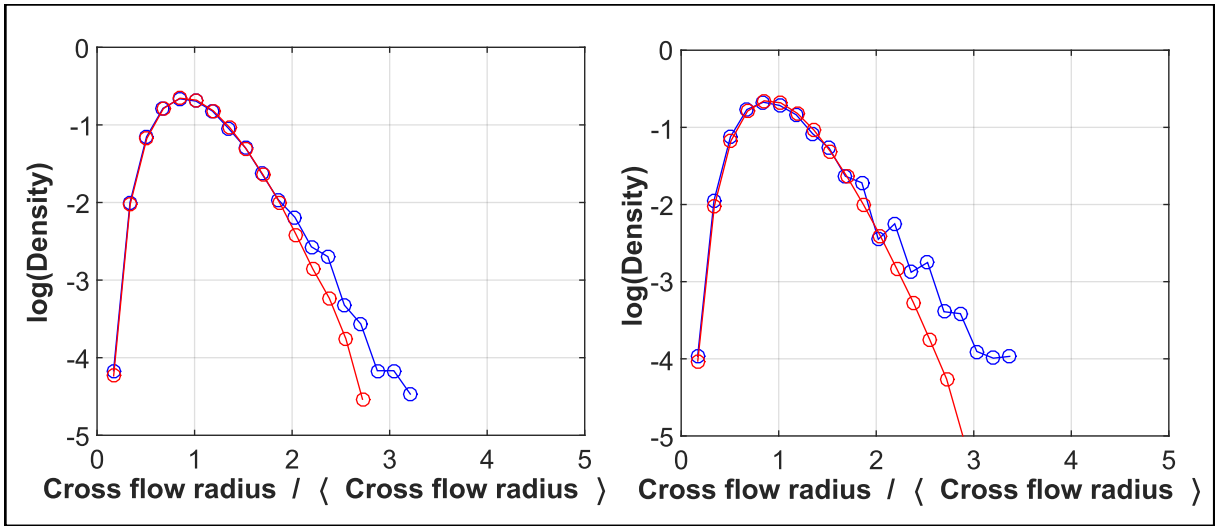

FIGURE V.13 – Histograms of the cross flow radius measured on synthetic videos counted by the same algorithm as the one that measured the droplets on the experimental videos (in blue). We have chosen the synthetic droplets using an apriori distribution of sizes equal to a gamma distribution of parameter $k = 10$ (in red). The left panel presents the results for a video made to simulate a cloud of droplets resulting from a 0.0186 m radius diapir and the right panel the results for a video made to simulate a cloud of droplet resulting from a 0.0389 m radius diapir. The analysis was made at a depth that would correspond to 1.3 m in an experimental video.

C Shape of the droplets

1 Static shapes

The shape of the droplets time averaged along their tracks is summarized in figure **??**. We define the aspect ratio E of a drop as its height over its width. One striking feature of the regime diagram is the propensity of the drops at large Re to have an aspect ratio, on average, close to 1. From the observations of the videos, drops are indeed oscillating between oblate and prolate shapes, but the average shape seems to be skewed towards oblate. Our method for computing average shape is here subject to caution, as it involves stacking images of the drops in order to have an average image, which ignores the axisymmetric distribution of mass. Therefore for drops at high Re, their static shape may not be very accurately captured. This however works well for drops at low Re for which we find the classical transition from spherical drops to ellipsoidal cap as we consider droplet of higher We (**?**, **?**, **?**). In addition, one can see that the evolution of the aspect ratio of the drops as the drop size increases is not entirely a function of the Weber number. In this range of Reynolds number, it is more than likely that the deformation has two main contributions, from the Weber number as well as from the Bond number (**?**).

While the full determination of the shape of the droplets is out of the scope of the present study, we notice that for non-oscillating droplets their aspect ratios are always above 0.5. If we approximate the drops with oblate ellipsoids, the ellipsoidal radius r_{ell} that is the radius of a sphere with the same volume can be expressed as :

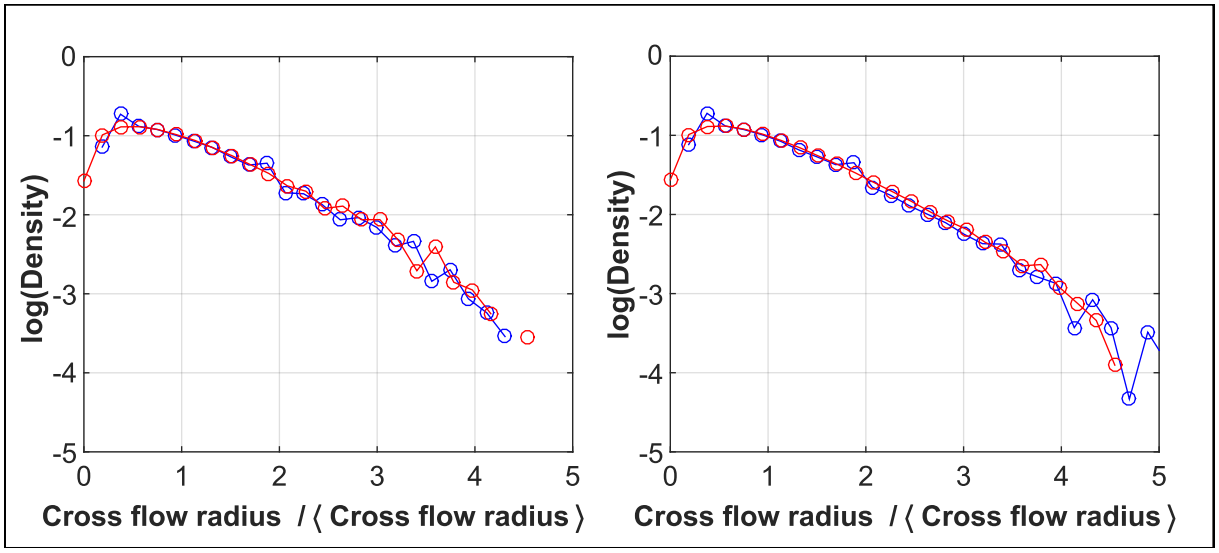

FIGURE V.14 – Histograms of the cross flow radius measured on synthetic videos counted by the same algorithm as the one that measured the droplets on the experimental videos (in blue). We have chosen the synthetic droplets using an apriori distribution of sizes equal to a gamma distribution of parameter $k = 2$ (in red). The left panel presents the results for a video made to simulate a cloud of droplets resulting from a 0.0186 m radius diapir and the right panel the results for a video made to simulate a cloud of droplet resulting from a 0.0389 m radius diapir. The analysis was made at a depth that would correspond to 1.3 m in an experimental video.

$$r_{ell} = \sqrt[3]{E.r^3_{crossflow}} \tag{V.15}$$

The interfacial area of the ellipsoid approximating the droplet then writes :

$$S = 2\pi\, r^2_{crossflow}\left(1 + \frac{E^2}{\sqrt{1-E^2}} \cdot \operatorname{arctanh}(\sqrt{1-E^2})\right) \tag{V.16}$$

Hence

$$S = 4\pi\, r^2_{ell}\left(\frac{\sqrt{1-E^2} + E^2 \cdot \operatorname{arctanh}(\sqrt{1-E^2})}{2E^{\frac{2}{3}}\sqrt{1-E^2}}\right) \tag{V.17}$$

In the interval between 0.5 and 1 where all the aspect ratios of non-oscillating drops sit, the function correcting the surface of the ellipsoid from its estimation with a sphere having the same volume ranges from 1.1 to 1. Given the fact that our drops are significantly departing from the ellipsoidal shape, this factor could be slightly higher. This in turn could affect the interpretation of the temperature measurements that we will present in the next chapter. Given their precision, this is unlikely hence we will neglect this effect from now on.

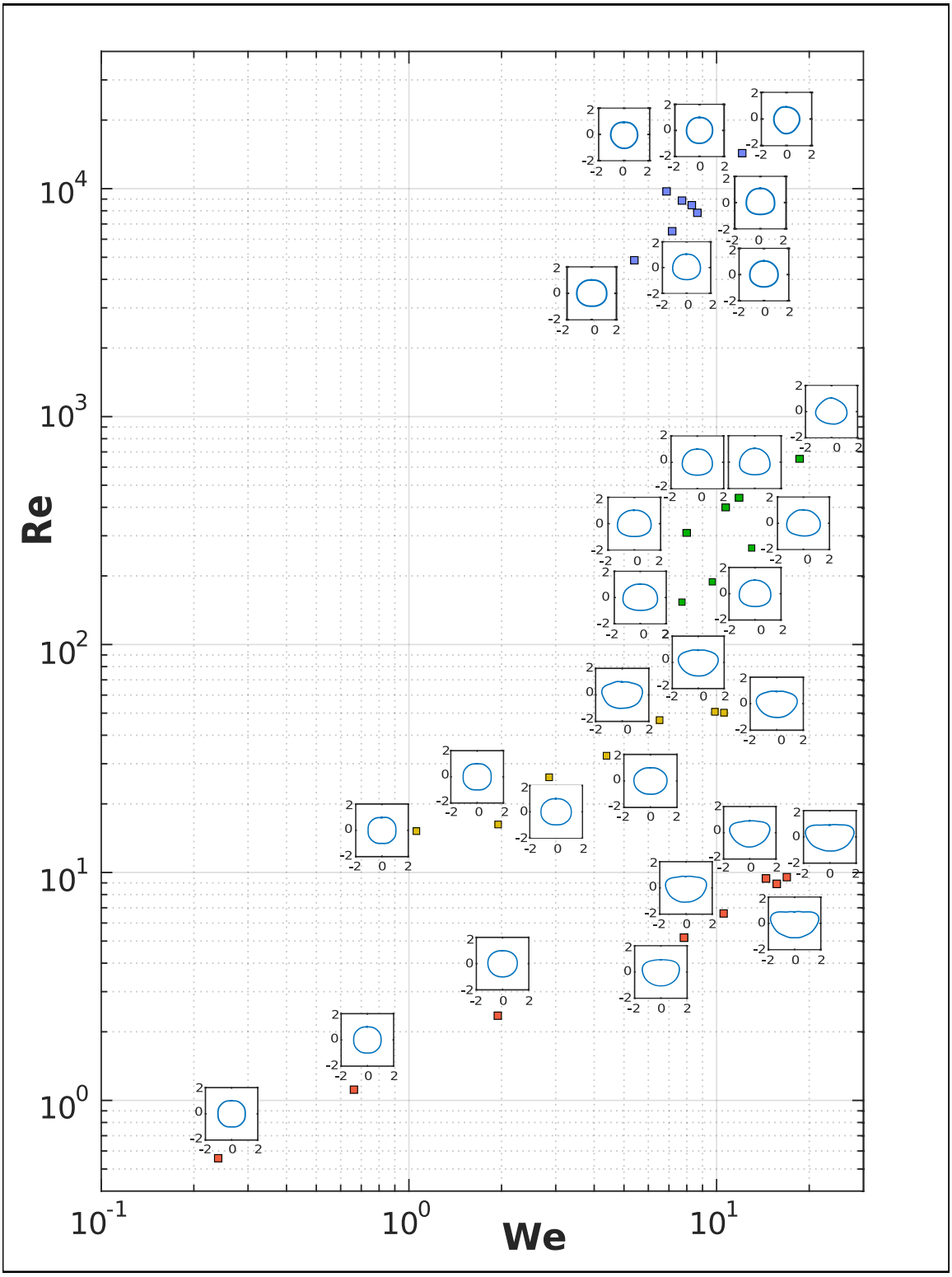

FIGURE V.15 – Regime diagram of the shape of the droplets in the (Re, We) plane. The contour of the droplets has been non dimensionalized by their radius.

2 Oscillations of the droplets

Frequency of oscillation

The question of the shape of the droplets becomes all the more important when considering oscillating droplets as it now introduces an other scale for the speed at the interface (**?**). It is crucial to assess which one between the oscillations or the flow associated with the settling of the drops is relevant for the diffusive transfers across the interface (**?**). In our experiments, drops vibrations are widespread for the 2 lowest viscosity ratios.

In the limit of small deformations, Lamb (**?**, **?**) showed that the decomposition of the interface of an inviscid droplet in the absence of gravity along spherical normal modes leads to oscillations with a frequency f_{lamb} that depends on the highest wave number l of the mode :

$$f_{lamb} = \frac{1}{2\pi} \cdot \sqrt{\frac{(l-1)(l+1)(l+2)\ \sigma}{((l+1)\rho_m + l\rho_a)\, r^3}} \tag{V.18}$$

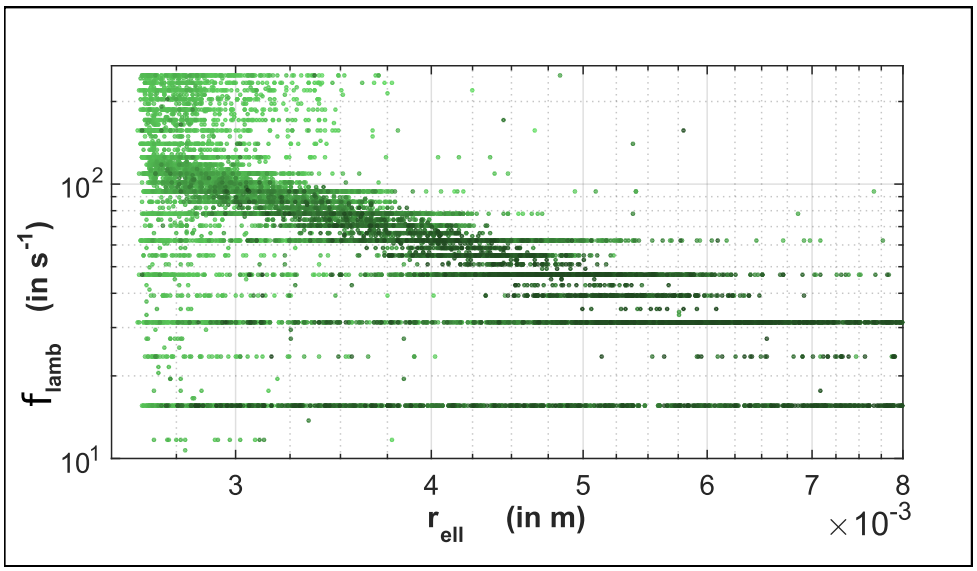

FIGURE V.16 – Graph of the frequency of oscillation of all drops measured at $R_\mu = 0.4$ as a function of their mean ellipsoidal radius. The colors are darker for droplets with an amplitude of oscillation larger compared to their radius.

From the space time diagrams of the droplet outline, we were able to extract the principal frequencies of oscillations. They are overwhelmingly associated to the wave numbers $l = 2$ and $l = 0$. In the latter case, since the droplets are only very rarely coalescing, we interpret this varying radius as a vibration with $l = 2$ in the line of sight. Every frequency that is associated with $l = 2$ is plotted on figure **??** for $R_\mu = 0.4$. We can see that the smallest drops have a wide range of frequencies. This is due to the pixelisation that brings an important noise on the outline of droplets while their amplitude of oscillation is on average smaller than bigger drops.

In addition, the droplet radius for all sizes tends to be very spread which can be imputed to the limited time the tracking of particles ends up providing in order to average the radius across oscillations. We have circumvented this problem by averaging the droplets

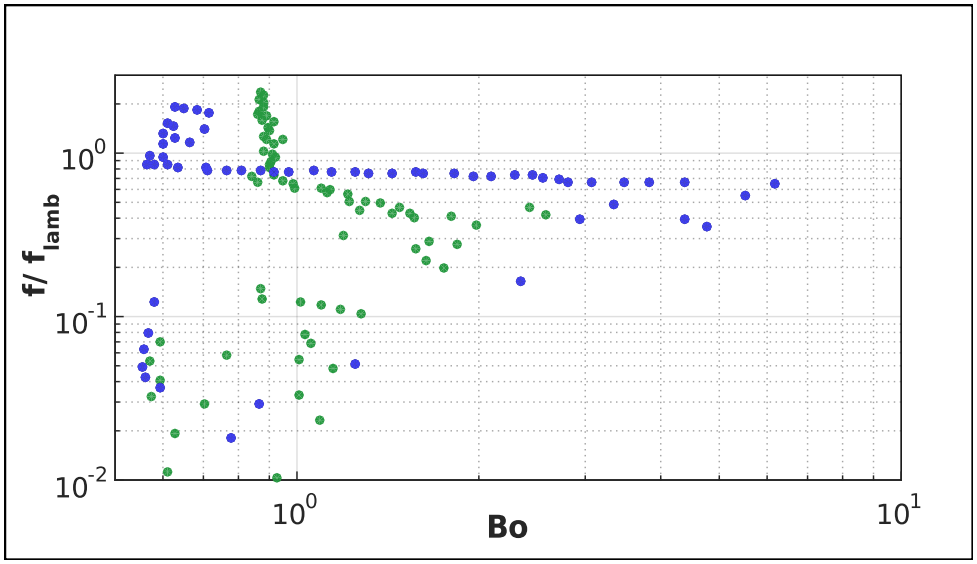

FIGURE V.17 – Frequency of the droplets rescaled by the frequency from Lamb's theory as a function of the Bond number of the droplet. The droplet radii are averaged around regularly spaced values of frequency. Blue circles are droplets having $R_\mu = 0.4$. Green circles are droplets having $R_\mu = 8$.

radius for a given frequency. The ratio between these values for the frequency and the frequency predicted by Lamb theory f_{lamb} is very close to one for $R_\mu = 0.4$ but is significantly decreasing for $R_\mu = 8$ (cf. fig. **??**). This trend is debatable as the interval of radii measured is much smaller for $R_\mu = 8$. If we make the analogy made by G.I. Taylor (**?**) between a vibrating drop and a damped mass-spring system, viscous dissipation lowers the frequency of the drop oscillation. The difference between the inviscid Lamb frequency and the frequency of viscous droplets would be on the order of the inverse of the damping time (**?**) which scales as $\frac{\mu_m}{\rho_a r_{ell}^2}$. Since the viscosity of the ambient fluid is higher for the case that departs the most from the inviscid theory, we have supposed that the relevant viscosity is the one of the ambient fluid. The ratio of the correcting term with f_{lamb} then writes :

$$\frac{\frac{\mu_a}{\rho_a r_{ell}^2}}{f_{lamb}} \simeq \frac{\mu_a}{\sqrt{\sigma \rho_m r_{ell}}} \tag{V.19}$$

Because it is the square of frequencies that are subtracted in a damped harmonic oscillator, the frequency follow the relationship :

$$f = f_{lamb}\left(1 - \frac{\mu_a^2}{\sigma \rho_m r_{ell}}\right)^{\frac{1}{2}} \tag{V.20}$$

This expression leads to corrections of the order of 1 % which is inconsistent with the results presented in figure **??** in term of both magnitude and trend with respect to r.

When considering the breakup of droplet by dynamic pressure (**?**), the inertia of the flow is opposing the surface tension in restoring the shape of the drop. Therefore it is conceivable that for free oscillations, the flow around or inside the drop is acting against the surface tension. In that case the Laplace pressure $\frac{\sigma}{r}$ would be offset in the equations

by ρU^2 in a mean sense. As for the inverse of the time scale of deformation in aerobreakup (**?**), the frequency would be written :

$$f = f_{lamb}\left(1 - \frac{We}{We_c}\right)^{\frac{1}{2}} \tag{V.21}$$

By fitting the values for the parameter We_c (cf. fig. **??**), we find a value of 3.91 for $R_\mu = 8$ and 13 for $R_\mu = 0.4$ which are indeed values close to the critical Weber numbers found for the breakup of droplets (cf. chapter **??**).

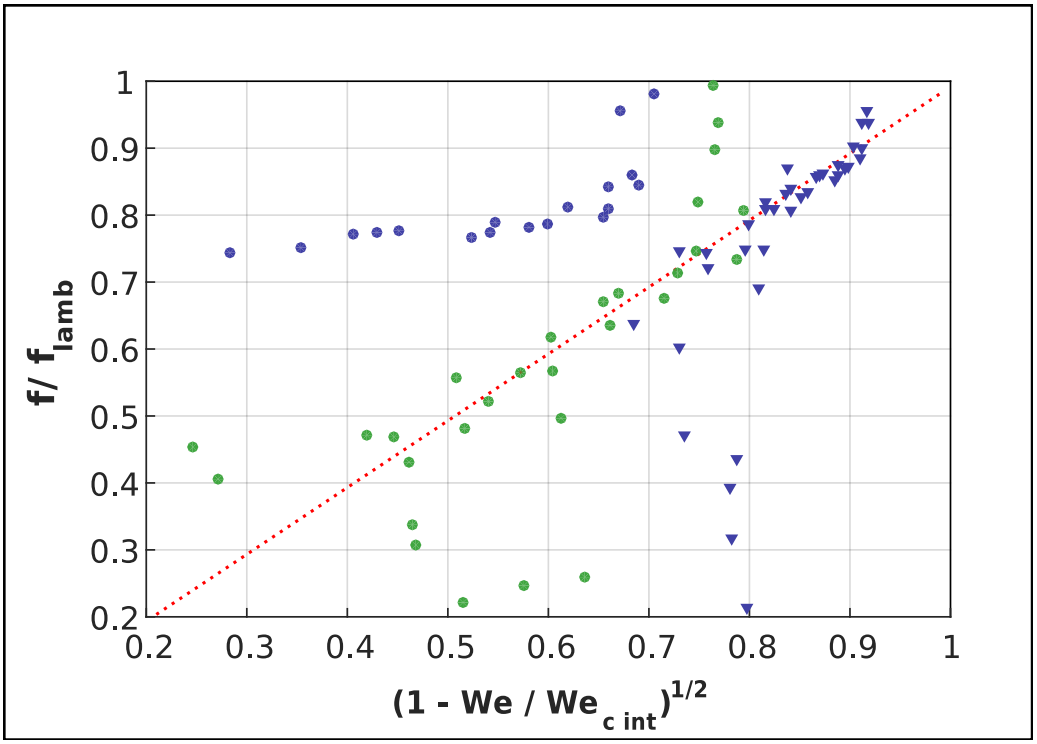

FIGURE V.18 – Graph of the ratio between experimental frequencies and f_{lamb} as a function of the corrective term $\left(1 - \frac{We}{We_c}\right)^{\frac{1}{2}}$. Green circle : frequencies for $R_\mu = 8$ are plotted with the parameter $We_c = 3.9$. Blue circle : frequencies for $R_\mu = 0.4$ are plotted with the parameter $We_c = 3.9$. Blue triangle : frequencies for $R_\mu = 8$ are plotted with the parameter $We_c = 13$. The red dashed line has for equation $f/f_{lamb} = \left(1 - \frac{We}{We_c}\right)^{\frac{1}{2}}$.

However, the ratio between these two values for We_c may suggest that the relevant Weber number is not based on the average falling speed of the droplet U. The interfacial speed u_i can be extracted from the continuity of strain at the interface :

$$\mu_a \cdot \frac{U - u_i}{\sqrt{\frac{\mu_a}{\rho_a}\frac{u_i}{R}}} = \mu_m \cdot \frac{u_i}{\sqrt{\frac{\mu_m}{\rho_m}\frac{u_i}{R}}} \tag{V.22}$$

$$\Rightarrow \quad u_i = \frac{U}{1 + \tilde{\rho}^{\frac{1}{2}}\ R_\mu^{-\frac{1}{2}}} \tag{V.23}$$

Here the viscous boundarly layers are assumed to scale as $\sqrt{\frac{\mu_a R}{\rho_a u_i}}$. Given equation **??**, the ratio between the two interfacial speeds for our two cases is 2.3. Elevated to the power

2, this yields 5.3 which is close enough for us to argue for a collapse of the expression for frequency in the form of :

$$f \;=\; f_{lamb}\left(1 \;-\; \frac{We}{We_{c2}} \cdot \frac{1}{\left(1+\tilde{\rho}^{\frac{1}{2}}\; R_{\mu}^{-\frac{1}{2}}\right)^{2}}\right)^{\frac{1}{2}} \tag{V.24}$$

The constant We_{c2} has a value of 0.56. The agreement between the measures and the predictions based on the interfacial speed allows us to argue for a more precise mechanism for frequency shifting. It seems like the frequencies are in fact affected by the Doppler shift of the two capillary waves that compose the mode $l = 2$. The point could be made that the wave has to travel as much distance with the flow or against the flow, but one has to average in time instead of in distance to have the actual frequency of the wave.

Amplitude of oscillation

From the Fourier transform of the space time diagrams of the droplets outline, the amplitude of the first six modes having the greatest amplitude were recorded. The amplitude of the modes associated with the wave number $l = 2$ were averaged with the same method as for their radius. These amplitudes were non-dimensionnalized by the radius of the droplet (cf. fig. **??**).

As we are mainly interested in the order of magnitude of the speed generated by the oscillations, we suppose that the drops only vibrate along the fundamental mode. While it is somewhat contrary to the data on amplitude, it is indeed the mode with the most energy for the vast majority of drops. Previously, we saw that the time scale for viscous dissipation is orders of magnitude larger than the period of oscillation, which is equivalent to say that the Reynolds number of the oscillations is very high. Therefore we suppose that both the dissipation and the excitation of the drop oscillations are due to the inertia of the flow. We suppose that the drop has reached on average its terminal velocity. Oscillating drops have also an oscillating falling speed (**?**). The work W_{front} of the dynamical pressure during one cycle on the front of the drop can be assumed to have the following form :

$$W_{front} \;=\; \left[\; \overline{C_d \cdot \frac{1}{2}\rho_a U^2 \cdot \pi r^2}^{\,+} - \overline{C_d \cdot \frac{1}{2}\rho_a U^2 \cdot \pi r^2}^{\,-} \;\right] \cdot A \tag{V.25}$$

A is here the amplitude of the fundamental mode of oscillation from prolate to oblate shape. $\overline{X}^{\,-}$ refers to the quantity X averaged over the half-period where the drop is elongating in a prolate form and $\overline{X}^{\,+}$ refers to the quantity X averaged over the half-period where the drop is shorten in an oblate form. The difference between the two contributing works is likely due to the velocity U as the radius r and the drag coefficient Cd are most likely in phase with the oscillation. The speed on the contrary, is likely to be in quadrature phase shift as the acceleration is determined by the time variable Cd. Since U has variations of a fraction of U at best, we parametrize W_{front} as :

$$W_{front} \;=\; c_{w1}\rho_a U^2 \cdot \pi r^2 \cdot A \tag{V.26}$$

c_{w1} is here a coefficient smaller than 1.

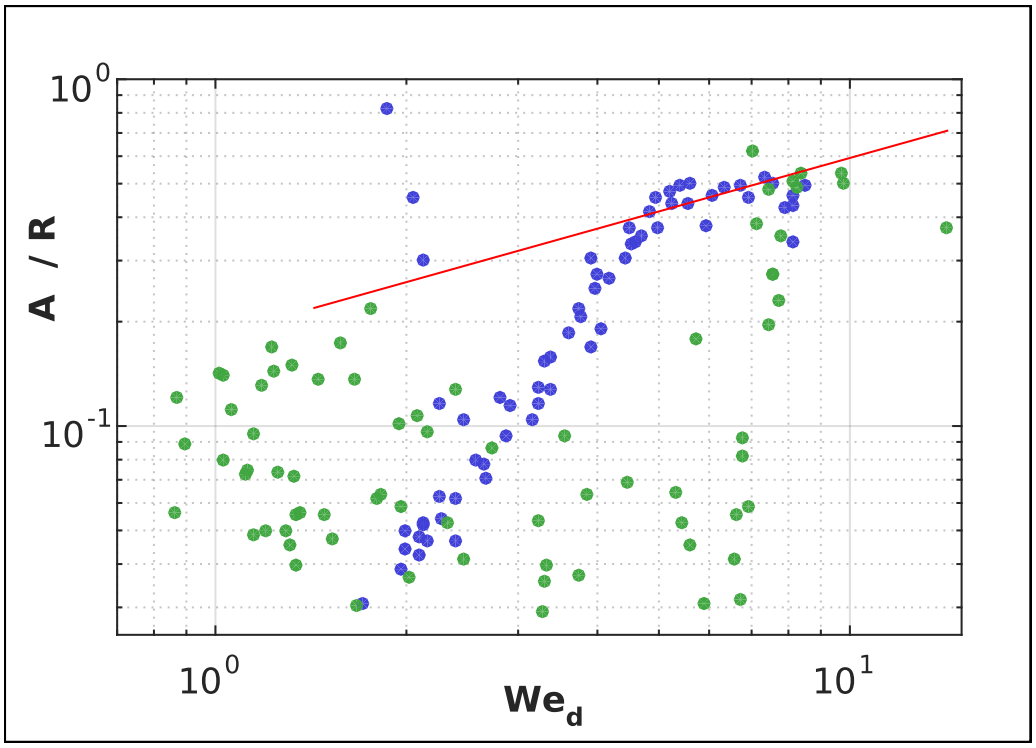

FIGURE V.19 – Amplitude of oscillations of the mode $l = 2$ divided by the radius of the droplet as a function of the Reynolds number of the droplets. The amplitudes and radii of the droplets were averaged around regularly spaced values of frequency of the mode $l = 2$. The red line represent the scaling **??** for the amplitude of oscillation.

Similarly, mechanical work is repaid by the droplet to the ambient fluid on its side when it expands in an oblate shape. Since this time the typical speed is $A.f$, the work done by dynamical pressure on the side of a drop during a period W_{side} is written :

$$W_{side} \;=\; -c_{w2}\rho_a(Af)^2 \cdot 2\pi r^2 \cdot A \tag{V.27}$$

c_{w2} is here a coefficient of the order of 1. One can then deduce a scaling law for the amplitude of the drop oscillations by assuming a steady state of energy. This implies that both mechanical works cancel each other out

$$W_{side} + W_{front} \;=\; 0 \qquad \Leftrightarrow \qquad A \;\simeq\; \sqrt{\frac{c_{w1}.U^2}{c_{w2}.f^2}} \tag{V.28}$$

$$\Leftarrow \qquad A \;\simeq\; r \cdot We^{\frac{1}{2}} \tag{V.29}$$

As the Weber number gets close to its critical value, the amplitude of oscillations becomes larger than the radius which is consistent with the fact that the drop is prone to breakup. This scaling is represented on figure **??**. The agreement with the data is poor for a large range of droplets except for the largest ones. Other scalings based on viscous dissipation did not meet more success when compared to the data. We could not find a

scaling in the literature for the amplitude of free falling droplets presenting spontaneous oscillations.

In conclusion, the breakup of the liquid metal after its phase of deformation produces a distribution of sizes well approximated by a distribution based on a modified Bessel function of the second kind with parameters $m = 1$ and $n = 3$. This distribution allows to calculate the relevant characteristic radii for diffusive exchanges given the mean radius. The later was found to scale with We^{-1}. There are strong evidences that the slope of the distribution as a function of the droplet radii or the mean diameters is influenced by the viscosity ratio although experimental limitations did not allow to quantify precisely this effect.

Drops oscillate for viscosity ratio under 8. Their frequency is well approximated by the frequency predicted by Lamb's calculus (**?**) corrected by a factor that takes into account the near criticality of the propagation of capillary waves on the surface of the droplet. Amplitudes were recovered but a scaling is still needed to extrapolate the observations.

Drops reach their terminal velocity but are still very much influenced by each others. Our experiment has an aspect ratio of 0.3, smaller than the aspect ratio given by the self-similar solution of a turbulent thermal having a comparable coefficient of entrainment, hence the lateral extension of droplets is probably constrained by our tank at a depth of about 1.5 m. For the geophysical case, this aspect ratio is improbable thus we expect interactions between droplets to be more limited and they should reach earlier their terminal velocity if the typical velocity of the flow decreases to a point where it is comparable to their terminal velocity ($\mathcal{R} \sim 1$). We have indeed swept under the rug the description of the transition between a turbulent thermal and a cloud of droplets falling independently, a rain. Since the Weber numbers we are able to reach are limited, the ratio of length scales between the initial diapir and the drops formed after the fragmentation is small enough so that the Rouse number is on the order of 1 as soon as drops are formed : this is why the computation of the Rouse number as a function of depth was not shown. Therefore, the transition between thermal and rain happens shortly after the breakup in our experiments. This is coherent with the slope transition around $z = 20R$ seen in chapter **??**. However, assumptions on the evolution of the Rouse number as a function of depth will be made in chapter **??** in order to use the data collected on drops to extrapolate the diffusive exchanges in the divided state to the case of the post impact flow.

Chapitre VI

Integrated diffusive thermal exchanges

Let us now apply what we have learnt on the dynamic of the fall of a large mass of liquid metal in a viscous medium to the diffusive transfer during that fall. The measures of temperature differences between the liquid metal before and after its fall integrate the conditions that govern the diffusive exchanges when the galinstan deforms, when it breaks up and when it falls as a rain.

We will neglect the transfers associated with the breakup for 2 reasons. Breakup is powered by surface tension and as such corresponds to an "unstretching" procedure. The retraction of the sheets and the ligaments breakup both fit this description. Hence these flows involve a reduction of the interfacial area and probably a local dilatation of the gradients. This is in opposition to stirring processes that involves contraction of gradients that enhances them and therefore speed up diffusion. Secondly, breakup happens when the local dynamic has a larger characteristic time than the breakup time. Therefore, advection should be negligible perpendicular to the interfaces moved by the breakup in all its forms. Concerning advection due to the flow parallel to the retracting surfaces, it is more than likely that its effect can be neglected because the retraction of the liquid metal will involve the liquid metal flowing in its own diffusive boundary layers.

Yet, the possibility of diffusive transfer before and after the breakup implicitly introduces a supplementary parameter that makes the partition between the time available for diffusive transfer before breakup and the time available after breakup. This parameter is somewhat constrained by the values of breakup time. However we have seen that the formation of droplets could happen continuously during the phase preceding the apparition of holes at the front interface of the diapir, that is to say it could be a continuous process instead of a unique event. Additionally, there may be a latency time for the droplets to reach their permanent regime of advection-diffusion after the breakup. These incertitudes could obviously be addressed by additional experiments which would specify the kinematics of the flow inside the diapir. Here, we will resort to hypothesis.

A Time scale of thermal equilibration of an unbroken diapir.

First, the deformation of the liquid metal prior to breakup can have tremendous repercussions on its equilibration time scale. Here we explore two different theories that

are relevant for the two regimes of advection-diffusion of an unbroken but highly deformed liquid metal mass.

1 Advection-diffusion from an interface passively advected in turbulence - crumpled sheet model

In the crumpled sheet model, the diffusion of a scalar of interest is slow compared to the dynamics of the flow ($Pe \gg 1$). Nevertheless, only diffusion can make the scalar cross the interface. Thus advection is setting the length scale upon which diffusion acts near the interface but since it is still a diffusion limited process the overall quantity of scalar exchanged is proportional to the area of the interface between the two fluids. In a reasoning developed thoroughly in **?**, a case is made for the importance of diffusive transfers before the breakup because of the large interfacial area during this phase. The main reason for this approach, and a hypothesis of the theory itself, is that the interface could increase by several orders of magnitude by cumulative deformation created by turbulence across scales.

This is due to the fact that the particular randomness associated with turbulent motions at all scales is producing fractal interfaces. In fully developed 3D homogeneous turbulence, a material surface passively advected by turbulence should have a fractal exponent D close to $\frac{8}{3}$ (**?**). The flows we are interested in are in the limit of asymptotically large Weber number, which implies that surface tension should have a negligible influence over a wide range of scales as the inertia of the flow is much larger. In our case, one can expect the interface between liquid metal and ambient fluid to be fractal in nature (**?**). A truly fractal surface in the mathematical sense would be infinite and therefore an interface between two phases would bear an infinite energy in a finite mass. Thus the fractal nature of the surface holds until a cutoff length scale l^* below which turbulence is damped. In this context, the area of the interface S writes :

$$S = S_0 \cdot \left(\frac{l^*}{R}\right)^{2-D} \tag{VI.1}$$

S_0 is here the interfacial area measured by only considering the large scales. Typically one could choose for our diapir either the surface of a sphere or a torus, that is to say S_0 is of the order of $4\pi R^2$. There are 2 forces that can damp the turbulent movements at small scale. The Laplace pressure due to surface tension is of the same order of magnitude as the dynamic pressure fluctuations due to turbulence at the Hinze scale r_σ. Alternatively viscosity is also bound to overcome turbulent motions at the Kolmogorov scale l_ν. It is therefore reasonable that l^* would be chosen to scale as the largest of these two scales. However, in reality the turbulent movements are affected by viscosity before the Kolmogorov scale. The scale at which two distant fluid particles start to have their movements coupled by viscosity is the Taylor microscale l_λ. It has been shown experimentally that in the 2D case this length scale can indeed be the most relevant to approximate l^* (**?**). It is generally observed that the ratio between the Taylor microscale and the Kolmogorov length scales as (**?**) :

$$\frac{l_\lambda}{l_\nu} \sim Re^{\frac{1}{4}} \tag{VI.2}$$

The scaling for l_ν (cf. chapter **??**) yields :

$$l_\lambda \sim R \cdot Re^{-\frac{1}{2}} \tag{VI.3}$$

Secondly, the other ingredient for the transfer between the two phases that is imposed by the kinematics of the flow is the gradient of temperature across the interface. One constraint must be respected, only diffusion can make a scalar cross the interface. Yet it is the typical time of surface renewal at the scale of the boundary layer that sets the time scale at which diffusion acts, and therefore the length scale on which the gradients are built across the interface. One simplification can be added in the case of the transfer of heat : the capacity to conduct heat, the thermal conductivity, is orders of magnitude higher for liquid metals compared to the mixture water/UCON oil or silicate magma. The capacity to store, the specific heat is typically lower but of the same order of magnitude (cf. table **??**). Therefore the liquid metal will always be much more efficiently mixed than the ambient fluid. Only the gradients on the side of the ambient fluid need to be considered.

In turbulence, every length presents movements that can renew the surface (**?**) and therefore impose the gradients. However, the relative advection time associated with these movements scale with the length at which they take place. In the inertial sub-range, the velocity fluctuations u at scale l give a local turnover time scale t that is a decreasing function of l :

$$u \sim U \cdot \left(\frac{l}{R}\right)^{\frac{1}{3}} \qquad \Rightarrow \qquad t \sim \frac{R}{U}\left(\frac{l}{R}\right)^{\frac{2}{3}} \tag{VI.4}$$

This makes the smallest scale of turbulence the most important for the surface renewal. If we suppose that turbulence is not altered significantly by the presence of the interface (it stays homogeneous and isotropic even at short distance) the shorter time scale of advection is the time scale at the Kolmogorov length scale (**?**, **?**, **?**). Hence, the length scale l_T on which the gradient of temperature in the boundary layer is built is the length of diffusion based on the turnover time scale at the Kolmogorov length scale. It can be expressed the following way :

$$l_T = \sqrt{D_T \cdot \frac{R}{U} \cdot \left(\frac{l_\nu}{R}\right)^{\frac{2}{3}}} \qquad \Rightarrow \qquad l_T = R \cdot Pe_T^{-\frac{1}{2}} \cdot Re^{-\frac{1}{4}} \tag{VI.5}$$

Let us now go back to the balance equation concerning the total amount of heat contained in the liquid metal :

$$\frac{dT}{dt} \simeq \frac{\rho_a\, Cp_a}{\rho_m\, Cp_m} \cdot \frac{S}{V} \cdot D_{T/a}\, \frac{\Delta T}{l_T} \tag{VI.6}$$

We simplify this linear equation by just considering the excess of temperature (negative or positive) of the liquid metal compared to the ambient fluid (on average). Taking the surface at the large scale S_0 as the surface of the equivalent sphere of liquid metal allows to have a simple expression for the ratio surface over volume that yields :

$$\frac{dT}{dt} \simeq \frac{\rho_a\, Cp_a}{\rho_m\, Cp_m} \cdot \frac{D_{T/a}}{R^2} \cdot \left(\frac{l^*}{R}\right)^{2-D} \cdot Pe_T^{\frac{1}{2}} \cdot Re^{\frac{1}{4}} \cdot T \tag{VI.7}$$

Both in the experiments and in case of the post impact flow the underlying constraint is a fixed depth of fall. We then transform the equation **??** in variable z :

$$\frac{dT}{dz} \simeq \frac{1}{R} \cdot \frac{\rho_a \, Cp_a}{\rho_m \, Cp_m} \cdot Pe_T^{-\frac{1}{2}} \cdot Re^{\frac{1}{4}} \cdot \left(\frac{l^*}{R}\right)^{2-D} \cdot T \tag{VI.8}$$

From equation **??**, one extracts the typical length scale of equilibration l_{eq} of a diapir prior to its breakup is :

$$l_{eq} = R \cdot \frac{\rho_m \, Cp_m}{\rho_a \, Cp_a} \cdot Pe_T^{\frac{1}{2}} \cdot Re^{-\frac{1}{4}} \cdot \left(\frac{l^*}{R}\right)^{D-2} \tag{VI.9}$$

We have three possible candidates for the length scale at which the interface is smoothed and that determines the range of scales where the interface can be described as a fractal. In consequence, we consider three possible length scales of equilibration :

Taking $l^* = l_\nu$ yields :

$$l_{eq} = R \cdot \frac{\rho_m \, Cp_m}{\rho_a \, Cp_a} \cdot Pe_T^{\frac{1}{2}} \cdot Re^{-\frac{1}{4}-\frac{3}{4}(D-2)} \tag{VI.10}$$

Taking $l^* = r_\sigma$ yields :

$$l_{eq} = R \cdot \frac{\rho_m \, Cp_m}{\rho_a \, Cp_a} \cdot Pe_T^{\frac{1}{2}} \cdot Re^{-\frac{1}{4}} We^{-\frac{3}{5}(D-2)} \tag{VI.11}$$

Taking $l^* = l_\lambda$ yields :

$$l_{eq} = R \cdot \frac{\rho_m \, Cp_m}{\rho_a \, Cp_a} \cdot Pe_T^{\frac{1}{2}} \cdot Re^{-\frac{1}{4}-\frac{1}{2}(D-2)} \tag{VI.12}$$

It is crucial to remember here that this is not a three way alternative. The Taylor microscale is always larger than the Kolmogorov scale. But since it is still unclear for us if the fractal nature of the interface is killed by viscosity at the Kolmogorov length scale or at the Taylor length scale, both are considered as an alternative for Hinze length scale. However, given the fact that even in Deguen and colleagues (**?**), the length scale where the fractal nature of the interface disappeared was larger than r_σ, we will favor an alternative between Hinze and Taylor scale. The largest of the two is the most likely the one setting the order of magnitude of l^*. In our system, we have mainly varied our Reynolds number with the viscosity of the ambient fluid, therefore r_σ is only smaller than l_ν for the highest viscosity. In that particular case the ratio between r_σ and l_ν is still of order one, hence the scaling of l_{eq} built with r_σ seems the most adequate to interpret our data. In contrast, because of the particular case of the free fall, we have $Re \sim R^{\frac{3}{2}}$ and $We \sim R^2$. This means that $l_\lambda \sim R^{\frac{1}{4}}$ and $r_\sigma \sim R^{-\frac{1}{5}}$. In that context, the asymptotic scaling for l^* in the limit of large radius is certainly following the same one as l_λ.

Lastly, an interesting bridge between this theory and our experimental results can be made. If the surface of the liquid metal is indeed fractal up until the moment of breakup, it means that its value at that point can be approximated by taking a large scale radius of the order of 10 initial radius. This gives for the surface at the moment of breakup S_{bk} :

$$S_{bk} \simeq 4\pi 100 R^2 \cdot \left(\frac{l^*}{R}\right)^{2-D} \tag{VI.13}$$

If one builds a length scale with this surface and the actual volume of the diapir, it yields a scaling for the average thickness of the liquid metal h_{bk} :

$$h_{bk} \;=\; \frac{4\pi R^3}{3S_{bk}} \;=\; \frac{1}{300}\cdot R\cdot\left(\frac{l^*}{R}\right)^{D-2} \tag{VI.14}$$

If we are in the case where the Hinze scale is the largest of the scale able to smooth the interface liquid metal/ ambient fluid, h_{bk} is expressed the following way

$$h_{bk} \;=\; \frac{1}{300}\cdot R\cdot We^{-\frac{3}{5}(D-2)} \tag{VI.15}$$

The fractal dimension D is close to $\frac{8}{3}$ for homogeneous isotropic turbulence and is likely to be between $\frac{8}{3}$ and 2 due to the fact that turbulence may be structured by the presence of a toroidal vortex at the scale of the diapir.

If the Hinze scale is not the one determining l^*, then l^* is higher than r_σ and therefore expression given by equation **??** is a lower bound for h_{bk}.

Let us now compare h_{bk} to the scale at which the Taylor-Culik speed of retraction compensates the speed of the diapir. This seems to be the scale that the liquid metal reaches just before fragmenting into droplets (cf. chapter **??**). According to our experiments, this length scale h_{tl-ck} is related to the large scale flow :

$$h_{tl-ck} \;\simeq\; R\cdot We^{-1} \tag{VI.16}$$

Consequently, in any case the asymptotic ratio of h_{bk} over h_{tl-ck} is higher than one. This is coherent with a process of drop formation for which the fragmentation comes from a local intense stretching at the rear of the diapir where it reaches the length scale h_{tl-ck}. Meanwhile the rest of the liquid metal stays relatively thick because it has its own deformation dynamic (its width is closer to h_{bk}). We argue that this is what happens in our experiments as the galinstan sheet stays stable until the breakup distance is reached (its average Taylor Culik speed stays too low on average to fight against deformation, except on the side).

2 Stretching enhanced diffusion theory

In the previous theory, it is assumed that gradients of scalar that rule the transfer are built on a length scale which is set by diffusion during a particular advection time scale. In that regime diffusion is slower than advection. The transient phase of gradient build up can be ignored because advection imposes steep gradients. We now consider a situation where diffusion becomes as strong as advection in both fluids, that is to say the local Péclet Pe number is of order one. This is a configuration where the transfer of scalar during the phase of gradient building is large enough for the metal to nearly equilibrate. It is indeed a change of equilibration regime that implies a different time scale.

This conceptualization comes from the fact that stretching is enhancing the effect of diffusion. Given a constant stretching rate, a patch of a scalar in thermodynamical disequilibrium will be stretched until its width is thin enough for the diffusion to be as fast as the stretching (**?**, **?**). The dimension of the volume of material that initially contains the patch follows then an exponential decrease :

$$s(t) \;=\; s_0 \exp\;(-\gamma t) \tag{VI.17}$$

γ is here the stretching rate $\frac{U}{s_0}$. The width at which the diffusion compensates stretching is called the Batchelor length scale l_B. Assuming the stretching rate constant, it is found by simply setting the local Péclet number to 1 :

$$\frac{l_B^2\,\gamma}{D_T} \;\simeq\; 1 \qquad \Rightarrow \qquad l_B \;\simeq\; s_0 \cdot Pe^{-\frac{1}{2}} \tag{VI.18}$$

Since the diffusion goes as fast as the advection, once the Batchelor length scale is reached only one advection time is needed for all the scalar to cross the material contour it was initially confined in.

A precise relationship for typical time of equilibration can be rigorously determined by non-dimensionlizing the advection-diffusion equation by the local length scale $s(t)$ and replacing the time by a time warped by the local diffusion time scale $D_T \int \frac{1}{s(t)^2} dt$ (**?**, **?**). It gives :

$$\tau_{eq} \;=\; \frac{1}{2\gamma} \cdot \ln\left(1 + 2Pe\right) \tag{VI.19}$$

This theory is blind to the fact that we are interested in a two phase flow and can indeed be applied to our problem provided we take into account the fact that the patch of scalar is here contained in the liquid metal. As such, the patch stretching will be stopped by surface tension at a scale that it is crucial to compare to the Batchelor length scale (**?**). In our case, the relevant length scale that would correspond to the limit value for $s(t)$ seems to be the length scale h_{tl-ck} at which the Taylor-Culik speed of retraction of the liquid metal sheet is matching the speed of the flow.

A contentious point is the determination of the Batchelor length scale itself. If we suppose that the stretching rate that sets the length scale at which Taylor-Culik matches the speed of the flow is the large scale stretching rate, it is reasonable to assume the same for the Batchelor length scale. It is indeed conceivable that turbulence is not well developed in the ambient fluid at the location where the liquid metal film is the thinnest. This would take place at the rear of the diapir just before the ambient fluid is entrained inside it. Since it takes about one dynamical time for the unperturbed ambient fluid at the front of the diapir to get to the rear of the diapir, turbulence might not be developed at this point. The Batchelor length scale would therefore scale similarly to the idealized case (cf. equation **??**).

Alternatively we can suppose that the local stretching rate is determined by the turbulence. Since for our problem the Prandtl or Schmidt number is always larger than 1, the local Reynolds number is always reaching a value of the order of 1 before the local Péclet as we go downscale. In the case of fully developed turbulence the Batchelor length scale is therefore smaller than the Kolmogorov length scale, which means we have to use the stretching rate at the Kolmogorov length scale.

$$\frac{u(l_\nu)}{l_\nu} \sim \frac{U}{R} \cdot Re^{\frac{1}{2}} \tag{VI.20}$$

The constraint of the the local Péclet to be of the order of one yields :

$$\frac{l_B^2 \cdot \frac{u(l_\nu)}{l_\nu}}{D_T} \simeq 1 \qquad \Rightarrow \qquad l_B \simeq R \cdot Pe_T^{-\frac{1}{2}} \cdot Re^{-\frac{1}{4}} \tag{VI.21}$$

Let us now compare the Batchelor length scale to the minimal length scale that can be reached by the liquid metal. For our experiment, the thermal diffusivity of the ambient fluid is so low (of the order of 10^{-7} $m^2.s^{-1}$) that the Batchelor length scale is always smaller than the length scale at which the liquid metal is stretched just prior to its breakup. In the most conservative case (the stretching rate at large scale), the ratio of the two length scales is $\frac{We}{Pe_T^{\frac{1}{2}}}$. This ratio for our parameters has a maximal value of 0.1. Since the Batchelor length scale is at least 10 time smaller than the typical size of the liquid metal sheet at the breakup, we will neglect the effect of stretching enhanced diffusion for the interpretation of our measurements of temperature.

In conclusion, our experiments suggest that the extreme stretching that is driving the formation of droplets is not necessarily equal the average stretching undergone by the liquid metal as a whole. The evolution of the average thickness can be different from the one of the region where fragmentation occur, therefore the time scales of equilibration of the crumpled sheet model and of the stretching enhanced diffusion both seem relevant for the overarching problem of the post impact flow.

B Time scale of thermal equilibration in the divided state

We now develop length scales of equilibration for the liquid metal when it is in the form of a cloud of droplets. As stated above, the Batchelor length scale in our experiments is most likely smaller than the size of the drop, therefore the following reasoning for the transfer will assume that we are limited by diffusion. For a cloud of drops, a complexity comes from knowing whether the flow can pass through it or not. As a result, the large scale advection speed and the speed at the scale of the drops that is determining the gradient of scalar can be related in different ways.

1 The case of individual drops

Here we consider a drop for which the large scale advection speed and the speed at the scale of the drops are the same. As seen in chapter **??**, for a single non-oscillating drop falling freely in a quiescent medium with a higher viscosity, the time scale for surface renewing in the boundary layer is the advection time scale at the scale of the drops $\frac{r}{U}$ (**?**, **?**, **?**, **?**, **?**). Therefore the time scale of equilibration writes :

$$\tau_{eq} \; = \; \frac{r^2}{D_{T/a}} \cdot \frac{\rho_m \cdot Cp_m}{\rho_a \cdot Cp_a} \cdot Pe_d^{-\frac{1}{2}} \tag{VI.22}$$

Pe_d is here the Péclet number of the drop. Hence, the equilibration length can be expressed as :

$$l_{eq} \; = \; r \cdot \frac{\rho_m \cdot Cp_m}{\rho_a \cdot Cp_a} \cdot Pe_d^{\frac{1}{2}} \tag{VI.23}$$

Given our scaling for the size of the droplets, the length scale of equilibration can be expressed as a function of the Weber number and the large scale Péclet number :

$$l_{eq} \;=\; R \cdot \frac{\rho_m \cdot Cp_m}{\rho_a \cdot Cp_a} \cdot Pe_T^{\frac{1}{2}} \cdot We^{-\frac{3}{2}} \cdot \left(\frac{u_d}{U}\right)^{\frac{1}{2}} \tag{VI.24}$$

$\frac{u_d}{U}$ is the ratio between the speed of the drop and the large scale flow that comes from the droplet's Péclet number. In the case of drops falling freely, this term is rather complex as it involves the drag coefficient curves as a function of the apriori dimensionless number of the drops Bo, Mo, R_μ and $\tilde{\rho}$ in order to calculate their terminal velocity.

However for our experiments, we are departing from the simple theory of freely falling drops in a quiescent medium. It is crucial to remember that in our experiments the drops have a Rouse number $\mathcal{R}$ close to one as soon as they form because of the limited separation of scales between them and their parent diapir. This means that the transition from a cloud of droplet falling as a turbulent thermal to a rain is happening soon after the breakup (**?**, **?**, **?**, **?**). However, the limited depth of fall of our setup also means that the velocity of the cloud of droplets has not entirely relaxed by the end of its fall (cf. chapter **??** fig. **??** and **??**). The drops are in a sense inheriting their velocity from the diapir and have not yet slowed down. Although we could not measure the individual drop velocities in the first setup because of the drops volume fraction, it is at this point reasonable to assume that they never slowed down to their terminal velocity. We assume then that their speed is a fraction of the large scale speed :

$$\frac{u_d}{U} \;=\; c_v \tag{VI.25}$$

In the absence of data relating the velocity of the droplets in this transition between turbulent thermal and independent fall, c_v is treated here as a constant dependent on the viscosity ratio.

The fact that the advection speed of the droplets can be different from the speed that is setting the gradients at the interface of the drops means that an other length scale of equilibration is necessary for the case of droplets in a turbulent thermal. As we mentionned earlier, our proximity with the transition in terms of Rouse number makes this scenario equally plausible to the previous one. In the case of the fall of the turbulent thermal, the large scale speed will not be the one experienced by the individual droplets. They will mainly experience the local movements of the turbulence.

Since the gradients of velocity at Kolmogorov scale have the smallest turnover time, this is likely to be the time scale at which the surface of the drops are renewed (**?**). The large scale speed is now replaced by the speed at the Kolmogorov scale, hence the terms in Pe_d become $Pe_T \cdot Re^{\frac{1}{2}}$ in the determination of the diffusive length scale l_T on which the gradients are built :

$$l_T \;=\; \sqrt{D_T \cdot \frac{R}{U} \cdot Re^{-\frac{1}{2}}} \;=\; R \cdot Pe_T^{-\frac{1}{2}} \cdot Re^{-\frac{1}{4}} \tag{VI.26}$$

With our scaling for the size of the droplets, this yields for the time scale of equilibration :

$$\tau_{eq} \;=\; \frac{R^2}{D_{T/a}} \cdot We^{-1} \cdot \frac{\rho_m \cdot Cp_m}{\rho_a \cdot Cp_a} \cdot Pe_T^{-\frac{1}{2}} \cdot Re^{-\frac{1}{4}} \tag{VI.27}$$

Since the drops are falling in the turbulent thermal at the large scale advection speed, the length of equilibration is simply :

$$l_{eq} \;=\; R \cdot \frac{\rho_m \cdot Cp_m}{\rho_a \cdot Cp_a} \cdot Pe_T^{\frac{1}{2}} \cdot Re^{-\frac{1}{4}} \cdot We^{-1} \tag{VI.28}$$

Lastly for oscillating drops, we have supposed that they are well mixed with respect to temperature, in consequence the effects of oscillations are mostly limited to an increase of the surface of exchanges (**?**, **?**). Because a significant increase of the time averaged surface mainly concerns very big drops that have a low participation in the distribution of sizes, we will suppose that this effect is negligible in front of the experimental variations.

2 Equilibration time scale of a distribution of droplets

The evolution of the average temperature $\overline{T}$ of a distribution of sizes integrates all the time scales of equilibration of droplets :

$$\frac{d\overline{T}}{dt} \;=\; \frac{1}{R^3} \int_0^{+\infty} n(r) \cdot r^3 \cdot \frac{dT(r)}{dt}\, dr \tag{VI.29}$$

$$\Rightarrow\; \frac{d\overline{T}}{dt} \;=\; \int_0^{+\infty} n(r) \cdot \left(\frac{r}{R}\right)^3 \cdot \frac{S}{V}(r) \cdot D_T\, \frac{1}{l_T(r)}\, T(r) \tag{VI.30}$$

If drops have the same initial temperature, the value for the time scale at early time depends on the integration of the boundary layer thickness $l_T(r)$ on which the gradient is built. This can involve different moments of the distribution of sizes depending on the scaling for this length as a function of the radius of the droplet. For example, the Sauter mean radius R_{32} is certainly the best in case of turbulent boundary layers. On the contrary, when droplets are falling freely, the most important radius depends on the regime of fall (Stokes or Newton).

In our case, we will see that the quantity of lost heat puts us in a case far from the start of the evolution where the temperature in all the drops can be supposed equal. Instead, the drops that represent the most part of the mass and therefore are able to retain the most heat $n(r)r^3T(r)$ are certainly the ones imposing their time scale of equilibration to the distribution ; hence we will use the volume mean radius in the following part to calculate the time scale of equilibration in the divided state.

C Comparison with the thermal measurements

The non-dimensional differences of temperatures T^* were transformed in experimental length scales of equilibration L_{equ} by assuming an exponential decrease of the temperature (because of the linearity of the advection-diffusion equation) as a function of depth with the expression :

$$L_{equ} \;=\; -H \cdot \frac{1}{ln\,(T^*)} \tag{VI.31}$$

H is here the depth of fall of the experiment. The length scales of equilibration developed for the diapir in its unbroken state and in its divided state are reported in figure ?? and ??.

The length scales of equilibration corresponding to the crumpled sheet model with the cutoff length scale equal to r_σ and the ones with the cutoff length scale equal to l_λ are shown alongside with the experimental length scales of equilibration in figure ??. The equilibration length scale with the Hinze scale r_σ seems more accurate in predicting the trends both in viscosity and in initial radius. The use of the Taylor length scale results in an overall overestimation of the effect of viscosity for our experiments which is coherent with the fact that the Hinze length is larger and therefore more suited in that case.

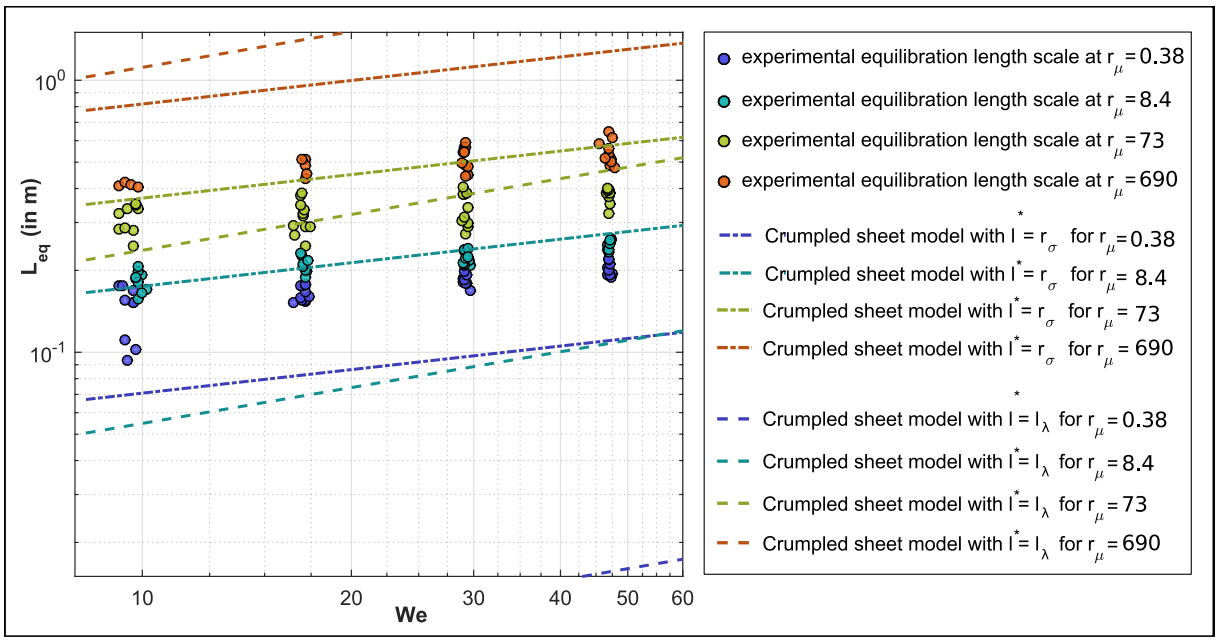

FIGURE VI.1 – Graph of the equilibration length scale in the unbroken state for all viscosity ratios as a function of the Weber number. The experimental length scales are represented by colored circles. The crumpled sheet theory was calculated for a cutoff length scale equal to the Hinze scale (dashed-dotted lines) and for a cutoff length scale equal to the Taylor microscale (dash lines).

The length scales of equilibration corresponding to drops falling at a velocity inherited from the diapir with a laminar boundary layer and the one with a turbulent boundary layer are plotted alongside with the experimental length scales of equilibration in figure ??. Both theoretical equilibration length scales decrease rapidly when the Weber number increases as a consequence of the rapid increase of the surface to volume ratio (cf. the decrease in the typical size of droplets). However, part of the decrease is also due to the assumption made on the length scale of the thermal gradient in the boundary layer which relied on heavy assumptions on the speed of the flow.

We test the possibility that the length scale of equilibration of an unbroken diapir l_{un} and the one for the divided state l_{div} have to be used successively to explain the integrated thermal exchanges. We have taken for l_{un} the length scale of equilibration of the crumpled sheet with a cutoff length scale $l^* = r_\sigma$. We have taken for l_{div} the length scale of equilibration of droplets having inherited their speed from the large scale and a laminar

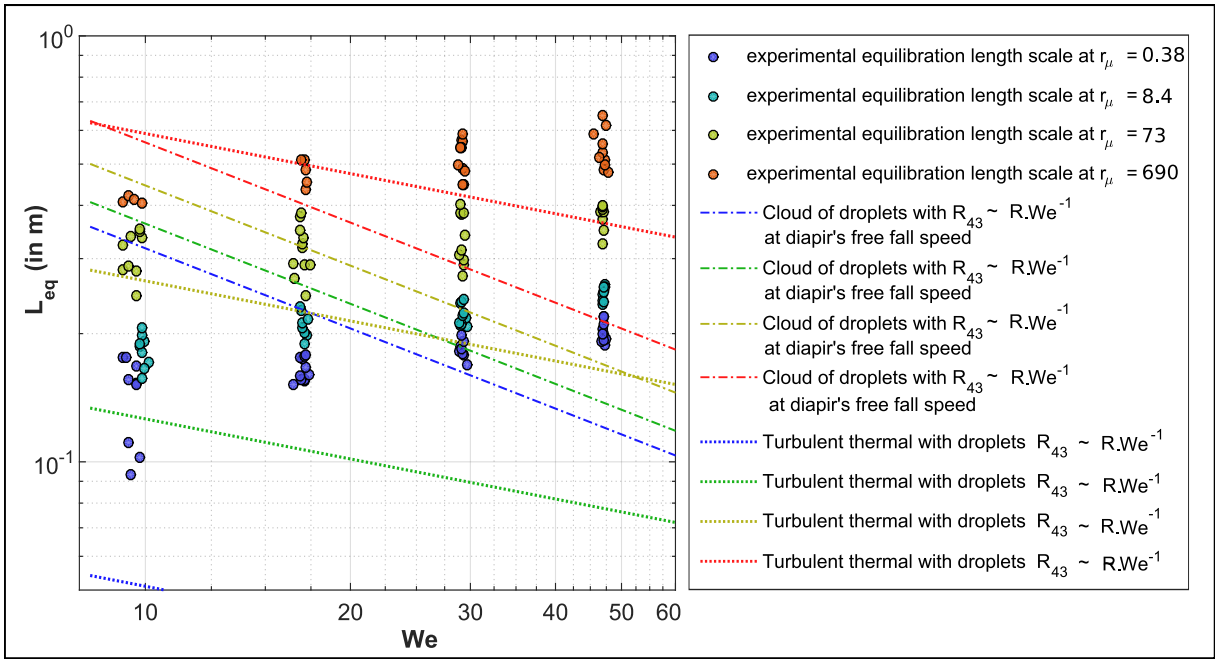

FIGURE VI.2 – Graph of the equilibration length scale in the divided state as a function of the Weber number. Colored circles are the experimental equilibration length scales. The equilibration length scales calculated assuming a laminar boundary layer are plotted for all viscosity ratios in dash dotted lines. The shifts are uniquely due to the different conductivities and specific heat of the different mixtures of water and UCON oil. The equilibration length scales calculated assuming a boundary layer dominated by turbulence are plotted for all viscosity ratios in dotted lines.

boundary layer. These choices are made for their trend concerning the heat transfer as a function of viscosity of the ambient fluid as well as for their coherence with all other observations and data.

In first approximation, in order to integrated the effect of the transfer in the unbroken state and the one in the divided state, we have assumed that the length scales of equilibration are constant and are appliable one after the other. This yields an exponential decrease of the temperature for the two phases of the fall. In order to produce theoretical final differences of temperature T^*, the exponential decrease due to the transfers in the unbroken state gives the temperature at breakup and multiplying it by the decrease due to the transfer in the divided state gives the following expression for the final temperature :

$$T^* = \exp\left(-\frac{R \cdot l_{bk}}{b.l_{un}}\right) \cdot \exp\left(-\frac{H - R \cdot l_{bk-m}}{a.l_{div}}\right) \tag{VI.32}$$

a and b are constant that were kept of the order of one, l_{bk-m} is the breakup length that is of the order of 10.

This equation with the set of parameters that fits the best the experimental T^* is reported in figure **??** together with the experimental T^*. The right range of T^* considering the range of the viscosity was attained for the largest size of diapir but a decreasing trend is predicted, in entire contradiction with the data. This trend is most certainly due to the length scale of equilibration for the divided state which is heavily influenced by the size of

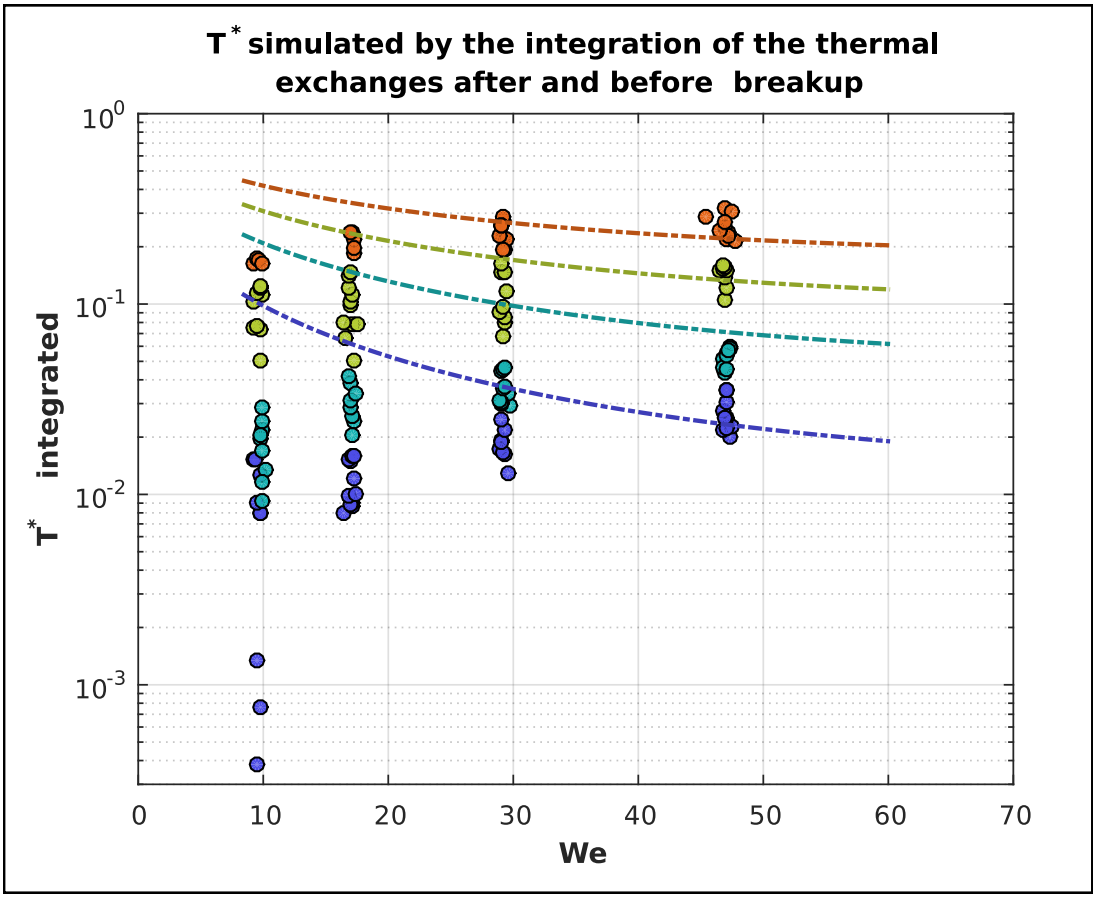

FIGURE VI.3 – Graph of the temperature difference calculated at the bottom of the tank by integrating the transfers before and after the breakup as a function of the Weber number plotted alongside with the experimental temperature differences (circles). The crumpled sheet model with a cutoff length scale equal to the Hinze length scale is used for the transfer before breakup. The length scale of equilibration of drops falling at the diapir's speed with a laminar boundary layer is used for transfers after fragmentation.

droplets. Indeed, the typical size of the drops is rapidly decreasing as a function of the Weber number. In an article published during the course of this study (**?**), we hypothesized that the mean radius of droplet was controlled by the capillary length scale l_σ, leading to a closer fit of the data. With further data on the size of droplets as a function of the Weber number, this agreement was improved for the tendency with respect to the influence of viscosity but worsen for the agreement with respect to the initial radius of the diapirs.

The most likely explanation for this discrepancy given the fact that the biggest diapirs are the ones for which the prediction is the most accurate is the fluid kinematic of the transition between turbulent thermal and rain. This transition seems to highly influence the heat transfer in our experiments. The hypothesis of droplets having at the moment of this transition a speed inherited from the large scale that is both relevant for setting the scale large scale advection and setting the width of the thermal boundary layer is conservative but seems insufficient. Alternatively, the fact that droplets become smaller when the speed of fall of the diapir becomes greater (i.e when Weber increases) means that their transition from turbulent thermal to rain will make them experience large scale

advection speed not necessarily related to the slip velocity at the scale of their interface (the transition indeed involves two speed scales). Therefore it is possible that the ratio between the two speeds that experience the droplets around the transition depends on the initial size of the diapir. For the smallest diapirs, droplets resulting from their breakup would have around the transition their large scale advection speed smaller and their slip speed at their interface larger, comparatively to droplets resulting from the breakup of larger diapirs. Consequently, the equilibration length scale of droplets resulting from the breakup of a small diapir would be overestimated compared to length scale of equilibration for the one resulting from the breakup of a large diapir.

In a very raw manner, we can take into account this effect by adding a parameter corresponding to the length scale of transition l_{trans}. We assume that in this transition the diffusive transfers are negligible because of the minimization of the ratio between the two speeds that experience the droplets. If we pose that this length scale of transition is proportional to R, the normalized temperature difference becomes :

$$T^* \;=\; \exp\left(-\frac{R\cdot l_{bk}}{b.l_{un}}\right)\cdot\exp\left(-\frac{H-R\cdot(l_{bk-m}+l_{trans})}{a.l_{div}}\right) \tag{VI.33}$$

Here the length scale of transition l_{trans} is non dimensional. This equation as well as the experimental length scales are reported in figure **??**. The agreement is better than for the previous equation but the concavity is still not well predicted. Further work are therefore needed to characterize the relevant speeds during this transition.

In conclusion, the crumpled sheet model (**?**) seems to explain reasonably well our thermal measurements and may be applied for the tranfer of scalar between a free falling diapir in a viscous medium as long as the Batchelor length scale is not reached for the majority of the mass of liquid metal. If the Batchelor length scale is reached, the equilibration is most likely happening within one advection time. Additional experiments are needed to understand the condition of heat exchanges at the transition between turbulent thermal and iron rain.

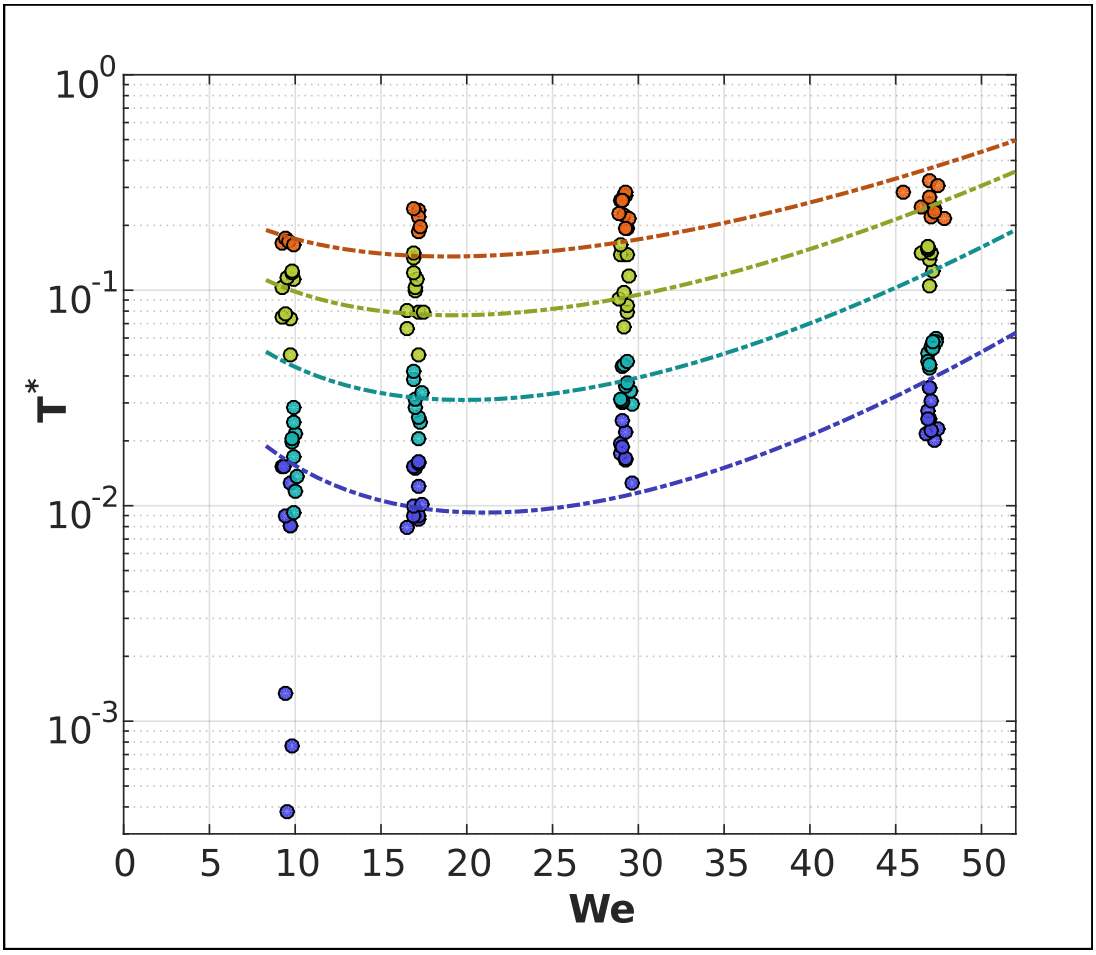

FIGURE VI.4 – Graph of the temperature difference at the bottom the tank calculated by integrating the transfers before and after the breakup as a function of the Weber number plotted alongside with the experimental temperature differences (circles). The crumpled sheet model with a cutoff length scale equal to the Hinze length scale is used for the transfer before breakup. The length scale of equilibration of drops falling at the diapir's speed with a laminar boundary layer is used for transfers after fragmentation. A parameter l_{trans} is added allowing to protract equilibration during the transition.

Chapitre VII

Conclusion on the flow following an impact between planets

When transposing the results of this study to the post impact flow, one has to be careful about the initial size of the remnant structures left over by the impact. Our initial condition indeed ignores the impact itself. Whatever the product of the mixing process during that step is, it should be taken as the analog of our initial condition. While some authors have suggested that big mass of liquid iron could stay unmixed at the surface of the magma ocean (**?**, **?**), the fact that impacts are likely to induce a large horizontal spread of the material of the impactor (**? ?**) is making a case for describing the result of the impact with two length scales. The first one is the size of the impactor's core and the second one is the typical size of the remnant structures after the impact. In such a framework, these structures would be analog to the diapirs of our experiment. However, they would probably merge within a depth of several of their initial size. From that point on, taking the length scale of the impactor's core to rescale our results to the case of the post impact flow would be more adequate. It is unclear if during this merging the relevant scale for the speed should be switched between the Newtonian speed based on the size of the remnant structures and the one based on the size of the impactor's core, or should stay the same. That is why a study on the multiscale flow taking place at the impact is much needed in order to discuss the relative importance of these two initial length scales. In the following we will summarize how the dynamics of the post impact flow as we uncovered it in our experiments can be plugged into a general model of planet building at the stage of impact between differentiated terrestrial planets.

A Equilibration equations for a turbulent thermal

We have found in our experiments that the fall, the deformation and the dilution of the liquid metal can be usefully described by turbulent entrainment. But we noticed that the initial phase of the fall was marked with discrepancies in the falling speed compared to the classical turbulent thermal or toroidal vortex. These discrepancies could have a significant effect on the diffusive exchanges in the case of a giant impact because if the initial size of the diapir is larger than one tenth of the depth of the magma ocean (i.e. of the order of 100 km) the initial phase is the only phase of the fall of the diapir that will have the depth

to develop. We support for now the use of the turbulent vortex model we have developed (cf. equation **??** chapitre IV) because of the correction regarding the dependency of the drag coefficient *cd* with respect to the circulation of the diapir. Meanwhile, the effect of the spinup of the toroidal vortex has to be confirmed with additional experiments. The goal of these experiments could be to map the density in the region contained in the surface of control. Alternatively, it could be interesting to measure the pressure difference between the front and the rear of the diapir with the help of small pressure sensors placed in the way of the diapir's fall in order to have an estimation of the work of the pressure forces in that first phase.

In addition, the ratio of the impactor's core over its mantle is a parameter that it is also important to consider. In the case of an impactor with a large core, the result of the impact is likely to start its fall from a very shallow position with respect to the surface of the magma ocean. In that case, the depth at which the remnant structures start their free fall may be small enough so as to produce large amounts of vorticity when departing from the surface. The classic turbulent thermal with lower values for the turbulent entrainment is to be used in this configuration (**?**).

By measuring the difference of the galinstan's temperature before and after its fall, we have produced data integrating the characteristics of the flow that determine the transfer of scalars. We found that transfer happens before and after the breakup (cf. chapter **??**). However, integration of the theories of transfer before and after the fragmentation is still not providing a satisfactory fit for the data. There are strong arguments in our opinion that a large portion of these discrepancies is due to the theory of the transfer in the divided state. While we know the drops size rather accurately, we were not able to inquire much about the flow at their scale which is in question because of the transition from a large scale flow (i.e. turbulent thermal) to a flow dominated by the scale of the drops (i.e. a rain). The importance of this transition phase is largely due to our moderate Weber number because it determines the separation of scales between the average drop and the initial diapir as well as their respective free fall velocities. In the geophysical flow, we expect larger Weber numbers thus shorter time of transition compared to the time of the turbulent thermal phase. Accordingly, we will keep the same hypothesis in building a more general model, neglecting the specificity of the conditions of diffusive transfer during the transition.

A general procedure to take into account the effect of impact between molten terrestrial planets goes the following way : a length scale for the initial condition must be determined. As said earlier, future experiments will have to precise how the different length scales created by the impact interplay in the post impact flow. Then, the mass of liquid iron that is quantified by this length scale falls, entraining a precise quantity of the surrounding magma that is described by the turbulent thermal model. In the meantime, it equilibrates with the fluid it has entrained integrating the condition of pressure, temperature (notably for the physical parameters), and composition (notably for the mass entrained) during the fall. This falling mass of magma and of liquid iron should in our view be treated as a third and fourth reservoirs for the planet in the models of planet building, at least temporally, because their story does not end when reaching the bottom of the magma ocean. In current models (**?**, **?**, **?**), it is assumed that they are not particular reservoir and that the falling iron equilibrates with the magma ocean at a certain depth. This means that what has been exchanged between silicate and magma at depth z stays at depth z. This is for us

the most questionable assumption made by the planet building models. If one consider the exchanges between metal and silicate to be of any importance, the location where the mass of silicate and the mass of iron in the turbulent thermal will eventually settle and mix should be treated with the same importance. They will be mixed later with the rest of the mantle and core respectively.

As pointed out recently (**?**), their mixing with the rest of the planet could happen in possibly very different ways. To be more specific, the level of neutral buoyancy of each of these two fluids is most likely determined by all their exchanges during their fall. After the settling of the iron, the entrained magma could be entirely mixed with the magma ocean if this ocean is small enough compared to the size of the impactor (**?**). It could also stay at the bottom of the magma ocean and form a partially mixed layer as a result of a gravity current if it gained negative buoyancy during the mixing with the iron (**?**). It could also reach any altitude in the magma ocean because the modification of its composition may imply a different slope of its adiabatic curve of temperature as a function of pressure and viscous dissipation of kinetic energy could affect its reference temperature. In addition, diapirism from bottom to top following the settling of iron is also a possibility (**?**, **?**). In conclusion, an alternative between these different scenarii should stay open until a quantitative estimation of the buoyancy resulting from the thermal and compositional exchanges can be made.

Our experiments were based on a simple passive scalar, the temperature, which was convenient for 2 reasons : because of the ratio of diffusivities, the temperature of the galinstan volume could be approximated as homogene. Secondly the specific heat of the ambient fluid was large enough so as not to worry about the average temperature of the entrained fluid to saturate near the initial temperature. As these features are not general for all chemical elements exchangeable between magma and silicate, we propose a general model for the evolution of the concentrations in the two reservoirs of fluid entrained in the turbulent thermal.

The dynamics of the fall being addressed by the turbulent thermal equation, two equations must be added for the evolution of the concentration of a scalar in the ambient fluid A_a and its concentration in the metal A_m as a function of time :

$$\begin{cases} \dfrac{dA_a \cdot M_a}{dt} = F + M_{Ae} \\ \dfrac{dA_m \cdot M_m}{dt} = -F \end{cases} \tag{VII.1}$$

M_a is the mass of ambient fluid at instant t inside the turbulent thermal. M_m is the mass of liquid metal at instant t inside the turbulent thermal. F is the diffusive flux between the metal and the ambient fluid. M_{Ae} is the quantity of scalar carried by the entrained fluid. When non-dimensionalized by the initial mass of liquid metal, this leads to :

$$\begin{cases} \dfrac{d}{dt}\left[A_a \cdot \left(\left(\dfrac{r}{R}\right)^3 - 1\right)\right] = \dfrac{3}{4\pi\ R^3}\ F\ +\ 3\alpha\dfrac{r^2}{R^3} \cdot v \cdot A(z) \\ \dfrac{dA_m}{dt} = -\dfrac{3}{4\pi R^3}\ F \end{cases} \tag{VII.2}$$

v is the vertical speed of the turbulent thermal and r is its radius. The term with α comes from the entrainment hypothesis and brings ambient fluid with a concentration of $A(z)$. The radius of the turbulent thermal can be expressed as a linear function of its depth, and the time derivatives can be transformed in depth derivatives, hence :

$$\begin{cases} \dfrac{dA_a}{dz} = \dfrac{3}{4\pi R^3}\dfrac{1}{\left(\left(1+\frac{\alpha z}{R}\right)^3 - 1\right)} \cdot \dfrac{1}{v}F\ +\ \dfrac{3\alpha}{R}\dfrac{\left(1+\frac{\alpha z}{R}\right)^2}{\left(\left(1+\frac{\alpha z}{R}\right)^3 - 1\right)} \cdot (A(z) - A_a) \\ \dfrac{dA_m}{dz} = -\dfrac{1}{v}\dfrac{3}{4\pi\ R^3}\ F \end{cases} \tag{VII.3}$$

Since we have not yet injected any physics into the diffusive flux F, equation **??** is a general framework that can be used for an entirely fragmented or entirely unfragmented iron diapir.

However, since our experiments suggest that fragmentation may happen continuously before the breakup length, an alternative system of equation may be needed. We now have to consider the mass flux between the continuous mass of liquid iron and the fragmented portion :

$$\begin{cases} \dfrac{dA_a \cdot M_a}{dt} = F_u + F_f + M_{Ae} \\ \dfrac{dA_{mu} \cdot M_m \varepsilon_u}{dt} = -\ F_u + A_{mu} \cdot \dfrac{dM_m \varepsilon_u}{dt} \\ \dfrac{dA_{mf} \cdot M_m\,(1-\varepsilon_u)}{dt} = -\ F_f - A_{mu} \cdot \dfrac{dM_m \varepsilon_u}{dt} \end{cases} \tag{VII.4}$$

ε_u is the mass fraction of the unfragmented portion of the molten iron. A_{mf} is the concentration of scalar in the fragmented part of the molten iron. A_{mu} is the concentration of scalar in the unbroken part of the molten iron. In first approximation one can write the mass fraction ε_u as a linear function of the depth :

$$\varepsilon_u\ =\ 1 - \frac{z}{l_{bk}} \tag{VII.5}$$

This gives the system of equations :

$$\begin{cases} \dfrac{dA_a}{dz} = & \dfrac{3}{4\pi R^3}\dfrac{1}{\left(\left(1+\frac{\alpha z}{R}\right)^3-1\right)}\cdot\dfrac{1}{v}\left(F_u+F_f\right)+\dfrac{3\alpha}{R}\dfrac{\left(1+\frac{\alpha z}{R}\right)^2}{\left(\left(1+\frac{\alpha z}{R}\right)^3-1\right)}\cdot\left(A(z)-A_a\right) \\ \dfrac{dA_{mu}}{dz} = & -\dfrac{1}{\left(1-\frac{z}{l_{bk}}\right)}\cdot\dfrac{3}{4\pi R^3}\dfrac{1}{v}\,F_u \\ \dfrac{dA_{mf}}{dz} = & -\dfrac{1}{\left(\frac{z}{l_{bk}}\right)}\cdot\dfrac{3}{4\pi R^3}\dfrac{1}{v}\,F_f\;+\;\dfrac{1}{l_{bk}}\,\dfrac{1}{\left(\frac{z}{l_{bk}}\right)}\cdot\left(A_{mu}-A_{mf}\right) \end{cases} \tag{VII.6}$$

Before integrating the systems of equations **??** and **??**, one must also parametrize the diffusive fluxes F, F_f and F_u. These diffusive fluxes are not rescaled by the volume of the mass of fluid, hence the terms $\frac{3}{4\pi R^3}\,F$ should be replaced with terms of the form $\frac{1}{l_{eq}}\Delta A$. The same type of physical considerations can be held here about the choice of relevant length scales as we have discussed in chapter **??** and therefore the same types of scalings for l_{eq} will be used (see next section for the regime diagram).

In our experiments, the temperature was a well mixed scalar in the metal. Therefore the transfer was limited by the diffusion on the silicate side of the interface. In consequence, we have used the Péclet number of the silicate so as to parametrize the gradient in the boundary layer on the ambient fluid side. The longest time of diffusion compared to the time of advection (in practice the higher Péclet number) at the interface is imposing its dynamics.

More careful considerations have to be taken for the determination ΔA (**?**). Especially for compositional equilibration, the jump of concentration between the bulk of the fluid and the interface that determines the intensity of the gradients is not trivial and depends on the conductivities and partition coefficients of the elements (see **?** for a detailed analysis on how to determine ΔA).

The coefficients like diffusivites, conductivities and partition coefficients depend on pressure and therefore on depth. Thus, it appears necessary to integrate the systems of equations **??** and **??** because the length scales of equilibration also have variation with respect to depth that they owe to the coefficients. Additionally, the need for full integration also comes from the variable partition coefficient as they imply displacements of equilibrium between metal and silicate during their fall as a turbulent thermal. Because of these displacements of equilibrium, we also could not find a satisfactory rescaling of the concentration A that would simplify the systems of equations **??** and **??**. The concentrations have to be integrated in dimensional form. After that the post "turbulent thermal" phase has to be considered. Here other remixing models redistribute the mass of scalar in the magma ocean and in the core depending on the final buoyancy of the silicate and of the iron.

Finally several caveats must be added. When the Batchelor length scale is reached the diffusion is no longer limiting the transfer. In this regime a different length scale of equilibration must be used. For objects whose size is of the same order of magnitude as the Batchelor length scale and below, a good approximation can be given by the time of diffusion based on the width of the considered object. Since even the small objects (for

example droplets) potentially fall at a speed determined by the large scales of the flow (e.g when they fall as a turbulent thermal), the length scale of equilibration is derived by multiplying this time scale with the large scale advection speed. For example our experiments suggest that the mean radius of the droplets scales as $R.We^{-1}$. When their mean radius is below the Batchelor length scale (see section **??** for the regime diagrams), their equilibration length scale is :

$$l_{eq} \;=\; U \cdot \frac{(R.We^{-1})^2}{D} \;=\; R \cdot Pe^1 \cdot We^{-2} \tag{VII.7}$$

In addition, there is a strong assumption made in the equations **??** and **??** : all the metal is equilibrating with all the silicate magma in the thermal. This problem of the fraction of ambient fluid and liquid metal that actually equilibrated with each other compared to their absolute quantity in the diapir was in fact highlighted by Deguen and colleagues (**?**). Full equilibration between metal and silicate composing the turbulent thermal is not an outrageous assumption as the turbulence in both fluids should be able to mix their interior and transport scalars from the bulk of the fluid to the interface and from the interface to the bulk of the fluid. However, a certain time is associated with this process. We propose to describe this as a random agitation problem as the representative quantity of the scalar in the bulk has to be brought by agitation to the interface but not necessarily mixed. In that framework, every quantity and every physical constant in the systems of equations **??** and **??** that depends indirectly on the depth can be taken at a smaller depth defined by the backward integration of the velocity during a time lag. This time lag is the time it takes on average for two particles to be randomly relocated in the thermal (i.e. a full agitation time scale of the system). It may be chosen as a turbulent diffusive time based on the local speed of the turbulent thermal and the typical size of the liquid considered (the local radius of diapir for the silicate and the typical width of the metal sheet for the iron).

B Transition from turbulent thermal to iron rain

Since we know the size of the drops formed by the fragmentation of a large mass of liquid iron falling in a magma ocean, and since we know the falling speed of this mass as a function of depth, let us now derive the depth from which drops should start to fall independently from each others.

In our experiment, we have found that the scaling for the average radius of the droplets likely follows $R \cdot We^{-1}$ in the explored zone of the regime diagram. We interpreted this scaling as a consequence of a fragmentation process controlled by the large scale stretching rate. This stretching produces undulations of the liquid metal and their subsequent thinning until they are thin enough to detach from the unfragmented mass.

It is still possible that this scaling is not the asymptotic scaling for R_{10} as the initial mass of liquid metal increases. As it gets larger the speed of the flow becomes larger and therefore the viscous forces become larger than the capillary forces (as measured by the capillary number Ca). This could trigger the striping of droplets at the top of the undulations grown by Kelvin-Helmholtz instabilities. Thus a somewhat likely asymptotic scaling is the one developed in **?** and in **?** :

$$R_{10} \;=\; R\cdot\tilde{\rho}^{\,-\frac{1}{3}}\frac{Ca^{\frac{2}{3}}}{We} \;=\; R\cdot We^{-\frac{1}{3}}\,Re^{-\frac{2}{3}} \tag{VII.8}$$

In the absence of experimental evidences for such a regime in our problem, let us suppose that our scaling holds until the largest Weber numbers in planetary applications. Since the average radius is decreasing so fast, the drops that are formed at very high Weber number are likely to have their terminal velocity close to the Stokes velocity :

$$U_{set}\simeq\frac{2}{9}\,\frac{\Delta\rho g R_{10}^2}{\mu_a} \tag{VII.9}$$

Drops can be stirred and stay suspended in a turbulent thermal as long as the large scale speed can overcome their settling velocity. This is equivalent to set their Rouse number to one and gives a condition for the limit speed where the drops no longer evolve as a thermal :

$$\frac{\frac{2}{9}\frac{\Delta\rho g R_{10}^2}{\mu_a}}{u(z)}\;\sim\;1 \qquad\Leftrightarrow\qquad u(z)\sim\frac{2}{9}\frac{\Delta\rho g R^2}{\mu_a}\cdot We^{-2} \tag{VII.10}$$

$u(z)$ is the speed of fall of the thermal. From the equation **??**, the asymptotic relationship for the speed of the turbulent thermal as a function of depth writes :

$$u(z)\;\simeq\;\left(\frac{\Delta\rho}{\rho_a}gR\right)^{\frac{1}{2}}\cdot\left(2\alpha^3\left(1+k+\frac{3}{16}\frac{c_d}{\alpha}\right)\right)^{-\frac{1}{4}}\cdot\frac{R}{z} \tag{VII.11}$$

Hence we can derive the transition depth between turbulent thermal and iron rain z_{ir} (**?**)

$$z_{ir}\;\sim\;R\cdot\frac{2}{9}\left(2\alpha^3\left(1+k+\frac{3}{16}\frac{c_d}{\alpha}\right)\right)^{\frac{1}{4}}\cdot\frac{\mu_a}{\rho_a^{\frac{1}{2}}\Delta\rho^{\frac{1}{2}}g^{\frac{1}{2}}R^{\frac{3}{2}}}\cdot We^2 \tag{VII.12}$$

As we have set our velocity scale to the Newtonian scaling, the dimensionless number $\frac{\mu_a}{\rho_a^{\frac{1}{2}}\Delta\rho^{\frac{1}{2}}g^{\frac{1}{2}}R^{\frac{3}{2}}}$ is equivalent to the Reynolds number based on the initial parameters. It yields for z_{ir} :

$$z_{ir}\;\sim\;R\cdot\frac{9}{2}\left(2\alpha^3\left(1+k+\frac{3}{16}\frac{c_d}{\alpha}\right)\right)^{\frac{1}{4}}\cdot Re^{-1}\cdot We^2 \tag{VII.13}$$

With the same scaling for the velocity, the Reynolds number scale as :

$$Re\sim We^{\frac{3}{4}} \tag{VII.14}$$

This implies :

$$z_{ir}\;\sim\;R\cdot We^{\frac{5}{4}} \tag{VII.15}$$

In conclusion even for a moderately large diapir (about 10 m), the diapir does not slow down enough so that the transition occurs before a depth of $10^9 m$ which is already much larger than any magma ocean.

C Regime diagram for the diffusive transfer

The regime diagrams of the relevance of the different length scales are computed for the thermal equilibration (cf fig. **??** **??**, **??**). These can also be computed for the equilibration of chemical elements knowing their diffusivity. In general the diffusivities of minor elements are at least one order of magnitude below the one of heat. This would correspond for the regime diagrams of elements to a shift down of any limit involving a Batchelor length scale approximately one order of magnitude.

The different scalings for the cutoff length scale l^* are presented in figure **??**. As mentioned in chapter **??**, the most likely relevant length scale for viscosity to smooth the interface is not the Kolmogorov length scale l_ν but the Taylor length scale l_λ. Assuming this is the correct hypothesis, it puts the planetary flows almost entirely in the part controlled by l_λ whereas our experiment is in the zone controlled by r_σ. In the large We limit, the length scale of equilibration for the unbroken part of the liquid metal should therefore be given by equation **??**. In the large Re limit, which was the case in our experiment, the length scale of equilibration should be given by equation **??**.

Figure **??** shows the different scalings for the Batchelor length scale compared to the different length scales for the unbroken part of the liquid metal. The length scale h_{tl-ck} is relevant for the width of the liquid metal just before fragmentation when a large scale stretching rate is assumed and is compared with the Batchelor length scale computed with the same hypothesis. The length scale r_σ is relevant for the width of the liquid metal just before fragmentation when a turbulent stretching rate is assumed and is compared with the Batchelor length scale computed with the same hypothesis. Our experiment indicates that fragmentation occurs for $h_{tl-ck} \sim R \cdot We^{-1}$ which is more compatible with a large scale stretching rate. This leaves the most part of planetary flow in a regime where drops are formed at the same scale or below the Batchelor length scale.

The approximate average length scale of the liquid metal h_{bk} is also compared to the largest Batchelor length scale (the one set by the large scale stretching rate). A large separation of scales between the two is found suggesting that the diapir is not entirely stretched down to the Batchelor scale prior to fragmentation (at least the part that is not fragmented). This is only based on a constant large scale surface for the fractal interface and definitely needs to be confirmed by experiments. Recent 2D numerical simulations suggest that it may not be the case (**?**).

The two Batchelor length scales are also compared to probable scalings for droplets average radius in figure **??**. Comparing the mean radius to the Batchelor length scale based on the large scale stretching rate may be interesting for the drops formation. For the long time evolution on the contrary, it is more interesting to compare their radius to the turbulent Batchelor length scale. From figure **??**, in the largest part of the region relevant for planetary flow, drops are smaller than the turbulent Batchelor length scale. In that case, the length scale of equilibration should be given by equation **??**. However, in the moderate We and Re, drops in a turbulent thermal should have an equilibration length scale given by equation **??**.

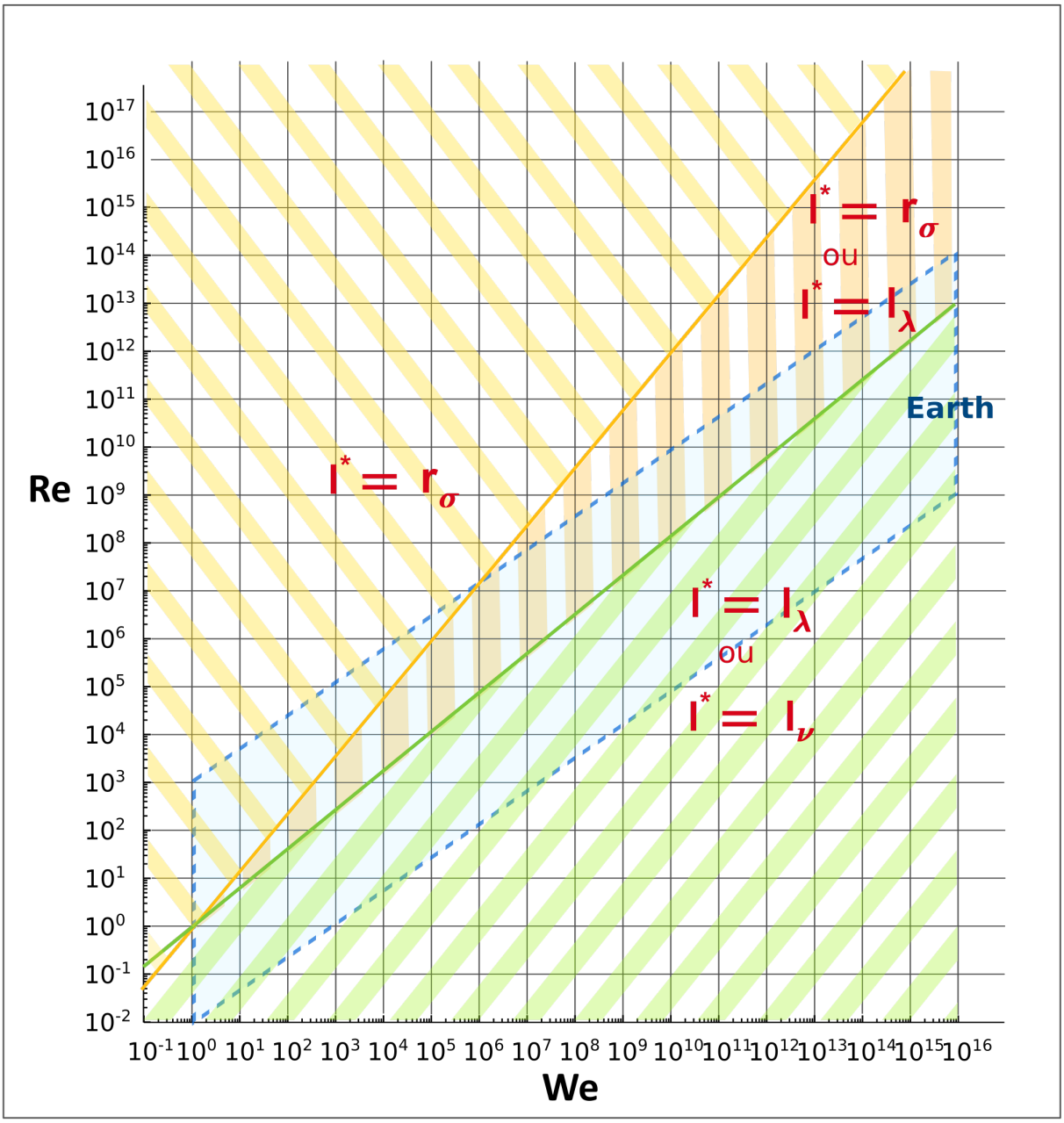

FIGURE VII.1 – Regime diagram in the plane (Re,We) for the cutoff length scale for the fractal aspect of the deformed liquid metal prior to fragmentation. That length scale determines the interfacial area between iron and silicate. The crosshatched regions are the domain of usage of the different length scales. The orange line is a characteristic line where the Hinze length scale is equal to the Taylor length scale. The green line is a characteristic line where the Hinze length scale is equal to the Kolmogorov length scale.

D Future experiments

Many important questions could be tackled by experiments in continuity with this thesis. The possibility of partially filling the balloons with air and ambient fluid on top of the liquid metal and matching the free surface in the balloon and the one in the tank

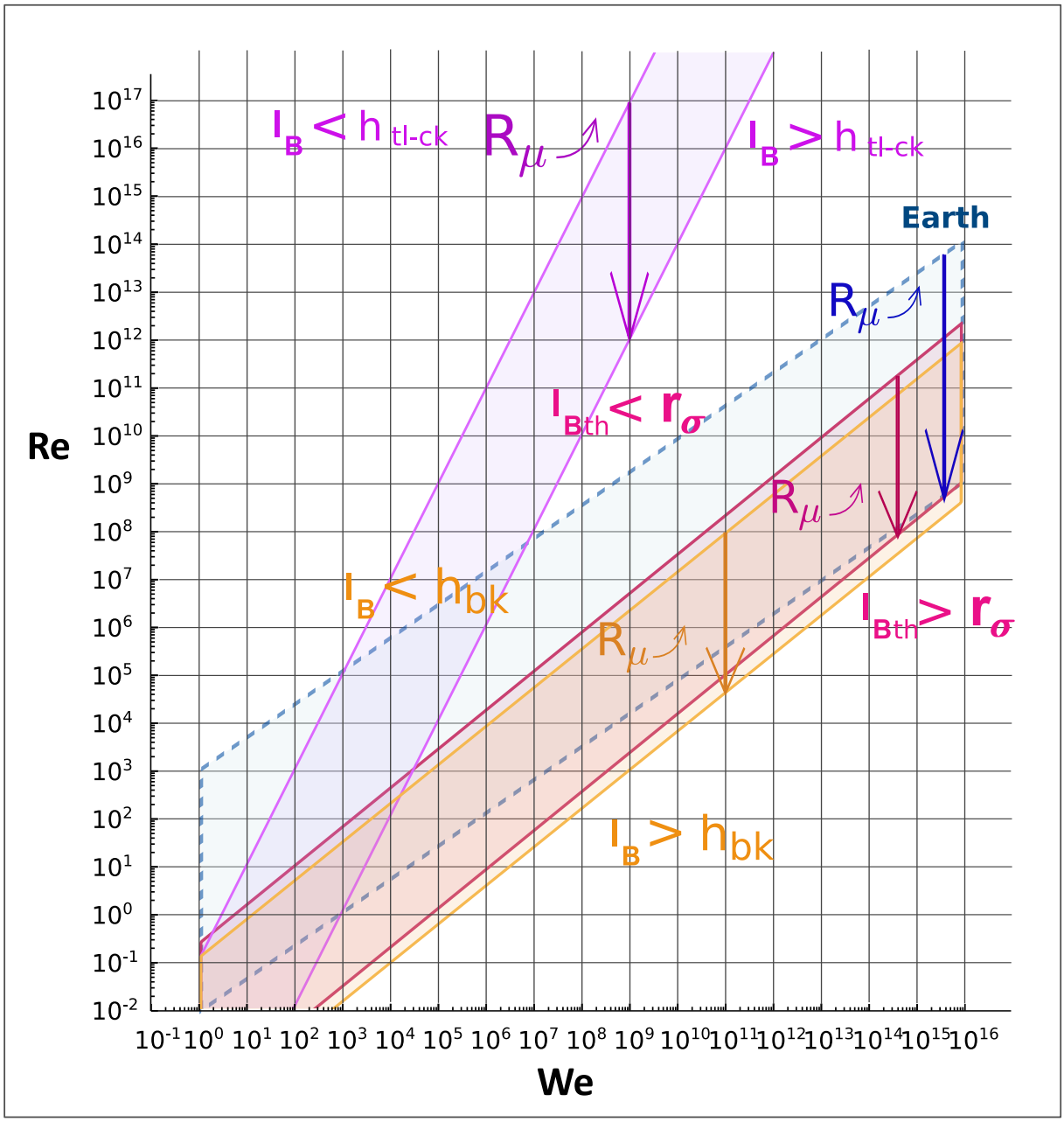

FIGURE VII.2 – Regime diagram in the plane (Re,We) of the different length scales relevant for the typical width of the metal prior to fragmentation compared to the Batchelor length scale. The zones in solid lines are the projection in the (Re,We) plane of limits that depend on the viscosity of the ambient fluid. The violet zone is the characteristic plane where the thickness of the liquid metal where it breaks up h_{tl-ck} is equal to the Batchelor length scale. The orange zone is the characteristic plane where the mean thickness of the liquid metal h_{bk} is equal to the Batchelor length scale. The fuschia zone is the characteristic plane where the Hinze scale r_σ is equal to the turbulent Batchelor length scale.

could allow a wide range of initial conditions that may be interesting to study the probable results of the impact flow. The impact flow itself is worth a lot of attention, one hope that experiments could help to understand better than simulation the mixing during oblique

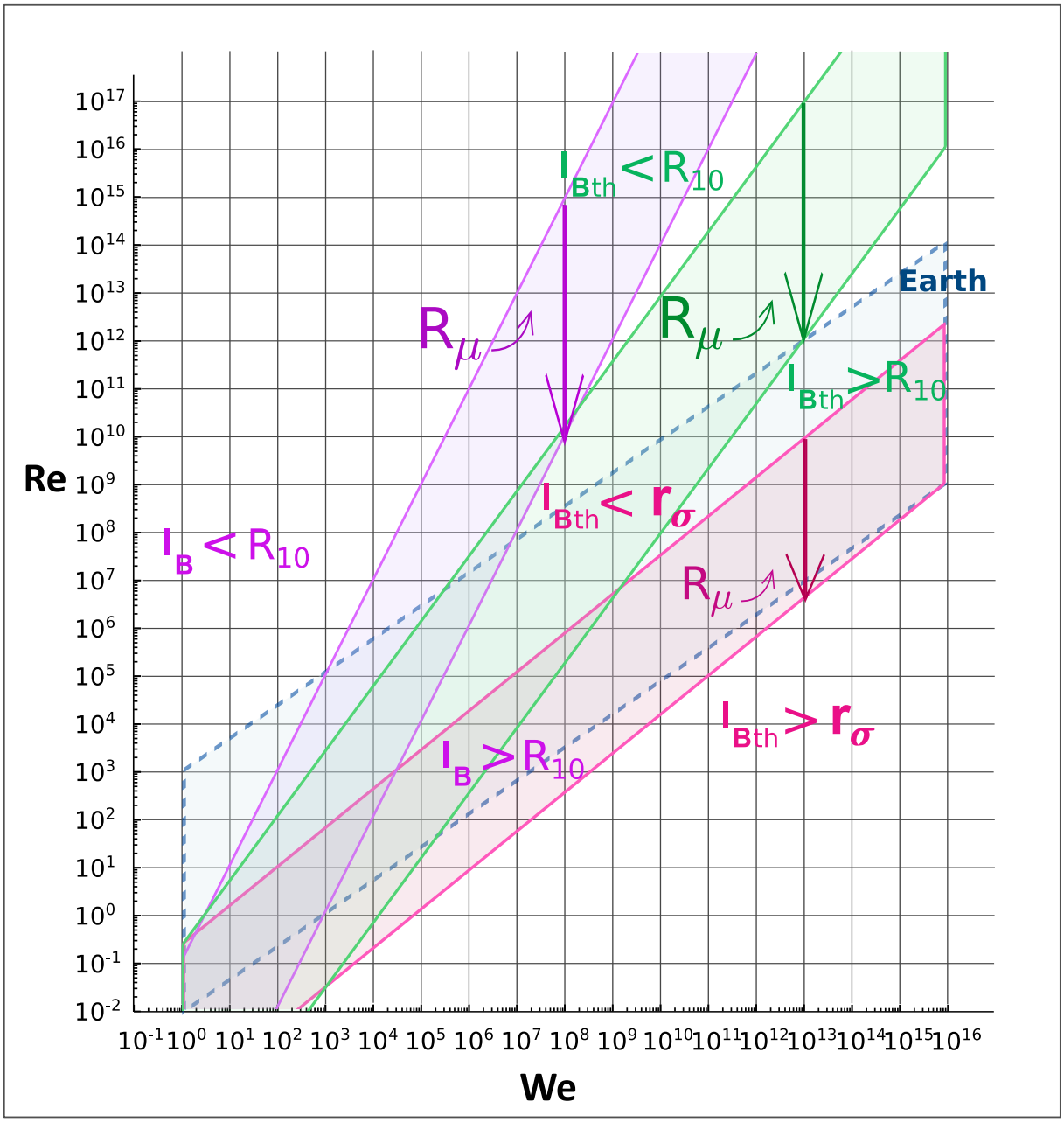

FIGURE VII.3 – Regime diagram in the plane (Re,We) of the different length scales relevant for the size of droplets compared to the different Batchelor length scales. The violet zone is the characteristic plane where the mean radius of the droplets R_0 is equal to the Batchelor length scale. The green zone is the characteristic plane where the mean radius of the droplets R_0 is equal to the turbulent Batchelor length scale. The fuschia zone is the characteristic plane where the Hinze length scale is equal to the turbulent Batchelor length scale. The scaling delimiting the region with a larger Hinze scale than the laminar Batchelor length scale and the inverse was removed as this dichotomy has incompatible hypothesis.

impacts.

The spinup phase of the turbulent thermal definitely needs more attention for both the

geophysical problem and the theory of the toroidal vortex ; the measure of pressure could be helpful for the drag coefficient, as well as the measure of the density field and velocity fields in a system of fluids where index are matched. If such a system does not come handy because of a $\tilde{\rho}$ too close to one, buoyant flakes colored on each face may allow to access the rotation rate inside the diapir even if the interface is deforming the ray path dramatically.

Finally the measures of heat could be developed by varying the height of fall. In order to improve significantly the overall interpretation, a PIV method could be set-up to study the transition from thermal to rain as a function of the initial radius of the diapir. This would allow to study how the different speeds interplay at the scale of the droplet during this transition. These measures would also need a system of fluids with matched refractive index and an unknown trick may be needed in order to know if the laser sheet is crossing the drops at their centers or not.

Bibliographie

Y. Abe. Thermal and chemical evolution of the terrestrial magma ocean. *Physics of the Earth and Planetary Interiors*, 100(1-4) :27–39, March 1997. ISSN 00319201. doi : 10.1016/S0031-9201(96)03229-3. URL http://linkinghub.elsevier.com/retrieve/pii/S0031920196032293.

Y. Amelin. Lead Isotopic Ages of Chondrules and Calcium-Aluminum-Rich Inclusions. *Science*, 297(5587) :1678–1683, September 2002. ISSN 00368075, 10959203. doi : 10.1126/science.1073950. URL http://www.sciencemag.org/cgi/doi/10.1126/science.1073950.

Jacob B. Angelo, Edwin N. Lightfoot, and David W. Howard. Generalization of the penetration theory for surface stretch : Application to forming and oscillating drops. *AIChE Journal*, 12(4) :751–760, July 1966. ISSN 0001-1541, 1547-5905. doi : 10.1002/aic.690120423. URL http://doi.wiley.com/10.1002/aic.690120423.

S.V. Apte, M. Gorokhovski, and P. Moin. LES of atomizing spray with stochastic modeling of secondary breakup. *International Journal of Multiphase Flow*, 29(9) : 1503–1522, September 2003. ISSN 03019322. doi : 10.1016/S0301-9322(03)00111-3. URL http://linkinghub.elsevier.com/retrieve/pii/S0301932203001113.

N. Ashgriz, editor. *Handbook of atomization and sprays : theory and applications*. Springer, New York, NY, 2011. ISBN 978-1-4419-7263-7 978-1-4419-7264-4. OCLC : 731927924.

W.D Baines and E.J Hopfinger. Thermals with large density difference. *Atmospheric Environment (1967)*, 18(6) :1051–1057, January 1984. ISSN 00046981. doi : 10.1016/0004-6981(84)90137-9. URL http://linkinghub.elsevier.com/retrieve/pii/0004698184901379.

S. Banerjee, D.S. Scott, and E. Rhodes. Mass Transfer to Falling Wavy Liquid Films in Turbulent Flow. *Industrial & Engineering Chemistry Fundamentals*, 7(1) :22–27, February 1968. ISSN 0196-4313, 1541-4833. doi : 10.1021/i160025a004. URL http://pubs.acs.org/doi/abs/10.1021/i160025a004.

C.K. Batchelor and G.K. Batchelor. *An introduction to fluid dynamics*. Cambridge university press, 1967.

G. K. Batchelor. Heat convection and buoyancy effects in fluids. *Quarterly Journal of the Royal Meteorological Society*, 80(345) :339–358, July 1954. ISSN 00359009, 1477870X. doi : 10.1002/qj.49708034504. URL http://doi.wiley.com/10.1002/qj.49708034504.

G.K. Batchelor. The stability of a large gas bubble rising through liquid. *Journal of Fluid Mechanics*, 184(-1) :399, November 1987. ISSN 0022-1120, 1469-7645. doi : 10.1017/S0022112087002945. URL http://www.journals.cambridge.org/abstract_S0022112087002945.

N. Baumann, D. D. Joseph, P. Mohr, and Y. Renardy. Vortex rings of one fluid in another in free fall. *Physics of Fluids A : Fluid Dynamics*, 4(3) :567–580, March 1992. ISSN 0899-8213. doi : 10.1063/1.858328. URL http://aip.scitation.org/doi/10.1063/1.858328.

M.S.G. Bettelini and T.K. Fanneløp. Underwater plume from an instantaneously started source. *Applied Ocean Research*, 15(4) :195–206, January 1993. ISSN 01411187. doi : 10.1016/0141-1187(93)90008-L. URL http://linkinghub.elsevier.com/retrieve/pii/014111879390008L.

D. Bhaga. *Bubbles in viscous : shapes, wakes and velocities*. PhD thesis, Ph. D. Thesis, McGill University, Montreal, Canada, 1976.

D. Bhaga and M. E. Weber. Bubbles in viscous liquids : shapes, wakes and velocities. *Journal of Fluid Mechanics*, 105 :61–85, 1981. URL http://journals.cambridge.org/abstract_S002211208100311X.

J. Bühler and D. A. Papantoniou. On the motion of suspension thermals and particle swarms. *Journal of Hydraulic Research*, 39(6) :643–653, December 2001. ISSN 0022-1686, 1814-2079. doi : 10.1080/00221686.2001.9628293. URL http://www.tandfonline.com/doi/abs/10.1080/00221686.2001.9628293.

A. Blanco and J. Magnaudet. The structure of the axisymmetric high-Reynolds number flow around an ellipsoidal bubble of fixed shape. *Physics of Fluids*, 7(6) :1265–1274, June 1995. ISSN 1070-6631, 1089-7666. doi : 10.1063/1.868515. URL http://aip.scitation.org/doi/10.1063/1.868515.

V.M. Boiko and S.V. Poplavski. Experimental study of two types of stripping breakup of the drop in the flow behind the shock wave. *Combustion, Explosion, and Shock Waves*, 48(4) :440–445, July 2012. ISSN 0010-5082, 1573-8345. doi : 10.1134/S0010508212040107. URL http://link.springer.com/10.1134/S0010508212040107.

D. Bond and H. Johari. Impact of buoyancy on vortex ring development in the near field. *Experiments in Fluids*, 48(5) :737–745, May 2010. ISSN 0723-4864, 1432-1114. doi : 10.1007/s00348-009-0761-z. URL http://link.springer.com/10.1007/s00348-009-0761-z.

M.A. Bouchiat and J. Meunier. Spectre des fluctuations thermiques de la surface libre d'un liquide simple. *Journal de Physique*, 32(7) :561–571, 1971. ISSN 0302-0738. doi : 10.1051/jphys:01971003207056100. URL http://www.edpsciences.org/10.1051/jphys:01971003207056100.

A. Boujibar, D. Andrault, M. A. Bouhifd, N. Bolfan-Casanova, J.-L. Devidal, and N. Trcera. Metal–silicate partitioning of sulphur, new experimental and thermodynamic constraints on planetary accretion. *Earth and Planetary Science Letters*, 391 :42–54, April 2014. ISSN 0012821X. doi : 10.1016/j.epsl.2014.01.021. URL http://linkinghub.elsevier.com/retrieve/pii/S0012821X14000314.

N. Bremond, C. Clanet, and E. Villermaux. Atomization of undulating liquid sheets. *Journal of Fluid Mechanics*, 585 :421, August 2007. ISSN 0022-1120, 1469-7645. doi : 10.1017/S0022112007006775. URL http://www.journals.cambridge.org/abstract_S0022112007006775.

H. Brenner and R.G. Cox. The resistance to a particle of arbitrary shape in translational motion at small Reynolds numbers. *Journal of Fluid Mechanics*, 17(04) :561, December 1963. ISSN 0022-1120, 1469-7645. doi : 10.1017/S002211206300152X. URL http://www.journals.cambridge.org/abstract_S002211206300152X.

R.S. Brodkey. *The phenomena of fluid motions*. Courier Corporation, 1995.

C. Burkhardt, T. Kleine, B. Bourdon, H. Palme, J. Zipfel, J. M. Friedrich, and D. S. Ebel. Hf–W mineral isochron for Ca,Al-rich inclusions : Age of the solar system and the timing of core formation in planetesimals. *Geochimica et Cosmochimica Acta*, 72 (24) :6177–6197, December 2008. ISSN 00167037. doi : 10.1016/j.gca.2008.10.023. URL http://linkinghub.elsevier.com/retrieve/pii/S0016703708006352.

J.W.M. Bush, B.A. Thurber, and F. Blanchette. Particle clouds in homogeneous and stratified environments. *Journal of Fluid Mechanics*, 489 :29–54, July 2003. ISSN 00221120, 14697645. doi : 10.1017/S0022112003005160. URL http://www.journals.cambridge.org/abstract_S0022112003005160.

P.H. Calderbank. Physical rate processes in industrial fermentations part i : The interfacial area in gas-liquid contacting with mechanical agitation. *Trans. Inst. Chem. Engrs*, 36 : 443–463, 1958.

R. M. Canup. Simulations of a late lunar-forming impact. *Icarus*, 168(2) :433–456, April 2004. ISSN 00191035. doi : 10.1016/j.icarus.2003.09.028. URL http://linkinghub.elsevier.com/retrieve/pii/S0019103503002999.

J.E. Chambers and G.W. Wetherill. Making the Terrestrial Planets : N-Body Integrations of Planetary Embryos in Three Dimensions. *Icarus*, 136(2) :304–327, December 1998. ISSN 00191035. doi : 10.1006/icar.1998.6007. URL http://linkinghub.elsevier.com/retrieve/pii/S0019103598960079.

S. Chandrasekhar. *Hydrodynamic and hydromagnetic stability*. Courier Corporation, 2013.

S.S.-H. Chang. Motion of a Large Dusty Buoyant Thermal With a Vortex Ring. *Journal of Applied Mechanics*, 45(4) :711, 1978. ISSN 00218936. doi : 10.1115/1.3424407. URL http://AppliedMechanics.asmedigitalcollection.asme.org/article.aspx?articleid=1404062.

Hsiao Tsung Chen and Stanley Middleman. Drop size distribution in agitated liquid-liquid systems. *AIChE Journal*, 13(5) :989–995, September 1967. ISSN 0001-1541, 1547-5905. doi : 10.1002/aic.690130529. URL http://doi.wiley.com/10.1002/aic.690130529.

W.-H. Chou, L.-P. Hsiang, and G.M. Faeth. Temporal properties of drop breakup in the shear breakup regime. *International Journal of Multiphase Flow*, 23(4) :651–669, August 1997. ISSN 03019322. doi : 10.1016/S0301-9322(97)00006-2. URL http://linkinghub.elsevier.com/retrieve/pii/S0301932297000062.

R. Clift. The motion of particles in turbulent gas-streams. *Proc. Chemeca'70*, 1 :14, 1970.

R. Clift, J. R. Grace, and M. E. Weber. *Bubbles, drops, and particles*. Acad. Press, New York, NY, 3. print edition, 1992. ISBN 0-12-176950-X 0-12-176950-X. OCLC : 258197988.

B. Cochain, C. Sanloup, C. Leroy, and Y. Kono. Viscosity of mafic magmas at high pressures. *Geophysical Research Letters*, 44(2) :818–826, January 2017. ISSN 00948276. doi : 10.1002/2016GL071600. URL http://doi.wiley.com/10.1002/2016GL071600.

R.D. Cohen. Steady-state cluster size distribution in stirred suspensions. *Journal of the Chemical Society, Faraday Transactions*, 86(12) :2133–2138, 1990.

R.D. Cohen. Shattering of a liquid drop due to impact. *Proceedings of the Royal Society of London. Series A : Mathematical and Physical Sciences*, 435(1895) :483–503, 1991.

D. Colombet, D. Legendre, A. Cockx, P. Guiraud, F. Risso, C. Daniel, and S. Galinat. Experimental study of mass transfer in a dense bubble swarm. *Chemical Engineering Science*, 66(14) :3432–3440, July 2011. ISSN 00092509. doi : 10.1016/j.ces.2011.01.020. URL http://linkinghub.elsevier.com/retrieve/pii/S0009250911000303.

D. Colombet, D. Legendre, A. Cockx, and P. Guiraud. Mass or heat transfer inside a spherical gas bubble at low to moderate Reynolds number. *International Journal of Heat and Mass Transfer*, 67 :1096–1105, December 2013. ISSN 00179310. doi : 10.1016/j.ijheatmasstransfer.2013.08.069. URL http://linkinghub.elsevier.com/retrieve/pii/S001793101300731X.

E. Cottrell, M.J. Walter, and D. Walker. Metal–silicate partitioning of tungsten at high pressure and temperature : Implications for equilibrium core formation in Earth. *Earth and Planetary Science Letters*, 281(3-4) :275–287, May 2009. ISSN 0012821X. doi : 10.1016/j.epsl.2009.02.024. URL http://linkinghub.elsevier.com/retrieve/pii/S0012821X0900140X.

Y. Couder, E. Fort, C.-H. Gautier, and A. Boudaoud. From Bouncing to Floating : Noncoalescence of Drops on a Fluid Bath. *Physical Review Letters*, 94(17), May 2005. ISSN 0031-9007, 1079-7114. doi : 10.1103/PhysRevLett.94.177801. URL https://link.aps.org/doi/10.1103/PhysRevLett.94.177801.

F.E.C. Culick. Comments on a Ruptured Soap Film. *Journal of Applied Physics*, 31(6) : 1128–1129, June 1960. ISSN 0021-8979, 1089-7550. doi : 10.1063/1.1735765. URL http://aip.scitation.org/doi/10.1063/1.1735765.

Leonardo da Vinci. *Codex Leicester*. 1508.

Tais W. Dahl and David J. Stevenson. Turbulent mixing of metal and silicate during planet accretion — And interpretation of the Hf–W chronometer. *Earth and Planetary Science Letters*, 295(1-2) :177–186, June 2010. ISSN 0012821X. doi : 10.1016/j.epsl.2010.03.038. URL http://linkinghub.elsevier.com/retrieve/pii/S0012821X10002220.

W. Dahm. Fundamental Analysis of Liquid Atomization by Fuel Slingers in Small Gas Turbines. In *32nd AIAA Fluid Dynamics Conference and Exhibit*, St. Louis, Missouri, June 2002. American Institute of Aeronautics and Astronautics. ISBN 978-1-62410-113-7. doi : 10.2514/6.2002-3183. URL http://arc.aiaa.org/doi/10.2514/6.2002-3183.

P.V. Danckwerts. Significance of liquid-film coefficients in gas absorption. *Industrial & Engineering Chemistry*, 43(6) :1460–1467, 1951.

R.M. Davies and G. Taylor. The Mechanics of Large Bubbles Rising through Extended Liquids and through Liquids in Tubes. *Proceedings of the Royal Society A : Mathematical, Physical and Engineering Sciences*, 200(1062) :375–390, February 1950. ISSN 1364-5021, 1471-2946. doi : 10.1098/rspa.1950.0023. URL http://rspa.royalsocietypublishing.org/cgi/doi/10.1098/rspa.1950.0023.

R.H. Davis and K.H. Birdsell. Hindered settling of semidilute monodisperse and polydisperse suspensions. *AIChE Journal*, 34(1) :123–129, January 1988. ISSN 0001-1541, 1547-5905. doi : 10.1002/aic.690340114. URL http://doi.wiley.com/10.1002/aic.690340114.

R. Deguen, P. Olson, and P. Cardin. Experiments on turbulent metal-silicate mixing in a magma ocean. *Earth and Planetary Science Letters*, 310(3-4) :303–313, October 2011. ISSN 0012821X. doi : 10.1016/j.epsl.2011.08.041. URL http://linkinghub.elsevier.com/retrieve/pii/S0012821X1100505X.

R. Deguen, M. Landeau, and P. Olson. Turbulent metal–silicate mixing, fragmentation, and equilibration in magma oceans. *Earth and Planetary Science Letters*, 391 :274–287, April 2014. ISSN 0012821X. doi : 10.1016/j.epsl.2014.02.007. URL http://linkinghub.elsevier.com/retrieve/pii/S0012821X14000806.

S. Dorbolo, H. Caps, and N. Vandewalle. Fluid instabilities in the birth and death of antibubbles. *New Journal of Physics*, 5 :161–161, December 2003. ISSN 1367-2630. doi : 10.1088/1367-2630/5/1/161. URL http://stacks.iop.org/1367-2630/5/i=1/a=161?key=crossref.27b1e48258f44967582b7312a6ffb93a.

C. Dumouchel. The Maximum Entropy Formalism and the Prediction of Liquid Spray Drop-Size Distribution. *Entropy*, 11(4) :713–747, November 2009. ISSN 1099-4300. doi : 10.3390/e11040713. URL http://www.mdpi.com/1099-4300/11/4/713.

J. Duplat and E. Villermaux. Mixing by random stirring in confined mixtures. *Journal of Fluid Mechanics*, 617 :51, December 2008. ISSN 0022-1120, 1469-7645. doi : 10.1017/S0022112008003789. URL http://www.journals.cambridge.org/abstract_S0022112008003789.

J.K. Eaton and J.R. Fessler. Preferential concentration of particles by turbulence. *International Journal of Multiphase Flow*, 20 :169–209, 1994.

J. Eggers and E. Villermaux. Physics of liquid jets. *Reports on Progress in Physics*, 71 (3) :036601, March 2008. ISSN 0034-4885, 1361-6633. doi : 10.1088/0034-4885/71/3/036601. URL http://stacks.iop.org/0034-4885/71/i=3/a=036601?key=crossref.48060c984f03ab3753a7a04ea86dae4e.

M. Epstein and H.K. Fauske. Applications of the turbulent entrainment assumption to immiscible gas-liquid and liquid-liquid systems. *Chemical Engineering Research and Design*, 79(4) :453–462, 2001. URL http://www.sciencedirect.com/science/article/pii/S0263876201720692.

M.P. Escudier and T. Maxworthy. On the motion of turbulent thermals. *Journal of Fluid Mechanics*, 61(03) :541, November 1973. ISSN 0022-1120, 1469-7645. doi : 10.1017/S0022112073000856. URL http://www.journals.cambridge.org/abstract_S0022112073000856.

G. Facchini, B. Favier, P. Le Gal, M. Wang, and M. Le Bars. The linear instability of the stratified plane couette flow. *Journal of Fluid Mechanics*, 853 :205–234, 2018.

J.R. Fleck, C.L. Rains, D.S. Weeraratne, C.T. Nguyen, D.M. Brand, S.M. Klein, J.M. McGehee, J.M. Rincon, C. Martinez, and P.L. Olson. Iron diapirs entrain silicates to the core and initiate thermochemical plumes. *Nature Communications*, 9(1), December 2018. ISSN 2041-1723. doi : 10.1038/s41467-017-02503-2. URL http://www.nature.com/articles/s41467-017-02503-2.

S.K. Friedlander and C.S. Wang. The self-preserving particle size distribution for coagulation by brownian motion. *Journal of Colloid and interface Science*, 22(2) :126–132, 1966.

S. Galinat, F. Risso, O. Masbernat, and P. Guiraud. Dynamics of drop breakup in inhomogeneous turbulence at various volume fractions. *Journal of Fluid Mechanics*, 578 :85, May 2007. ISSN 0022-1120, 1469-7645. doi : 10.1017/S0022112007005186. URL http://www.journals.cambridge.org/abstract_S0022112007005186.

J. Garside and M.R. Al-Dibouni. Velocity-Voidage Relationships for Fluidization and Sedimentation in Solid-Liquid Systems. *Industrial & Engineering Chemistry Process Design and Development*, 16(2) :206–214, April 1977. ISSN 0196-4305, 1541-5716. doi : 10.1021/i260062a008. URL http://pubs.acs.org/doi/abs/10.1021/i260062a008.

B. E. Gel'fand, S. A. Gubin, S. M. Kogarko, and S. P. Komar. Singularities of the breakup of viscous liquid droplets in shock waves. *Journal of Engineering Physics*, 25(3) :1140–1142, September 1973. ISSN 0022-0841, 1573-871X. doi : 10.1007/BF00838143. URL http://link.springer.com/10.1007/BF00838143.

B.E. Gelfand. Droplet breakup phenomena in flows with velocity lag. *Progress in energy and combustion science*, 22(3) :201–265, 1996. URL http://www.sciencedirect.com/science/article/pii/S0360128596000056.

J.R. Grace, T. Wairegi, and J. Brophy. Break-up of drops and bubbles in stagnant media. *The Canadian Journal of Chemical Engineering*, 56(1) :3–8, 1978. URL http://onlinelibrary.wiley.com/doi/10.1002/cjce.5450560101/full.

D.R. Guildenbecher, C. López-Rivera, and P.E. Sojka. Secondary atomization. *Experiments in Fluids*, 46(3) :371–402, March 2009. ISSN 0723-4864, 1432-1114. doi : 10.1007/s00348-008-0593-2. URL http://link.springer.com/10.1007/s00348-008-0593-2.

F.C. Haas. Stability of droplets suddently exposed to a high velocity gas stream. *AIChE Journal*, 10(6) :920–924, November 1964. ISSN 0001-1541, 1547-5905. doi : 10.1002/aic.690100627. URL http://doi.wiley.com/10.1002/aic.690100627.

J.S. Hadamard. Mouvement permanent lent d'une sphère liquid et visqueuse dans un liquide visqueux. *CR Hebd. Seances Acad. Sci. Paris*, 152 :1735–1738, 1911a.

J.S. Hadamard. Mouvement permanent lent d'une sphère liquid et visqueuse dans un liquide visqueux. *CR Hebd. Seances Acad. Sci. Paris*, 152 :1735–1738, 1911b.

M. Hadj Achour. *Fragmentation of molten metal in water*. Theses, Université de Lorraine, December 2017. URL https://tel.archives-ouvertes.fr/tel-01684708.

A.N. Halliday and T. Kleine. Meteorites and the Timing, Mechanisms, and Conditions of Terrestrial Planet Accretion and Early Differentiation. page 27, 2006.

J. Han and G. Tryggvason. Secondary breakup of axisymmetric liquid drops. II. Impulsive acceleration. *Physics of Fluids*, 13(6) :1554–1565, June 2001. ISSN 1070-6631, 1089-7666. doi : 10.1063/1.1370389. URL http://aip.scitation.org/doi/10.1063/1.1370389.

L. Han, H. Luo, Y. Liu, K. You, and P. Liu. A multi-scale theoretical model for gas-Liquid interface mass transfer based on the wide spectrum eddy contact concept. *AIChE Journal*, 57(4) :886–896, April 2011. ISSN 00011541. doi : 10.1002/aic.12327. URL http://doi.wiley.com/10.1002/aic.12327.

R. Higbie. The rate of absorption of a pure gas into a still liquid during short periods of exposure. *Trans. AIChE*, 31 :365–389, 1935.

J. O. Hinze. Fundamentals of the hydrodynamic mechanism of splitting in dispersion processes. *AIChE Journal*, 1(3) :289–295, September 1955. ISSN 0001-1541, 1547-5905. doi : 10.1002/aic.690010303. URL http://doi.wiley.com/10.1002/aic.690010303.

L.-P. Hsiang and G.M. Faeth. Near-limit drop deformation and secondary breakup. *International Journal of Multiphase Flow*, 18(5) :635–652, September 1992. ISSN 03019322. doi : 10.1016/0301-9322(92)90036-G. URL http://linkinghub.elsevier.com/retrieve/pii/030193229290036G.

L.-P. Hsiang and G.M. Faeth. Drop properties after secondary breakup. *International Journal of Multiphase Flow*, 19(5) :721–735, 1993. URL http://www.sciencedirect.com/science/article/pii/030193229390039W.

H. Ichikawa, S. Labrosse, and K. Kurita. Direct numerical simulation of an iron rain in the magma ocean. *Journal of Geophysical Research*, 115(B1), January 2010. ISSN 0148-0227. doi : 10.1029/2009JB006427. URL http://doi.wiley.com/10.1029/2009JB006427.

M. Jain, R.S. Prakash, G. Tomar, and R.V. Ravikrishna. Secondary breakup of a drop at moderate Weber numbers. *Proceedings of the Royal Society A : Mathematical, Physical and Engineering Sciences*, 471(2177) :20140930–20140930, April 2015. ISSN 1364-5021, 1471-2946. doi : 10.1098/rspa.2014.0930. URL http://rspa.royalsocietypublishing.org/cgi/doi/10.1098/rspa.2014.0930.

S.S. Jain, N. Tyagi, R.S. Prakash, R.V. Ravikrishna, and G. Tomar. Secondary breakup of drops at moderate Weber numbers : Effect of Density ratio and Reynolds number. *arXiv :1803.02989 [physics]*, March 2018. URL http://arxiv.org/abs/1803.02989. arXiv : 1803.02989.

M. Jalaal and K. Mehravaran. Fragmentation of falling liquid droplets in bag breakup mode. *International Journal of Multiphase Flow*, 47 :115–132, December 2012. ISSN 03019322. doi : 10.1016/j.ijmultiphaseflow.2012.07.011. URL http://linkinghub.elsevier.com/retrieve/pii/S0301932212001140.

M. Jalaal and K. Mehravaran. Transient growth of droplet instabilities in a stream. *Physics of Fluids*, 26(1) :012101, January 2014. ISSN 1070-6631, 1089-7666. doi : 10.1063/1.4851056. URL http://aip.scitation.org/doi/10.1063/1.4851056.

D. D. Joseph. Rise velocity of a spherical cap bubble. *Journal of Fluid Mechanics*, 488 : 213–223, July 2003. ISSN 00221120, 14697645. doi : 10.1017/S0022112003004968. URL http://www.journals.cambridge.org/abstract_S0022112003004968.

D.D. Joseph, J. Belanger, and G.S. Beavers. Breakup of a liquid drop suddenly exposed to a high-speed airstream. *International Journal of Multiphase Flow*, 25(6-7) :1263–1303, September 1999. ISSN 03019322. doi : 10.1016/S0301-9322(99)00043-9. URL http://linkinghub.elsevier.com/retrieve/pii/S0301932299000439.

Shun-ichiro Karato and V. Rama Murthy. Core formation and chemical equilibrium in the Earth—I. Physical considerations. *Physics of the Earth and Planetary Interiors*, 100 (1-4) :61–79, March 1997. ISSN 00319201. doi : 10.1016/S0031-9201(96)03232-3. URL http://linkinghub.elsevier.com/retrieve/pii/S0031920196032323.

B. B. Karki and L. P. Stixrude. Viscosity of MgSiO3 Liquid at Earth's Mantle Conditions : Implications for an Early Magma Ocean. *Science*, 328(5979) :740–742, May 2010. ISSN 0036-8075, 1095-9203. doi : 10.1126/science.1188327. URL http://www.sciencemag.org/cgi/doi/10.1126/science.1188327.

I. Kataoka, M. Ishii, and K. Mishima. Generation and Size Distribution of Droplet in Annular Two-Phase Flow. *Journal of Fluids Engineering*, 105(2) :230, 1983. ISSN 00982202. doi : 10.1115/1.3240969. URL http://FluidsEngineering.asmedigitalcollection.asme.org/article.aspx?articleid=1425865.

William M. Kaula. Thermal evolution of Earth and Moon growing by planetesimal impacts. *Journal of Geophysical Research*, 84(B3) :999, 1979. ISSN 0148-0227. doi : 10.1029/JB084iB03p00999. URL http://doi.wiley.com/10.1029/JB084iB03p00999.

D.H. Kelley and N.T. Ouellette. Using particle tracking to measure flow instabilities in an undergraduate laboratory experiment. *American Journal of Physics*, 79(3) : 267–273, March 2011. ISSN 0002-9505, 1943-2909. doi : 10.1119/1.3536647. URL http://aapt.scitation.org/doi/10.1119/1.3536647.

J.D. Kendall and H.J. Melosh. Differentiated planetesimal impacts into a terrestrial magma ocean : Fate of the iron core. *Earth and Planetary Science Letters*, 448 : 24–33, August 2016. ISSN 0012821X. doi : 10.1016/j.epsl.2016.05.012. URL http://linkinghub.elsevier.com/retrieve/pii/S0012821X16302217.

B. Keshavarz, E.C. Houze, J.R. Moore, M.R. Koerner, and G.H. McKinley. Ligament Mediated Fragmentation of Viscoelastic Liquids. *Physical Review Letters*, 117(15), October 2016. ISSN 0031-9007, 1079-7114. doi : 10.1103/PhysRevLett.117.154502. URL https://link.aps.org/doi/10.1103/PhysRevLett.117.154502.

J. Kitscha and G. Kocamustafaogullari. Breakup criteria for fluid particles. *International Journal of Multiphase Flow*, 15(4) :573–588, July 1989. ISSN 03019322. doi : 10.1016/0301-9322(89)90054-2. URL http://linkinghub.elsevier.com/retrieve/pii/0301932289900542.

T. Kékesi, G. Amberg, and L. Prahl Wittberg. Drop deformation and breakup. *International Journal of Multiphase Flow*, 66 :1–10, November 2014. ISSN 03019322. doi : 10.1016/j.ijmultiphaseflow.2014.06.006. URL http://linkinghub.elsevier.com/retrieve/pii/S0301932214001141.

T. Kleine, K. Mezger, H. Palme, and C. Münker. The W isotope evolution of the bulk silicate Earth : constraints on the timing and mechanisms of core formation and accretion. *Earth and Planetary Science Letters*, 228(1-2) :109–123, November 2004. ISSN 0012821X. doi : 10.1016/j.epsl.2004.09.023. URL http://linkinghub.elsevier.com/retrieve/pii/S0012821X04005679.

T. Kleine, K. Mezger, H. Palme, E. Scherer, and C. Münker. Early core formation in asteroids and late accretion of chondrite parent bodies : Evidence from 182hf-182w in CAIs, metal-rich chondrites, and iron meteorites. *Geochimica et Cosmochimica Acta*, 69 (24) :5805–5818, December 2005. ISSN 00167037. doi : 10.1016/j.gca.2005.07.012. URL http://linkinghub.elsevier.com/retrieve/pii/S0016703705005958.

E. Kokubo and S. Ida. Runaway Growth of Planetesimals. In *Chaos in Gravitational N-Body Systems*, pages 297–302. Springer, 1996. URL http://link.springer.com/chapter/10.1007/978-94-009-0307-4_33.

E. Kokubo and S. Ida. Oligarchic Growth of Protoplanets. *Icarus*, 131(1) :171–178, January 1998. ISSN 00191035. doi : 10.1006/icar.1997.5840. URL http://linkinghub.elsevier.com/retrieve/pii/S0019103597958401.

A.N. Kolmogorov. The local structure of turbulence in incompressible viscous fluid for very large Reynolds numbers. In *Dokl. Akad. Nauk SSSR*, volume 30, pages 301–305. JSTOR, 1941. URL http://www.jstor.org/stable/pdf/51980.pdf.

A.N. Kolmogorov. On the breakage of drops in a turbulent flow. *Doklady Akademii Nauk SSSR*, 66 :825–828, 1949.

S. Kooij, R. Sijs, M.M. Denn, E. Villermaux, and D. Bonn. What Determines the Drop Size in Sprays ? *Physical Review X*, 8(3), July 2018. ISSN 2160-3308. doi : 10.1103/PhysRevX.8.031019. URL https://link.aps.org/doi/10.1103/PhysRevX.8.031019.

R.G. Kraus, S. Root, R.W. Lemke, S.T. Stewart, S.B. Jacobsen, and T.R. Mattsson. Impact vaporization of planetesimal cores in the late stages of planet formation. *Nature Geoscience*, 8(4) :269–272, March 2015. ISSN 1752-0894, 1752-0908. doi : 10.1038/ngeo2369. URL http://www.nature.com/doifinder/10.1038/ngeo2369.

S.A. Krzeczkowski. Measurement of liquid droplet disintegration mechanisms. *International Journal of Multiphase Flow*, 6(3) :227–239, June 1980. ISSN 03019322. doi : 10.1016/0301-9322(80)90013-0. URL http://linkinghub.elsevier.com/retrieve/pii/0301932280900130.

B. Lalanne, S. Tanguy, and F. Risso. Effect of rising motion on the damped shape oscillations of drops and bubbles. *Physics of Fluids*, 25(11) :112107, November 2013. ISSN 1070-6631, 1089-7666. doi : 10.1063/1.4829366. URL http://aip.scitation.org/doi/10.1063/1.4829366.

H. Lamb. *Hydrodynamics*. Cambridge university press, 1993.

J.C. Lamont and D.S. Scott. An eddy cell model of mass transfer into the surface of a turbulent liquid. *AIChE Journal*, 16(4) :513–519, 1970. URL http://onlinelibrary.wiley.com/doi/10.1002/aic.690160403/full.

M. Landeau, R. Deguen, and P. Olson. Experiments on the fragmentation of a buoyant liquid volume in another liquid. *Journal of Fluid Mechanics*, 749 :478–518, June 2014. ISSN 0022-1120, 1469-7645. doi : 10.1017/jfm.2014.202. URL http://www.journals.cambridge.org/abstract_S002211201400202X.

M. Landeau, P. Olson, R. Deguen, and B.H. Hirsh. Core merging and stratification following giant impact. *Nature Geoscience*, 9(10) :786–789, October 2016. ISSN 1752-0894, 1752-0908. doi : 10.1038/ngeo2808. URL http://www.nature.com/articles/ngeo2808.

J.C. Lasheras, C. Eastwood, C. Martınez-Bazán, and J.L. Montañés. A review of statistical models for the break-up of an immiscible fluid immersed into a fully developed turbulent flow. *International Journal of Multiphase Flow*, 28(2) :247–278, February 2002. ISSN 03019322. doi : 10.1016/S0301-9322(01)00046-5. URL http://linkinghub.elsevier.com/retrieve/pii/S0301932201000465.

Der-Chuen Lee and Alex N. Halliday. Hf-W Isotopic Evidence for Rapid Accretion and Differentiation in the Early Solar System. *Science (New York, N.Y.)*, 274(5294) : 1876–1879, December 1996. ISSN 1095-9203.

A.H. Lefebvre. Atomization and sprays, hemisphere pub. *Corp., New York*, 1989, 1989.

X. Lei, B. J. Ackerson, and P. Tong. Settling Statistics of Hard Sphere Particles. *Physical Review Letters*, 86(15) :3300–3303, April 2001. ISSN 0031-9007, 1079-7114. doi : 10.1103/PhysRevLett.86.3300. URL https://link.aps.org/doi/10.1103/PhysRevLett.86.3300.

P. Lenard. *Ueber regen.* 1904.

J. Levine. Spherical vortex theory of bubble-like motion in cumulus clouds. *Journal of Meteorology*, 16(6) :653–662, 1959.

V. Lherm and R. Deguen. Small-Scale Metal/Silicate Equilibration During Core Formation : The Influence of Stretching Enhanced Diffusion on Mixing. *Journal of Geophysical Research : Solid Earth*, 123(12) :10,496–10,516, December 2018. ISSN 21699313. doi : 10.1029/2018JB016537. URL http://arxiv.org/abs/1812.07855. arXiv : 1812.07855.

H. Lhuissier and E. Villermaux. 'Effervescent' atomization in two dimensions. *Journal of Fluid Mechanics*, 714 :361–392, January 2013. ISSN 0022-1120, 1469-7645. doi : 10.1017/jfm.2012.481. URL http://www.journals.cambridge.org/abstract_S0022112012004818.

C. Liebske, B. Schmickler, H. Terasaki, B. Poe, A. Suzuki, K. Funakoshi, R. Ando, and D. Rubie. Viscosity of peridotite liquid up to 13 GPa : Implications for magma ocean viscosities. *Earth and Planetary Science Letters*, 240(3-4) :589–604, December 2005. ISSN 0012821X. doi : 10.1016/j.epsl.2005.10.004. URL http://linkinghub.elsevier.com/retrieve/pii/S0012821X05006825.

K.D. Litasov and A.F. Shatskiy. Composition of the Earth's core : A review. *Russian Geology and Geophysics*, 57(1) :22–46, January 2016. ISSN 10687971. doi : 10.1016/j.rgg.2016.01.003. URL http://linkinghub.elsevier.com/retrieve/pii/S1068797116000043.

E. Loth. Quasi-steady shape and drag of deformable bubbles and drops. *International Journal of Multiphase Flow*, 34(6) :523–546, June 2008. ISSN 03019322. doi : 10.1016/j.ijmultiphaseflow.2007.08.010. URL http://linkinghub.elsevier.com/retrieve/pii/S0301932207001711.

J. Magnaudet and I. Eames. The Motion of High-Reynolds-Number Bubbles in Inhomogeneous Flows. *Annual Review of Fluid Mechanics*, 32(1) :659–708, January 2000. ISSN 0066-4189, 1545-4479. doi : 10.1146/annurev.fluid.32.1.659. URL http://www.annualreviews.org/doi/10.1146/annurev.fluid.32.1.659.

G. Magnus. On the deviation of projectiles ; and on a remarkable phenomenon of rotating bodies. *Memoirs of the Royal Academy*, page 210, 1852.

B.B. Mandelbrot. On the geometry of homogeneous turbulence, with stress on the fractal dimension of the iso-surfaces of scalars. *Journal of Fluid Mechanics*, 72(03) :401, December 1975. ISSN 0022-1120, 1469-7645. doi : 10.1017/S0022112075003047. URL http://www.journals.cambridge.org/abstract_S0022112075003047.

S. Marchi, R.M. Canup, and R.J. Walker. Heterogeneous delivery of silicate and metal to the Earth by large planetesimals. *Nature Geoscience*, 11(1) :77–81, January 2018. ISSN 1752-0894, 1752-0908. doi : 10.1038/s41561-017-0022-3. URL http://www.nature.com/articles/s41561-017-0022-3.

P. Marmottant and E. Villermaux. Fragmentation of stretched liquid ligaments. *Physics of Fluids*, 16(8) :2732–2741, August 2004. ISSN 1070-6631, 1089-7666. doi : 10.1063/1.1756030. URL http://aip.scitation.org/doi/10.1063/1.1756030.

C. MartíNez-BazáN, J. L. MontañéS, and J. C. Lasheras. On the breakup of an air bubble injected into a fully developed turbulent flow. Part 1. Breakup frequency. *Journal of Fluid Mechanics*, 401 :157–182, December 1999. ISSN 00221120. doi : 10.1017/S0022112099006680. URL http://www.journals.cambridge.org/abstract_S0022112099006680.

T. Maxworthy. The observed motion of a sphere through a short, rotating cylinder of fluid. *Journal of Fluid Mechanics*, 31(04) :643, March 1968. ISSN 0022-1120, 1469-7645. doi : 10.1017/S0022112068000388. URL http://www.journals.cambridge.org/abstract_S0022112068000388.

T. Maxworthy. Turbulent vortex rings. *Journal of Fluid Mechanics*, 64(02) :227, June 1974. ISSN 0022-1120, 1469-7645. doi : 10.1017/S0022112074002370. URL http://www.journals.cambridge.org/abstract_S0022112074002370.

E. Mayer. Theory of liquid atomization in high velocity gas streams, 1961.

J.C. Meng and T. Colonius. Numerical simulation of the aerobreakup of a water droplet. *Journal of Fluid Mechanics*, 835 :1108–1135, January 2018. ISSN 0022-1120, 1469-7645. doi : 10.1017/jfm.2017.804. URL https://www.cambridge.org/core/product/identifier/S0022112017008047/type/journal_article.

R. Merk, D. Breuer, and T. Spohn. Numerical Modeling of 26al-Induced Radioactive Melting of Asteroids Considering Accretion. *Icarus*, 159(1) :183–191, September 2002. ISSN 00191035. doi : 10.1006/icar.2002.6872. URL http://linkinghub.elsevier.com/retrieve/pii/S0019103502968727.

P. Meunier and T. Leweke. Analysis and treatment of errors due to high velocity gradients in particle image velocimetry. *Experiments in Fluids*, 35(5) :408–421, November 2003. ISSN 0723-4864, 1432-1114. doi : 10.1007/s00348-003-0673-2. URL http://link.springer.com/10.1007/s00348-003-0673-2.

E. Michaelides. *Particles, bubbles & drops : their motion, heat and mass transfer*. World Scientific, Hackensack, NJ, 2006. ISBN 978-981-256-647-8 978-981-256-648-5. OCLC : ocm70861465.

C.A. Miller and L.E. Scriven. The oscillations of a fluid droplet immersed in another fluid. *Journal of Fluid Mechanics*, 32(03) :417, May 1968. ISSN 0022-1120, 1469-7645. doi : 10.1017/S0022112068000832. URL http://www.journals.cambridge.org/abstract_S0022112068000832.

J. Monteux, N. Coltice, F. Dubuffet, and Y. Ricard. Thermo-mechanical adjustment after impacts during planetary growth. *Geophysical Research Letters*, 34(24), December 2007. ISSN 0094-8276. doi : 10.1029/2007GL031635. URL http://doi.wiley.com/10.1029/2007GL031635.

D.W. Moore. The velocity of rise of distorted gas bubbles in a liquid of small viscosity. *Journal of Fluid Mechanics*, 23(04) :749, December 1965. ISSN 0022-1120, 1469-7645. doi : 10.1017/S0022112065001660. URL http://www.journals.cambridge.org/abstract_S0022112065001660.

B. R. Morton, G. Taylor, and J. S. Turner. Turbulent gravitational convection from maintained and instantaneous sources. In *Proceedings of the Royal Society of London A : Mathematical, Physical and Engineering Sciences*, volume 234, pages 1–23. The Royal Society, 1956. URL http://rspa.royalsocietypublishing.org/content/234/1196/1.short.

W. Neumann, D. Breuer, and T. Spohn. Differentiation and core formation in accreting planetesimals. *Astronomy & Astrophysics*, 543 :A141, July 2012. ISSN 0004-6361, 1432-0746. doi : 10.1051/0004-6361/201219157. URL http://www.aanda.org/10.1051/0004-6361/201219157.

W. Ockham. *Quaestiones et decisiones in quatuor libros Sententiarum cum centilogio theologico*, volume 2. 1319.

M. Ohta and M. Sussman. The buoyancy-driven motion of a single skirted bubble or drop rising through a viscous liquid. *Physics of Fluids (1994-present)*, 24(11) : 112101, 2012. URL http://scitation.aip.org/content/aip/journal/pof2/24/11/10.1063/1.4765669.

M. Ohta, S. Yamaguchi, Y. Yoshida, and M. Sussman. The sensitivity of drop motion due to the density and viscosity ratio. *Physics of Fluids*, 22(7) :072102, 2010. ISSN 10706631. doi : 10.1063/1.3460906. URL http://scitation.aip.org/content/aip/journal/pof2/22/7/10.1063/1.3460906.

M. Ohta, Y. Akama, Y. Yoshida, and M. Sussman. Influence of the viscosity ratio on drop dynamics and breakup for a drop rising in an immiscible low-viscosity liquid. *Journal of Fluid Mechanics*, 752 :383–409, August 2014. ISSN 0022-1120, 1469-7645. doi : 10.1017/jfm.2014.339. URL http://www.journals.cambridge.org/abstract_S0022112014003395.

Eiji Ohtani, Hisayoshi Yurimoto, and Shuji Seto. Element partitioning between metallic liquid, silicate liquid, and lower-mantle minerals : implications for core formation of the Earth. *Physics of the Earth and Planetary Interiors*, 100(1-4) :97–114, March 1997. ISSN 00319201. doi : 10.1016/S0031-9201(96)03234-7. URL http://linkinghub.elsevier.com/retrieve/pii/S0031920196032347.

P. Olson and D. Weeraratne. Experiments on metal-silicate plumes and core formation. *Philosophical Transactions of the Royal Society A : Mathematical, Physical and Engineering Sciences*, 366(1883) :4253–4271, November 2008. ISSN 1364-503X, 1471-2962.

doi : 10.1098/rsta.2008.0194. URL http://rsta.royalsocietypublishing.org/cgi/doi/10.1098/rsta.2008.0194.

A.T. Onufriev. Theory of the motion of a vortex ring under gravity. Rise of the cloud from a nuclear explosion. *Journal of Applied Mechanics and Technical Physics*, 8 (2) :1–7, 1971. ISSN 0021-8944, 1573-8620. doi : 10.1007/BF00918021. URL http://link.springer.com/10.1007/BF00918021.

P.J. O'Rourke and A.A. Amsden. The tab method for numerical calculation of spray droplet breakup. 1 1987.

P.D. Patel and T.G. Theofanous. Hydrodynamic fragmentation of drops. *Journal of Fluid Mechanics*, 103(-1) :207, February 1981. ISSN 0022-1120, 1469-7645. doi : 10.1017/S0022112081001304. URL http://www.journals.cambridge.org/abstract_S0022112081001304.

M. Petitti, A. Nasuti, D.L. Marchisio, M. Vanni, G. Baldi, N. Mancini, and F. Podenzani. Bubble size distribution modeling in stirred gas-liquid reactors with QMOM augmented by a new correction algorithm. *AIChE Journal*, 56(1) :36–53, January 2010. ISSN 00011541. doi : 10.1002/aic.12003. URL http://doi.wiley.com/10.1002/aic.12003.

Miriam Petitti, Marco Vanni, Daniele L. Marchisio, Antonio Buffo, and Fabrizio Podenzani. Simulation of coalescence, break-up and mass transfer in a gas–liquid stirred tank with CQMOM. *Chemical Engineering Journal*, 228 :1182–1194, July 2013. ISSN 13858947. doi : 10.1016/j.cej.2013.05.047. URL http://linkinghub.elsevier.com/retrieve/pii/S1385894713006670.

M. Pilch and C.A. Erdman. Use of breakup time data and velocity history data to predict the maximum size of stable fragments for acceleration-induced breakup of a liquid drop. *International Journal of Multiphase Flow*, 13(6) :741–757, November 1987. ISSN 03019322. doi : 10.1016/0301-9322(87)90063-2. URL http://linkinghub.elsevier.com/retrieve/pii/0301932287900632.

H. Rahimipour. Dynamic behavior of particle clouds. In *11th International Fluid Dynamics Conference*, pages 743–746, 1992.

A.A. Ranger and J.A Nicholls. Atomization of liquid droplets in a convective gas stream. *International Journal of Heat and Mass Transfer*, 15(6) :1203–1211, June 1972. ISSN 00179310. doi : 10.1016/0017-9310(72)90185-8. URL http://linkinghub.elsevier.com/retrieve/pii/0017931072901858.

W.E. Ranz. Applications of a stretch model to mixing, diffusion, and reaction in laminar and turbulent flows. *AIChE Journal*, 25(1) :41–47, January 1979. ISSN 0001-1541, 1547-5905. doi : 10.1002/aic.690250105. URL http://doi.wiley.com/10.1002/aic.690250105.

B. Ray and A. Prosperetti. On skirted drops in an immiscible liquid. *Chemical Engineering Science*, 108 :213–222, April 2014. ISSN 00092509. doi : 10.1016/j.ces.2014.01.007. URL http://linkinghub.elsevier.com/retrieve/pii/S0009250914000098.

Lord Rayleigh. On the capillary phenomena of jets. *Proc. R. Soc. London*, 29(196-199) : 71–97, 1879.

C Reese and V Solomatov. Fluid dynamics of local martian magma oceans. *Icarus*, 184 (1) :102–120, September 2006. ISSN 00191035. doi : 10.1016/j.icarus.2006.04.008. URL http://linkinghub.elsevier.com/retrieve/pii/S0019103506001308.

é. Reyssat, F. Chevy, A.-L. Biance, L. Petitjean, and D. Quéré. Shape and instability of free-falling liquid globules. *Europhysics Letters (EPL)*, 80(3) : 34005, November 2007. ISSN 0295-5075, 1286-4854. doi : 10.1209/0295-5075/80/34005. URL http://stacks.iop.org/0295-5075/80/i=3/a=34005?key=crossref.4e32996390c5c8fa3fe0ad731157acd9.

J.M. Richards. Experiments on the penetration of an interface by buoyant thermals. *Journal of Fluid Mechanics*, 11(03) :369, November 1961. ISSN 0022-1120, 1469-7645. doi : 10.1017/S0022112061000585. URL http://www.journals.cambridge.org/abstract_S0022112061000585.

F. Risso and J. Fabre. Oscillations and breakup of a bubble immersed in a turbulent field. *Journal of Fluid Mechanics*, 372 :323–355, October 1998. ISSN 00221120. doi : 10.1017/S0022112098002705. URL http://www.journals.cambridge.org/abstract_S0022112098002705.

G.G. Rooney. Descent and spread of negatively buoyant thermals. *Journal of Fluid Mechanics*, 780 :457–479, October 2015. ISSN 0022-1120, 1469-7645. doi : 10.1017/jfm.2015.484. URL http://www.journals.cambridge.org/abstract_S002211201500484X.

P. M. Rose and R. C. Kintner. Mass transfer from large oscillating drops. *AIChE Journal*, 12(3) :530–534, May 1966. ISSN 0001-1541, 1547-5905. doi : 10.1002/aic.690120325. URL http://doi.wiley.com/10.1002/aic.690120325.

D.C. Rubie, H.J. Melosh, J.E. Reid, C. Liebske, and K. Righter. Mechanisms of metal–silicate equilibration in the terrestrial magma ocean. *Earth and Planetary Science Letters*, 205(3-4) :239–255, January 2003. ISSN 0012821X. doi : 10.1016/S0012-821X(02)01044-0. URL http://linkinghub.elsevier.com/retrieve/pii/S0012821X02010440.

D.C. Rubie, D.J. Frost, U. Mann, Y. Asahara, F. Nimmo, K.i Tsuno, P. Kegler, A. Holzheid, and H. Palme. Heterogeneous accretion, composition and core–mantle differentiation of the Earth. *Earth and Planetary Science Letters*, 301(1-2) :31–42, January 2011. ISSN 0012821X. doi : 10.1016/j.epsl.2010.11.030. URL http://linkinghub.elsevier.com/retrieve/pii/S0012821X10007375.

D.C. Rubie, S.A. Jacobson, A. Morbidelli, D.P. O'Brien, E.D. Young, J. de Vries, F. Nimmo, H. Palme, and D.J. Frost. Accretion and differentiation of the terrestrial planets with implications for the compositions of early-formed Solar System bodies and accretion of water. *Icarus*, 248 :89–108, March 2015a. ISSN 00191035. doi : 10.1016/j.icarus.2014.10.015. URL http://linkinghub.elsevier.com/retrieve/pii/S0019103514005545.

D.C. Rubie, F. Nimmo, and H.J. Melosh. Formation of the Earth's Core. In *Treatise on Geophysics*, pages 43–79. Elsevier, 2015b. ISBN 978-0-444-53803-1. URL http://linkinghub.elsevier.com/retrieve/pii/B9780444538024001548.

W. Rybczynski. Uber die fortschreitende Bewegung einer flussigen Kugel in einem zahen Medium. *Bull. Acad. Sci. Cracovie A*, 1 :40–46, 1911.

V. S. Safronov. The heating of the Earth during its formation. *Icarus*, 33(1) :3–12, 1978. URL http://www.sciencedirect.com/science/article/pii/0019103578900192.

V.S. Safronov. Evolution of the protoplanetary cloud and formation of the earth and the planets. page 212.

H. Samuel. A re-evaluation of metal diapir breakup and equilibration in terrestrial magma oceans. *Earth and Planetary Science Letters*, 313-314 :105–114, January 2012. ISSN 0012821X. doi : 10.1016/j.epsl.2011.11.001. URL http://linkinghub.elsevier.com/retrieve/pii/S0012821X11006406.

T.E.W. Schumann. Theoretical aspects of the size distribution of fog particles. *Quarterly Journal of the Royal Meteorological Society*, 66(285) :195–208, September 2007. ISSN 00359009, 1477870X. doi : 10.1002/qj.49706628508. URL http://doi.wiley.com/10.1002/qj.49706628508.

R.S. Scorer. Experiments on convection of isolated masses of buoyant fluid. *Journal of Fluid Mechanics*, 2(06) :583, August 1957. ISSN 0022-1120, 1469-7645. doi : 10.1017/S0022112057000397. URL http://www.journals.cambridge.org/abstract_S0022112057000397.

G.A. Simons. Entrainment by a rising thermal. *Physics of Fluids*, 16(12) :2060, 1973. ISSN 00319171. doi : 10.1063/1.1694266. URL https://aip.scitation.org/doi/10.1063/1.1694266.

P.G. Simpkins and E.L. Bales. Water-drop response to sudden accelerations. *Journal of Fluid Mechanics*, 55(04) :629, October 1972. ISSN 0022-1120, 1469-7645. doi : 10.1017/S0022112072002058. URL http://www.journals.cambridge.org/abstract_S0022112072002058.

D.J. Stevenson. Fluid dynamics of core formation. In *Topical Conference Origin of the Earth*, volume 681, page 87, 1988.

D.J. Stevenson. Fluid dynamics of core formation. *Origin of the Earth*, 1 :231–249, 1990.

M.J. Tan and S.G. Bankoff. On the Fragmentation of Drops. *Journal of Fluids Engineering*, 108(1) :109, 1986. ISSN 00982202. doi : 10.1115/1.3242528. URL http://FluidsEngineering.asmedigitalcollection.asme.org/article.aspx?articleid=1426396.

P. Tanga, P. Michel, and D. C. Richardson. Planetesimal clusters in a Keplerian disk : I. gravitational evolution. *Astronomy & Astrophysics*, 395(2) :613–623, November 2002. ISSN 0004-6361, 1432-0746. doi : 10.1051/0004-6361:20021274. URL http://www.aanda.org/10.1051/0004-6361:20021274.

A. Tarnogrodzki. Theory of free fall breakup of large drops. *International Journal of Mechanical Sciences*, 43(4) :883–893, April 2001. ISSN 00207403. doi : 10.1016/S0020-7403(00)00057-6. URL http://linkinghub.elsevier.com/retrieve/pii/S0020740300000576.

G. Taylor. The Dynamics of Thin Sheets of Fluid. II. Waves on Fluid Sheets. *Proceedings of the Royal Society A : Mathematical, Physical and Engineering Sciences*, 253(1274) : 296–312, December 1959. ISSN 1364-5021, 1471-2946. doi : 10.1098/rspa.1959.0195. URL http://rspa.royalsocietypublishing.org/cgi/doi/10.1098/rspa.1959.0195.

H. Tennekes, J.L. Lumley, J.L. Lumley, et al. *A first course in turbulence*. MIT press, 1972.

R.S. Thompson, W.H. Snyder, and J.C. Weil. Laboratory simulation of the rise of buoyant thermals created by open detonation. *Journal of Fluid Mechanics*, 417 : 127–156, August 2000. ISSN 00221120. doi : 10.1017/S0022112000001191. URL http://www.journals.cambridge.org/abstract_S0022112000001191.

W. Brian Tonks and H. Jay Melosh. Core formation by giant impacts. *Icarus*, 100(2) : 326–346, December 1992. ISSN 00191035. doi : 10.1016/0019-1035(92)90104-F. URL http://linkinghub.elsevier.com/retrieve/pii/001910359290104F.

W.B. Tonks and H.J. Melosh. Magma ocean formation due to giant impacts. *Journal of Geophysical Research*, 98(E3) :5319, 1993. ISSN 0148-0227. doi : 10.1029/92JE02726. URL http://doi.wiley.com/10.1029/92JE02726.

M.K. Tripathi, K.C. Sahu, and R. Govindarajan. Why a falling drop does not in general behave like a rising bubble. *Scientific Reports*, 4, April 2014. ISSN 2045-2322. doi : 10.1038/srep04771. URL http://www.nature.com/articles/srep04771.

J. S. Turner. Turbulent entrainment : the development of the entrainment assumption, and its application to geophysical flows. *Journal of Fluid Mechanics*, 173(-1) :431, December 1986. ISSN 0022-1120, 1469-7645. doi : 10.1017/S0022112086001222. URL http://www.journals.cambridge.org/abstract_S0022112086001222.

J.S. Turner. Buoyant vortex rings. *Proceedings of the Royal Society of London. Series A. Mathematical and Physical Sciences*, 239(1216) :61–75, April 1957. ISSN 2053-9169. doi : 10.1098/rspa.1957.0022. URL http://www.royalsocietypublishing.org/doi/10.1098/rspa.1957.0022.

J.S. Turner. A comparison between buoyant vortex rings and vortex pairs. *Journal of Fluid Mechanics*, 7(03) :419, March 1960. ISSN 0022-1120, 1469-7645. doi : 10.1017/S0022112060000189. URL http://www.journals.cambridge.org/abstract_S0022112060000189.

J.S. Turner and G.I. Taylor. Buoyant vortex rings. *Proceedings of the Royal Society of London. Series A. Mathematical and Physical Sciences*, 239(1216) :61–75, April 1957. ISSN 2053-9169. doi : 10.1098/rspa.1957.0022. URL http://www.royalsocietypublishing.org/doi/10.1098/rspa.1957.0022.

M. Ulvrová, N. Coltice, Y. Ricard, S. Labrosse, F. Dubuffet, J. Velímský, and O. rámek. Compositional and thermal equilibration of particles, drops, and diapirs in geophysical flows. *Geochemistry, Geophysics, Geosystems*, 12(10) :n/a–n/a, October 2011. ISSN 15252027. doi : 10.1029/2011GC003757. URL http://doi.wiley.com/10.1029/2011GC003757.

J.H. Vanderveen. Coalescence and dispersion rates in agitated liquid-liquid systems.(thesis). Technical report, California. Univ., Berkeley. Lawrence Radiation Lab., 1960.

A.R. Vasel-Be-Hagh, R. Carriveau, and D.S.-K. Ting. A balloon bursting underwater. *Journal of Fluid Mechanics*, 769 :522–540, April 2015. ISSN 0022-1120, 1469-7645. doi : 10.1017/jfm.2015.126. URL http://www.journals.cambridge.org/abstract_S0022112015001263.

E. Villermaux. Fragmentation. *Annual Review of Fluid Mechanics*, 39(1) :419–446, January 2007. ISSN 0066-4189, 1545-4479. doi : 10.1146/annurev.fluid.39.050905.110214. URL http://www.annualreviews.org/doi/10.1146/annurev.fluid.39.050905.110214.

E. Villermaux. On shapes and forms : Population balance dynamics of corrugated stirred fronts. *Comptes Rendus Physique*, 19(5) :306–315, July 2018. ISSN 16310705. doi : 10.1016/j.crhy.2018.10.009. URL https://linkinghub.elsevier.com/retrieve/pii/S1631070518300756.

E. Villermaux and B. Bossa. Single-drop fragmentation determines size distribution of raindrops. *Nature Physics*, 5(9) :697–702, September 2009. ISSN 1745-2473, 1745-2481. doi : 10.1038/nphys1340. URL http://www.nature.com/doifinder/10.1038/nphys1340.

E. Villermaux and B. Bossa. Drop fragmentation on impact. *Journal of Fluid Mechanics*, 668 :412–435, February 2011. ISSN 0022-1120, 1469-7645. doi : 10.1017/S002211201000474X. URL http://www.journals.cambridge.org/abstract_S002211201000474X.

E. Villermaux and J. Duplat. Mixing as an Aggregation Process. *Physical Review Letters*, 91(18), October 2003. ISSN 0031-9007, 1079-7114. doi : 10.1103/PhysRevLett.91.184501. URL https://link.aps.org/doi/10.1103/PhysRevLett.91.184501.

E. Villermaux, Ph. Marmottant, and J. Duplat. Ligament-Mediated Spray Formation. *Physical Review Letters*, 92(7), February 2004. ISSN 0031-9007, 1079-7114. doi : 10.1103/PhysRevLett.92.074501. URL https://link.aps.org/doi/10.1103/PhysRevLett.92.074501.

E. Villermaux, V. Pistre, and H. Lhuissier. The viscous Savart sheet. *Journal of Fluid Mechanics*, 730 :607–625, September 2013. ISSN 0022-1120, 1469-7645. doi : 10.1017/jfm.2013.354. URL http://www.journals.cambridge.org/abstract_S0022112013003546.

J-B. Wacheul and M. Le Bars. Experiments on fragmentation and thermo-chemical exchanges during planetary core formation. *Physics of the Earth and Planetary Interiors*,

276 :134–144, March 2018. ISSN 00319201. doi : 10.1016/j.pepi.2017.05.018. URL https://linkinghub.elsevier.com/retrieve/pii/S0031920117300262.

J-B. Wacheul, M. Le Bars, J. Monteux, and J.M. Aurnou. Laboratory experiments on the breakup of liquid metal diapirs. *Earth and Planetary Science Letters*, 403 : 236–245, October 2014. ISSN 0012821X. doi : 10.1016/j.epsl.2014.06.044. URL http://linkinghub.elsevier.com/retrieve/pii/S0012821X1400435X.

J. Wade and B.J. Wood. Core formation and the oxidation state of the Earth. *Earth and Planetary Science Letters*, 236(1-2) :78–95, July 2005. ISSN 0012821X. doi : 10.1016/j.epsl.2005.05.017. URL http://linkinghub.elsevier.com/retrieve/pii/S0012821X05003286.

M. Wadhwa, G. Srinivasan, and R.W. Carlson. Timescales of Planetesimal Differentiation in the Early Solar System. page 17, 2015.

T. Wairegi and J. R. Grace. The behaviour of large drops in immiscible liquids. *International Journal of Multiphase Flow*, 3(1) :67–77, 1976. URL http://www.sciencedirect.com/science/article/pii/0301932276900367.

M.J. Walter and R.G. Trønnes. Early Earth differentiation. *Earth and Planetary Science Letters*, 225(3-4) :253–269, September 2004. ISSN 0012821X. doi : 10.1016/j.epsl.2004.07.008. URL http://linkinghub.elsevier.com/retrieve/pii/S0012821X04004285.

Y. Watanabe and D. M. Ingram. Size distributions of sprays produced by violent wave impacts on vertical sea walls. *Proceedings of the Royal Society A : Mathematical, Physical and Engineering Science*, 472(2194) :20160423, October 2016. ISSN 1364-5021, 1471-2946. doi : 10.1098/rspa.2016.0423. URL http://rspa.royalsocietypublishing.org/lookup/doi/10.1098/rspa.2016.0423.

Stuart J. Weidenschilling. Formation of Planetesimals and Accretion of the Terrestrial Planets. In W. Benz, R. Kallenbach, and G. W. Lugmair, editors, *From Dust to Terrestrial Planets*, volume 9, pages 295–310. Springer Netherlands, Dordrecht, 2000. ISBN 978-94-010-5807-0 978-94-011-4146-8. doi : 10.1007/978-94-011-4146-8_19. URL http://www.springerlink.com/index/10.1007/978-94-011-4146-8_19.

A. Wierzba. Deformation and breakup of liquid drops in a gas stream at nearly critical Weber numbers. *Experiments in Fluids*, 9(1-2) :59–64, 1990. ISSN 0723-4864, 1432-1114. doi : 10.1007/BF00575336. URL http://link.springer.com/10.1007/BF00575336.

B.J. Wood, J. Wade, and M.R. Kilburn. Core formation and the oxidation state of the Earth : Additional constraints from Nb, V and Cr partitioning. *Geochimica et Cosmochimica Acta*, 72(5) :1415–1426, March 2008. ISSN 00167037. doi : 10.1016/j.gca.2007.11.036. URL http://linkinghub.elsevier.com/retrieve/pii/S0016703708000173.

B. Woodward. The motion in and around isolated thermals. *Quarterly Journal of the Royal Meteorological Society*, 85(364) :144–151, April 1959. ISSN 00359009, 1477870X. doi : 10.1002/qj.49708536407. URL http://doi.wiley.com/10.1002/qj.49708536407.

J.-W. Yang and H.-S. Yang. Liquid-liquid mixing for the breakup of accelerating drops. *Korean Journal of Chemical Engineering*, 7(1) :22–30, January 1990. ISSN 0256-1115, 1975-7220. doi : 10.1007/BF02697338. URL http://link.springer.com/10.1007/BF02697338.

M.A. Zeitlin and L.L. Tavlarides. Fluid-fluid interactions and hydrodynamics in agitated dispersions : A simulation model. *The Canadian Journal of Chemical Engineering*, 50 (2) :207–215, April 1972. ISSN 00084034, 1939019X. doi : 10.1002/cjce.5450500212. URL http://doi.wiley.com/10.1002/cjce.5450500212.

Abstract :
The accretion of terrestrial planets like Earth proceeds partly by impacts of proto-planets already differentiated in a silicate mantle and an iron core. Those impacts result in a two phase flow where the two main components of the planets partially mix for the last time. In order to study the conditions of diffusive transfer of heat and elements during this flow, we have performed experiments using an analog system of fluids. A gallium alloy is used to represent the molten iron core and a viscous fluid is used to represent the molten silicate mantle. Video recordings of the fall of liquid metal spheroids through the viscous fluid are analyzed as a way to study the dynamics of the post impact flow. Measurements of the temperature of the liquid metal before and after its fall are performed in order to probe the conditions of the diffusive transfer between the two phases integrated along the fall. The diapir is found to dilute by entraining ambient fluid during its fall in a manner that is well described by the entrainment hypothesis. Its falling speed is found to be larger than expected by the equations classically used with the turbulent entrainment hypothesis (turbulent thermal) during the phase prior to breakup. A model is proposed to explain these discrepancies by assuming a link between the organization of the flow and the drag coefficient. The fragmentation of the liquid metal is quantified in terms of the breakup distance, the mean radius of the droplets as a function of the spheroid's initial radius and the distribution of sizes of the droplets. The mean radius of the droplets is marked by the large scale falling speed which we interpret as a sign of a continuous breakup process. The distribution of sizes is given by a Bessel function whose parameter is consistent with a single origin but suggests a wide distribution of ligament sizes from the breakup during which droplets are formed. The data on the dynamics, on the fragmentation and on the temperature are then used to test the existing thermal equilibration models between the two phases. A general procedure for quantifying the diffusive exchanges between liquid iron and molten silicate in the post impact flow is then proposed.

Résumé :
L'accrétion de planètes telluriques comme la Terre se déroule par collisions successives entre proto-planètes déjà différenciées en un manteau de silicate et un noyau de fer. Le résultat de ces impacts est un écoulement diphasique qui est la dernière occasion pour les deux composants principaux des planètes de partiellement se mélanger. Afin d'étudier les conditions des échanges diffusifs de chaleur et d'éléments chimiques dans cet écoulement, nous avons fait des expériences sur un système de fluide analogue. Le fer liquide est représenté par un alliage de gallium et l'océan de magma est représenté par un liquide visqueux. Les vidéos de la chute d'un sphéroïde de métal liquide dans le fluide visqueux sont analysées par ordinateur pour en extraire la dynamique de l'écoulement post-impact. La température du métal liquide avant et après sa chute est mesurée dans le but d'analyser les conditions des échanges diffusifs entre les deux phases intégrées sur toute la chute. Nous montrons que la dilution du diapir produit par l'entrainement de fluide ambient au cours de sa chute suit l'hypothèse d'entrainement turbulent. Sa vitesse de chute est plus grande que prévu par les équations habituellement utilisé avec l'hypothèse d'entrainement turbulent (le thermique turbulent) pendant la phase précédant la fragmentation. Nous proposons un modèle expliquant ces écarts en faisant l'hypothèse d'un lien entre l'organisation de l'écoulement et le coefficient de trainée. La fragmentation du métal liquide est caractérisée par la mesure de la distance de fragmentation, par la mesure du rayon moyen des gouttes produites en fonction du rayon initial du diapir et par la mesure de la distribution des

tailles de goutte. La distribution est donnée par une fonction de Bessel dont les paramètres sont cohérents avec un unique mécanisme mais indique une distribution ample de taille des ligaments se fragmentant en gouttes. Les données sur la dynamique, sur la fragmentation et sur la température sont ensuite utilisées pour tester les différents modèles d'équilibration entre les deux phases. Nous proposons en conclusion une procédure pour calculer les échanges diffusifs entre le fer et les silicates pendant l'écoulement post-impact.